UNIVERSITY OF SOUTHAMPTON

FACULTY OF PHYSICAL SCIENCES AND ENGINEERING

Optoelectronics Research Centre

Power Scaling Architectures for Solid-State and Fiber Lasers

By

Callum Robertson Smith

Thesis for the degree of Doctor of Philosophy

September 2017

UNIVERSITY OF SOUTHAMPTON

<u>ABSTRACT</u>

FACULTY OF PHYSICAL SCIENCES AND ENGINEERING

Optoelectronics Research Centre

<u>Doctor of Philosophy</u>

Power Scaling Architectures for Solid-State and Fiber Lasers

By Callum Robertson Smith

This thesis focuses on developing power scaling architectures for solid-state and fiber lasers. The thermally-guided fiber-rod (TGFR) laser is suggested as a novel power scalable concept. This device lies in a domain between bulk rod lasers and traditional fiber lasers. The motivation is to benefit from the excellent thermal management properties of fibers, whilst negating deleterious nonlinear effects owing to the tight beam confinement and long interaction lengths that plague high power fiber lasers. An elegant thermal guiding technique is proposed to provide mode control with the TGFR. We derive the refractive index profile that ensues as a result of end-pumping the TGFR with a fiber-coupled diode laser. Furthermore, we construct a model that predicts the resulting impact on Gaussian beam propagation through the TGFR for various pump configurations. A model describing the gain within the device is derived from the laser rate equations. These two models allow us to predict amplifier and laser performance of the TGFR device.

We initially suggest soft glass as a host material for the TGFR, owing to the ability to dope this material with rare-earth ions in significantly higher concentrations than silica which is the traditional material of choice for fiber lasers, thus allowing the realisation of shorter devices. The requirements of a soft glass host are discussed in terms of both device fabrication and laser operation. Three potential sources are identified, including an in-house manufactured neodymium-doped and undoped phosphate glass, a commercial neodymium-doped and undoped silicate glass, and a neodymium-doped and undoped phosphate glass obtained through collaboration. The fabrication of potential TGFR devices with these three sources is described. This is followed by a laser investigation of these devices, where the issues of glass homogeneity and transmission loss become apparent, which are largely attributed to poor glass quality and unsuitable compatibility between the doped and undoped glasses. The neodymium-doped phosphate obtained through collaboration performed best, with a maximum output power around 1054nm of 2.5W, with a slope efficiency with respect to launched pump power of 28.5%. However, the poor glass quality

prevented the thermal guiding investigation, and thus the beam quality was dictated by the highly multimode guide, resulting in a beam propagation factor of $M^2 = 60$. Additionally, although this device had the lowest loss of the three sources, a significant loss of 5.7dB/m was measured using the Findlay-Clay analysis.

In light of these glass quality issues, the TGFR concept was fully tested using an extra-large mode area silica fiber. A mode guiding investigation revealed that an in-built non-uniform refractive index profile was responsible for providing a degree of guiding, even in the absence of pumping. This guiding was well predicted by assuming a parabolic refractive index profile and utilising the mode guiding model. Furthermore, the thermal guiding model gave excellent agreement with measured data across a range of launched pump powers up to 30W. The device was operated as an amplifier for seed beams at 976nm and 1030nm, and good agreement with the gain model was observed. At 976nm a maximum gain of 4.1dB was achieved for a 60mW seed resulting in an output power of 155mW, and 2.2dB for a 450mW seed resulting in an output power of 750mW. For 1030nm a maximum gain of 5.0dB was achieved for a 50mW seed resulting in an output power of 160mW, and 3.9dB for a 1.1W seed resulting in an output power of 2.7W. Excellent beam quality was maintained throughout amplification with $M^2 < 1.1$ at the maximum gain levels for both 976nm and 1030nm. The concept was extended to a laser configuration at for both the 975nm and 1030nm transition. A device operating at 1032.5nm achieving a maximum output power of 13.1W with a slope efficiency of 44% with respect to launched power and 53% with respect to absorbed power. Excellent beam quality was achieved at maximum output power with $M^2 < 1.1$. Additionally, a device operating at 978.5nm achieved a maximum output power of 1W with a slope efficiency of 8% with respect to launched power. Again, excellent beam quality was achieved at maximum output power with $M^2 < 1.1$. The slope efficiencies of both of these devices, particularly the latter, are expected to increase with higher pump powers.

An Yb:YAG thin-slab architecture is suggested as a power scalable architecture for cylindrical vector (CV) beams, which have promising applications within materials processing. A seed source is constructed for operation at 1030nm, which exploits thermally-induced bi-focusing to produce a radially polarised output beam with a maximum output power of 6.9W, with a conversion efficiency of 41% with respect to absorbed pump power. The beam quality was measured as $M^2 = 2.3$, whilst the radial polarisation extinction ratio (RPER) was > 15dB. It was demonstrated that the seed source could be amplified in a highly asymmetric thin-slab gain medium whilst maintaining radial polarisation purity. The implications of the Gouy phase shift owing to astigmatic focusing within the slab are discussed. Amplifier experiments yielded a gain of 7.5dB for a 25mW seed input power, and 4.4dB for a 1.45W seed input power, resulting in a maximum output power of 4W. The beam propagation factor at the maximum gain level was maintained at the lowest seed input power at $M^2 = 2.3$, and was only slightly degraded to $M^2 = 2.4$ at the highest seed input powers. Crucially, the RPER was maintained at >15dB for both cases.

Contents

List of Tables

List of Figures

Declaration of Authorship

I, Callum Robertson Smith, declare that the thesis entitled *Power Scaling Architectures for Solid-State and Fiber Lasers* and the work presented in it are my own and has been generated by me as the result of my own original research.

I confirm that:

1. This work was done wholly or mainly while in candidature for a research degree at this University;
2. Where any part of this thesis has previously been submitted for a degree or any other qualification at this University or any other institution, this has been clearly stated;
3. Where I have consulted the published work of others, this is always clearly attributed;
4. Where I have quoted from the work of others, the source is always given. With the exception of such quotations, this thesis is entirely my own work;
5. I have acknowledged all main sources of help;
6. Where the thesis is based on work done by myself jointly with others, I have made clear exactly what was done by others and what I have contributed myself;
7. Parts of this work have been published as journal papers and conference contributions listed in Appendix P.

Signed: ....

Date: ....

Acknowledgements

Without the incredible help of colleagues, friends and family I would not be in a position to submit this thesis. Firstly I would like to express my sincere gratitude to my Supervisor, Professor Andy Clarkson, for providing teaching, guidance, interesting experiments and countless hours of help over the past four years. I would also like to thank Dr. Bill Brocklesby for initially inspiring me to attempt this PhD, and for working to get me a position at the ORC. Furthermore, I would like to thank my co-supervisor Dr. Jacob Mackenzie for his help and direction through my four years at the ORC. I would also like to thank Fianium for their support, especially Dr. Mike Yarrow for useful discussions.

An enormous deal of thanks go to Dr. Stephen Beecher, who tirelessly answered my questions, no matter how big or small, and always did so in a manner that would inspire me. Likewise, Dr. Peter Shardlow was a constant source of inspiration, and was always willing to help with enthusiasm, providing guidance and ideas that proved essential to this work. I wish to thank Dr. Nikita Simakov for his direction and enthusiasm for my project. Special thanks go to Dr. Alex Butler and Dr. Matt Eckold for arming me with the basic knowledge needed to get started in a laser lab. I also wish to thank Dr. Di Lin, Dr. Sung Jin Yoon and Dr. Jaclyn Chan. I am extremely grateful to all the members of the Advance Solid-State Sources and Planar Waveguide group, especially Antonin, Henry, Stan, Robin and Florian, for both their academic help and their friendship. I would like to express my gratitude to Dr. Paul Bastock for his help with fiber fabrication, and to Mr. Tim Hoad and Mr. Mark Scully for their essential help in the mechanical workshop.

I owe a great deal of thanks to my amazing friends, particularly to all the guys down at NPR. Likewise, I would like to thank CHAPSOC for hosting countless excellent events over the last four years. I have been fortunate enough to live with great housemates during my time in Southampton, and would like to thank them all for making my time here so enjoyable. I would especially like to thank Julie for the love and happiness she gave me during my PhD.

Finally, the biggest thanks of all go to my family, who have provided for me in every way imaginable. Without their constant support I would not even be in a position to start this work, let alone finish it.

"Don't be afraid to fail.

Anything I have ever attempted, I was always willing to fail."

Arnold Schwarzenegger

List of Symbols

A, B, C, D	ABCD matrix parameters
A	Area
A_{ij}	Einstein A coefficient describing a transition between level i and level j
B_{ij}	Einstein B coefficient describing a transition between level i and level j
c	Speed of light
d_i	Distance
$\underline{E}$	Electric Field
E_i	Energy of energy level i
f	Focal length of a lens
g	Gain coefficient
g_i	Degeneracy of energy level i
$g(v_s, v_0)$	Lineshape function centred on v_0 for signal radiation centred on v_s
G	Gain
h	Planck's constant
h_T	Heat transfer coefficient
I	Intensity
k	Wavenumber
k_B	Boltzmann's constant
l_i	Length
L	Unwanted cavity losses
m	Grating diffraction order
M^2	Beam propagation factor
n	Refractive index
n_{th}	Rate of change of refractive index with radial distance
n_m	Maximum refractive index of parabolic refractive index profile
n_T	Total population density
N_i	Number of atomic systems in energy level i
N_T	Total number of atomic systems
NA	Numerical aperture
P	Power
q	Complex beam parameter
Q	Heat power deposition density
r	Radial coordinate
r_p	Pump rate density
r_0	Normalised pump rate density
R_T	Total pump rate

R_i	Mirror reflectivity of i
R_{OC}	Radius of curvature of beam wavefronts
R_S	Thermal shock parameter
t	Time
t_i	Thickness
T	Temperature
TR	Mirror transmission
v_p	Phase velocity of light
V	Volume
VN	V-number
w	Radius of laser mode
w_0	Radius of beam waist
x, y, z	Spatial coordinates in Cartesian space
z_R	Rayleigh range
α	Grating incident angle
$\alpha(v_s)$	Absorption/gain coefficient at v_s
β	Grating diffraction angle
dn/dT	Thermo-optic coefficient
φ	Phase
η_{abs}	Fraction of launched pump power that is absorbed
η_h	Fraction of absorbed power converted to heat
η_{QD}	Quantum defect
η_{QE}	Quantum efficiency
η_s	Slope efficiency
κ	Thermal conductivity
λ	Wavelength
v	Frequency
ξ	Angle between incident beam and surface normal for metal cutting
$\rho(v)$	Incident radiation energy density per unit frequency at central frequency v
$\sigma_{ij}(v_s)$	Transition cross-section for a transition from level i to level j
τ_c	Cavity lifetime
τ_f	Fluorescence lifetime of laser transition
τ_{ij}	Lifetime of a transition between level i and level j
τ_{RT}	Round-trip time
ϕ	Photon density
ϕ_0	Normalised photon density
Φ_T	Total number of photons in the cavity

θ	Azimuthal angle on beam cross-section
χ	Extinction coefficient of refractive index
Ψ_G	Gouy phase shift
ω_i	Width
Ω	Total number of pump photons required per unit time to maintain transparency
$\Im$	Imaginary part of inverse of complex beam parameter
$\mathbb{R}$	Real part of inverse of complex beam parameter
$\mathbb{X}$	Real part of complex beam parameter
$\mathbb{Y}$	Imaginary part of complex beam parameter

Chapter 1 Introduction

Lasers are truly remarkable. These extraordinary devices have been manipulated to recreate the tremendous pressure and temperature conditions present in the core of a star [1]. Lasers designed with incredible accuracy are able *feel* ripples in the fabric of space and time, resulting from the merger of distant black holes [2]. Operating as a source of ultrashort pulses, lasers have produced the shortest events under our control [3], allowing the dynamics of electron interactions to be investigated in an unprecedented manner. These are merely a few examples of the groundbreaking developments that have stemmed from the birth of the laser.

1.1   Lasers

The exceptional attributes of directionality and spectral purity are unique to laser radiation. These properties allow lasers to propagate over long distances as thin beams of light, occupying a narrow wavelength band. The underlying explanation for this unique light source lies in coherence, which ensures the oscillating electric field of the laser emission has a fixed phase relationship in space and time. Spatial coherence across the cross-section of a laser beam is maximised for the lowest-order fundamental propagation mode. These diffraction-limited modes can be tightly focused to dimensions on the scale of a wavelength, and will diffract at a slower rate compared to lower quality laser beams. High temporal coherence implies the electric fields oscillate with a fixed phase relationship at a single location over time. Certain lasers are constrained to operate on a single longitudinal mode, thereby achieving excellent temporal coherence since the electric field will evolve as a pure sinusoid. In contrast, supercontinuum lasers emit radiation across a broad spectrum, and therefore display relatively low temporal coherence. Coherence, and in particular spatial coherence between emitted photons, demonstrates the clearest distinction between laser light and other sources of light such as sunlight or an incandescent bulb. These incoherent sources emit photons with a random direction and spectral phase, and therefore cannot realise the unique properties achieved by lasers.

As with much of our modern day understanding of physics, the original seeds of the laser concept were planted by the great mind of Albert Einstein, when in 1917 he postulated the pivotal idea of stimulated emission [4]. Stimulated emission is essential to understanding the laser concept, and consequently is responsible for its name: **L**ight **A**mplification by **S**timulated **E**mission of **R**adiation. This concept states that a laser ion in an excited state can be stimulated by an incoming photon, resulting in the emission of a second photon which is indistinguishable from the stimulating photon, possessing the same directional, spectral, phase and polarisation properties. Thus the stimulated photon is coherent with the stimulating photon. Furthermore, the presence of a population inversion

between two energy levels can lead to coherent amplification and ultimately laser emission. This concept was first realised in the microwave regime by Charles Townes in the mid-1950s [5]. In 1958 Arthur Schawlow and Townes developed the theory to extend the maser into the optical regime, suggesting feedback for oscillating radiation could be provided by a Fabry-Perot resonator [6]. The first laser device was demonstrated with a flashlamp pumped ruby rod laser in 1960 by Theodore Maiman [7].

Today, almost sixty years after its invention, the excellent properties of lasers are essential in numerous applications such as materials processing, which includes and is not limited to cutting, drilling, welding, surface treatment and engraving. Lasers in the form of optical fibers are employed to provide high capacity data transmission over long distances, contributing to the infrastructure of the internet. The military utilises lasers for tasks such as rangefinding, target illumination, target designation and for countermeasures. Lasers are exploited in medicine in areas including vision correction and surgery. Exciting scientific research such as inertial confinement fusion and gravitational wave detection make use of laser devices. Other applications include data storage, microscopy and the entertainment industry.

Clearly, a particular laser should have properties that are well suited to its intended application. In the years following its birth, lasing was demonstrated in a range of geometries and in a whole host of materials including crystals, glasses, gases, semiconductors and liquids. Lasers can be operated to produce a constant output power, known as continuous-wave (cw) operation, or they can be pulsed via techniques including Q-switching, gain-switching and mode-locking. Thus, depending on the application, parameters such as average power, peak power, pulse energy and repetition rate will take precedence.

The orientation of electric field oscillation, known as the polarisation, constitutes another important parameter of laser radiation that should be considered. Traditional polarisation states, such as linear or circular polarisation, are often desired. However exotic cylindrical vector (CV) beams with spatially inhomogeneous polarisation distributions are attracting growing interest, particularly beams with radial and azimuthal polarisation states, which form an interesting subset of CV beams. These unique beams can form doughnut-shaped intensity distributions owing to a polarisation discontinuity at the centre, and have been shown to have promising applications with particle trapping [8], high-resolution imaging [9], and materials processing where they have demonstrated higher cutting and drilling efficiencies when compared to traditional polarisation states [10, 11].

1.2   Power Scaling Solid-State Lasers

Many of the discussed applications, such as those within the military and materials processing, and a whole host of emerging applications, require lasers with high power (average and/or peak) and excellent beam quality. The objective of this thesis is to design, demonstrate and analyse novel

laser concepts that are capable of scaling output power. Whilst the demonstrations within this thesis consider cw operation, it should be noted that the techniques are equally applicable to pulsed operation.

This thesis will concentrate on power scaling techniques for solid-state lasers. Solid-state lasers based on crystal and glass hosts doped with laser-active ions constitute the most versatile source of laser radiation. Typically the host material is doped with rare-earth ions providing radiation in the near-infrared region. These systems display impressive performance across a range of parameters including good efficiency, high pulse energy, high peak power, high average power and excellent beam quality. There is huge flexibility in the geometry of the laser medium, with solid-state lasers broadly being divided into bulk and fiber geometries.

Bulk lasers are typically based on a bulk piece of rare-earth doped crystal or glass, with common designs including the rod, slab and thin-disc. Generally, these devices can deliver high pulse energies and peak powers, but are limited by deleterious thermal effects that arise as a result of high power operation. Effects such as thermal lensing and stress-induced birefringence can act to distort the laser beam, whilst thermally-induced fracture can result in catastrophic failure of the device. Therefore, the design of these devices for high power operation is usually focused on providing effective thermal management. For example, the design of the slab laser, which provides a large cooling area in close proximity to the heated region, provides a superior power-handling capability compared to the rod laser, however the effects of thermal lensing and stress-induced birefringence are an issue. The thin-disc laser provides an example of a design which provides excellent thermal management, and is a clear frontrunner for high power bulk lasers. This results from its extreme geometry which establishes an essentially axial heat flow, allowing it to largely bypass thermal degradation effects. Consequently, 4kW of average power has been achieved from a single-disc laser with impressive beam quality [12].

Fiber lasers constituent another extreme, fabricated from rare-earth-doped glass into a long, thin structure. This geometry provides a large surface area to volume ratio, allowing the fiber to display excellent thermal management properties. The fiber laser was originally demonstrated in 1961 [13], however it was not until 1985, with the development of a low-loss fabrication technique for silica fibers [14], that these devices began to show their true potential as high power lasers. Today, fiber lasers have evolved dramatically, and are fabricated with a range of materials, taking various forms including microstructured and very large core area designs. Furthermore, fiber lasers have reached the 10kW level with diffraction limited beam quality [15]. Unlike their bulk counterparts, the laser modes within a fiber are guided by total internal reflection, leading to very high intensities over long interaction lengths. This environment favours nonlinear effects which can act to shift power to undesired spectral regions and act to destabilise laser operation. Additionally, the tight confinement

of radiation can lead to laser-induced damage in the fiber core. Thus further power scaling in fiber devices, and particularly the scaling of peak power, is limited by these nonlinear effects. The energy storage, and therefore the ability to extract high pulse energies, is limited by amplified spontaneous emission which acts to deplete the upper-state population in these high gain devices.

1.3   Thesis Overview

Following this brief introduction to the topic of interest; this thesis will begin in Chapter 2, where we will introduce background theory relevant to laser devices. Here we will mathematically describe essential concepts of laser operation including gain and the energy level systems required to achieve a population inversion. We will introduce the concept of the laser resonator and discuss performance in terms of output power. Finally, we will expand on the discussion above, explaining the origin and effect of high power limitations, followed by a description of how different solid-state geometries have been devised to overcome these limitations.

Chapter 3 introduces the concept of the thermally-guided fiber-rod (TGFR) laser, which forms the major component of this thesis. The TGFR has dimensions which fill the regime between traditional solid-state and fiber gain media. The motivation for this concept will be presented, covering the improved thermal management properties compared to bulk devices such as rod and slab lasers, and the improved immunity to nonlinear effects compared to fiber lasers. A unique aspect of the TGFR is the method of laser mode control, which utilises thermally-induced lensing to guide the mode through the device. A model will be presented which estimates the strength of the thermally-induced lensing effect and predicts the corresponding evolution of the guided laser mode. The chapter will conclude by introducing a model for predicting gain within the TGFR device, which will be useful for analysing power scaling potential.

In Chapter 4 we suggest neodymium-doped soft glass as a host material for the TGFR. Soft glasses exhibit a less defined glass network than silica; the traditional material of choice. Consequently, these materials can be doped with rare-earth ions in significantly higher concentrations, leading to shorter device lengths. Combining this with the physically larger transverse dimensions of the TGFR over traditional fibers will lead to reduced deleterious nonlinearities. Furthermore, these devices can be realised with excellent uniformity in doping concentration and refractive index, which will be extremely important for the proposed thermally-induced guiding technique. Therefore, in this chapter we will present the requirements of a soft glass host glass in terms of fabrication and laser properties. The manufacture of a glass host from constituent materials will be described, along with the fabrication of suitable devices from three different soft glass hosts.

Chapter 5 will then assess the power scaling potential of these fabricated soft glass devices. The chapter will begin with the introduction of a tunable fiber laser, which will act as a useful tool for measuring gain or loss in a device, and will be utilised as a probe beam for thermally-induced

guiding experiments. The devices fabricated from the three host glasses will then be characterised and analysed in terms of laser performance, with particular emphasis on device losses and homogeneity.

Chapter 6 follows on from the developments of Chapter 5, and suggests an alternative host material for the TGFR device. Here, we acquired an extra-large mode area ytterbium-doped silica fiber, which is known to have excellent optical quality and impressive doping uniformity. The quality of this device is such that we can perform an investigation into the thermally-induced guiding technique. Following this, the TGFR device is investigated in an amplifier and laser configuration, utilising the gain and thermal guiding model to predict and optimise performance.

In Chapter 7 we explore an exciting concept that follows a different novel power scaling approach. Here we are concerned with achieving high power CV beams, predominantly for applications within materials processing. Contrary to the conventional approach of amplifying these beams in cylindrically symmetric gain media, we suggest amplification in a highly asymmetric ytterbium-doped YAG thin-slab. We introduce a radially polarised seed laser required for the amplification experiments. This simple and robust seed laser exploits thermally-induced bi-focussing for direct generation of a radially polarised beam with excellent polarisation purity. The amplification of this seed source in the slab architecture will be presented, along with the important implications of the Gouy phase shift and how this effect is compensated. Further power scaling considerations will be discussed.

Finally, Chapter 8 will conclude the results and key findings of this thesis. We will suggest future experiments, which based on the results of this thesis, show great potential.

References

1. C. A. Haynam, et al. "National Ignition Facility laser performance status," Appl. Opt. **46**, 3276 (2007).

2. B. P. Abbot, et al. "Observation of Gravitational Waves from a Binary Black Hole Merger," Phys. Rev. Lett. **116**, 061102 (2016).

3. M. Hentschel, R. Kienberger, Ch. Spielmann, G. A. Reider, N. Milosevic, T. Brabec, P. Corkum, U. Heinzmann, M. Drescher, F. Krausz, "Attosecond metrology," Nature **414**, 509 (2001).

4. A. Einstein, "Quantentheorie der strahlung," Phys. Z. **18**, 121 (1917).

5. J. P. Gordon, H. J. Zeiger, C. H. Townes, "The Maser – New Type of Microwave Amplifier, Frequency Standard, and Spectrometer," Phys. Rev. **99**, 1264 (1955).

6. A. L. Schawlow, C. H. Townes, "Infrared and Optical Masers," Phys. Rev. **112**, 1940 (1958).

7. T. H. Maiman, "Stimulated Optical Radiation in Ruby," Nature **187**, 493 (1960).

8. Q. Zhan, "Trapping metallic Rayleigh particles with radial polarization," Opt. Expr. **12**, 3377 (2004).

9. Q. Zhan, "Cylindrical vector beams: from mathematical concepts to applications," Adv. Opt. Photon. **1**, 1 (2009).

10. V.G. Niziev, A.V. Nesterov, "Influence of beam polarization on laser cutting efficiency," J. Phys. D: Appl. Phys. **32**, 1455 (1999).

11. M. Meier, V. Romano, T. Feurer, "Material processing with pulsed radially and azimuthally polarized laser radiation," Appl. Phys. A **86**, 329 (2007).

12. S. Schad, V. Kuhn, T. Gottwald, V. Negoita, A. Killi, K. Wallmeroth, "Near fundamental mode high-power thin-disk laser," Proc. SPIE **8959**, 89590U (2014).

13. E. Snitzer, "Optical Maser Action of Nd^{+3} in a Barium Crown Glass," Phys. Rev. Lett. **7**, 444 (1961).

14. S. B. Poole, D. N. Payne, M. E. Fermann, "Fabrication of low-loss optical fibres containing rare-earth ions," Electron. Lett. **21**, 737 (1985).

15. E. Stiles, "New developments in IPG fiber laser technology," Proceedings of the 5th International Workshop on Fiber Lasers (2009).

Introduction

Chapter 2 Background

2.1   Chapter Overview

Following the motivation to achieve high power laser sources presented in section 1.1, this chapter introduces relevant background theory concerning lasers. We begin in section 2.2 with a microscopic view, considering light and matter interactions at the atomic level. Here we will introduce the essential concept of gain and describe basic laser energy level structures. Section 2.3 introduces the laser resonator and describes the essential components required to achieve lasing. The laser performance in terms of power will be presented along with a discussion on the modes of a laser resonator. In section 2.4 we will describe some of the key limitations faced when scaling lasers to higher output powers, whilst section 2.5 will introduce several prevalent laser geometries that are employed for high power operation. Section 2.6 will conclude the chapter.

2.2   Interaction of Light and Matter

This introductory section is inspired by the derivation given by Koechner [1], and is intended to provide a basic overview of the key concepts involved in laser operation at the atomic level.

2.2.1   Two-Level System

Atomic Interactions

To understand the basic operation of a laser, it is important to consider the interaction of light and matter at the atomic scale. Here, *light* refers to infrared, visible and ultraviolet electromagnetic radiation. A simple introduction to this concept can be made by representing a piece of matter by an atomic ensemble, consisting of N_T identical atomic constituents. Each atomic system comprises of an electron in one of two discrete energy levels, a lower energy level, E_1, and a higher energy level, E_2, with degeneracy (states with the same energy) g_1 and g_2, as depicted in fig. 2.1. For this simplified introduction, it can be assumed that each atomic system can only be in one of its two states at any one time. Hence, N_i represents the number of atomic systems with an electron in E_i, and N_T represents the total number of systems i.e. $N_T = N_1 + N_2$. Since degenerate states are equally populated, the number of systems in each degenerate state, N_i', is given simply by N_i/g_i.

Electron transitions between the two energy levels are possible. A transition from the lower energy level, E_1, to the higher energy level, E_2, corresponds to the absorption of a photon with energy equal to the difference between the two levels, $\Delta E = E_2 - E_1 = h\nu_{12}$, where h is Planck's constant

and v_{12} is the frequency relating to the energy gap. In contrast, a transition from E_2 to E_1 corresponds to the emission of a photon with energy hv_{12}.

$$\rule{4cm}{1pt} \quad E_2,\, N_2,\, g_2$$

$$\rule{4cm}{1pt} \quad E_1,\, N_1,\, g_1$$

Figure 2.1: Simple two-level system.

In the early 20th century, when much of modern physics was being developed, Einstein postulated on the probability of three processes by which the atomic system can undergo a transition, namely, absorption, spontaneous emission and stimulated emission (fig. 2.2) [2]. The first and last of these processes are stimulated by radiation, and are consequently related to the incident radiation energy density per unit frequency, denoted by $\rho(v)$, which was described by Planck for a black body in thermal equilibrium [3]:

$$\rho(v)dv = \frac{8\pi v^2 dv}{c^3} \frac{hv}{\exp\left(\frac{hv}{k_B T}\right) - 1} \tag{2.1}$$

where $\rho(v)dv$ is the radiation energy density centred on frequency v within bandwidth dv, c is the speed of light, k_B is Boltzmann's constant and T is the temperature.

Absorption occurs when a photon of energy hv_{12} is absorbed by an electron in E_1, thus increasing the atomic system from E_1 to E_2 (fig. 2.2, left). The rate of change of N_1 due to this process can be described by:

$$\frac{dN_1}{dt} = -B_{12}\rho(v_{12})N_1 \tag{2.2}$$

where B_{12} is the Einstein coefficient which describes the probability of an absorption event per unit time per unit spectral energy density of the incident radiation.

Spontaneous emission is the stimulus-free decay of an electron from E_2 to E_1, resulting in the emission of a photon of energy hv_{12} (fig. 2.2, middle). Photons are emitted with random phase and are incoherent. The upper-state lifetime, τ_{21}, determines the rate of decrease of N_2, which is given by:

$$\frac{dN_2}{dt} = -A_{21}N_2 \tag{2.3}$$

where $A_{21} = 1/\tau_{21}$ is the Einstein coefficient describing spontaneous emission, and represents the probability per unit time of a decay.

Stimulated emission results when an incident photon of energy $h\nu_{12}$ initiates an electronic transition from E_2 to E_1, resulting in the emission of a second, indistinguishable photon (fig. 2.2, right). The emitted photon is coherent with the stimulating photon and has an identical phase, polarisation, energy and direction. The rate of decrease of N_2 due to this process is given by:

$$\frac{dN_2}{dt} = -B_{21}\rho(\nu_{12})N_2 \tag{2.4}$$

where B_{21} is the Einstein coefficient which describes the probability of an stimulated emission event per unit time per unit spectral energy density of the incident radiation. This stimulated emission of photons is the underlying mechanism that allows amplification of radiation and thus laser action.
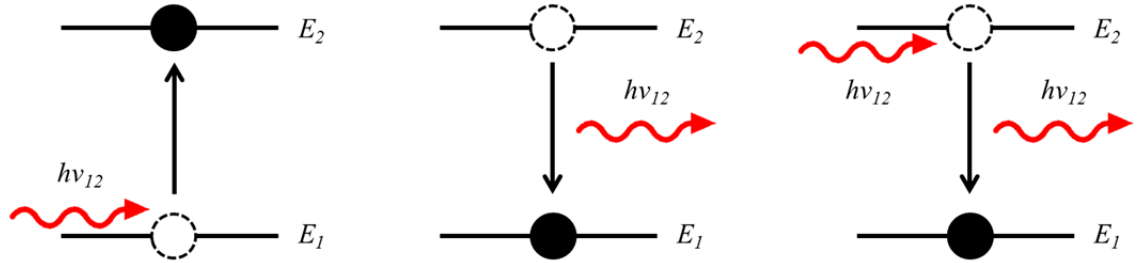
Figure 2.2: Absorption (left), spontaneous emission (middle) and stimulated emission (right).

Combining equations 2.2-2.4, we can describe the overall rate of change of the populations:

$$\frac{dN_1}{dt} = -\frac{dN_2}{dt} = -B_{12}\rho(\nu_{12})N_1 + A_{21}N_2 + B_{21}\rho(\nu_{12})N_2 \tag{2.5}$$

For an ensemble of atomic systems in thermal equilibrium, the rate of transitions from E_1 to E_2 is equal to the rate of transitions from E_2 to E_1, i.e. what goes up must come down. Hence the derivatives in equation 2.5 go to zero, and one obtains the logical result:

$$B_{12}\rho(\nu_{12})N_1 = A_{21}N_2 + B_{21}\rho(\nu_{12})N_2 \tag{2.6}$$

Another property of an ensemble in thermal equilibrium is that it will obey a Boltzmann distribution, which describes the relative electron population density according to:

$$\frac{N_2}{N_1} = \frac{g_2}{g_1}\exp\left(-\frac{E_2 - E_1}{k_B T}\right) \tag{2.7}$$

Equation 2.7 implies that for $E_2 > E_1$ and $T > 0$, $(g_2/g_1)N_1 > N_2$. In thermal equilibrium the lower state always has a higher population that the upper state. Combining equation 2.5 and equation 2.7, we can write:

Background

$$\rho(v_{12}) = \frac{\left(\frac{A_{21}}{B_{21}}\right)}{\left[\left(\frac{g_1}{g_2}\right)\left(\frac{B_{12}}{B_{21}}\right)\exp\left(\frac{hv_{12}}{k_B T}\right)\right] - 1} \qquad (2.8)$$

which when compared to equation 2.1 gives the Einstein relations:

$$\frac{A_{21}}{B_{21}} = \frac{8\pi v_{12}{}^2 hv_{12}}{c^3} \qquad (2.9)$$

$$B_{21} = \frac{g_1}{g_2} B_{12} \qquad (2.10)$$

Equation 2.10 indicates that for a non-degenerate system, the rate of absorption is equal to the rate of stimulated emission.

Absorption/Gain

An over-simplification of this model has been to assume that the energy gap is discrete. In reality the energy levels will be broadened by a combination of homogeneous effects, including lifetime broadening, and inhomogeneous effects, which can result from crystal impurities. Therefore, the transition has an associated lineshape function, $g(v,v_0)$, which is centred on v_0 with bandwidth Δv. This lineshape defines the fraction of each energy level which is capable of performing a transition corresponding to photons of energy between hv_s and $h(v_s + dv)$. Consequently, equation 2.5 can be rewritten accounting for the lineshape function:

$$-\frac{dN_1}{dt} = \rho(v_s)g(v_s, v_0)dv[B_{12}N_1 - B_{21}N_2] \qquad (2.11)$$

Note that the term relating to spontaneous emission has been omitted from equation 2.11.

It is worth noting that the signal bandwidth is typically significantly narrower than the atomic linewidth, $dv \ll \Delta v$, and can thus be approximated as a monochromatic wave at frequency v_s. Equation 2.11 can be recast in terms of the rate of change of energy density and subsequently integrated over dv to obtain the rate of absorbed energy density per unit frequency:

$$-\frac{d\rho(v_s)}{dt} = \rho(v_s)hvg(v_s, v_0)[B_{12}n_1 - B_{21}n_2] \qquad (2.12)$$

where n_i represents the population density of each level. One can transform this integral to the spatial domain using the relation: $dt = dz/c$, and integrate over material length dz to obtain:

$$\rho(v_s) = \rho_0(v_s)\exp(-\alpha(v_s)z) \qquad (2.13)$$

where $\rho_0(v_s)$ is the incident radiation energy density per unit frequency and:

$$\alpha(v_s) = n_1\sigma_{12}(v_s) - n_2\,\sigma_{21}(v_s) \tag{2.14}$$

$$\sigma_{ij}(v_s) = \frac{h v_s g(v_s, v_0) B_{ij}}{c} \tag{2.15}$$

where $\alpha(v_s)$ is the absorption/gain coefficient and $\sigma_{ij}(v_s)$ is the transition cross-section for a transition from E_i to E_j, which quantifies the probability of a stimulated transition.

Consequently, in thermal equilibrium, we have from equation 2.7: $(g_2/g_1) > n_2/n_1$, thus from equation 2.10 and equation 2.15 we can write $n_1\sigma_{12} > n_2\sigma_{21}$. Therefore, the radiation energy density per unit frequency decreases exponentially as a function of distance in the material. Hence, to achieve an increase in radiation energy density per unit frequency, we must depart from thermal equilibrium to achieve $n_2\sigma_{21} > n_1\sigma_{12}$, a situation known as population inversion. This would result in a negative value for $\alpha(v_s)$, and consequently the radiation energy density would increase exponentially as a function of distance through the material. Providing a net gain through the stimulated amplification of radiation is essential to laser operation.

A population inversion can be achieved by optically pumping the system to increase n_2. If we consider pumping a non-degenerate two-level system, with $B_{12} = B_{21}$ (equation 2.10) and thus $\sigma_{12} = \sigma_{21}$ (equation 2.15), we can at most achieve a situation where $n_2 = n_1$, known as transparency. At this point, the probability of an absorption event, quantified by equation 2.2, is exactly equal to the probability of a stimulated emission, quantified by equation 2.4. Therefore additional pump photons will be absorbed and emitted equally and we will not be able to overcome transparency. Furthermore, to achieve a population inversion we must increase the reality of our model and abandon our two-level picture.

2.2.2 Three/Four-Level Systems

Real atomic systems are more complicated than this simple two-level picture. An extension of the previous section, whilst maintaining simplicity, is the three-level system and four-level system (fig. 2.3), which can be used to describe real lasers. These systems incorporate additional states not only with different energies, but also with different lifetimes. More specifically, the inclusion of a long-lived, metastable, indirectly populated state allows a population inversion to be created.

Three-Level System
A true three-level system (fig. 2.3, left) comprises of a ground state and lower laser level at energy E_1, a maximum energy level at E_3 and an upper lasing level at E_2. In thermal equilibrium all the atomic systems are in the ground state. The system is optically pumped at a frequency v_{13}, where E_3

$- E_1 = h\nu_{13}$, therefore raising electrons to E_3. The majority of the excited electrons decay to E_2 by a rapid, non-radiative process, with a lifetime τ_{32}. This fast decay is possible due to the comparatively small energy gap between E_3 and E_2, which can be carried away as vibrational energy by phonons into the lattice of the material. The energy gap between E_3 and E_1 is larger than the maximum phonon energy supported by the lattice, eliminating the possibility of very rapid single-phonon decay, leading to a long lifetime for this transition, τ_{31}. The same reasoning can explain the long lifetime experienced by electrons in E_2, given by τ_{21}. Therefore, the transition between E_2 and E_1 is radiative, and thus corresponds to the emission of a photon with energy $h\nu_{21}$, where $E_2 - E_1 = h\nu_{21}$. A population inversion between E_2 and E_1 can now be initiated when the optical pumping intensity is sufficient, as the pump photons no longer depopulate the upper lasing level as with the two-level model. In this model, it is assumed that the decay between from E_3 to E_2 is extremely rapid such that no atomic systems exist in that state, i.e. $\tau_{32} \ll \tau_{21}$ and $n_3 = 0$. Therefore the total population density is given by $n_T = n_1 + n_2$.
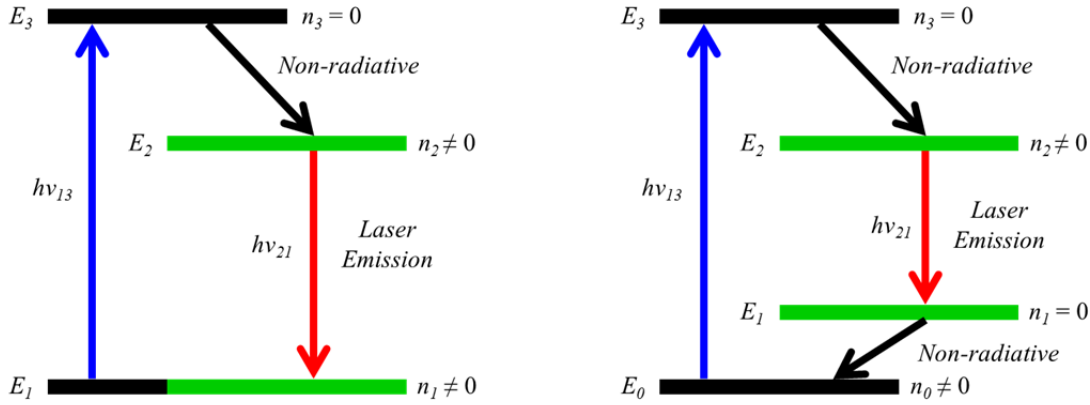
Figure 2.3: Three-level system (left), and four-level system (right).

For clarity, the radiation energy density can be written in terms of the photon density, ϕ:

$$\rho(\nu) = h\nu g(\nu)\phi \tag{2.16}$$

Combining this result, with equation 2.15, leads to an expression for the Einstein B coefficients:

$$B_{ij}\rho(\nu) = c\sigma_{ij}(\nu_{ij})\phi \tag{2.17}$$

The rate of change of population density can be described utilising equation 2.5:

$$\frac{dn_2}{dt} = -\frac{dn_1}{dt} = r_P - \frac{n_2}{\tau_{21}} - (n_2\sigma_{21} - n_1\sigma_{12})c\phi \tag{2.18}$$

where r_P is the pump rate density, i.e. the number of excitations per unit time per unit volume. Thus the rate of change of the populations is determined by optical pumping, spontaneous emission and the net stimulated emission. It is worth noting that to achieve a population inversion in a true three-level system more than half of the atomic systems have to be excited to the upper laser level.

Four-Level System

The four-level system (fig. 2.3, right) differs from the three-level system in that an additional level is incorporated below the lower lasing level. This extra level, E_0, is the ground state, and is separate from the lower laser level, E_1. As before, the system is optically pumped, raising the electrons to E_3 where they again undergo rapid decay into the upper laser level, E_2. The lasing transition occurs between the metastable level E_2 and E_1. The electrons then rapidly decay from E_1 to E_0, in the same manner as from E_3 to E_2. Therefore, since τ_{32}, $\tau_{10} \ll \tau_{21}$, it is assumed that a population only ever exists in E_0 and E_2, thus $n_T = n_0 + n_2$. The rate of change of population for the upper laser level can be written as:

$$\frac{dn_2}{dt} = r_P \ - \frac{n_2}{\tau_{21}} - \ n_2 c \sigma_{21} \phi \tag{2.19}$$

where it has been assumed that the lifetimes of non-radiative decays are effectively zero. In contrast to a three-level system, a four-level system does not require a significant fraction of the population to be excited in order to achieve a population inversion between level E_2 and E_1, and can in principle be achieved with just a single excited atomic system.

Quasi-Three-Level System

Many lasers can be categorised as quasi-three-level systems, which exist in a regime between three-level and four-level systems. The lower laser level of a quasi-three-level system is in close proximity to the ground state, and is therefore thermally populated according to the Boltzmann distribution (equation 2.7). Consequently, in the absence of pumping, a quasi-three-level medium will absorb at the signal frequency and therefore a certain degree of inversion is required to reach transparency and subsequently to achieve gain.

As the energy gap between the ground state and the lower laser level increases, the scenario tends to a four-level system. This is because the thermal occupancy of the lower laser level decreases, and as a result, so does the effective absorption cross-section at the signal frequency. Effective cross-sections allow one to describe the transition probability between the sublevels of Stark manifolds. Furthermore, transparency is achieved for $\sigma_{E\_A} n_1 = \sigma_{E\_E} n_2$, where $\sigma_{E\_A}/\sigma_{E\_E}$ is the effective absorption/emission cross-section for a particular transition. Note that the cross-sections used in the remainder of this work refer to effective cross-sections. It follows that the upper-state population density required to reach transparency, n_{2_Tr}, is defined by:

$$n_{2\_Tr} = n_T \left(\frac{\sigma_{E\_A}}{\sigma_{E\_A} + \sigma_{E\_E}} \right) \tag{2.20}$$

2.3   Laser Resonator

In this section we introduce the concept of a laser resonator. Initially we briefly cover the essential components of a laser, before discussing the necessary condition to achieve lasing and explain how the performance of a laser can be estimated. The modes of a laser resonator are introduced and beam evolution is discussed.

2.3.1   Laser Components

There are just three essential components required to construct a laser:

1. Laser medium: an ensemble of atomic systems which can store energy and release this energy to the stimulating laser radiation to achieve amplification.
2. Pump: a process which can excite the atomic systems to a higher energy level.
3. Optical feedback: to confine the radiation within the resonator, ensuring that the gain experienced by the laser radiation exceeds the losses on each round-trip.

A wide variety of approaches have been used to satisfy these three requirements. Crystals, glasses, dyes, gases and semiconductors are examples of materials that have been employed as a laser medium. Electric discharge and optical pumping through the use of diode lasers, flashlamps and even solar power can excite these materials. Flat or curved mirrors, gratings or simply a cleaved fiber end are possible ways to provide the feedback essential for laser operation. In this thesis we confine our research to novel power-scaling techniques for diode-laser pumped solid-state configurations. Fig. 2.4 depicts these components schematically.
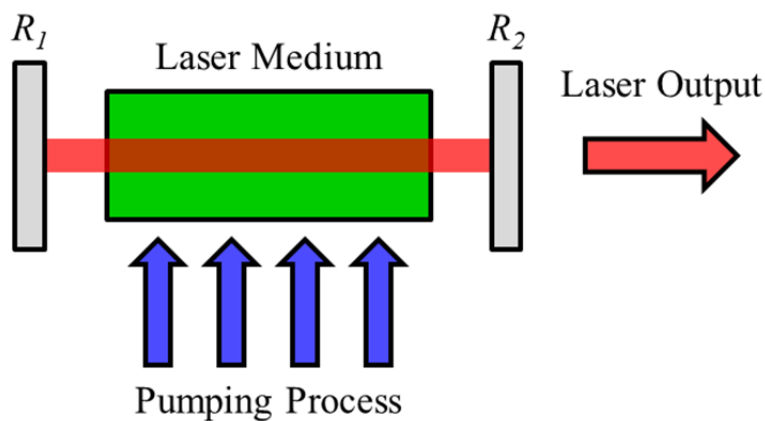
Figure 2.4: Essential components of a laser.

Here we have shown the pumping process in a direction perpendicular to the laser medium, known as side-pumping. The technique can make use of low brightness sources, and can result in an even distribution of pump radiation longitudinally, i.e. along the direction of laser beam propagation. However, due to the high inversion and thus gain at the edge of the laser beam, higher order modes

(section 2.3.3) can become excited and reduce beam quality. Additionally, cooling of the laser medium is complicated by the fact that the edge of the medium must be heat-sunk whilst simultaneously being transparent to pump radiation. An alternative approach, and the one used throughout this PhD, is end-pumping. Here, the pump beam is launched along the axis of the laser beam, allowing a superior overlap between the pumped region and laser mode. It should be noted that this approach requires the use of higher brightness pump sources, which are readily available due to the vast improvements of pump diodes in recent years.

As stated previously, this research considers solid-state laser materials. More specifically, we explore novel configurations of rare-earth ion doped crystal and glass media. These materials typically exhibit electronic transitions involving the $4f$ shell and can exist in various architectures depending on the specific application, as discussed in section 2.5. Both bulk and fiber geometries will be explored.

Resonator modes are discussed in more detail in section 2.3.3. The laser mode of a bulk laser is typically confined in the resonator using specialist mirrors with dielectric coatings, which can display different reflection properties at the pump and laser wavelength. In fig. 2.4 we have denoted the reflectivity of each mirror at the laser wavelength by R_1 and R_2. At least one of the mirrors needs to be partially transmissive at the laser wavelength in order to extract a useful output beam. These mirrors can be plane, with stability provided by intracavity lenses or a thermally-induced lens within the laser medium, or the mirrors can be curved to control the laser mode size within the cavity. In the case of a fiber laser, the mode is guided through total internal reflection, and can be confined using an external arrangement of lenses and mirrors, or through butt-coupled mirrors or fiber Bragg gratings.

2.3.2   Laser Performance

Due to the wide variety of possible laser configurations, it is not surprising that the performance characteristics can vary considerably. Two important and useful factors to consider are the laser threshold power and slope efficiency. The former essentially dictates the power expenditure required to achieve lasing within the resonator, whilst the latter quantifies the relationship between output power and pump power, which can often be expressed as a single efficiency factor assuming a linear relationship. In this section we will present a derivation of these two factors for a four-level laser.

In order to derive expressions for the threshold power and slope efficiency, it is helpful to consider equation 2.19, which describes the rate of change of population density for the upper laser level of a four-level system. Additionally, one can write the rate of change of photons in the laser mode within the resonator as:

$$\frac{d\Phi_T}{dt} = \int_{cavity} n_2 c \sigma_{21} \phi \, dV - \frac{\Phi_T}{\tau_c} \qquad (2.21)$$

where Φ_T is the total number of photons in the laser mode and τ_c is the cavity lifetime, which describes the rate of decrease of photons in the cavity due to losses such as output coupling or unwanted losses such as absorption or scattering within the gain medium. Thus the cavity lifetime is related to the total photon number, at time t, by:

$$\Phi_T(t) = \Phi_T(t = 0)\exp\left(-\frac{t}{\tau_c}\right) \qquad (2.22)$$

The total photon number decreases over the round-trip time, τ_{RT}, according to:

$$\Phi_T(t + \tau_{RT}) = \Phi_T(t)(1 - L)(1 - TR) \qquad (2.23)$$

where L represents unwanted losses within the cavity, and TR represents the transmission of the output coupler. A simple combination of equation 2.22 and equation 2.23 results in an expression for τ_c:

$$\tau_c = \frac{2l_{cav}}{c(L + TR)} \qquad (2.24)$$

where we have used the fact that $\tau_{RT} = 2l_{cav}/c$ where l_{cav} is the cavity length, and assumed L, TR << 1. Furthermore, we can define a normalised pump rate density, r_0, and normalised photon density, ϕ_0, according to:

$$r_0 = \frac{r_p}{R_T} \qquad (2.25)$$

$$\phi_0 = \frac{\phi}{\Phi_T} \qquad (2.26)$$

where R_T is the total pump rate. The terms in equation 2.25 and equation 2.26 can be defined as:

$$R_T = \int_{cavity} r_p \, dV \qquad (2.27)$$

$$\Phi_T = \int_{cavity} \phi \, dV \qquad (2.28)$$

$$\int_{cavity} \phi_0 \, dV = \int_{cavity} r_0 \, dV = 1 \qquad (2.29)$$

18

Background

Hence equation 2.19 and equation 2.21 can be rewritten for steady-state operation as:

$$\frac{dn_2}{dt} = R_T r_0 - \frac{n_2}{\tau_{21}} - n_2 c \sigma_{21} \Phi_T \phi_0 = 0 \tag{2.30}$$

$$\frac{d\Phi_T}{dt} = \int\limits_{cavity} n_2 c \sigma_{21} \Phi_T \phi_0 \, dV - \frac{c(L + TR)\Phi_T}{2l_{cav}} = 0 \tag{2.31}$$

Equation 2.30 can be rearranged in terms of the excited state population density:

$$n_2 = \frac{R_T r_0 \tau_{21}}{1 + c \sigma_{21} \tau_{21} \Phi_T \phi_0} \tag{2.32}$$

which in turn can be substituted into equation 2.31:

$$\int\limits_{cavity} \frac{c \phi_0 r_0}{1 + c \sigma_{21} \tau_{21} \Phi_T \phi_0} dV = \frac{c(L + TR)}{2l_{cav} \sigma_{21} \tau_{21} R_T} \tag{2.33}$$

One can relate the total pump rate to the launched pump power, P_P:

$$R_T = \frac{P_P \eta_{abs} \eta_{QE}}{h \nu_P} \tag{2.34}$$

where η_{abs} is the fraction of launched pump power that is absorbed, η_{QE} is the quantum efficiency which defines the fraction of absorbed pump photons which result in an excited atomic system and ν_P is the frequency of the pump radiation. Additionally, one can relate the output power, P_O, to the total photon number:

$$P_O = \Phi_T h \nu_L TR \left(\frac{c}{2l_{cav}} \right) \tag{2.35}$$

where ν_L is the frequency of the signal radiation. Equation 2.34 and equation 2.35 allow us to write equation 2.33 in a manner which relates the launched pump power to the laser output power for arbitrary pump mode and laser mode distributions:

$$\int\limits_{cavity} \frac{\phi_0 r_0}{1 + \frac{2 P_O l_{cav} \sigma_{21} \tau_{21} \phi_0}{h \nu_L TR}} dV = \frac{(L + TR) h \nu_P}{2l_{cav} \sigma_{21} \tau_{21} P_P \eta_{abs} \eta_{QE}} \tag{2.36}$$

From equation 2.36 we can calculate the laser threshold and slope efficiency for specified system. If we consider the simplified but insightful scenario where both the pump and laser mode have top-hat intensity distributions (fig. 2.5), we can write the normalised pump rate and photon number in terms of radial distance from beam centre, r, and longitudinal position, z:

Background

$$r_0(r,z) = \frac{1}{\pi w_P^2 l} \qquad\qquad r \leq w_P, \quad 0 \leq z \leq l$$

(2.37)

$$r_0(r,z) = 0 \qquad\qquad\qquad Elsewhere$$

$$\phi_0(r,z) = \frac{1}{\pi w_L^2 l} \qquad\qquad r \leq w_L, \quad 0 \leq z \leq l$$

(2.38)

$$\phi_0(r,z) = 0 \qquad\qquad\qquad Elsewhere$$

where w_P/w_L is the pump/laser mode radius respectively.
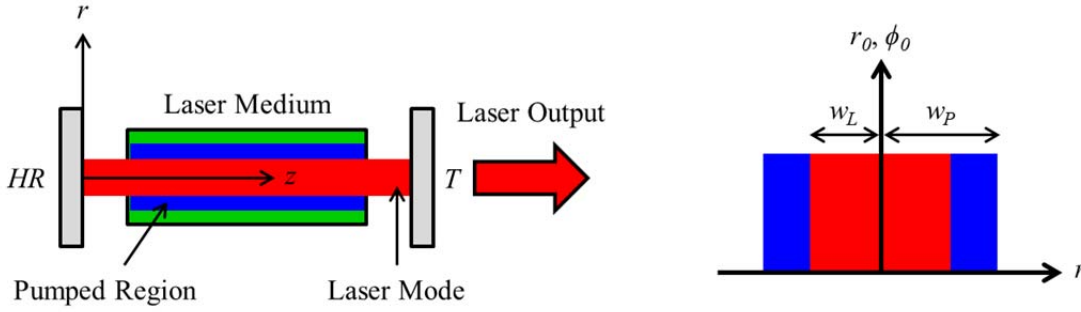
Figure 2.5: Laser with top-hat pump and laser intensity distribution.

The threshold power, P_{P_TH}, is defined by the onset of lasing, and thus at threshold $P_O = 0$. Furthermore, one can rearrange equation 2.36, utilising equation 2.37 and equation 2.38 to obtain:

$$P_{P\_TH} = \frac{\pi w_P^2 (L + TR) h \nu_P}{2\sigma_{21} \tau_{21} \eta_{abs} \eta_{QE}} \qquad\qquad w_L \leq w_P$$

(2.39)

The slope efficiency, η_s, is defined as the rate of change of laser output power with respect to launched pump power. Thus, if we consider the scenario where we are sufficiently far above threshold, we can rearrange equation 2.36 to obtain the ratio P_o/P_p:

$$\eta_S = \frac{dP_O}{dP_P} = \left(\frac{TR}{L + TR}\right)\left(\frac{\nu_L}{\nu_P}\right)\left(\frac{w_L^2}{w_P^2}\right)\eta_{abs}\eta_{QE} \qquad\begin{array}{c} w_L \leq w_P \\[1em] P_P \gg P_{P\_TH} \end{array}$$

(2.40)

Equation 2.39 and equation 2.40 show that a laser will operate efficiently if intracavity losses are minimised, the pump and signal beams overlap effectively, the quantum efficiency is close to unity, the pump power is absorbed efficiently in the laser medium and the difference in energy between pump and signal photons is minimised. Essentially the quantum defect, η_{QD}, defined as the ratio of the signal frequency and pump frequency, i.e. $\eta_{QD} = \nu_L/\nu_P$, stipulates the maximum theoretical achievable efficiency for the laser, since the other efficiency factors can approach unity with

20

careful design. Intuitively, a low laser threshold is achieved with a small pumped area (i.e. high pump intensity), by maximising the efficiency factors and minimising the intracavity losses. Additionally, a material which exhibits a large product of $\sigma_{21}\tau_{21}$ will lead to a low threshold.

As previously mentioned, the above analysis is valid for a four-level laser with low intracavity losses and a high reflectivity output coupler, and is designed to give a physical understanding of the relevant parameters which impact two important laser performance characteristics. A quasi-three-level laser is complicated by the fact that the lower laser level absorbs the laser radiation, and thus an additional saturable loss term [1], L_{3L}, occurs:

$$L_{3L} = 2\sigma_{12}n_1 l \qquad (2.41)$$

This term will be incorporated in the L term in equation 2.39. Therefore, this reabsorption term will increase the threshold pump power relative to a four-level system. Due to the saturable nature of the reabsorption term, as the intracavity intensity increases, the reabsorption loss becomes less significant, and thus at high intracavity intensities the slope efficiency of a quasi-three-level laser will approach that of a four-level laser.

2.3.3 Laser Modes

The resonator depicted in fig. 2.4 is essential to laser operation since it provides the feedback required for the round-trip gain to exceed the losses in the cavity. A resonator is designed such that the circulating photon flux repeatedly passes through the gain medium. One can define longitudinal and transverse modes of the resonator by considering that the electric field distribution and phase are reproduced after each round-trip through the resonator [4]. The transverse modes of the resonator are defined as self-reproducing electric field distributions. In a bulk resonator, the mode size along the device can be determined by cavity mirrors, intracavity lenses and thermal lensing effects (section 2.4.1), whereas the mode size in a fiber laser is predominantly defined by the engineered waveguiding structure which maintains a constant transverse distribution along the length of the device. Oscillating modes must experience a round-trip phase shift equal to an integer multiple of 2π. Therefore, resonant modes typically oscillate on multiple longitudinal modes separated in frequency by the free spectral range of the resonator, which is inversely proportional to the resonator length. However, operation on a single longitudinal mode can be achieved with careful cavity design.

One can approximate the electric field distribution of a cavity mode under the paraxial approximation (i.e. beam divergence angles are sufficiently small) by solving the Helmholtz equation [5]:

Background

$$(\nabla^2 + k^2)E = 0 \tag{2.42}$$

where ∇^2 is the Laplacian operator, k is the wavenumber given by $k = 2\pi/\lambda$ where λ is the wavelength, and E is the electric field. Solving equation 2.42 in Cartesian or cylindrical coordinates gives rise to two different families of solutions known as Hermite-Gaussian (HG) modes and Laguerre-Gaussian (LG) modes respectively. The transverse intensity profiles of several of the lowest-order HG_{nm} modes are shown in fig. 2.6 for reference. Note that the indices n and m indicate the number of nodes in the x and y-direction respectively. The HG_{00} mode corresponds to the fundamental mode and has a Gaussian intensity distribution characterised by:

$$I(x,y) = I_0 exp\left(\frac{-2r^2}{w^2}\right) \tag{2.43}$$

where I_0 represents he maximum on-axis intensity, r is the radial distance from the beam centre, and w is the beam radius which corresponds to the transverse position where the intensity is equal to $1/e^2$ (or 13.5%) of the maximum on-axis intensity.
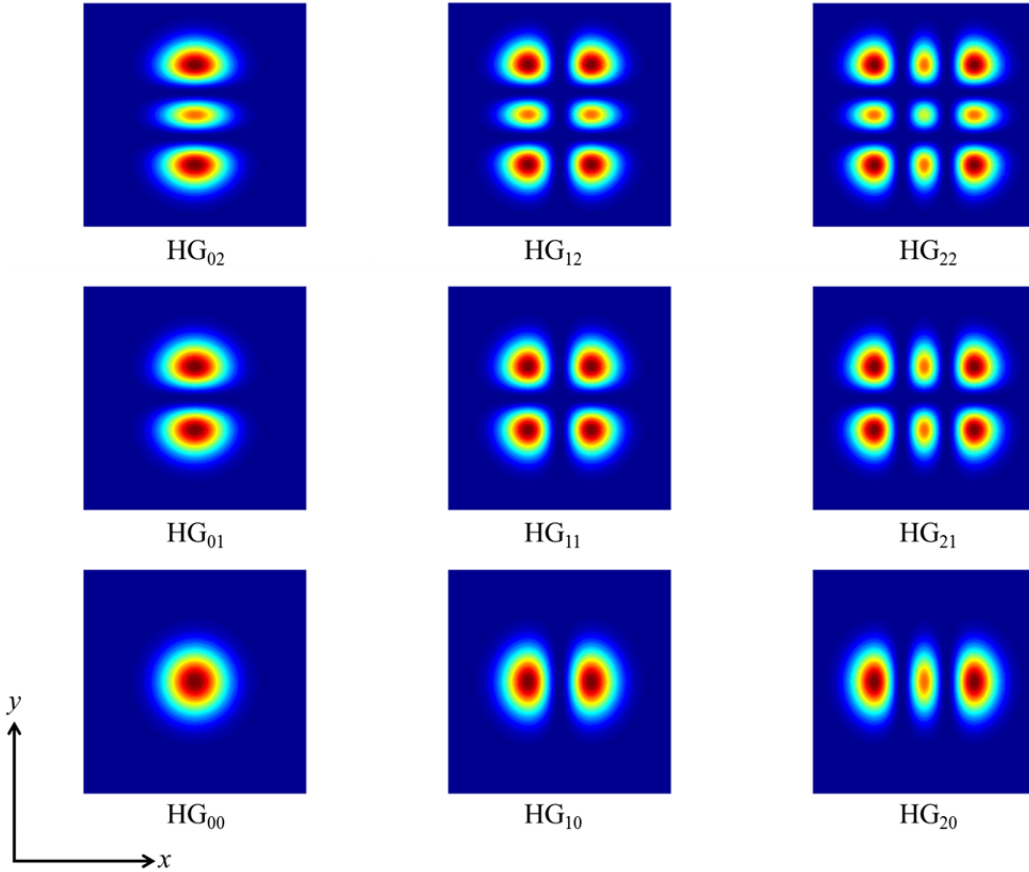
Figure 2.6: Intensity profile of several of the lowest-order HG_{nm} modes.

A very important property of these Gaussian modes is that they retain their profile throughout propagation, although the beam radius can change. For example, a beam can be focused to form a waist, which is where the beam radius decreases to a minimum value of w_0. The radius of curvature

of the beam wavefronts, R_{OC}, which represent transverse surfaces with constant phase, will increase or decrease depending on the proximity to the beam waist, and is infinite at the waist itself. Under the paraxial approximation the following equations can be used to describe the evolution of the beam radius, and radius of curvature of the beam wavefronts for the fundamental Gaussian mode, as a function of longitudinal position, z, where $z = 0$ corresponds to the position of the beam waist:

$$w(z) = w_0 \sqrt{1 + \left(\frac{z}{z_R}\right)^2} \tag{2.44}$$

$$R_{OC}(z) = z\left[1 + \left(\frac{z_R}{z}\right)^2\right] \tag{2.45}$$

$$z_R = \left(\frac{n\pi w_0^2}{\lambda}\right) \tag{2.46}$$

where z_R is known as the Rayleigh range and n is the refractive index of the medium the beam is propagating through. These equations are depicted in fig. 2.7, which shows the beam radius evolution and wavefront radius of curvature evolution for the fundamental mode with a wavelength of 1030nm, focused to a 100μm waist. The Rayleigh range for this beam is $z_R = 30.5$mm, which equates to the distance from the beam waist position whereby the beam has expanded by a factor of $\sqrt{2}$, and can therefore be thought of as the distance over which the beam does not diverge substantially.
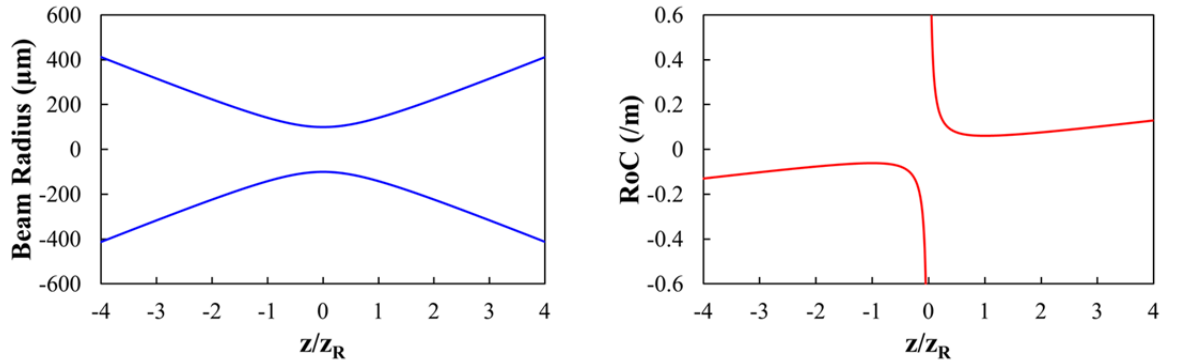
Figure 2.7: Beam radius evolution (left) and wavefront radius of curvature evolution (right).

The beam radius and wavefront radius of curvature can therefore be used to describe a Gaussian beam. These two factors can be combined and described by a single parameter known as the complex beam parameter, q, given by:

$$q(z) = \frac{1}{\frac{1}{R_{OC}(z)} - i\frac{\lambda}{\pi w^2(z)}} \tag{2.47}$$

23

The complex beam parameter can describe the propagation of a Gaussian beam through various optical elements with the use of the ABCD matrix formalism, as will be discussed in detail in section 3.3.2.

Whilst the objective of this work is to develop novel power scaling architectures, it is very important to preserve high beam quality in order to be useful for applications. The beam propagation factor, M^2, can be used to quantify beam quality, with the highest beam quality being achieved for $M^2 = 1$. Considering the HG_{nm} modes depicted in fig. 2.6, the M^2 factor has a value $(2n + 1)$ in the x direction and $(2m + 1)$ in the y direction. Therefore, the fundamental HG_{00} mode has a beam propagation factor of $M^2 = 1$, and is thus desirable beam for numerous applications. A beam with $M^2 = 1$ has the highest potential for tight focusing, and has the lowest divergence for a given beam waist radius. Ultimately, this means that for a fixed output power, the brightness, defined as power over emitting area and solid-angle divergence, will be maximised for these beams. Lower quality beams, with correspondingly higher beam propagation factors, can be accounted for by multiplying the wavelength in equation 2.46 and equation 2.47 by the corresponding M^2 factor.

2.4   High Power Limitations

Unfortunately, despite the precedent set by equation 2.40, one cannot increase the pump power of a laser system and expect an indefinite linear increase of output power at the signal wavelength. As the power deposition density and photon flux increase various deleterious effects can act to reduce or prevent a further increase in output power. A brief overview of the more prevalent effects is presented in this section. Note that laser design has a considerable impact on the consequences of these various effects, as will be discussed in section 2.5.

2.4.1   Thermal Limitations

Heating within the laser medium is predominantly a result of the quantum defect. Since the pump photons have a higher energy than the signal photons, the energy difference is carried away as vibrational energy by phonons (section 2.2.2), resulting in a heating of the host lattice. Further sources of heating include non-radiative decay directly from the upper laser level, excited-state absorption, energy transfer upconversion, non-radiative sites and absorption of power due to impurities. The associated temperature rise and particularly the temperature gradients which are established within the gain medium can have severe implications for power scaling. Thermal limitations are more relevant in bulk geometries such as rod and slab lasers, whilst fiber lasers perform better due to their high surface area to volume ratio and long length.

Background

Thermally-Induced Lensing

The electronic structure and density of a material vary with temperature, which in turn results in a variation of refractive index with temperature, quantified by the thermo-optic coefficient, *dn/dT*. Therefore, a transverse temperature variation across a laser medium leads to a locally-varying refractive index. Since gain media are typically periphery-cooled, the temperature is higher towards the beam centre, creating a focusing/diverging thermal lens for a material with a positive/negative *dn/dT*. For example, pumping a laser rod can lead to a spherical lens whilst a cylindrical lens can be generated in a slab geometry. This thermally-induced lens will typically have significant aberrations, which can act to reduce beam quality. Additionally, the focal length of the thermally-induced lens is dependent on pump power. Therefore, varying pump power can adversely impact laser stability and potentially prevent laser operation entirely.

Stress-Induced Effects

As previously mentioned the density of a material is dependent on temperature. Generally, materials display a positive coefficient of thermal expansion (CTE), and therefore increase in volume with temperature. Thus for the common case of a material which is hotter towards its centre, the inner regions will expand to a greater extent than the outer regions. Consequently, stresses will be established within the material, as the hotter centre is constrained by the cooler outer region.

These stresses can impact laser beam propagation. Firstly, the difference in expansion of various regions of the material can result in the deformation of material surfaces, resulting in lens-like profiles forming which can focus and aberrate the laser beam. Furthermore, the induced stresses produce strains which modify the refractive index via the photoelastic effect. As with thermally-induced lensing, a lens-like profile can occur across the laser medium, influencing laser stability and beam quality. The orientation of the generated strains are dictated by the laser geometry and heat extraction process for the laser medium, and thus a polarisation dependent refractive index profile is created which can subsequently lead to depolarisation losses. Finally, ultimate device failure occurs if the generated stresses exceed the stress-fracture limit. Since fracture typically occurs at the material surface, the surface quality can have a significant influence on the maximum tolerated stress.

2.4.2   Nonlinear Limitations

As the name suggests, nonlinear effects display a nonlinear response to an intense photon flux. These effects are utilised in numerous applications across laser physics, including supercontinuum generation and parametric amplification. Nonlinear effects are particularly limiting for high average and peak power fiber lasers, where the high product of intensity and propagation length

encourages nonlinearities. This section describes several important power scaling limitations imposed by nonlinear interactions.

Stimulated Raman Scattering

Stimulated Raman scattering (SRS) is an inelastic scattering process whereby high intensity radiation stimulates vibrational modes in the lattice medium. This process involves the conversion of a signal photon to an optical phonon and a lower energy Stokes shifted photon. This conversion is stimulated by the incident radiation which produces an atomic transition between different vibrational states. The energy of the phonon is absorbed in the host lattice contributing heat to the gain medium.

SRS becomes a limiting factor when the signal intensity and interaction length become large, such that the Raman gain for the Stokes photon is substantial and significant energy is shifted to this longer wavelength. Furthermore, SRS is a limitation in fiber lasers, where the tight beam confinement and long interaction lengths promote the effect. The Raman gain and associated frequency shift of the process are a property of the interacting material. Amorphous materials, such as silica, have an inherently broad Raman gain spectrum, and therefore SRS provides a limitation to high power broadband cw lasers and reasonably modest peak power pulsed lasers [6, 7]. Eventually a threshold is reached, whereby a further increase in pump power merely results in an increase of power at undesired wavelengths.

Stimulated Brillouin Scattering

Stimulated Brillouin scattering (SBS) is an inelastic process involving the conversion of a signal photon into an acoustic phonon and a lower energy Stokes photon via electrostriction. The acoustic phonon can generate a travelling periodically varying refractive index profile which acts to reflect the signal beam. This results in a Doppler-shifted Stokes wave travelling in the opposite direction to the signal beam. The frequency shift associated with SBS is significantly smaller than that associated with SRS. This backward propagating power can extract gain, thereby reducing the gain available for the signal beam.

As with SRS the fiber geometry provides conditions which can effectively generate SBS. The gain bandwidth of SBS in silica, ~10MHz [8], is considerably narrower than SRS, ~40THz [9]. Consequently, SBS gain is considerably higher for narrowband signals, and is a major limiting factor in high power single frequency cw fiber lasers. The onset power for both SRS and SBS can be increased by reducing beam intensity (i.e. increasing beam area) and interaction length (i.e. shorter devices) [7].

Background

Self-Focusing

Self-focusing is a consequence of the Kerr effect. The Kerr effect occurs when radiation with sufficient intensity generates a nonlinear polarisation, which instantaneously modifies the refractive index according to: $n = n_0 + n_2 I$, where n_2 is the nonlinear coefficient of the material and I is the radiation intensity. A Gaussian beam has a higher intensity towards it centre, therefore a radially varying refractive index can be established, producing a Kerr lens. This lens results in beam focusing, assuming a positive n_2. At sufficiently high intensities the laser mode can be focused to a sufficient degree to achieve complete beam collapse and ultimately material damage. This effect cannot be alleviated by increasing mode size, since the reduction in Kerr-lens strength is balanced by the increased sensitivity of the larger beam to focusing. Furthermore, self-focusing imposes a hard limit for the maximum peak power of an ultrashort pulse of approximately 4MW in silica at a wavelength of 1μm [10].

Self-phase modulation

Another consequence of the Kerr effect relevant to high peak power pulsed operation is self-phase modulation (SPM). Here the temporal intensity profile of the pulse modifies the refractive index, leading to a time-dependent phase shift. Furthermore, this can lead to the pulse becoming chirped, and result in a broadened optical spectrum and ultimately the transfer of power to a region outside the intended bandwidth.

2.4.3   Damage Limitations

Optical damage can occur for lasers operating in both cw and pulsed regimes. In the former regime, thermally-induced stress fracture can occur as a consequence of excess heat deposition, as discussed in section 2.4.1. In the latter regime, high pulse intensity can result in multiphoton absorption and the production of free-electrons, which are subsequently accelerated and can produce further free-electrons creating an avalanche process. Furthermore, this can lead to a high level of radiation absorption and ultimately fracture due to extreme heat loading. Damage is especially prevalent at the surface of a material due to the higher degree of impurities. Due to tight beam confinement in fibers, high peak power devices can be limited by optical damage.

2.5   Laser Architectures

Since the invention of the laser, numerous architectures have been utilised to achieve the desired performance. Laser sources which can provide high power (average and/or peak), large pulse energy and excellent beam quality are utilised for numerous applications within materials processing, the medical sector, the military and fundamental science. Various solid-state

architectures have been developed to achieve these desirable characteristics, with two distinct types emerging, namely: bulk lasers and fiber lasers. This section will discuss the relative advantages and limitations of these designs in terms of the power scaling limitations described in section 2.4.

2.5.1   Bulk Architectures

Bulk solid-state lasers are generally based on a bulk piece of rare-earth doped crystal or glass. Fig. 2.8 depicts some common bulk geometries including the rod, slab and thin-disc design. Here, the direction of heat flow is represented by the red arrows and the direction of laser beam propagation is indicated by the blue arrows. Thermal effects are extremely important when considering power scaling, and therefore different geometries have been developed to mitigate these effects. The laser beam in a bulk laser propagates as a free-space mode, and its size is determined by cavity design for a laser or by an optical system of lenses and mirrors for an amplifier.
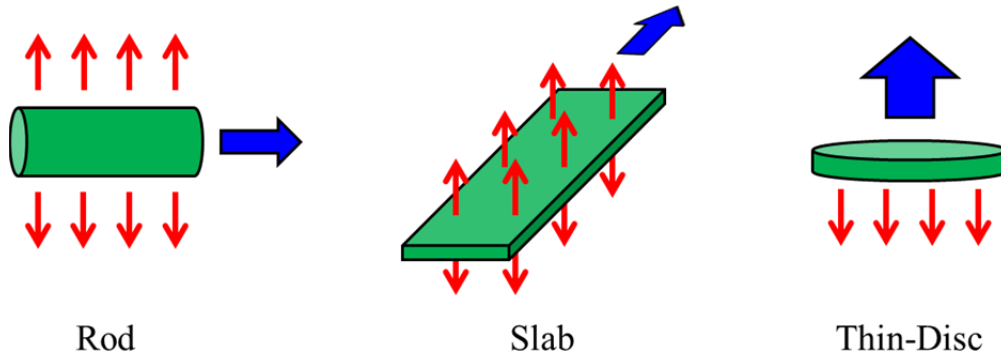
Figure 2.8: Schematic of rod, slab and thin-disc bulk laser geometries.

Rod

Rod lasers form a prevalent laser configuration and typically have a diameter on the order of millimetres and a length on the order of centimetres. The rod laser can be end-pumped through an end-face by a diode laser, allowing efficient operation as the laser mode extracts gain along the length of the rod. Here, care must to taken to ensure a good spatial overlap between the signal and pump mode, to ensure a high quality output beam. Side-pumping is another option, which has the benefit of allowing pumping with significantly reduced beam quality. This configuration was utilised by Maiman to achieve the first ever demonstration of a laser in a flash lamp side-pumped ruby rod [11].

Heat generated from absorbed laser radiation is extracted from the cylindrical surface of the rod, resulting in a radial temperature gradient which leads to thermal lensing. When operated at high pump power aberrations of this thermal lens act to distort the fundamental mode, leading to multimode operation and reduced beam quality. Additionally, the radial temperature gradient results in stress-induced birefringence which can lead to depolarisation losses due to a variation in birefringence direction across the beam cross-section. Furthermore, although kW-level average

power operation has been achieved the beam quality is heavily compromised [12]; suggesting fundamental mode operation is limited to the 100W level [13] for the rod configuration.

It is thermal gradients, rather than absolute temperature, that present the main thermal limitation in bulk devices. The temperature distribution in cylindrical laser media will be presented in detail in section 3.3. For reference, the temperature difference between the centre of the rod and the edge of the rod, ΔT_{rod}, is given by:

$$\Delta T_{rod} = \frac{P_p \eta_{abs} \eta_h}{4\pi\kappa l_r}$$
(2.48)

where η_h is the fraction of the absorbed pump power which is converted to heat, κ is the thermal conductivity of the rod material, l_r is the length of the rod and we have made the simplifying assumption that the pump displays a top-hat intensity distribution. Equation 2.48 indicates that a lower pump absorption per unit length will lead to a lower temperature difference. An example of how this may be achieved is to use a lower doping concentration over a longer rod length.

Slab

The slab configuration offers a route to higher power diffraction-limited operation. Slab lasers typically have a thickness on the order of a millimetre whilst the other two dimensions are on the order of 10s of millimetres. Pump radiation can be injected through the thin edges using diode lasers, or through the large faces which allow the beam quality of the pump source to be relaxed. The slab is cooled through the two large faces, ensuring effective heat removal due to the close proximity to the generated heat, thus resulting in a one-dimensional temperature gradient. The temperature difference between the centre of the slab and the surface of the large faces, ΔT_{slab}, can be described by:

$$\Delta T_{slab} = \frac{P_p \eta_{abs} \eta_h t_s}{8\kappa\omega_s l_s}$$
(2.49)

where t_s is the thickness of the slab, ω_s is the width of the slab and l_s is the length of the slab. Here, we can see that by ensuring $t_s \ll \omega_s$, the temperature difference can be kept small in comparison to the rod design.

The one-dimensional temperature gradient leads to several notable differences to the rod design, including a cylindrical rather that spherical thermal lens, and birefringence axes which are perpendicular with respect to the slab cross-section. This fact allows one to circumvent depolarisation losses, as a beam that is polarised in the direction of one of the birefringence axes will not incur polarisation losses as the birefringence is constant across the beam cross-section.

Additionally, the improved heat extraction of the slab laser ensures a higher stress fracture limit compared to the rod architecture, as discussed in 6.2.2.

However, power extraction can be more challenging in this highly asymmetric device. One solution is to use external mirrors to send the beam on a zig-zag path across the width of the slab i.e. perpendicular to the edge-pumped pump direction and the temperature gradient. This Innoslab concept operating in a master oscillator power amplifier (MOPA) configuration achieved an output power of 620W with beam quality $M^2 < 1.5$, and 1.1kW for 615fs pulses with a pulse energy of 55μJ at 20MHz repetition rate with a peak power of 80MW and a slightly reduced beam quality [14].

Thin-Disc

Thin-disc lasers consist of a crystal disc a few hundred microns thick and several millimetres in diameter. A multi-pass pump configuration is generally employed to increase pump absorption in the thin-disc. Heat is extracted from the back face of the disc, where a dielectric coating reflects both the signal and pump beams. This configuration ensures a low maximum crystal temperature due to the very close proximity of the heat-sink to the generated heat. Additionally, an essentially one-dimensional axial temperature gradient is established, therefore transverse thermal lensing and birefringence are significantly reduced. We can describe the maximum temperature difference between the front face and the back face of the thin-disc, ΔT_{disc}, by:

$$\Delta T_{disc} = \frac{P_p \eta_{abs} \eta_h t_d}{2\kappa \pi r_d^2} \tag{2.50}$$

where t_d is the thickness of the thin-disc and r_d is the radius of the thin-disc. The very low temperature rise in the thin-disc can thus by attributed the fact that $t_d << r_d^2$.

The thin-disc design has allowed excellent beam quality to be obtained at high output powers. Impressive results include 4kW obtained from a single disc resonator with $M^2 < 1.4$ [15], and 242W from a modelocked laser operating at a repetition rate of 3.03MHz, producing pulses of 80μJ with a peak power of 66MW and pulse duration of 1.07ps [16].

This architecture can be considered as a truly power scalable concept, since a doubling of the pump beam power and area (with a corresponding change in resonator design) does not significantly impact the maximum temperature, thermal distortions and peak intensity. An issue for high power operation is transverse amplified spontaneous emission (ASE), which can be totally internally reflected by the faces of the disc and deplete gain for the signal radiation.

2.5.2   Fiber Architectures

Fiber lasers are long, thin devices typical constructed from silica glass. These devices can be single-clad or double-clad, and consist of a rare-earth-doped silica core with a diameter on the order of tens of microns, a silica cladding layer/s with a diameter on the order of hundreds of microns and a polymer protective layer with a slightly larger diameter. The fiber length is typically on the order of meters. Laser radiation is guided by a radially-varying refractive index profile. A schematic of a typical step-index double-clad fiber is shown in fig. 2.9 where once again the red arrows indicate heat extraction and the blue arrow indicates laser output. Also shown in fig. 2.9 is the associated refractive index profile, where r indicates radial position and n indicates refractive index. Signal radiation is guided along the core at the interface with the inner-cladding layer by total internal reflection. The core diameter and refractive index contrast between the core and inner-cladding can be engineered such that only the fundamental mode can be excited. Pump radiation is typically launched into the fiber through the use of a fiber-coupled diode laser, and is guided along the fiber at the interface between the inner-cladding and outer-cladding. The double-cladding structure allows the use of high power multimode pump sources, thus allowing these fibers to achieve higher output powers than single-clad devices. The pump radiation is absorbed as it propagates, with the absorption rate determined by the doping concentration and ratio of the inner-cladding and core area. This configuration ensures an excellent overlap between the signal and pump radiation, and essentials acts as a brightness converter.
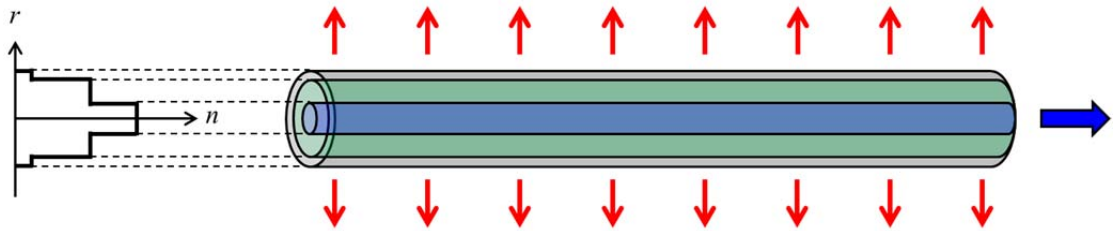
Figure 2.9: Step-index double-clad fiber and associated refractive index profile.

Fiber lasers have achieved great success in power scaling largely due to their extreme geometry, sophisticated low-loss fabrication techniques for silica fibers, brightness improvements in pump sources and excellent properties of Yb-doped silica including low quantum defect heating. Furthermore, the ability to directly write Bragg gratings directly into the fiber and to achieve low-loss splices between the pump delivery fiber and the active fiber leads to fully fiberised configurations which provide robust and reliable operation.

The fiber geometry provides a very large surface-area to volume ratio, allowing excellent thermal dissipation and granting a high level of immunity from the thermal limitations that tend to plague rod and slab lasers. Considering equation 2.48, we see that the temperature gradient of a fiber is

reduced compared to that of the rod owing to its low pump absorption per unit length. This thermal resilience combined with the in-built engineered guide has allowed the development of kW-level fiber lasers with excellent beam quality. However, a consequence of the fiber design is extremely high intensities over long lengths, which despite the inherently low nonlinearity of silica generates a regime where nonlinear effects and optical damage can occur, thus limiting maximum obtainable average and peak power.

In light of these limitations, efforts have been made to increase mode area and therefore reduce intensities and device length, assuming the inner-cladding to core area ratio is maintained. This concept increases the onset power for nonlinear effects such as SRS and SBS in addition to increasing the optical damage threshold. An additional advantage of a larger mode is an increase in energy storage and therefore extractable pulse energy, which can be limited by ASE in the fiber configuration. Furthermore the excellent thermal management properties of the fiber design can still be maintained owing to its extreme geometry.

However, increasing the core area of a fiber increases the number of modes that can propagate, thus the numerical aperture (NA) must be simultaneously decreased in order to retain fundamental mode guidance. This approach cannot be continued indefinitely, since lowering the NA results in weaker guiding and a higher susceptibility to bend-induced losses. A practical lower limit for the NA of ~0.05 [8], suggests an upper limit for the core diameter of a step-index fiber of ~16μm at a wavelength of 1μm. One can circumvent this limitation by utilising a slightly multimode fiber, configured in such a way that only the fundamental mode can propagate. This can be achieved by coiling the fiber which a specific radius of curvature, thus employing bend-induced loss which can provide a significantly higher loss for physically larger higher-order modes, whilst the fundamental mode experiences a negligible loss. This approach has been employed to achieve an average cw power of 1.36kW for a near diffraction-limited beam in an Yb-doped fiber with a core diameter of 40μm [17], and more than 2.1kW for a single mode beam in a similar fiber with a core diameter of 50μm [18]. It should be noted that mode area varies quadratically with wavelength, thus operating at longer wavelengths increases the area of the fundamental mode and is therefore beneficial for power scaling. Additionally, the self-focusing limit varies quadratically with wavelength [19]. Therefore, large core fibers based on thulium-doped glass, which provides gain in the 2μm region could provide a route to higher output powers, with kW-level sources demonstrated [20].

Alternative fiber designs that stray from the traditional step-index design can offer a route to scaling mode area. Microstructured fibers are one such example, which consist of a periodic arrangement of air holes surrounding a solid core doped with the laser active ion. The guiding properties stem from the size and separation of the air holes, which through appropriate design can lead to large core low NA devices. This design concept can be combined with chirped-pulse amplification, a technique utilised in the ultrashort pulse regime whereby pulses are temporally stretched pulses prior to amplification to reduce the peak power and thus nonlinearities within the

device, followed by compression to retain the original pulse duration. Impressive results incorporating this approach include 830W of output power obtained for 640fs pulses at 78MHz [21] and 480fs pulses reaching a peak power of 3.8GW for a fiber with a 108μm diameter core [22].

A final important concept to consider is the fiber host material. Silica is clearly the material of choice for high power applications. However, soft glasses including phosphates and silicates show excellent potential owing to the ability to incorporate rare-earth ions in these hosts in significantly higher concentrations than silica. The use of these materials will form a major component of this thesis and will be discussed in detail in Chapter 4 and Chapter 5. Another concept is that of the single-crystal fiber (SCF). These devices are long thin crystalline rods, with typical lengths on the order of centimetres and diameters of a millimetre or less. Pump radiation is launched through an end-face of the SCF and is confined in the device through total internal reflection at the crystal/air interface whilst signal radiation propagates as a free-space mode. This design thus ensures effective pump/signal overlap, and the larger mode sizes result in a higher onset for nonlinear effects and damage. An Yb:YAG SCF achieved a cw output power of 250W with a beam quality was $M^2 \approx 15$ [23]. Poor beam quality is typical of these naturally multimode devices.

2.6   Conclusion

The purpose of this chapter is to introduce background theory relevant to laser sources and high power operation. We began by describing the interaction between light and matter on the atomic scale, introducing three interaction processes, namely; absorption, spontaneous emission and stimulated emission. We described how the gain necessary for laser operation can be achieved through a population inversion, and discussed simple three-level and four-level energy systems which can be used to approximate real lasers.

We then identified three essential components required for laser operation; a laser medium, a pumping process and a cavity to provide optical feedback. The power performance of a laser resonator was then discussed, and an equation approximating output power and slope efficiency was derived. Laser modes were then introduced as self-reproducing transverse electric field distributions, along with the concept and consequences of beam quality.

Various limiting factors applicable to high power operation were discussed, covering thermal and nonlinear effects. Following this common high power laser architectures were described, with the thin-disc and fiber laser emerging as the frontrunners in terms of high power, diffraction-limited performance. It should be noted that whilst bulk and fiber regimes have achieved impressive performance, neither are without their limitations. Additionally, these regimes act to complement each other in terms of performance, and there is no clear optimum geometry satisfying all

performance parameters. For example, bulk geometries are well suited to high pulse energy and high peak power operation, whereas fiber lasers can produced very high average powers with diffraction-limited beam quality. We will proceed in Chapter 3 to suggest a novel laser geometry that aims to benefit the relative advantages of the bulk and fiber regime, whilst negating the potential limitations, allowing the realisation of a high power laser concept.

References

1. W. Koechner, Solid-State Laser Engineering, 6 ed., Sixth Revised and Updated Edition (Springer, 2006).

2. A. Einstein, "Quantentheorie der strahlung," Phys. Z. **18**, 121 (1917).

3. M. Planck, "On the Law of Distribution of Energy in the Normal Spectrum," Ann. Phys. **4**, 553 (1901).

4. A. G. Fox, T. Li, "Resonant Modes in a Maser Interferometer," Bell Syst. Tech. J. **40**, 453 (1961).

5. Q. Zhan, "Cylindrical vector beams: from mathematical concepts to applications," Adv. Opt. Photon. **1**, 1 (2009).

6. C. Jauregui, J. Limpert, A. Tunnermann, "High-power fibre lasers," Nature **7**, 861 (2013).

7. J. W. Dawson, M. J. Messerly, R. J. Beach, M. Y. Shverdin, E. A. Stappaerts, A. K. Sridharan, P. H. Pax, J. E. Heebner, C. W. Siders, C. P. J. Barty, "Analysis of the scalability of diffraction-limited fiber lasers and amplifiers to high average power," Opt. Expr. **16**, 13240 (2008).

8. D. J. Richardson, J. Nilsson, W. A. Clarkson, "High power fiber lasers: current status and future perspectives," J. Opt. Soc. Am. B. **27**, (2010).

9. W. A. Clarkson, "High Power Fiber Lasers and Amplifiers," Conference on Lasers and Electro Optics (2013).

10. M. N. Zervas, C. A. Codemard, "High Power Fiber Lasers: A Review," IEEE J. Sel. Topics Quantum Electron. **20**, 0904123 (2014).

11. T. H. Maiman, "Stimulated Optical Radiation in Ruby," Nature **187**, 493 (1960).

12. H. Bruesselbach, D. S. Sumida, "A 2.65-kW Yb:YAG Single-Rod Laser," IEEE J. Sel. Topics Quantum Electron. **11**, 600 (2005).

13. H. J. Eichler, A. Haase, R. Menzel, "100-Watt Average Output Power 1.2 Diffraction Limited Beam from Pulsed Neodymium Single-Rod Amplifier with SBS Phase Conjugation," IEEE J. Quantum Electron. **31**, 600 (1995).

14. P. Russbueldt, T. Mans, J. Weitenberg, H. D. Hoffman, R. Poprawe, "Compact diode-pumped 1.1 kW Yb:YAG Innoslab femtosecond amplifier," Opt. Lett. **35**, 4169 (2010).

15. S. Schad, V. Kuhn, T. Gottwald, V. Negoita, A. Killi, K. Wallmeroth, "Near fundamental mode high-power thin-disk laser," Proc. SPIE **8959**, 89590U (2014).

16. C. J. Saraceno, F. Emaury, C. Schriber, M. Hoffman, M. Golling, T. Sudmeyer, U. Keller, "Ultrafast thin-disk laser with 80 μJ pulse energy and 242 W of average power," Opt. Lett. **39**, 9 (2014).

17. Y. Jeong, J. K. Sahu, D. N. Payne, J. Nilsson, "Ytterbium-doped large-core fiber laser with 1.36 kW continuous-wave output power," Opt. Expr. **12**, 6088 (2004).

18. Y. Jeong, A. J. Boyland, J. K. Sahu, S. Chung, J. Nilsson, D. N. Payne, "Multi-kilowatt Single-mode Ytterbium-doped Large-core Fiber Laser," J. Opt. Soc. Korea **13**, 416 (2009).

19. G. Fibich, A. L. Gaeta, "Critical power for self-focusing in bulk media and in hollow waveguides," Opt. Lett. **25**, 335 (2000).

20. S. D. Jackson, "Towards high-power mid-infrared emission from a fibre laser," Nature **6**, 423 (2012).

21. T. Eidam, S. Hanf, E. Seise, T. V. Andersen, T. Gabler, C. Wirth, T. Schreiber, J. Limpert, A. Tunnermann, "Femtosecond fiber CPA system emitting 830 W average output power," Opt. Lett. **35**, 94 (2010).

22. T. Eidam, J. Rothhardt, F. Stutzki, F. Jansen, S. Hadrich, H. Carstens, C. Jauregui, J. Limpert, A. Tunnermann, "Fiber chirped-pulse amplification system emitting 3.8 GW peak power," Opt. Expr. **19**, 255 (2011).

23. X. Delen, S. Piehler, J. Didierjean, N. Aubry, A. Voss, M. A. Ahmed, T. Graf, F. Balembois, P. Georges, "250 W single-crystal fiber Yb:YAG laser," Opt. Lett. **37**, 2898 (2012).

Chapter 3 Thermally-Guided Fiber-Rod Laser

3.1   Chapter Overview

This chapter begins in section 3.2 with the introduction of the thermally-guided fiber-rod (TGFR) laser concept, a novel solid-state power-scalable geometry with dimensions that lie in the domain between traditional bulk and fiber devices. The motivation is to benefit from the excellent thermal management properties of fibers by maintaining a thin geometry. Additionally, the deleterious nonlinear effects which plague high power fiber lasers are reduced by thermally guiding a laser mode with significantly larger transverse beam dimensions, and by utilising a shorter device length than traditional fibers. The profile of the thermally-induced guide will be derived in section 3.3, along with an explanation of how this provides guiding within the device. Section 3.4 presents a model for predicting the gain in the TGFR device operating in an amplifier configuration, which will be a useful tool for analysing its power scaling potential. Finally, section 3.5 will conclude the chapter.

3.2   Motivation

We are motivated by our desire to develop laser sources that can provide high power (average and/or peak), high pulse energy and excellent beam quality for use in applications within materials processing, the medical sector, the military and fundamental science. As described in section 2.5, various solid-state architectures have been developed to achieve the performance required by the specific application, which two distinct types emerging, namely bulk lasers and fiber lasers. The thin-disc and fiber laser are leading the way in high power performance and are capable of attaining kW power levels with diffraction-limited beam quality. However, bulk and fiber concepts are not without their limitations (section 2.4), with the former generally plagued by thermal effects (with the exception of the thin-disc laser) and the latter suffering from nonlinear, energy storage and damage limitations. In light of these limitations, we propose the concept of the TGFR laser, which occupies a domain between traditional fiber and bulk rod devices. The TGFR laser aims to benefit from the advantages of bulk and fiber lasers whilst avoiding their limitations thus paving the way for high power laser operation. A key novelty of the TGFR laser is its unique method of mode control, which utilises thermally-induced lensing to guide the signal mode.

The TGFR is a cylindrical device consisting of a rare-earth-doped core material and an undoped cladding material with a lower refractive index, creating a step-index structure. Unlike traditional fibers, the core has a significantly larger diameter, on the order of hundreds of microns, a cladding diameter ranging from hundreds of microns to a millimetre and a device length on the order of tens

of centimetres (fig. 3.1). The cylindrical surface of the fiber-rod is in contact with a medium with a lower refractive index to guide pump radiation thus providing good spatial overlap between the pump and signal radiation. This could be air, water or another cladding glass. Pump radiation can also be guided at the core/cladding interface, allowing some freedom in absorption length and therefore device length.
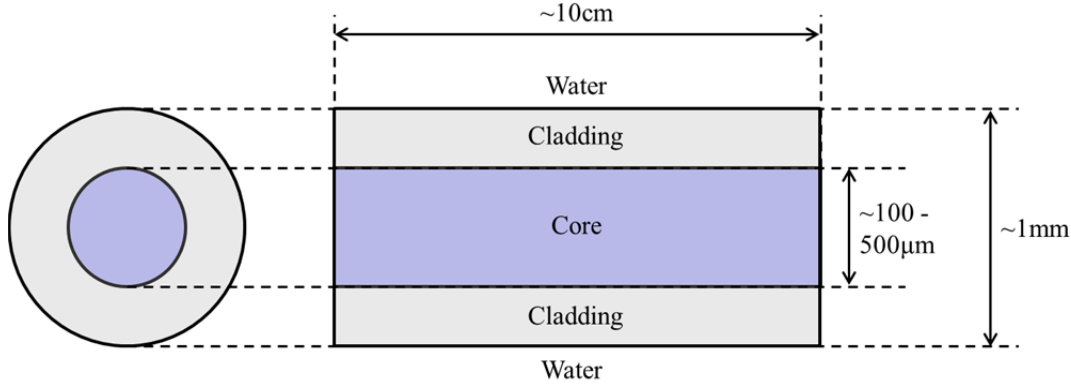
Figure 3.1: TGFR cross-section (left) and side profile (right).

This device utilises the key thermal management advantage of the fiber geometry by maintaining a high aspect ratio, with physical dimensions between conventional rod and fiber lasers. The larger transverse dimensions of the TGFR ensure a significantly larger mode size than traditional single-mode fiber lasers, leading to mode sizes closer to bulk geometries. This will result in a higher optical damage threshold, and combined with the relatively short device length, a higher threshold for deleterious nonlinear effects. The larger mode area will result in a higher device saturation energy, ultimately allowing larger pulse energies to be extracted before ASE limits performance.

3.3   Mode Control

Due to its large size, the TGFR core will form a highly multimode guide for signal radiation. However, we propose to take advantage of thermal lensing, which is typically a deleterious effect. This section will outline the principles of this thermal guiding technique by first describing the temperature distribution in the TGFR, before explaining how this distribution can be employed to control mode size through the device. A model is constructed that allows one to predict the influence of thermal guiding on mode size through the TGFR.

3.3.1   Radial Temperature Profile

To understand how thermal lensing can be exploited, it is first necessary to describe the temperature of the TGFR as a function of radial position, r, and longitudinal position, z. Consider the TGFR cross-section shown in fig. 3.2, which we have considered to consist of two regions, namely the core region, radius r_1, and the cladding layer(s), with radius r_2. Pump power is absorbed in the core region and a fraction of this power, η_h, is converted to heat.
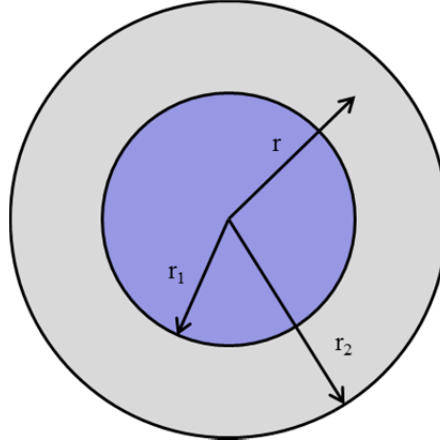
Figure 3.2: TGFR cross-section.

In deriving the radial temperature profile at each longitudinal position, the following assumptions were made:

1. Heat is only generated within the core and is solely due to the quantum defect.
2. Coolant on the cylindrical surface ensures heat flow is entirely radial.
3. The TGFR consists of an infinite number of infinitesimally thin slices of length dz and volume dV.
4. The TGFR is a cylindrically symmetric isotropic medium.
5. The cladding regions are concentric and can be considered as a single region.
6. The core and cladding regions have the same thermal and mechanical properties.

The steady-state heat equation describing the radial temperature, $T(r)$, of the TGFR at a particular longitudinal position, z, is given as [1]:

$$\frac{1}{r}\frac{d}{dr}\left(r\frac{dT(r)}{dr}\right) = -\frac{Q}{\kappa} \tag{3.1}$$

where Q is the heat deposited in volume dV at r, z. Equation 3.2 describes the heat density for the two regions of interest:

$$Q_1 = \frac{P_H}{\pi r_1^2 dz} \qquad\qquad 0 \leq r \leq r_1$$
$$\tag{3.2}$$
$$Q_2 = 0 \qquad\qquad r_1 \leq r \leq r_2$$

where P_H is the heat deposited in a slice at z. The following boundary conditions can be applied to this situation:

1. The temperature is continuous across the core/cladding interface, i.e. $T_1(r = r_1) = T_2(r = r_1)$.

39

2. The derivative of the temperature is continuous across the core/cladding interface, i.e. $\frac{dT_1(r=r_1)}{dr} = \frac{dT_2(r=r_2)}{dr}$.

3. The temperature is maximal at the centre of the TGFR i.e. $\frac{dT_1(r=0)}{dr} = 0$.

4. In a steady state, the heat removed from the cylindrical surface area, dA, of the TGFR by the coolant is equal to the generated heat [2]:

$$P_H = dAh_T[T_2(r = r_2) - T_C] \tag{3.3}$$

where T_C is the coolant temperature and h_T is the heat transfer coefficient, which varies between 0 for thermal insulation and ∞ for unrestricted heat flow to the heat sink.

By combining equation 3.2 and equation 3.3 and factoring in the boundary conditions, one can solve equation 3.1, to obtain a description of the radial temperature variation across the TGFR:

$$T_1(r) = T_C + \frac{Q_1 r_1^2}{4\kappa}\left[2ln\left(\frac{r_2}{r_1}\right) + \frac{2\kappa}{h_T r_2} + \left(1 - \left(\frac{r^2}{r_1^2}\right)\right)\right] \qquad 0 \leq r \leq r_1$$

$$\tag{3.4}$$

$$T_2(r) = T_C + \frac{Q_1 r_1^2}{2h_T r_2} - \frac{Q_1 r_1^2}{2\kappa}ln\left(\frac{r}{r_2}\right) \qquad r_1 \leq r \leq r_2$$

Therefore, a parabolic temperature variation occurs in the core region, whilst a logarithmic decay exists in the cladding region. This variation is shown for a typical example in fig. 3.3. Here we consider the temperature profile across an Yb-doped silica TGFR when pumped with a top-hat beam at 915nm, with 1030nm the intended operation wavelength. The TGFR in this example has a length of 10cm, a core radius of 150µm and a cladding radius of 240µm. It is assumed that 100W is absorbed within the core region, with no longitudinal dependence on absorption. A coolant temperature $T_C = 20°C$ is assumed, along with a thermal conductivity $\kappa = 1.38$W/mK [1] and a heat transfer coefficient $h_T = 570$W/mK [Appendix 3.1].

3.3.2   Thermal-Guiding Concept

The previous section describes the temperature profile of a TGFR when pumped. The thermo-optic coefficient, *dn/dT*, quantifies the change of refractive index with temperature:

$$n(r) = \frac{dn}{dT}T(r) \tag{3.5}$$

where *n(r)* is the refractive index at *z* and *r*. Trivial combination of equation 3.4 and equation 3.5 reveals that the thermally-induced refractive index profile follows the temperature profile, and thus exhibits a parabolic profile in the core region and a logarithmic profile in the cladding region:

$$n_1(r) = \frac{dn}{dT}\left(T_C + \frac{Q_1 r_1^2}{4\kappa}\left[2ln\left(\frac{r_2}{r_1}\right) + \frac{2\kappa}{h_T r_2} + 1\right]\right) - \frac{dn}{dT}\frac{Q_1 r_1^2}{4k}\left(\frac{r^2}{r_1^2}\right) + n_{mat} \qquad 0 \le r \le r_1$$

(3.6)

$$n_2(r) = \frac{dn}{dT}\left[T_C + \frac{Q_1 r_1^2}{2h_T r_2} - \frac{Q_1 r_1^2}{2\kappa}ln\left(\frac{r}{r_2}\right)\right] + n_{mat} \qquad r_1 \le r \le r_2$$

where n_{mat} represents the refractive index of the material at T_C.
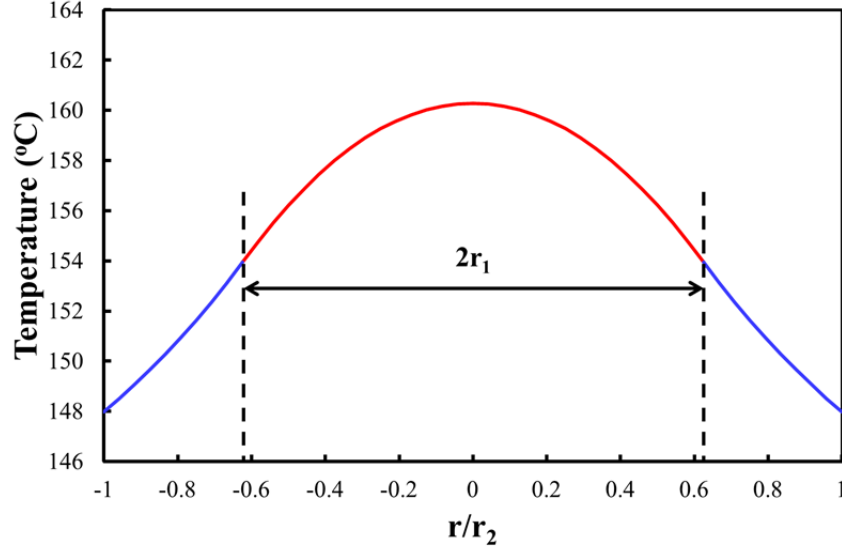
Figure 3.3: Example of the temperature profile across the core and cladding of a TGFR.

To understand how this parabolic refractive-index profile impacts beam propagation, it is useful to recall the discussion on Gaussian beam propagation from section 2.3.3, and in particular the complex beam parameter, q, given in equation 2.47. Gaussian beams will propagate differently through different optical elements. For example, a beam propagating through a block of glass has a longer Rayleigh range since $n_{glass} > n_{air}$ (equation 2.46), and therefore converges and diverges over a longer distance. In order to describe the effect of an optical element on a Gaussian beam, one can utilise ABCD formalism. This technique associates an optical element with a 2-by-2 matrix, known as an ABCD matrix. With knowledge of the input beam parameters, q_{in}, and the ABCD matrix of the optical element, the output beam parameters, q_{out}, can be calculated according to:

$$q_{out} = \frac{Aq_{in} + B}{Cq_{in} + D}$$

(3.7)

Table 3.1 lists three relevant ABCD matrices [3]. Scenario 1 describes beam propagation over a distance d through a medium with uniform refractive index n. Scenario 2 quantifies the effect of a thin lens of focal length f, where f is positive/negative for a converging/diverging lens. Scenario 3 is particularly interesting in the discussion of thermal guiding, and it describes beam propagation through a medium with a refractive index that exhibits a parabolic profile in the radial direction, namely:

41

$$n(r) = n_m - \frac{1}{2}n_{th}r^2 \tag{3.8}$$

where n_m represents the maximum refractive index in the centre of the medium, and n_{th} determines the rate of change of refractive index with radial distance. Equation 3.8 therefore describes the thermally-induced refractive index profile that occurs in the core region, $r \leq r_1$, which is the region of interest for signal beam propagation. From equation 3.2 and equation 3.6, we can write:

$$n_m = \frac{dn}{dT}\left(T_C + \frac{P_H}{4\pi\kappa dz}\left[1 + 2ln\left(\frac{r_2}{r_1}\right) + \frac{2\kappa}{h_T r_2}\right]\right) + n_{mat} \tag{3.9}$$

$$n_{th} = \frac{dn}{dT}\left(\frac{P_H}{2\pi r_1^2 \kappa dz}\right) \tag{3.10}$$

This result can be combined with the ABCD matrix in scenario 3 of table 3.1 to describe the effect of a thermally-induced lens on a Gaussian beam. Equation 3.10 confirms that the parabolic profile becomes stronger with an increase in heat power deposition density.
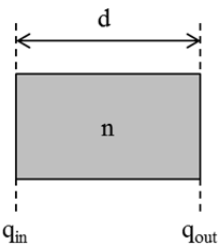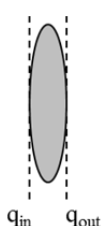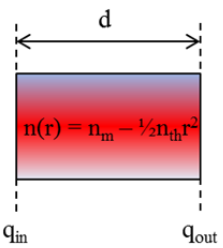
No.	Optical System	ABCD Matrix
1	Drift through a medium of refractive index n 	$\begin{pmatrix} 1 & \frac{d}{n} \\ 0 & 1 \end{pmatrix}$
2	Transmission through a lens of focal length f 	$\begin{pmatrix} 1 & 0 \\ -\frac{1}{f} & 1 \end{pmatrix}$
3	Transmission through a duct with a parabolic refractive index profile 	$\begin{pmatrix} \cos\left(d\sqrt{\frac{n_{th}}{n_m}}\right) & \frac{1}{\sqrt{n_m n_{th}}}\sin\left(d\sqrt{\frac{n_{th}}{n_m}}\right) \\ -\sqrt{n_m n_{th}}\sin\left(d\sqrt{\frac{n_{th}}{n_m}}\right) & \cos\left(d\sqrt{\frac{n_{th}}{n_m}}\right) \end{pmatrix}$

Table 3.1: Three relevant ABCD matrices.

Considering the example presented in fig. 3.3, we can use the ABCD matrix formulism to describe beam evolution. Fig. 3.4 depicts how a Gaussian beam, with a waist on the input face of the device, would propagate for various scenarios. The first scenario considers launching a 100μm beam waist on the input face of the TGFR. Here, the beam is initially focused by the parabolic refractive index profile. However, a smaller beam has a higher tendency to diffract, and so the beam forms a beam waist of 30.6μm before expanding. In contrast, a larger beam is more sensitive to lensing; therefore the beam reaches a maximum at 100μm before being focused again in an identical manner. The beam repeats this oscillation along the length of the device with a period of 42.6mm. A simple argument based on equating the two sides of equation 3.7 can be used to show that the beam oscillation period is proportional to $1/\sqrt{P_H}$ [Appendix 3.2]. Thus, if 1000W were absorbed in the device, (i.e. a 10-fold increase) the period would decrease by $1/\sqrt{10}$, to a value of 13.5mm. The beam waist radius within the device would also decrease, owing to the stronger thermal lens. It can be shown that the product of the maximum and minimum beam radii is also proportional to $1/\sqrt{P_H}$ [Appendix 3.2], hence the beam waist in the device would reduce to approximately 9.5μm. This scenario is shown for reference in the second scenario of fig. 3.4. The third scenario, assumes the original absorbed pump power of 100W, but instead launches a beam waist of 30.6μm. The period and beam size ratio are independent of input waist parameters, therefore the beam oscillates out of phase with scenario 1, i.e. initially expanding as diffraction outweighs focusing. By stipulating an equal beam waist at the input and output of the device, one can derive [Appendix 3.2] the beam waist radius that would neither focus nor diverge as it propagates along the device, w_G, as shown in equation 3.11:

$$w_G = \left(\frac{\lambda^2}{\pi^2 n_m n_{th}} \right)^{1/4} \tag{3.11}$$

In this example, a perfectly guided beam, where the focusing of the thermally-induced lens perfectly balances the diffraction of the beam, would occur for $w_G = 55.4$μm. This is shown in the fourth scenario of fig. 3.4. The final scenario shows the situation where no pump power is absorbed, assuming a flat refractive index profile. The beam experiences diffraction with no focusing component, and consequently interacts with the edge of the device after approximately 34mm, where the beam would be guided by the engineered step-index guide. This interaction can result in the beam coupling to higher-order modes, hence reducing beam quality, and resulting in increased power losses from scattering at the interface.
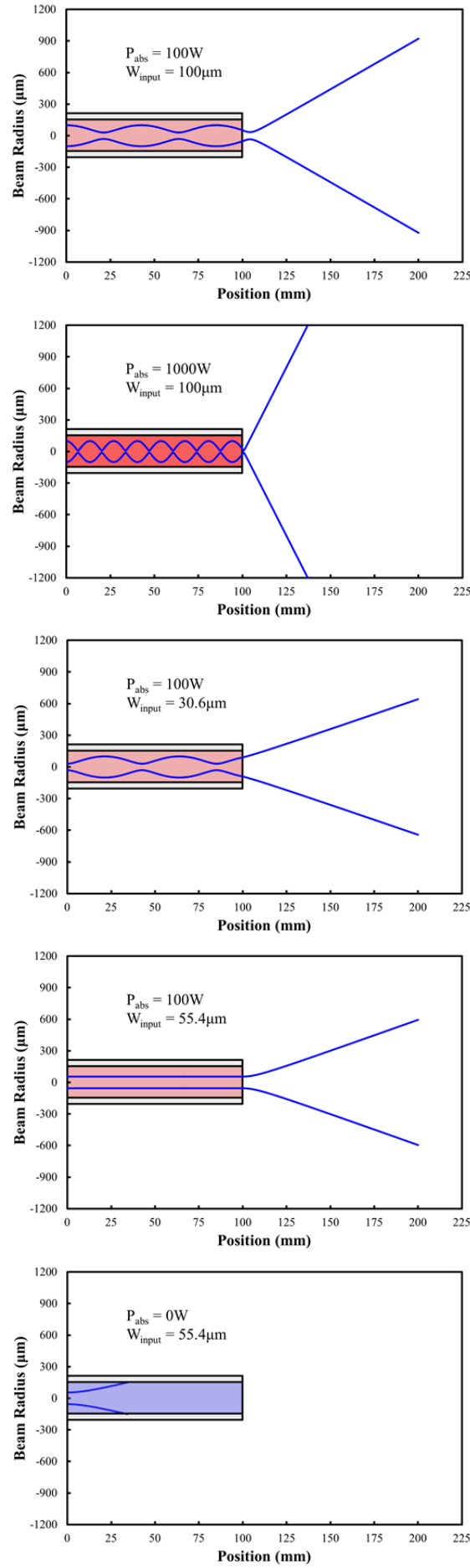
Figure 3.4: Beam radius evolution for a Gaussian input beam for scenario 1 (top) to 5 (bottom).

The scenarios presented here make the simplifying assumption that the heat power is absorbed uniformly both radially and longitudinally. The radial assumption is made due to the top-hat profile of the multimode diode pump beam, and the assumption that the core material has good ion-doping uniformity. However, assuming constant power absorption per unit length is a less reasonable assumption. In a low pump power regime, where the fraction of excited ions is negligible, the pump power absorption (and hence the heat power absorption) follows an exponential relationship (i.e. equation 2.13):

$$P_T = P_0 \exp(-n_T \sigma_{pa} z) \qquad (3.12)$$

where P_0 is the incident power and P_T is the power transmitted through a length, z, of a doped medium with the number of ions per unit volume given by n_T, and ion absorption cross-section at the pump wavelength σ_{pa}. Deviation from this simple relationship occurs as pump intensity increases, and is discussed further in the context of gain modelling in section 3.4.1. Consequently, for a device end-pumped through one end-face, the thermal lens at the pump input end will be stronger than the output end. To account for this longitudinal variation in thermal lens strength, the device was considered to consist of a very large number (ideally infinite) of thin slices, as shown in fig. 3.5. The heat power absorption in each slice was calculated, allowing each slice to be modelled as a thermal lens. The device was therefore essentially decomposed into an infinite number of thermal lenses, which typically get progressively weaker further from the pump input end.

The thermal-guiding model starts with an arbitrary input beam, with a defined beam size and radius of curvature, providing a known q_{in}. It then propagates the beam through a very thin longitudinal slice of medium (fig. 3.6) with the appropriate parabolic refractive index profile defined by the device configuration and pumping conditions. The model works by calculating q_{out}, from this slice, i.e. the output beam size and radius of curvature, which in turn becomes q_{in} for the next slice. This process is then applied to arbitrary lengths of gain media and free-space. The model allows each slice to be a different ABCD matrix, for example as the pump power is absorbed non-uniformly this will lead to each consecutive slice having a slightly different thermal lens strength.
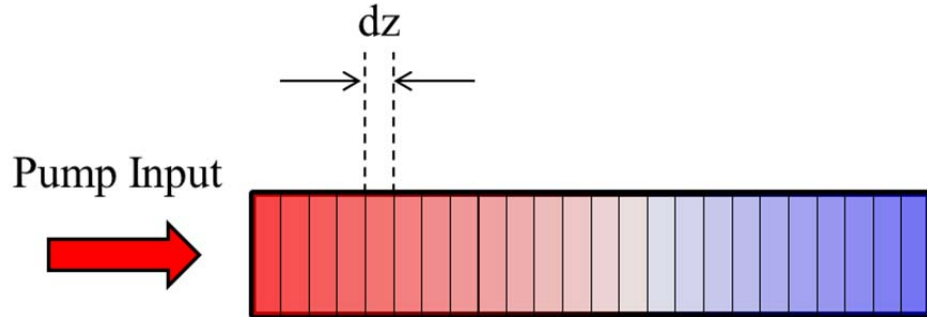
Figure 3.5: TGFR decomposed into an 'infinite' number of thermal lenses, which are stronger (red) at the pump input and weaker (blue) at the opposite end.
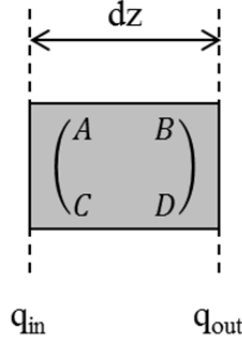
Figure 3.6: The model calculates the output beam parameters from predetermined input beam parameters and the appropriate ABCD matrix.

In order to calculate the output beam parameters, for any ABCD matrix, it is helpful to first recast equation 2.47 in the form:

$$\frac{1}{q(z)} = \frac{1}{R_{OC}(z)} - i\frac{\lambda}{\pi w^2(z)} = \mathbb{R} - i\mathfrak{I} \tag{3.13}$$

where $\mathbb{R}$ and $\mathfrak{I}$ represent the coefficient of the real and imaginary parts of the expression. Furthermore, one can now write q as:

$$q(z) = \frac{1}{\mathbb{R} - i\mathfrak{I}} \cdot \frac{\mathbb{R} + i\mathfrak{I}}{\mathbb{R} + i\mathfrak{I}} = \frac{\mathbb{R}}{\mathbb{R}^2 + \mathfrak{I}^2} + i\frac{\mathfrak{I}}{\mathbb{R}^2 + \mathfrak{I}^2} = \mathbb{X} + i\mathbb{Y} \tag{3.14}$$

where $\mathbb{X}$ and $\mathbb{Y}$ represent the real and imaginary parts of the complex q-parameter. We can now write equation 3.7 in the form:

$$\mathbb{R}_{out} - i\mathfrak{I}_{out} = \frac{C(\mathbb{X}_{in} + i\mathbb{Y}_{in}) + D}{A(\mathbb{X}_{in} + i\mathbb{Y}_{in}) + B} = \frac{(C\mathbb{X}_{in} + D) + iC\mathbb{Y}_{in}}{(A\mathbb{X}_{in} + B) + iA\mathbb{Y}_{in}} \cdot \frac{(A\mathbb{X}_{in} + B) - iA\mathbb{Y}_{in}}{A(A\mathbb{X}_{in} + B) - iA\mathbb{Y}_{in}}$$

$$\tag{3.15}$$

$$\mathbb{R}_{out} - i\mathfrak{I}_{out} = \frac{\left(AC\mathbb{X}_{in}^2 + AC\mathbb{Y}_{in}^2 + AD\mathbb{X}_{in} + BC\mathbb{X}_{in} + BD\right) - i\mathbb{Y}_{in}}{(A\mathbb{X}_{in} + B)^2 + A^2\mathbb{Y}_{in}^2}$$

Simply by equating real and imaginary parts we can determine the beam radius and radius of curvature of the output beam:

$$R_{out} = \frac{(A\mathbb{X}_{in} + B)^2 + A^2\mathbb{Y}_{in}^2}{AC\mathbb{X}_{in}^2 + AC\mathbb{Y}_{in}^2 + AD\mathbb{X}_{in} + BC\mathbb{X}_{in} + BD}$$

$$\tag{3.16}$$

$$w_{out} = \left[\frac{\lambda}{\pi} \cdot \frac{(A\mathbb{X}_{in} + B)^2 + A^2\mathbb{Y}_{in}^2}{\mathbb{Y}_{in}}\right]^{1/2}$$

Equation 3.16 quantifies the output beam parameters in terms of the input beam parameters and the appropriate ABCD matrix. This equation can be applied in a continuous fashion for any particular

ABCD matrix, assuming that the input beam parameters are known. Therefore the beam size through the TGFR device can be predicted under different pumping conditions.

3.4 Gain Performance

A model was constructed to predict the gain performance of the TGFR device operating in an amplifier configuration. This model allows one to investigate how the device geometry and composition impact performance.

The model considers how the intensity of a signal beam and a co-linear pump beam vary as they propagate along a length of gain medium (fig. 3.7). Both beams are considered to have a top-hat intensity profile, which remains constant in the transverse dimension along the length of the device. The background theory covered in section 2.2 provides the basis for constructing this model. We can recast equation 2.13 in terms of intensity:

$$I_T = I_0 \exp(-\alpha(\nu)z) \tag{3.17}$$

where I_0 is the incident intensity and I_T is the intensity transmitted through a length z, with an absorption/gain coefficient α at frequency ν. Therefore, the intensity of the signal and pump beam is a function of position through the material.
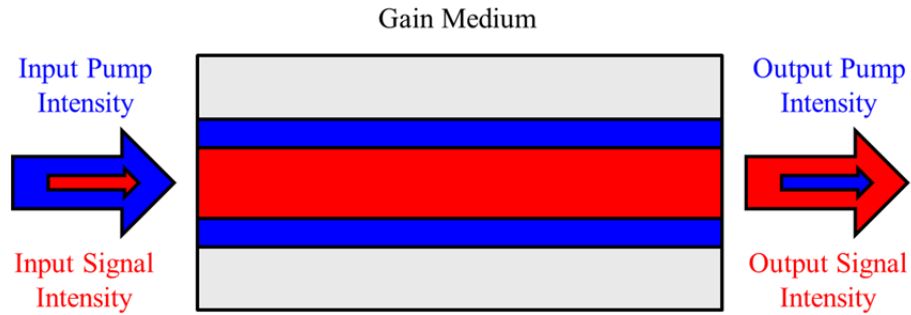
Figure 3.7: The model predicts the intensity evolution of the signal and pump beam along the length of the device.

3.4.1 Three-Level System

If we consider a quasi-three-level system, it is helpful to first consider equation 2.18, which describes the rate of change of the upper and lower laser level, and recast it in terms of signal and pump intensity. The pump rate density, r_P, is equal to the number of ions that are excited per unit time per unit volume, and can be written as [Appendix 3.3]:

$$r_P = \frac{I_P \sigma_{pa}}{h\nu_P} n_1 \tag{3.18}$$

where I_P is the pump intensity and ν_P is the frequency of the pump radiation. Additionally, one can show that the intensity of a beam can be related to photon density via [Appendix 3.4]:

$$I = h\nu c\phi \tag{3.19}$$

Incorporating equation 3.18 and equation 3.19 into equation 2.18, we obtain:

$$\frac{dn_1}{dt} = -\frac{dn_2}{dt} = -\frac{I_P\sigma_{pa}}{h\nu_P}n_1 + \frac{I_L\sigma_{se}}{h\nu_L}n_2 + \frac{I_P\sigma_{pe}}{h\nu_P}n_2 - \frac{I_S\sigma_{sa}}{h\nu_L}n_1 + \frac{n_2}{\tau_f} \tag{3.20}$$

where I_S is the signal intensity, σ_{sa} and σ_{se} are the transition cross-sections for signal absorption and signal emission respectively, σ_{pe} is the transition cross-sections for pump emission and τ_f is the upper-state lifetime for the laser transition. Looking at equation 3.20 term by term, we see that the lower state population increases (and hence the upper state population decreases) due to the desired stimulated emission at the signal wavelength, in addition to spontaneous emission and stimulated emission at the pump wavelength. The lower state population decreases (and hence the upper state population increases) due to optical pumping and a signal re-absorption term owing to the three-level nature of the system. In equilibrium, the rate of excitation is equal to the rate of decay, and therefore the left-hand side of equation 3.20 can be set to zero. Considering that this is a three-level system, we have $n_T = n_1 + n_2$, and thus we can calculate the population density in the upper laser level:

$$n_2 = \frac{\left(\frac{I_P\sigma_{pa}}{h\nu_P} + \frac{I_S\sigma_{sa}}{h\nu_L}\right)n_T}{\frac{I_P\sigma_{pa}}{h\nu_P} + \frac{I_P\sigma_{pe}}{h\nu_P} + \frac{I_S\sigma_{sa}}{h\nu_L} + \frac{I_S\sigma_{se}}{h\nu_L} + \frac{1}{\tau_f}} \tag{3.21}$$

Therefore, from an incident pump and signal intensity we can calculate the population density of the upper and lower laser levels, allowing one to calculate the absorption/gain coefficient, $\alpha(\nu_L)$, at the signal frequency. However, equation 3.17 indicates that since $\sigma_{pa}n_1 > \sigma_{pe}n_2$, the pump intensity will decrease as a function of position, therefore the pumping rate and hence the value of n_2 will vary with position.

The model accounts for this longitudinal variation by considering the gain medium to be constructed of a very large amount of very thin slices, with thickness dz (fig. 3.8), in a similar manner to the thermal guiding model presented in section 3.3.2. The input intensities of the pump and signal radiation are known, and this determines the relative population densities within the first slice. The population densities can then be used to calculate the absorption or gain experienced by the pump and signal beams across the slice, by considering equation 3.17 differentiated with respect to z:

$$dI_T = -\alpha(\nu)I_T dz \tag{3.22}$$

Therefore, the intensity of each beam will decrease/increase for a positive/negative value of $\alpha(v)$. The beam intensities leaving one slice then determine the population density within the next slice, and the process continues slice by slice along the device. The gain for the signal radiation is calculated by considering the ratio of the output and input signal power, which is calculated trivially from the intensity and beam sizes at these two positions.
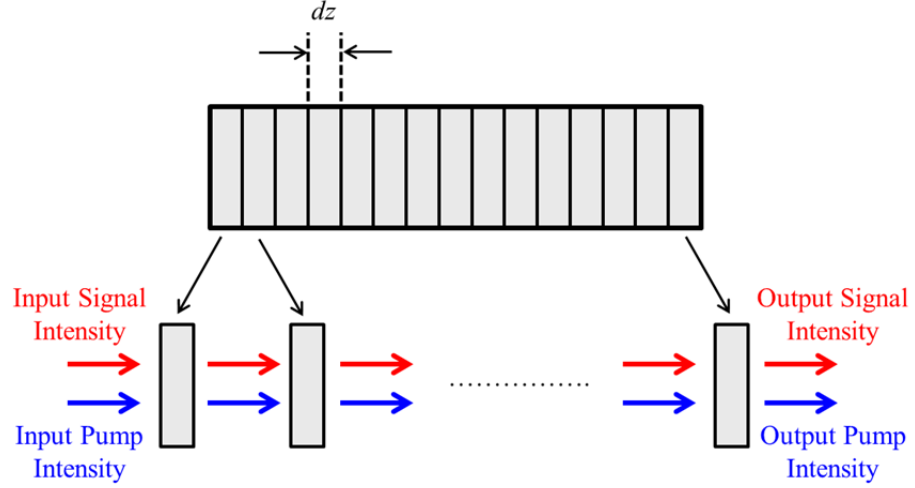
Figure 3.8: Gain medium considered as a very large number of thin slices.

3.4.2   Four-Level System

The same approach can be applied to the case of a four-level system, and it can be shown that equation 3.20 is also valid, but with the consideration that $\sigma_{sa} = 0$, i.e. the material is transparent to the signal, and replacing n_1 with n_0. Consequently, the gain of a four-level system will be unity with zero pump power, assuming negligible losses due to scattering/absorption at the signal wavelength. The gain in a quasi-three-level system will reach transparency for a pump intensity that achieves a situation where $\sigma_{sa} n_1 = \sigma_{se} n_2$, when averaged over the device length, again assuming negligible losses.

3.5   Conclusion

In this chapter we have introduced the concept of the TGFR laser, a device which occupies a domain between traditional fiber and bulk rod devices, benefitting from the thermal management properties of fibers, and the reduced non-linearities of bulk devices. A novel method for controlling the beam profile was introduced, which relies on thermally-induced guiding within the device. The thermally-induced refractive index profile was derived and shown to be parabolic in nature, and the resulting beam guidance for various scenarios was presented. A model was constructed which predicts beam evolution through the TGFR for the case of non-uniform heat distribution, utilising the ABCD matrix formulism. Finally, a gain model was presented, which allows one to predict the

gain experienced through the TGFR device operating in an amplifier device. The model can be employed to optimise the performance of an amplifier or laser, by predicting the gain level for various amplifier geometries and compositions. We have explained our motivation and have assembled the relevant tools necessary to characterise and predict the performance of the TGFR laser. Chapter 4 describes fabrication of three potential TGFR devices constructed from soft glass hosts, whilst Chapter 5 and Chapter 6 assess the potential of the TGFR concept based on a soft glass and silica host material respectively.

References

1. D. C. Brown, H. J. Hoffman, "Thermal, Stress, and Thermo-Optic Effects in High Average Power Double-Clad Silica Fiber Lasers," IEEE J. Quantum Electron. **37**, 207 (2001).

2. W. Koechner, Solid-State Laser Engineering, 6 ed., Sixth Revised and Updated Edition (Springer, 2006).

3. H. Kogelnik, T. Li, "Laser beams and resonators," Appl. Opt. **5**, 1550 (1966).

Chapter 4   Soft Glass Thermally-Guided Fiber-Rod Fabrication

4.1   Chapter Overview

In this chapter we suggest soft glass as the host material for a high power TGFR laser. Firstly, in section 4.2 we will discuss our motivation for this material choice. In section 4.3 we describe the background theory relating to the fiber-rod fabrication process. Section 4.4 will cover general glass requirements which should be met to allow successful fiber-rod fabrication with suitable properties for laser experiments. This section will also introduce three sources of glass material, which are identified as potential candidates to achieve the objective of power scaling in a TGFR structure. In section 4.5 the manufacture of one of these three glass sources will be described. Section 4.6 will describe the quantification of the absorption cross-section of each doped glass host, which has implications for the final fiber-rod dimensions. Section 4.7 will describe fiber-rod fabrication for each glass source, paving the way for the laser-based experiments conducted on each source in Chapter 5. Finally, section 4.8 will conclude the chapter.

4.2   Motivation

A TGFR device based on a soft glass host, such as phosphate or silicate, rather than silica which is the material of choice for traditional fibers, brings many attractive advantages. Soft glasses consist of a network former such as P_2O_5 or SiO_2, with additional components which impact the rare-earth solubility, the refractive index and glass fabrication properties. Due to their multicomponent nature, soft glasses possess a less defined glass network, ultimately resulting in a significantly increased solubility of rare-earth ions compared to silica glass. For example, negligible concentration quenching was observed in an Yb-doped phosphate fiber doped at 12 wt. % [1], whilst the doping level of rare-earth ions in silica is limited to the percent level before the onset of deleterious effects [2, 3]. Since soft glasses can have higher doping concentrations, the devices can be shorter, thereby increasing the threshold power for nonlinear effects such as SRS and SBS.

Further benefits from using soft glasses over silica stem from the fiber fabrication process. Due to the fact that some of the chemicals used in the fabrication of soft glass fiber devices cannot be volatised, modified chemical vapour deposition (MCVD) as used for silica fibers is not possible. Therefore the rod-in-tube approach is employed, which is covered in further detail in section 4.3. This technique involves drawing fiber structures from a preform consisting of a rod of core glass material sleeved in at least one tube of cladding glass. It is possible to commercially produce rare-

earth doped phosphates and silicates with very good homogeneity and precisely controlled refractive index. This allows fiber devices to have precisely controlled doping profiles, which is a significant challenge in the MCVD process. A major driving force for production of these materials stems from nuclear fusion research, which utilises large blocks of Nd:phosphate glass to deliver MJ-level pulse energies [4]. This excellent optical quality benefits laser experiments by minimising distortions to the beam profile and transmission losses, which will be vital to the thermal guiding concept.

Additionally, control over the fabrication process can provide a useful insight into device testing since it enables a holistic understanding. This allows a feedback loop to be developed whereby a device is made, characterised, and the results are utilised to suggest future fabrication improvements, leading to a superior device. This process can be iterated to optimise the TGFR for the desired outcome.

It is well understood that silica fibers have superior thermomechanical properties compared to soft glasses. This might suggest that thermally-induced stress fracture could prevent high power operation, since the pump radiation will deposit heat in the device owing to the quantum defect. The maximum permissible heat power per unit length for a cylindrical geometry is [5]:

$$P_{H/L} \approx 8\pi R_s \tag{4.1}$$

where $P_{H/L}$ is the heat power per unit length and R_s is the thermal shock parameter which quantifies the heat power per unit length to induce thermal fracture. Typical values of R_s for phosphate and silicate soft glasses are in the region of 100W/m [6], indicating a maximum heat load per unit length of approximately 2.5kW/m. If we consider pump power incident on the TGFR, we can recast equation 2.13 in terms of power and differentiate with respect to length to obtain:

$$\frac{dP_p}{dz} = -\alpha P_0 \exp(-\alpha z) \tag{4.2}$$

where P_p is the pump power at position z, P_0 is the incident pump power and α is the absorption coefficient as defined by equation 2.14. Logically, the highest power deposition will be at $z = 0$, i.e. at the pump input end of the device, and so this is where we would expect thermally-induced stress fracture to occur. If we assume the heat is deposited entirely due to the quantum defect, we can multiply equation 4.2 by $(1 - \eta_{QD})$ to obtain the maximum permissible heat power per unit length:

$$P_{H/L} = (1 - \eta_{QD})\alpha P_0 \tag{4.3}$$

To get an estimate for the maximum operating power regime, consider the example of 800nm pumping a Nd-doped phosphate glass, which typically has a peak emission wavelength at 1054nm. Operating on these transitions leads to a quantum defect of $\eta_{QD} \approx 0.76$. If we assume an absorption

length, $z_{abs} = 1/\alpha$, of 10cm, we obtain a maximum permissible launched pump power of $P_0 \approx$ 1.07kW, suggesting kW-level output powers should be possible in a soft glass based device.

Whilst the fabrication process for soft glass fibers is not as developed as their silica counterparts, research in this area is very active. Due to the ability to dope these glasses heavily, high gain per unit length values have been reported, such as a 7 wt. % thulium-doped silicate fiber amplifier which achieved a gain of 5.8dB/cm [7], and an 3/2 wt. % erbium/ytterbium-doped phosphate fiber amplifier which produced a gain of 5dB/cm [8]. A modelocked laser based on a 5 wt. % thulium-doped silicate fiber, produced 0.76nJ pulses at a repetition rate of 13.2MHz, and achieved a gain-per-unit-length of more than 2dB/cm [9]. An impressive 56.9W of output power was reached with a 12 wt. % ytterbium-doped phosphate fiber laser, and the same fiber used in an amplifier configuration achieved a gain of 27dB [1]. A significant draw-back of soft-glass fibers is the high propagation loss compared to silica which display sub dB/km losses for passive fibers around telecommunications wavelengths. These losses can be attributed to absorption due to impurities, which generate heat, and scattering, which can result from a non-perfect core/cladding interface. Although the fiber used in [7] displayed a relatively impressive propagation loss of 0.7dB/m at 976nm, this is considerably higher than silica and thus represents a limitation which needs to be addressed within this technology. The ability to achieve high gain per unit length can help to offset these high propagation losses.

4.3   Fabrication Background

Fiber-rod fabrication was carried out in-house on a fiber-drawing tower designed to operate in the temperature range suitable for soft glasses, i.e. < 1000°C. Essentially, a glass preform is heated by a furnace to a temperature whereby the viscosity becomes sufficiently low so as to allow a fiber or cane to be drawn down. The basic components of the tower are shown in fig. 4.1. The glass preform, which typically has a diameter between 10mm and 20mm and a length between 50mm and 100mm, is held by a silica support rod in the centre of a hollow cylindrical graphite susceptor, which is turn is held in position by a silica mount and centred in an RF induction coil (fig 4.2). Note that the silica is not deformed in the temperature range used for soft glass drawing. RF energy is coupled into the susceptor, producing Eddy currents which result in heating of the preform. Therefore, the RF coil and susceptor act as the furnace. During operation argon is passed over the preform and susceptor to create an inert atmosphere. A thermocouple inserted in the wall of the susceptor provides temperature information. Important drawing parameters are controlled through a user interface, including: furnace temperature, preform-lowering rate and pulling rate. The furnace temperature is critical, as this controls the viscosity of the glass, which determines whether the

glass will be able to be drawn down. The fiber-rod dimensions are suited to drawing using the cane-puller, however traditional fibers can be drawn using a much faster rotating drum.

There are three important temperatures to consider when drawing the preform into a fiber or cane: the transition temperature T_g, the crystallisation temperature T_x and the melting temperature T_m. At T_g the glass is considered to be a supercooled liquid, displaying liquid-like thermal properties. This is the temperature at which the glass would deform under its own weight, and is associated with a viscosity of approximately $10^{12.5}$Pa.s [10]. If the glass is heated above T_x, then crystals i.e. long-range atomic order, may form if the material is not cooled at a rate that prevents long-range bonds having adequate time to form. T_m is the point at which the glass becomes a liquid.
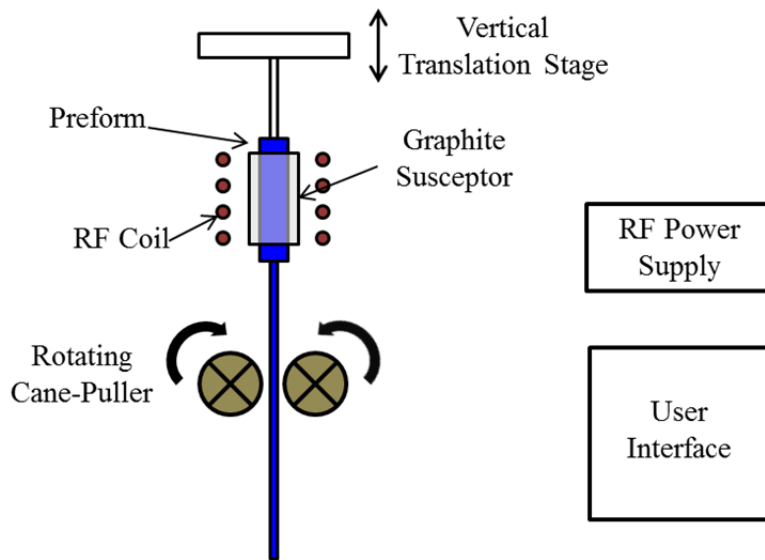
Figure 4.1: Basic components of the soft glass fiber-drawing tower.
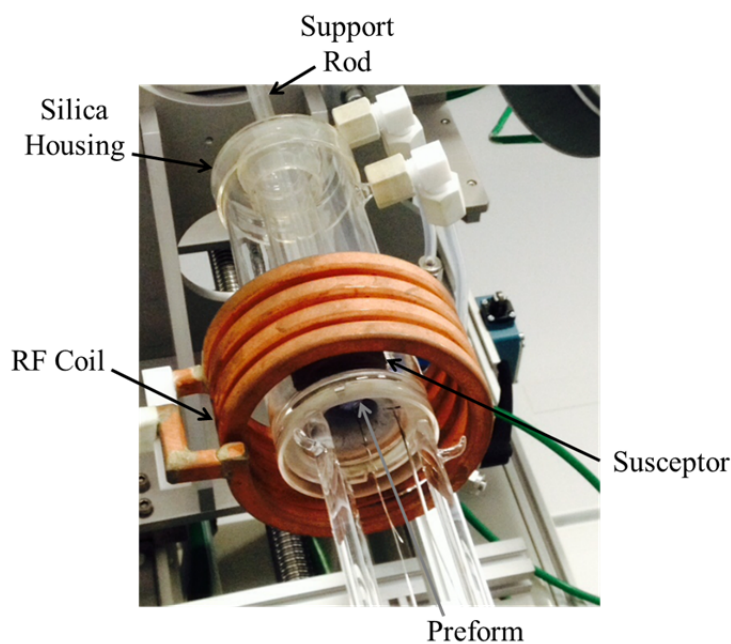
Figure 4.2: Furnace and preform mounting arrangement.

Knowledge of T_g and T_x is vital for glass pulling, since one must heat the glass above T_g, to reach the required viscosity for the glass to draw down, but keep it below T_x, to prevent deleterious crystal formation. The presence of crystals in the glass will at best significantly increase scattering losses in the device, and at worst prevent drawing of the glass completely. The glass stability parameter, ΔT_{gx}, quantifies the temperature difference between the crystallisation temperature and the transition temperature i.e. $\Delta T_{gx} = T_x - T_g$. Ideally ΔT_{gx} should be as large as possible, since it represents the temperature range through which the glass can be pulled down without suffering crystal formation.

In order to quantify these temperatures for a specific sample, one can carry out differential thermal analysis (DTA), as described in [10]. In this technique a glass sample and an inert sample (i.e. air) are provided with the same rate of heat input. The temperature difference between samples is recorded and any shifts due to endothermic and exothermic processes indicate the temperatures of interest. Below T_g the DTA trace exhibits a flat baseline, since the glass sample and inert sample are simply increasing in temperature subject to their thermal properties. As mentioned, T_g indicates the temperature whereby the glass sample transitions to a supercooled liquid state, corresponding to an endothermic peak as the thermal properties of the sample change. The point of deviation from the flat DTA baseline indicates T_g. Following T_g, a flat but shifted baseline resumes, as the supercooled liquid and inert sample continue to increase in temperature. Crystallisation of the supercooled liquid can occur in stages, associated with successive exothermic peaks. As before, the point of deviation from the DTA baseline and the first crystallisation stage indicates T_x. Above the crystallisation processes the baseline will continue until T_m is reached, which corresponds to an endothermic peak. An example of a DTA run that was performed in-house is shown in fig. 4.3. The glass sample used in this run is an undoped silicate glass, KF-2, which will be introduced in section 4.4.
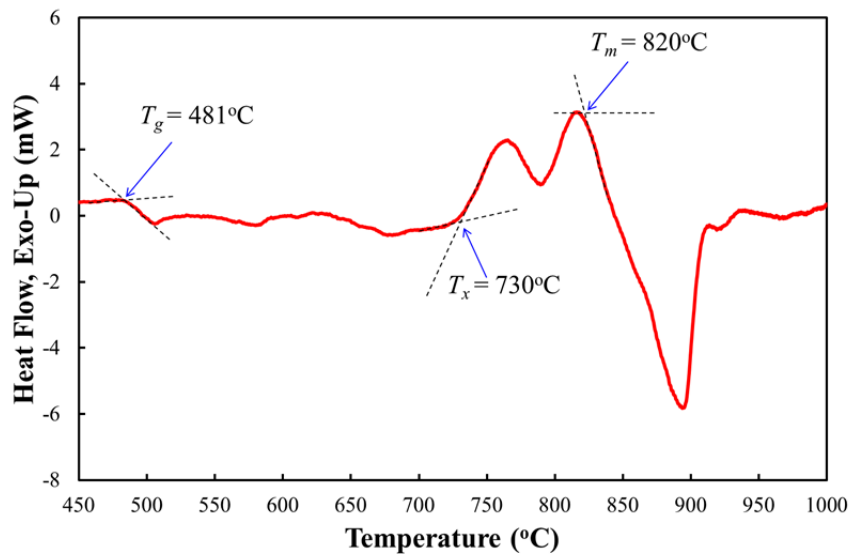
Figure 4.3: DTA example for KF-2 with T_g, T_x and T_m indicated.

Unlike silica preforms, soft-glass preforms are not produced via MCVD. The preferred fabrication method is the rod-in-tube technique. In this method, a higher refractive index core glass rod is inserted into a lower refractive index cladding glass tube. This process can be repeated for double-clad fibers. A slight gap of the order of 100μm should be maintained between the core and cladding to allow insertion. To keep losses to a minimum it is very important to ensure that air gaps do not form at the interface between the core and the cladding glass. This can be achieved using a vacuum pump above the preform (which has sealed at the bottom after the initial neck) to force air up and out of the preform during a draw. Additionally, surface quality of the two fusing surfaces must be good to ensure a high quality interface is produce.

Once the preform has reached the required viscosity, it will start to neck, or drop slightly, towards the bottom of the preform. One can attach a weight to the preform to encourage necking. The glass is then pulled down into a thin strand, and clamped in the cane-puller, which pulls the glass down at a specified rate. Simultaneously, the vertical translation stage lowers the preform into the furnace, thus the final dimensions of the cane are determined by the ratio of the lowering/pulling rates. Caning is a significantly slower process than fiber drawing, and results in thicker glass structures.

It is very important that the various glasses used in the rod-in-tube preform have similar thermal properties, i.e. a close match between drawing temperatures and the thermal expansion coefficient (CTE). A close drawing temperature is necessary so that the glasses involved have similar viscosities when being pulled down. If one glass reaches the required viscosity whilst another is too viscous, then the preform will not neck down. Furthermore, if the temperature is then increased to ensure the other glass reaches the required viscosity, one runs the risk of crystallisation in the first glass, which will be further above its drawing temperature and thus closer to its crystallisation temperature. A close match in the CTE is necessary to avoid the risk of cracking and the core/cladding interface. Expansion mismatch can lead to stresses in the fiber-rod, amplified by the rapid cooling within the glass as it is pulled down and out of the furnace. Furthermore, these stresses can be locked into the fiber-rod, and initiate fracture during laser operation, when the device is subject to high thermal loads.

4.4   Glass Requirements

The optical, thermal and mechanical properties of the glass host used for the TGFR investigation are of critical importance. As mentioned above, it is of vital importance, particularly for the fabrication process, that the thermal properties of the core and cladding glass should be well matched, especially T_g and the CTE. Furthermore, the glass should display good homogeneity, which will ensure the laser beam can propagate through the material without distortion, and will be essential for the proposed thermally-induced mode control. The thermal guiding technique also requires that the thermo-optic coefficient of the core glass is positive. Additionally, the transmission losses of the glass should be low, so that gain is sufficient to achieve lasing in the

fiber-rod device. Finally, the refractive index step between the core and cladding glass should be suitable for radiation guiding. Table 4.1 summarises these requirements. Note that the first three properties are important for fabrication, whilst the last five properties are important for lasing experiments (the CTE is important in both domains).

The core glass material was doped with neodymium, which exhibits a four-level character for transitions between the $^4F_{3/2}$ level and the $^4I_{11/2}$ level, promoting a low lasing threshold. Additionally, there are well-established fabrication techniques for Nd-doped soft glasses. Important spectroscopic information, relating to absorption cross-section and peak emission wavelength should be obtained, which will aid design.

Property	Requirement
Glass stability parameter	As large as possible
Transition temperature	Close match between doped/undoped glass
Coefficient of thermal expansion	Close match between doped/undoped glass
Thermo-optic coefficient	Positive for the doped glass
Transmission losses at lasing wavelength	As low as possible
Homogeneity	Beam distortions as low as possible
Refractive index	Doped glass higher than undoped glass

Table 4.1: General glass requirements.

In light of this brief overview, three sources of potential glass hosts were identified. The first and most desired source, labelled Source I, was in-house manufacture of a Nd-doped (NP35V) and undoped phosphate glass (NP35). This manufacture was done in collaboration with a GTS, a glass research and development company. In-house manufacture would allow the investigation to be truly holistic, as important fiber-rod fabrication and compositional issues that arise could be traced back to the glass manufacture and subsequently improved. The second source, Source II, was a commercial laser glass company Kigre Inc., which supplied bulk pieces of Nd-doped (Q246) and undoped silicate glass (KF-2) with very high optical quality. Finally, the third source, Source III, came from collaboration with the Politecnico di Torino, an academic research institute which specialises in soft glass manufacture and fiber fabrication. The institute provided fiber-rods with a Nd-doped phosphate core glass (CL1:Nd) and undoped phosphate cladding glass (CL1). The remainder of this chapter will discuss each glass source in more detail, covering the various fabrication stages, benefits of each source and relevant spectroscopy. Table 4.2 displays a brief description of each glass source, and the glass codes.

Source	Description	Doped Glass	Undoped Glass
I	In-house manufacture of Nd-doped and undoped phosphate glass.	NP35V	NP35
II	Purchase of Nd-doped and undoped silicate glass from Kigre Inc..	Q246	KF-2
III	Collaboration to obtain a fiber-rod device constructed from Nd-doped and undoped phosphate glass.	CL1:Nd	CL1

Table 4.2: Host glass sources.

4.5   Glass Manufacture

Source I required the glass to be manufactured in-house, whilst Source II and Source III made use of pre-manufactured glass. As stated previously, an important advantage of being involved with the glass manufacture process is gaining an insight into how issues occurring downstream in fiber-rod fabrication or laser characterisation experiments can be related to the glass host. The objective for this phase was to manufacture glasses suitable for a rod-in-tube fiber-rod device, therefore satisfying the criteria in table 4.1.

In order to keep the thermal properties closely matched, the compositions of the core and cladding glass were kept as similar as possible, with the exception that the core glass was doped with neodymium. The glass was predominantly formed from phosphorus oxide, which constitutes the glass network former and makes up over 80% of the glass composition. Other constituents include: lithium oxide and magnesium oxide which add strength to the glass, aluminium oxide which increases durability, niobium oxide which controls the refractive index, antimony oxide which acts as a refining agent and neodymium oxide which is added to the core glass to act as the laser active ion. The neodymium concentration was specified at 0.3 wt. % (section 4.7.2).

To manufacture the glass, the above oxides, which exist in powder form, are accurately weighed and mixed. The contents are then placed in a platinum crucible, utilised for its inert properties, and melted in a furnace at approximately $1200^{o}C$. Following the melt phase, oxygen is bubbled through the liquid to oxidise the constituents, which have been deoxidised by the ammonia present in the phosphorus powder. The melt is then poured onto a hotplate at around $100^{o}C$, with graphite blocks placed to determine the cast dimensions (fig 4.4 (left)). After approximately 1 minute the newly formed glass is transferred to an annealing oven at $500^{o}C$, which is cooled very slowly to ensure the glass does not crack due to thermal shock. This process was repeated for both the doped and undoped glasses.

It was immediately apparent from the first manufacturing attempt that the produced glass displayed poor homogeneity. This was confirmed visually, as clumps of constituents formed, as shown for the doped glass in fig 4.4 (right). Furthermore, the manufacture process was repeated, this time with the inclusion of a homogenisation element, which corresponded to mechanically stirring the glass in the melt phase, which achieved a more uniform glass composition. The doped/undoped glass from the first manufacture attempt is labelled NP35V(1)/NP35(1), whilst the doped/undoped glasses from the second improved manufacture attempt is labelled NP35V(2)/NP35(2).
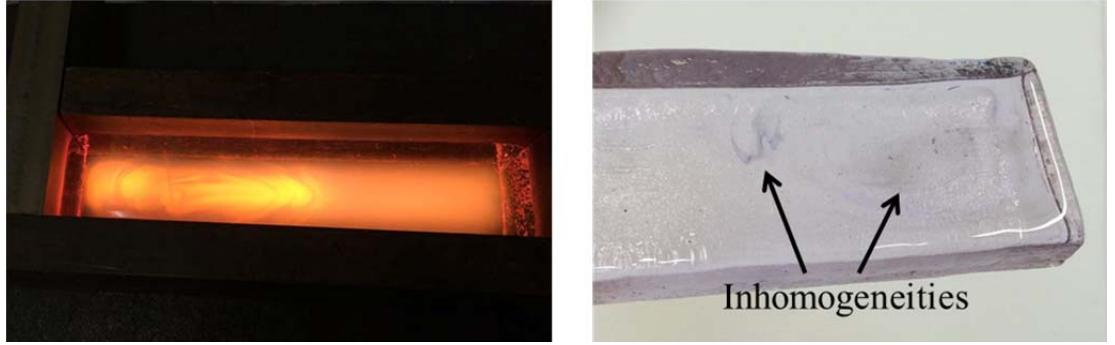
Figure 4.4: Poured melt (left) and inhomogeneities in NP35V(1).

4.6   Absorption Cross-Section

The absorption cross-section and doping concentration must be considered when designing the TGFR, since these parameters determine the absorption length and therefore device length. The absorption length is defined as the length after which the pump power has been reduce to 1/e of its initial value. Generally, a device on the order of three absorption lengths is necessary to ensure the majority of the pump power is absorbed, thus allowing efficient operation. For the case of a four-level system, with negligible lower state excitation, equation 2.13 can be used to write the absorption length, z_{abs}, as:

$$z_{abs}(\lambda) = \frac{1}{\sigma_{pa}(\lambda)\, n_T} \tag{4.4}$$

where, as before, σ_{pa} is the pump absorption cross-section and n_T is the total ion density.

The absorption cross-section of the doped glass from Source I and Source II was measured in-house, whilst the absorption cross-section for the doped glass from Source III was measured by the Politecnico di Torino as discussed in [11]. Disc samples were obtained from an early iteration of NP35V, labelled NP35V(0), and from Q246, to measure the absorption cross-section. The NP35V(0) sample measured 10mm in diameter and 11mm in length and was doped at 0.6 wt. %. The Q246 sample measured 10mm in diameter and 1.5mm in length and was doped at 3 wt. %. Both samples were polished on the flat surfaces.

To measure the absorption cross-section in NP35V(0), a sub-threshold 795nm fiber-couple diode laser was used as a broadband source. The output of the 200μm diameter delivery fiber was coupled into a 65μm diameter multimode fiber, which was connected to an optical spectrum analyser (OSA). A pair of identical aspheric lenses, with a focal length of 4mm, was used to couple the light, which was optimised for maximum transmission. Two transmission spectra were recorded, one with the NP35V(0) sample in the collimated section between the lenses, and one without. Fig. 4.5 shows this set-up schematically.
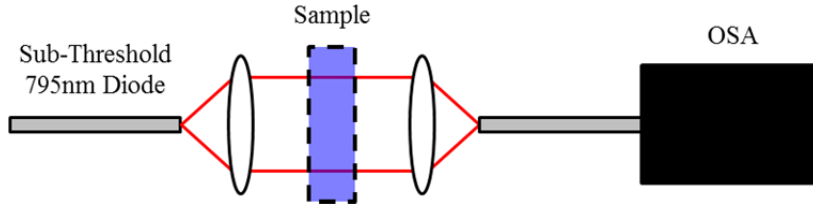
Figure 4.5: Experimental arrangement for absorption measurement.

The spectrum with the NP35V(0) sample exhibited maximum transmission across a range of wavelengths which do not correspond to neodymium absorption lines. These maxima were used to normalise the spectrum without the sample to account for Fresnel and scattering losses. This allowed a power transmission spectrum for the sample to be obtained. Consider equation 3.12 with wavelength dependence:

$$P_T(\lambda) = P_0(\lambda)\exp\left(-n_T\sigma_{pa}z\right) \tag{4.5}$$

Equation 4.5 can be rearranged in terms of absorption cross-section, since the other parameters are known. Fig 4.6 shows the absorption cross-section plotted as a function of wavelength for the NP35V(0) sample. A peak absorption cross-section of 3.5×10^{-24} m^2 occurred at 800nm. It is assumed this value is consistent across all NP35V iterations. This wavelength is well-suited to diode pumping, with available sources at 795nm and 808nm. An advantage of the Source I glass is the ability to specify the doping concentration and therefore control device length.
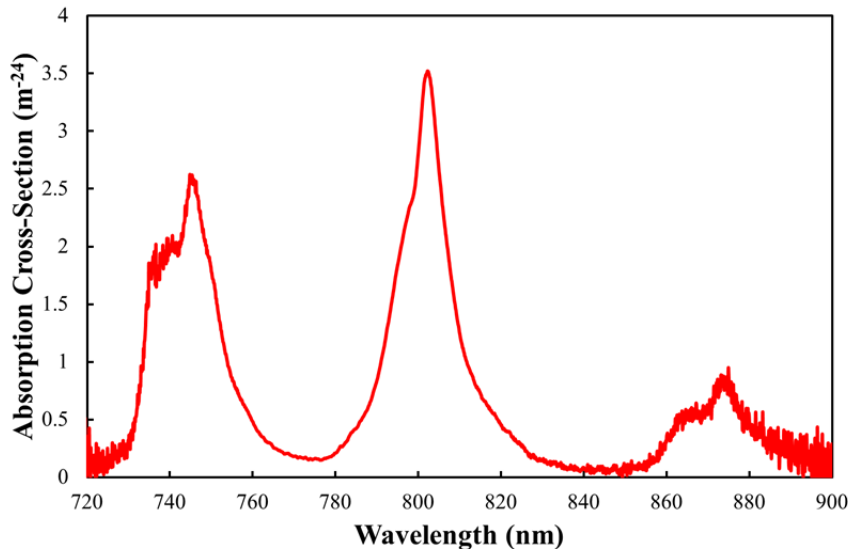
Figure 4.6: Absorption cross-section as a function of wavelength.

The experiment was repeated for the Q246 sample, with a white light source acting as the broadband radiation source. A peak absorption cross-section of $2.5 \times 10^{-24}\,m^2$ occurred at 807nm, which is again suitable for diode pumping. The doping concentration of the Source II glass was fixed at 3 wt. %. Finally, the absorption cross-section for the Source III glass was measured to be $2.3 \times 10^{-24}\,m^2$ at 800nm [11]. The absorption cross-sections are summarised in table 4.3.

Glass	Absorption Cross-Section (m^2)	Peak Wavelength (nm)
NP35V	3.5×10^{-24}	800
Q246	2.5×10^{-24}	807
CL1:Nd	2.3×10^{-24}	800

Table 4.3: Absorption cross-section values for each Nd-doped glass.

4.7 Fiber-Rod Fabrication

4.7.1 Fabrication Properties

Table 4.4 displays the thermal properties important for fabrication for the three glass sources. DTA was performed in-house to obtain T_g and T_x for the Source I and Source II glass, whilst the CTE for these glasses were provided by GTS and Kigre [12, 13] respectively. The properties for the Source III glass were provided by the Politecnico di Torino [11]. Also included in table 4.4 is the percentage difference between the doped and undoped glass for the relative thermal properties, which as previously discussed, should be minimised.

Property	In-House Manufactured			Commercial			Collaboration		
	NP35V	NP35	Δ%	Q246	KF-2	Δ%	CL1:Nd	CL1	Δ%
T_g (°C)	469	464	1.1	502	481	4.2	522	530	1.5
T_x (°C)	n/a	n/a	n/a	689	730	5.6	790	808	2.2
ΔT_{gx} (°C)	n/a	n/a	n/a	187	249	n/a	268	278	n/a
CTE (10^{-6} °C^{-1})	10.2	10.4	1.9	9.0	8.5	5.6	8.1	8.3	2.4

Table 4.4: Thermal properties important for fiber-rod fabrication.

Table 4.4 indicates that the Source I glass has excellent drawing properties. Firstly, T_g and the CTE are very close, with less than 2% difference in value between NP35V and NP35. Additionally, no crystallisation was observed, which is an excellent property for fabrication since it provides no upper limit for the glass stability parameter. The Source III glass, CL1:Nd and CL1, also displays impressive drawing properties, with less than 2.5% difference across the relevant thermal

properties and a glass stability parameter greater than 250°C for both glasses. The Source II glass displays the poorest performance in this analysis, with a percentage difference between Q246 and KF-2 around 2-3 times greater than the other two sources. Additionally, this source provides the lowest glass stability parameter, with both values coming in below 250°C.

These results are not surprising. The Source I and Source III glass was manufactured specifically so that the doped and undoped glass would be compatible for fiber-rod fabrication, and thus have very similar compositions. However, the doped and undoped glass from Source II are unrelated to each other and fulfil different applications. Furthermore, differences in the compositions and thermal properties are to be expected. In fact, Kigre Inc. suggested these glasses have a strong tendency to crystallise. Unlike the other two sources, the key advantage of the Source II glass is the excellent quality of the glass in terms of homogeneity and transmission losses, which are as low as 0.009dB/m for Q246 [12].

4.7.2   Source I Glass

Two batches of doped and undoped phosphate glass were obtained from the manufacturing process, with the first batch displaying visually poor homogeneity. Due to the concerns over homogeneity, it was decided that initially just the doped glass would be drawn down to fiber-rod dimensions. The devices would then be characterised in terms of laser performance, and should the performance be satisfactory, the full rod-in-tube preform would be drawn. This minimises financial burden, as processing the undoped glass into a tube is an expensive and time-consuming process, and should the doped glass not meet the required standard this processing will not be pursued. The absorption length in the bulk glass was estimated from the doping concentration and the absorption cross-section (table 4.3) to be approximately 18mm at 800nm, which corresponds to a device length in the desired operating regime.

Doped glass from both the first and second manufacture attempt was processed into preforms. NP35V(1), which displayed significant inhomogeneities, was processed by Crystran Ltd. into a barrel polished cylindrical preform, with a diameter of 15mm and a length of 70mm. NP35V(2), was processed in-house, and was diced into a preform with a square cross-section with dimensions 10mm × 11mm × 70mm long, with the outer surface polished.

Both preforms caned easily at 700°C, with no signs of crystallisation. Several meters of fiber-rod were obtained for each glass, with a diameter/width of approximately 1mm, and an NA, assuming water guidance, of 0.75. Fig. 4.7 shows typical cleaved cross-sections of the drawn fiber-rod. The left image shows NP35V(1), and clear inhomogeneities can be identified within the region contained by the white dashed lines, whilst the right image shows NP35V(2), which appears clear. Laser-based experiments were conducted on both samples and are discussed in section 5.3.
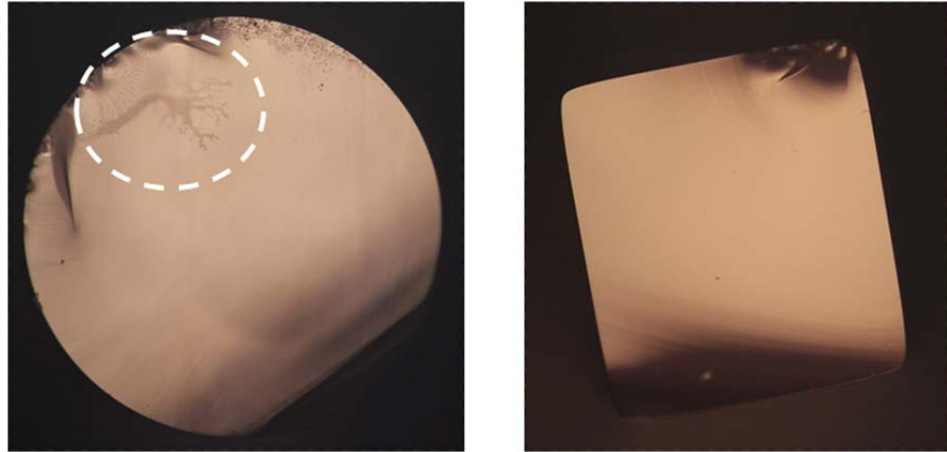
Figure 4.7:Cleaved cane image from the first (left) and second (right) manufactured glass.

4.7.3   Source II Glass

Despite the inferior thermal properties (table 4.3) of the doped, Q246, and undoped silicate glass, KF-2, fiber-rod fabrication was attempted. The bulk glass samples were processed by Crystran Ltd., as shown in fig. 4.8. The Q246 sample was barrel polished to produce an outer diameter of 19mm and a length of 60mm. The KF-2 sample was polished with a quasi-octagonal cross-section, with a diameter of 20mm and a flat-to-flat distance of 18.5mm, and length of 50mm. This non-circular profile was chosen to increase pump absorption through mode-scrambling. A 3.5mm diameter hole was drilled through the centre of the undoped glass to create a tube. The inner-surface of the tube was polished to some extent with 1μm diamond grit paper. The ratio of the outer diameter of the preform to the inner diameter of the hole was approximately 5.7, which leads to an intended cladding area to core area ratio of ~33. The absorption length of the bulk glass was estimated to be approximately 1.5mm (table 4.3), therefore the absorption length of the fiber-rod device should be on the order of 50mm at 807nm, since the absorption length is increased in proportion to the cladding/core area ratio. This puts the device length in the desired operating regime.

The Q246 preform was drawn down to allow insertion into the tube. The preform, although more difficult to draw than the in-house manufactured phosphate glass, came down at $680\,^{\circ}$C to produce approximately 500mm of cane with a diameter of approximately 3.2mm. A section of the drawn cane was inserted into the KF-2 tube, and the whole rod-in-tube preform was drawn down. Efforts made to encourage the preform to neck below the crystallisation temperature were unsuccessful. Therefore the temperature was increased to $840\,^{\circ}$C to initiate necking, at which point the preform had become clouded with surface crystals. This is not surprising since this is significantly higher than the crystallisation temperature of both glasses. The preform was caned with great difficultly. During caning a vacuum was maintained over the top of the preform at 450mbar to prevent air gaps between the core/cladding interface. A total length of 15 meters of fiber-rod was obtained with an approximate cladding diameter of 500μm and core diameter of 75μm. This core diameter is

approximately an order of magnitude larger than standard single-mode fibers, allowing us to explore the intended operating regime. This device has a core NA of approximately 0.24 and a cladding NA of 0.80 [12, 13].

Figure 4.8: Processed doped glass (left) and undoped glass (right).

Unfortunately, the obtained fiber-rod displayed significant crystallisation and damage. The entire outer surface of the cladding material was covered in surface crystals. Fig. 4.9 (left) shows these crystals, and one can clearly see where the glass has flowed around the crystals in the direction of the draw, indicated by the red arrow. Whilst these superficial crystals could be removed with careful polishing using 1µm diamond grit paper (fig. 4.9 (right)), the finished surface was far from ideal. Furthermore, damage at the core/cladding interface was apparent along the whole length of fiber-rod. The cause of this damage is attributed either to crystallisation or CTE mismatch, and cannot be improved by post-processing. Fig. 4.10 shows typical cross-sections of the fiber-rod, with a visually high/low quality interface in fig. 4.10 (left/right) respectively. The interface quality varied between these two regimes on a millimetre length scale, therefore a length of fiber-rod with a consistently high quality interface i.e. on the order of an absorption length, could not be obtained. These factors will have serious implications for the propagation losses of the device. Regardless of the major fabrication issues, laser experiments were performed on these fiber-rod devices in section 5.4.
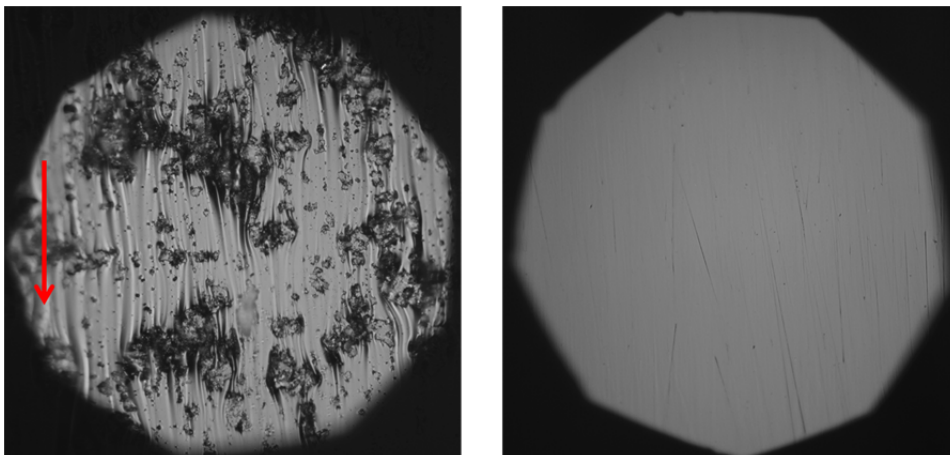
Figure 4.9: Surface crystallisation (left) and polished surface (right).
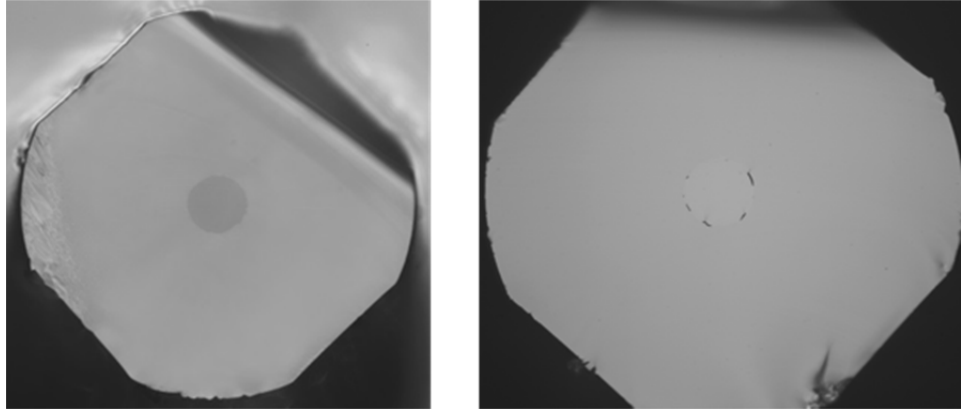
Figure 4.10: Visually good quality interface (left) and poor quality interface (right).

4.7.4   Source III Glass

The objective of the collaboration with the Politecnico di Torino was to manufacture compatible Nd-doped, CL1:Nd, and undoped, CL1, phosphate glasses, fabricate fiber-rod devices and conduct power scaling tests on these devices. The Politecnico di Torino has expertise in glass manufacture and fiber fabrication and was responsible for producing the fiber-rod devices, whilst the laser investigation took place at the University of Southampton.

Detailed information on the glass manufacture and fiber-rod fabrication can be found in [11]. The rod-in-tube technique was employed and several meters of fiber-rod device were obtained, with a core/cladding diameter of approximately 270μm/800μm respectively, with a core/cladding NA of 0.16/0.78. The doping concentration in CL1:Nd was approximately 1.3 wt. %, therefore from table 4.3 we would estimate an absorption length in this device of approximately 50mm at 800nm, in line with the desired operating regime. Fig. 4.11 shows the fiber cross-section which exhibited a visually high quality core/cladding interface along the entire length. Laser-based experiments on this device were conducted as discussed in section 5.5.
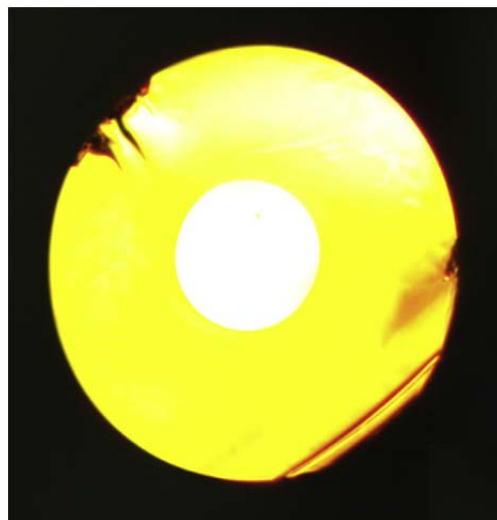
Figure 4.11: Visually high quality interface for CL1:Nd/CL1 fiber-rod.

4.8   Conclusion

In this chapter we suggest soft glass as the host material for the TGFR device, owing to its excellent solubility of rare-earth ions which allow short devices, reducing deleterious nonlinear effects. Additionally, these glasses can be commercially produced with a very uniform doping and refractive index profile.

A method for producing the fiber-rod devices using a soft glass drawing tower was discussed. The response of a glass to temperature was described and important transitions were highlighted. We stressed that the glasses must have suitable thermal properties to allow fabrication. Following this, we listed requirements that should be fulfilled by a host glass in order to allow successful fabrication and power scaling in a laser architecture. In light of these requirements we identified three potential sources of a suitable glass host. Source I involved in-house manufacture of the glass, and the various steps of this process were described. Source II corresponded to purchasing commercial glass from a laser glass company. Source III was obtained through collaboration with an academic institute specialising in glass manufacture and fiber fabrication. The absorption of pump radiation in each source was quantified.

Finally, each glass source was drawn into dimensions suitable for investigating the TGFR concept. The Source I glass displayed good drawing properties, but concerns over homogeneity postponed fabrication of the composite structure and only the doped glass was drawn, which was the subject of a laser investigation presented in section 5.3. The Source II glass was not well-suited to fiber-rod fabrication, and although a device was produced, significant crystallisation and damage sites will undoubtedly impact losses. This device is characterised in section 5.4. The Source III glass performed well during fabrication, and is characterised in section 5.5. The results from the fabrication stage are not surprising, since the Source I and Source III glasses were manufactured specifically to be compatible for drawing, whereas the Source II glasses were unrelated, and were therefore not as well-matched in terms of drawing parameters.

References

1. Y. W. Lee, M. J. F. Digonnet, S. Sinha, K. E. Urbanek, R. L. Byer, S. Jiang, "High-Power Yb3+-Doped Phosphate Fiber Amplifier," IEEE J. Quantum Electron. **15**, 93 (2009).

2. Y. W. Lee, S. Sinha, M. J. F. Digonnet, R. L. Byer, S. Jiang, "20W single-mode Yb^{3+}-doped phosphate fiber laser," Opt. Lett. **31**, 3255 (2006).

3. S. Jiang, "Two-micron thulium-doped fiber lasers achieve 10 kW peak power," Laser Focus World, February, 52 (2013).

4. J.H. Campbell, J.S. Hayden, A. Marker, "High-Power Solid-State Lasers: a Laser Glass Perspective," J. Appl. Glass Sci. **2**, 3 (2011).

5. W. Koechner, Solid-State Laser Engineering, 6 ed., Sixth Revised and Updated Edition (Springer, 2006).

6. W.F. Krupke, M.D. Shinn, J.E. Marion, J.A. Caird, S.E. Stokowski, "Spectroscopic, optical, and thermomechanical properties of neodymium- and chromium-doped gadolinium scandium gallium garnet," J. Opt. Soc. Am. B. **3**, 102 (1986).

7. Y.W. Lee, H.Y. Ling, Y.H. Lin, S. Jiang, "Heavily Tm3+-doped silicate fiber with high gain per unit length," Opt. Mat. Ex. **5**, 549 (2015).

8. Y. Hu, S. Jiang, T. Luo, K. Seneschal, M. Morrell, F. Smektala, S. Honkanen, J. Lucas, N. Peyghambarian, "Performance of High-Concentration Er3+–Yb3+-Codoped Phosphate Fiber Amplifiers," IEEE Photon. Technol. Lett. **13**, 657 (2001).

9. Q. Wang, J. Geng, T. Luo, and S. Jiang, "Mode-locked 2 m laser with highly thulium-doped silicate fiber," Opt. Lett. **34**, 3616 (2009).

10. P. Gabbott, Principles and Applications of Thermal Analysis, 1 ed, (Blackwell Publishing Ltd., 2008).

11. E. Ceci-Ginistrelli, C. Smith, D. Pugliese, J. Lousteau, N.G. Boetti, W.A. Clarkson, F. Poletti, D. Milanese, "Nd-doped phosphate glass cane laser: from materials fabrication to power scaling tests," J. Alloys Compd. **722**, 599 (2017).

12. Kigre Inc., "Q246" (2017), retrieved http://www.kigre.com/products/laser_glass.pdf

13. Kigre Inc., "KF-2" (2017), retrieved http://kigre.com/products/samariumfilter.pdf

Chapter 5   Soft-Glass Thermally-Guided Fiber-Rod Device Testing

5.1   Chapter Overview

Chapter 5 follows on from the fabrication efforts described in Chapter 4, and aims to assess the power scaling potential of the three fiber-rod devices fabricated in section 4.7. Section 5.2 describes a tunable fiber laser seed source, which was a useful tool utilised throughout this PhD to measure the gain or loss through a device, or to act as a probe beam. In section 5.3 the fiber-rod fabricated from the Source I glass is characterised, covering homogeneity, transmission losses and amplifier performance. Section 5.4 investigates the Source II glass fiber-rod device in terms of laser performance, whilst section 5.5 carries out this investigation on the Source III fiber-rod device. Section 5.6 will conclude the results of this chapter, in light of the results obtained for the characterisation of the three fiber-rod devices.

5.2   Tunable Laser

Tunability is an extremely useful property of a laser. In the context of this work, a single transverse mode tunable laser source was deemed a necessity in order to measure gain at various wavelengths around 1μm. Additionally, the ability to tune to a wavelength which is out-of-band, and therefore displays negligible absorption for a particular transition is valuable for loss characterisation purposes. Finally, a single-mode beam is useful as a probe, and can be used to test the thermal-guiding concept, as presented in section 6.3. To fulfil these requirements, a laser was constructed based on an ytterbium-doped, single-mode fiber, with tunability provided by a reflection grating employed in a feedback arm (fig. 5.1).
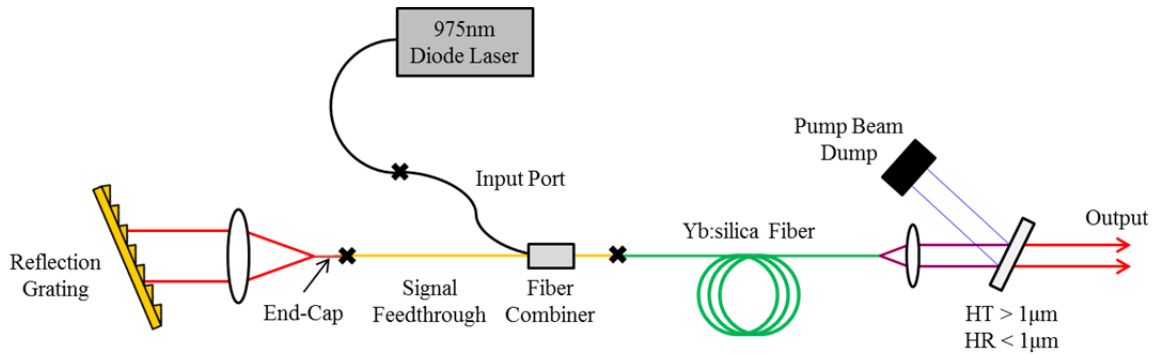

Figure 5.1: Tunable laser configuration.

5.2.1   Laser Components and Operation

The following describes the basic components required for laser operation:

Pump Laser
A fiber-coupled diode laser operating at 975nm was used to pump the ytterbium-doped silica fiber, which displays strong absorption at this wavelength (fig. 6.15). The pump fiber had a core diameter of 105µm with an NA of 0.22, and a cladding diameter of 125µm. This specification matched the input port of the pump combiner, allowing a low-loss splice (shown by a cross 'X') to be formed between these fibers with <0.3dB loss.

Pump Combiner
A (2+1) x 1 fiber combiner was used. This device consists of a total of three input fibers and one output fiber. Two of the input fibers are intended for multimode pump guidance and have core/cladding diameters of 105/125µm. Note that only one pump input was used and thus only one input fiber is shown in fig. 5.1. A double-clad, single-mode fiber, which had a core/cladding diameter of 10/125µm and core/cladding NA of 0.08/0.46, is combined with the multimode pump fibers through a fusing and tapering process. The output thus consists of one single-mode fiber, which can guide the pump radiation at its cladding/polymer interface.

Active Fiber
An ytterbium-doped silica fiber matching the properties of the single-mode fiber discussed above was employed as the active medium. The emission spectrum of ytterbium-doped silica, as shown in fig. 6.15 exhibits a peak at 1030nm and spans a wide wavelength range in this region as a result of inhomogeneous broadening within the glass host. Approximately 1m of active fiber was spliced onto the combiner output fiber with negligible losses. The other end of the fiber was cleaved perpendicularly, with the Fresnel reflection from this flat end-face acting as an output coupler with approximately 3.4% reflectivity. The fiber absorption at 975nm was 4.8dB/m.

End-Cap
It is important to suppress the feedback due to Fresnel reflections from the end-face of the fiber on the input to the combiner, so that feedback can be entirely defined by the external cavity. To achieve this, a core-less end-cap matching the cladding diameter was spliced onto the fiber end, providing a homogeneous glass structure with a seamless interface through which the beam can expand. Ideally, the beam reflected from the cleaved end-cap end-face would be significantly larger than the core when it returns to the fiber, ensuring the fraction of light coupled back into the core is minimised. This scenario is depicted in fig. 5.2, where the top figure demonstrates effective feedback suppression. Evidently, the length of the end-cap has important consequences for

feedback. An end-cap that is too short (fig. 5.2 (middle)) or overly long (fig. 5.2 (bottom)), can result in a higher coupling efficiency back into the core, preventing the desired suppression.
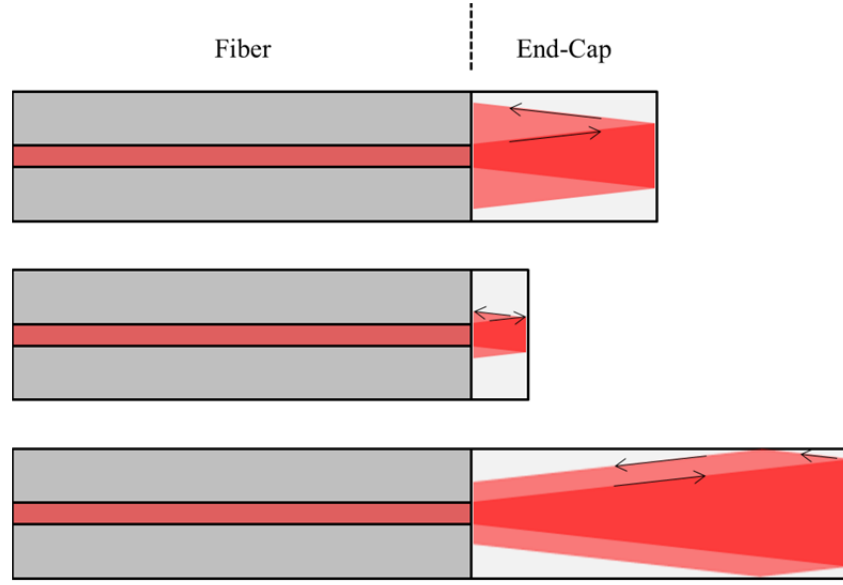
Figure 5.2: End-cap principle.

Basic Gaussian beam propagation can be utilised to estimate the optimal end-cap length. The output of the fiber will form a beam waist, with radius w_0, which can be estimated for a step-index, single-mode fiber by use of Marcuse's equation [1]:

$$\frac{w_0}{r_{co}} \approx 0.65 + \frac{1.619}{VN^{1.5}} + \frac{2.879}{VN^6} \tag{5.1}$$

where r_{co} represents the core radius and VN is the V-number, a parameter used to quantify the number of modes in a step-index fiber, given by:

$$VN = \frac{2\pi}{\lambda} r_{co} \, NA \tag{5.2}$$

where NA is the numerical aperture of the core. Fundamental operation is achieved for fibers with a V-number less than or equal to 2.405. Using the values above for the combiner fiber, we obtain VN = 2.44 at λ = 1030nm. Thus, using equation 5.1, we obtain an estimated output beam waist radius of 5.44μm. We can now utilise equation 2.44 and equation 2.46 to calculate the distance necessary for the beam to expand to the maximum possible size when it completely fills the cladding, i.e. w = 62.5μm. This desire is fulfilled for a length of silica of approximately 1.5mm, therefore indicating an end-cap length of 0.75mm would be required. To achieve this requirement, a length of coreless silica fiber with an outer diameter of 125μm was spliced onto the active fiber. The length of coreless fiber was then cleaved at the required distance from the splice point to create an end-cap of suitable length. This resulted in an end-cap length of approximately 0.8mm.

A simple experiment was conducted to investigate the performance of the end-cap. Consider the cavity shown in fig. 5.3, which is formed by a Fresnel reflection at the end-face of core-less end-cap with reflectivity R_1, and by a Fresnel reflection at the end-face of the active fiber, with reflectivity R_2.
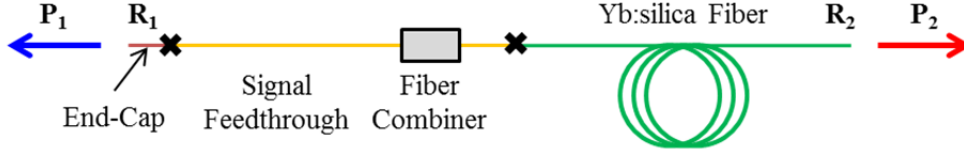
Figure 5.3: Cavity constructed to investigate the performance of the end-cap.

Due to very high single-pass gain of fiber lasers, this configuration will lase with a low threshold. The power emitted from the end-cap end is denoted by P_1, whilst the power emitted from the active fiber cleave is denoted by P_2. Using the Rigrod analysis [2] [Appendix 5.1], one can show that the ratio of P_1 and P_2 for this scenario obeys the condition:

$$\frac{P_1}{P_2} = \frac{1 - R_1}{1 - R_2}\sqrt{\frac{R_2}{R_1}} \tag{5.3}$$

Measured values for P_1 and P_2 at a range of launched pump powers are shown in fig. 5.4. Additionally, the signal power ratio at each pump power level is shown to be constant at a value of 5.1 with less than ±1% deviation across the measured range. Assuming $R_2 = 3.4\%$, equation 5.3 can be solved for R_1 using a simple solver function. This results in an effective reflectivity from the end-cap of $R_1 = 0.14\%$. The end-cap is therefore effective at reducing feedback, with a reflectivity over 20 times less than the cleaved fiber end-face.
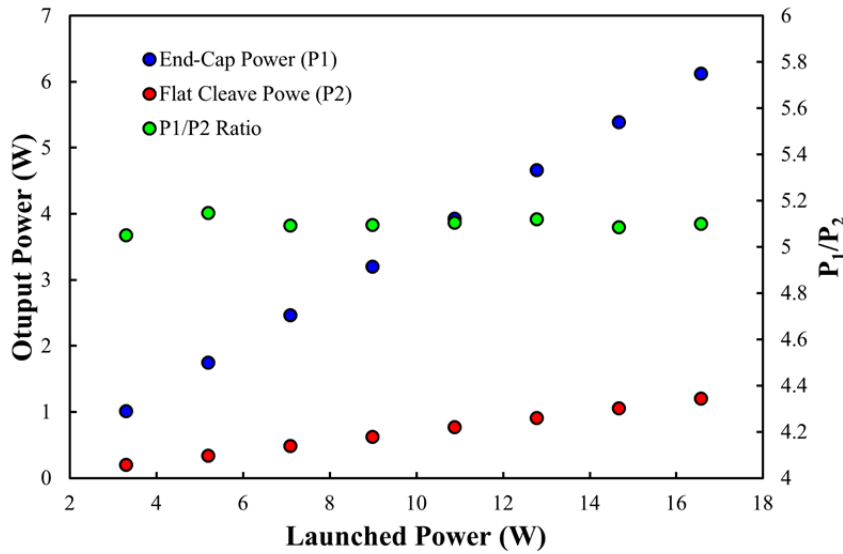
Figure 5.4: Output power and power ratio for the cavity as a function of pump power.

Grating Feedback

Wavelength selection is provided by a reflection grating with a groove separation of $d_s = 1.67\mu m$, optimised for operation around $\lambda = 1000nm$, providing a reflectivity of approximately 95% in the first diffracted order. The grating equation quantifies the diffraction angle, β, for each diffraction order, m, for a particular incident angle, α:

$$m\lambda = d_s(\sin\alpha + \sin\beta) \qquad (5.4)$$

Note that all angles are taken relative to the grating normal. The term on the right of equation 5.4 corresponds to the path length difference of light between adjacent grooves, hence when this difference is equal to an integer number of wavelengths, constructive interference occurs, leading to intensity maxima. For the zeroth order, i.e. $m = 0$, we obtain $\alpha = -\beta$, and the beam is reflected as it would be by a normal mirror, with no wavelength dependence. For higher orders, i.e. $m = \pm 1$, we observe intensity maxima at angles $\beta_{\pm 1}$, which will depend on incident wavelength. This is shown schematically in fig. 5.5 (left).

The grating was operated in the Littrow configuration, whereby the angle of the first diffracted order is equal to the incident beam angle, i.e. $\alpha = \beta$. This transforms the grating equation to the simple form:

$$m\lambda = 2d_s\sin\alpha \qquad (5.5)$$

Consequently, a variation of the incident beam angle results in a quantifiable change in the wavelength satisfying the Littrow condition. The fluorescence from the ytterbium-doped fiber contains a broad wavelength spectrum, which is collimated by a 20mm focal length lens, before travelling to the grating. The grating can be angled to change the wavelength which satisfies the Littrow condition. This wavelength will then travel in the exact opposite direction, where it will be focused by the lens and coupled into the fiber, providing feedback. Above threshold, the laser will operate on the wavelength which provides the highest feedback. This scenario is shown schematically in fig. 5.5 (right). The black arrow represents the spectrally broad input beam and the green arrow represents the wavelength that satisfies the Littrow condition and is fed back into the fiber. The blue/red arrow represents a shorter/longer wavelength, both of which are diffracted at different angles and are not fed back into the fiber. Therefore a cavity is formed between the reflection grating and the Fresnel reflection from the cleaved end-face of the active fiber. Simply by adjusting the grating angle, and thus the incident beam angle, one can vary the feedback and ultimately the lasing wavelength.
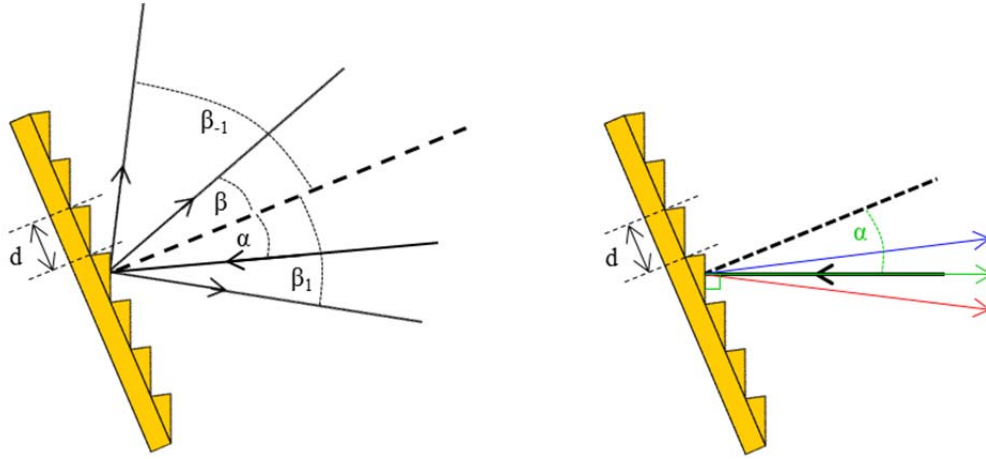
Figure 5.5: Reflection grating (left), Littrow configuration (right).

5.2.2   Laser Performance

The performance of the tunable seed laser was characterised. The laser could be continuously tuned from 1024nm-1090nm, with a full width half maximum (FWHM) of 0.2nm over the entire power range, as shown in fig. 5.6 for 5W output power at each wavelength. Fig. 5.7 shows the output power as a function of launched pump power at 1030nm and 1090nm. The laser performed well, achieving a slope efficiency of 47%/74% with respect to launched/absorbed pump power at 1030nm, and a slope efficiency of 40%/61% with respect to launched/absorbed pump power at 1090nm. The slight drop in efficiency at the longer wavelength can be partially attributed to the larger non-radiative transition associated with this wavelength. Additionally, the operating regime is better suited for high efficiency for the 1030nm laser, since we would expect the slope efficiency to increase as the laser is operated more times above threshold. The laser operated on the fundamental mode across the power and wavelength range, with $M^2 < 1.1$ in both the x- and y-direction. The data for a beam quality measurement in the x-direction at 5W of output power at 1030nm is shown in fig. 5.8, with the beam profile shown in the inset.
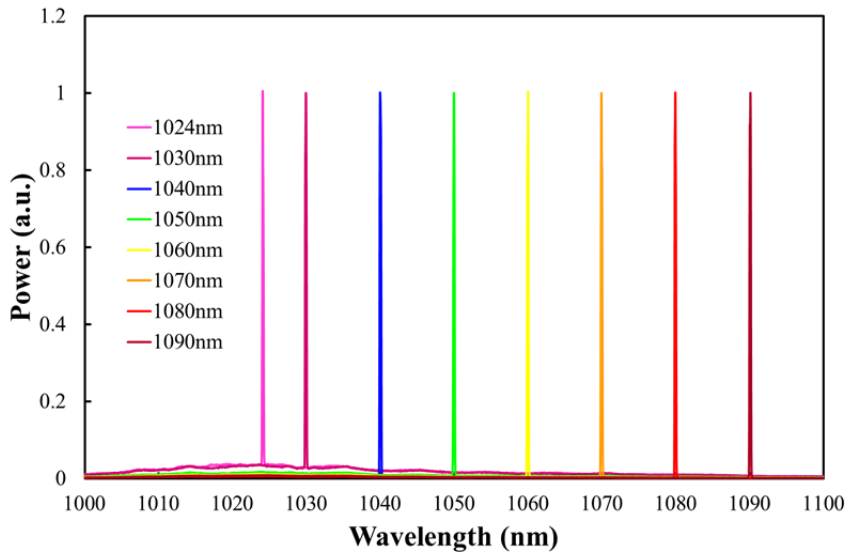
Figure 5.6: The laser was continuously tunable from 1024nm-1090nm.

76
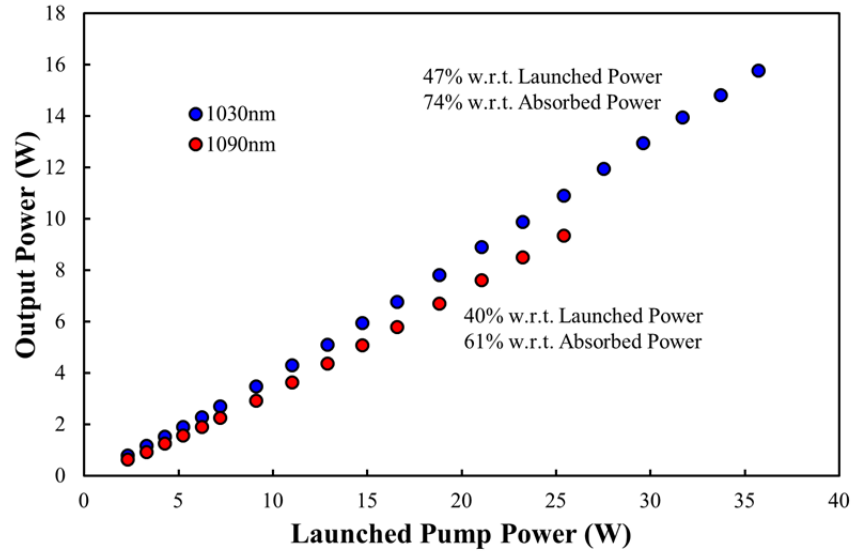
Figure 5.7: Output power at 1030nm and 1090nm as a function of launched pump power.
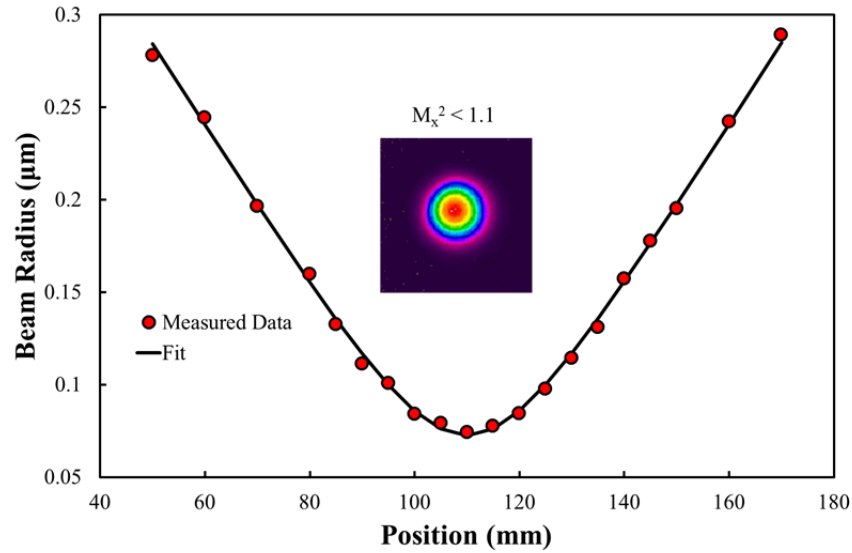
Figure 5.8: Beam quality measurement for the x-direction and beam profile (inset).

5.3   Fiber-Rod Characterisation: Source I Glass

The fiber-rod devices fabricated from NP35V(1) and NP35V(2) (section 4.7.2) were tested to determine suitability for power scaling. Initially, glass homogeneity and transmission losses were investigated at 1054nm, the peak emission wavelength in Nd:phosphate (fig. 5.19). The device was then characterised in terms of amplifier performance.

5.3.1   Transmission Investigation

Homogeneity Investigation

To test the effect of inhomogeneities on beam transmission, a HeNe beam was focused through a 35mm section of ~1mm diameter/width fiber-rod fabricated from NP35V(1)/NP35V(2), and the

output beam was studied qualitatively for distortions using a CCD camera. The end-faces of the fiber-rods were polished using 1μm diamond grit paper, and care was taken to ensure the beam did not interact with the outer surface of the fiber-rod, with an average beam radius through the device of approximately 100μm. The transmitted beam profiles are displayed in fig. 5.9, which clearly shows extreme beam degradation for the NP35V(1) fiber-rod, whilst the NP35V(2) fiber-rod transmits the beam with no discernible degradation. This result is not surprising, since the manufacture of NP35V(1) did not include a homogenisation element, and the bulk and drawn glass displayed visible inhomogeneities (fig. 4.4 and fig. 4.7). Consequently, NP35V(1) was abandoned for future investigation, and all further tests were conducted on NP35V(2).

Transmission Losses

The transmission losses at the intended operation wavelength, 1054nm, were characterised using the tunable laser as a seed source. Several fiber-rod samples were tested, ranging in length from 26mm to 48mm. The beam was focused through the fiber-rod in the same manner as the above homogeneity investigation. An average transmission loss of approximately 11dB/m was measured. This is a very significant loss term, which is believed to be due to contaminants in the glass.
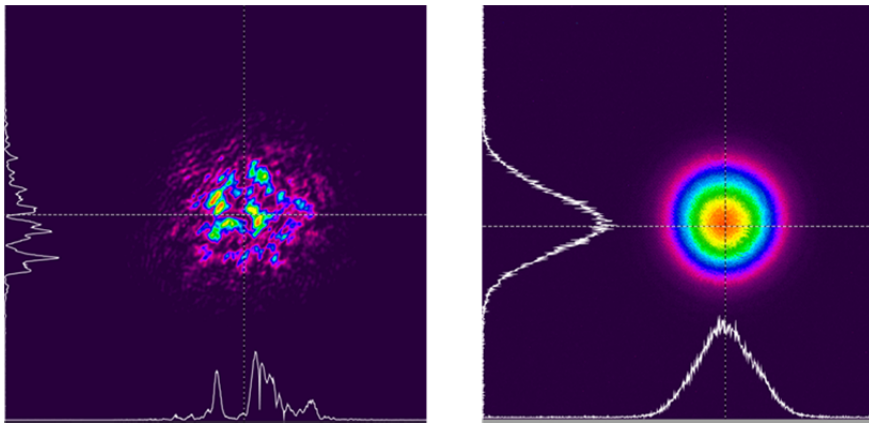
Figure 5.9: Transmitted beam through NP35V(1) (left) and NP35V(2) (right).

5.3.2   Amplifier Configuration

A section of NP35V(2) fiber-rod, with a side length of approximately 700μm and length of 48mm was investigated in an amplifier configuration. This length of fiber-rod corresponds to approximately 2.7 absorption lengths, and therefore ensures the majority of the pump radiation is absorbed, i.e. ~93%. The end-faces of the fiber-rod were polished using 1μm diamond grit paper. The ends of the fiber-rod were waxed into an aluminium bath, which was filled with water to provide guiding for the pump radiation and cooling. A seed beam at 1054nm was focused through the fiber-rod, without interacting with the glass/water interface, with an average beam size through the device of approximately 100μm. The output of a fiber-coupled diode laser, operating at 808nm, was imaged in the fiber-rod in a counter-propagation configuration. The diode delivery fiber had a core diameter of 200μm and an NA of 0.22, and was 1:2 imaged into the fiber-rod, creating a

400μm diameter pump beam on the input face of the fiber-rod. The pump radiation was guided along the device at the glass/water interface. This set-up is shown schematically in fig. 5.10.

The pump losses due to scattering at the interface and unwanted absorption (i.e. absorption not due to neodymium-induced transitions) in the glass were estimated by measuring the transmission through the fiber-rod for similar launch conditions using a 975nm fiber-coupled diode laser, which exhibits negligible absorption due to optical transitions in Nd:phosphate. This experiment yielded a pump-guiding loss along the device of 12dB/m.
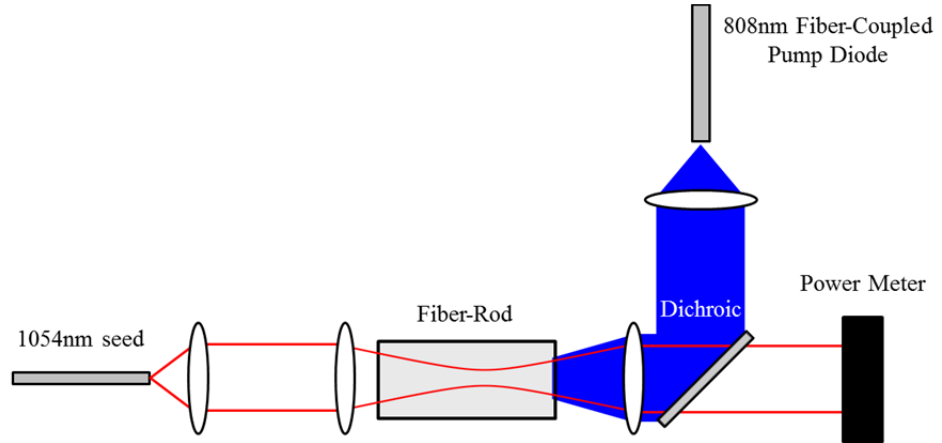
Figure 5.10: Amplification experiment.

5.3.3 Amplifier Performance

The small-signal gain was measured as a function of pump power for a 90mW input beam. Fig. 5.11 shows the measured gain up to a maximum launched pump power of 31.5W. A net gain was not achieved, with a maximum gain of -0.14dB obtained at the maximum pump power. Also shown in fig. 5.11 is the modelled gain which shows good agreement with the measured data. The modelling investigation will be discussed further in the next section.
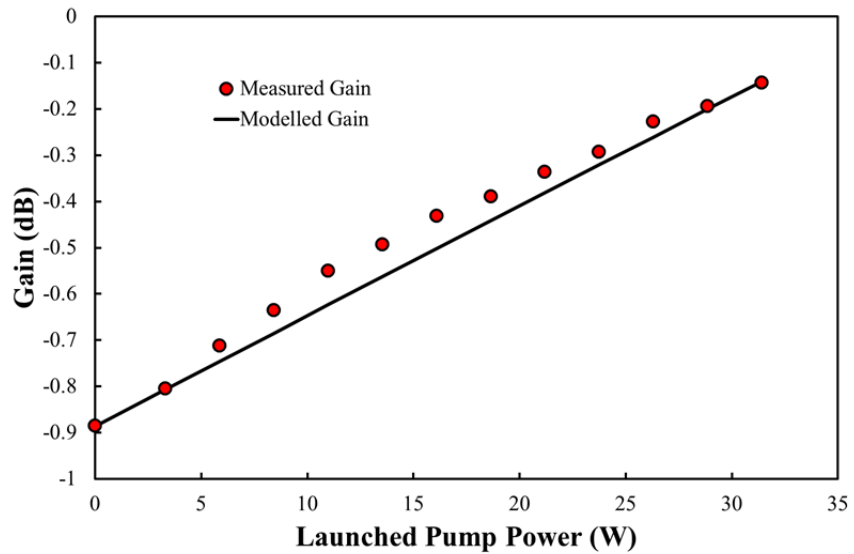
Figure 5.11: Measured and modelled gain for NP35V(2) fiber-rod.

5.3.4   Analysis

Fig. 5.11 shows good agreement between measured and modelled gain data. The model assumed the measured losses for the signal and pump radiation of 11dB/m and 12dB/m respectively, the measured pump absorption cross-section of 1.75×10^{-24}m^2 at 808nm (section 4.6), the specified doping concentration of 0.3 wt. % (3.2×10^{25} ions/m^3), a quantum efficiency of 0.85 [3], and an upper-state lifetime of 300μs and emission cross-section of 3.2×10^{-24}m^2, which is in good agreement for typical Nd:phosphate glasses [4, 5]. Note that the fit was optimised by allowing some freedom in the value for the upper-state lifetime and emission cross-section, whilst keeping these values within close agreement with the literature.

Due to the large area of the pump beam the average inversion density was lower than desired, resulting in low gain. Additionally, Fresnel losses from the fiber-rod end-faces and the high losses at the signal and pump wavelength negatively impacted performance and thus a net gain was not achieved. Based on the model one would expect this device to reach net gain at 37.5W of launched pump power. This suggests that an amplifier or laser device based on this configuration would not be suitable, since the power levels required to reach net gain are significantly higher than desired.

The gain model can be utilised to predict the performance of the fiber-rod amplifier in a more suitable configuration. Since we obtained good agreement with the tested device, we can investigate how other geometries would perform under the same pumping conditions and with the same propagation losses for the pump and signal radiation. The transverse dimensions of the tested device were significantly larger than the desired operating regime. We can reduce the core dimensions to a circular cross-section with a diameter of 200μm. This is still within the intended TGFR operating regime, but is considerably smaller than the tested device, allowing a higher inversion density to be achieved with the device and thus a higher gain. We can also include a circular cladding layer, with a diameter of 400μm, which will help to reduce pump guidance losses and will benefit device handling. Since we have increased the cladding to core area ratio from 1 to 4, we can subsequently increase the doping concentration by a factor of four to 1.2 wt. %, to achieve the same absorption length in a low power regime.

Fig. 5.12 displays the small-signal gain values for this hypothetical device. Here we see a considerable improvement on the tested device, with a maximum small-signal gain level of 11.9dB reached at the maximum pump power. These gain levels make this fiber-rod design interesting both as an amplifier and as a laser device. However, the considerable losses of this device would adversely impact laser efficiency as will be discussed in the following sections for the Source II and Source III devices.
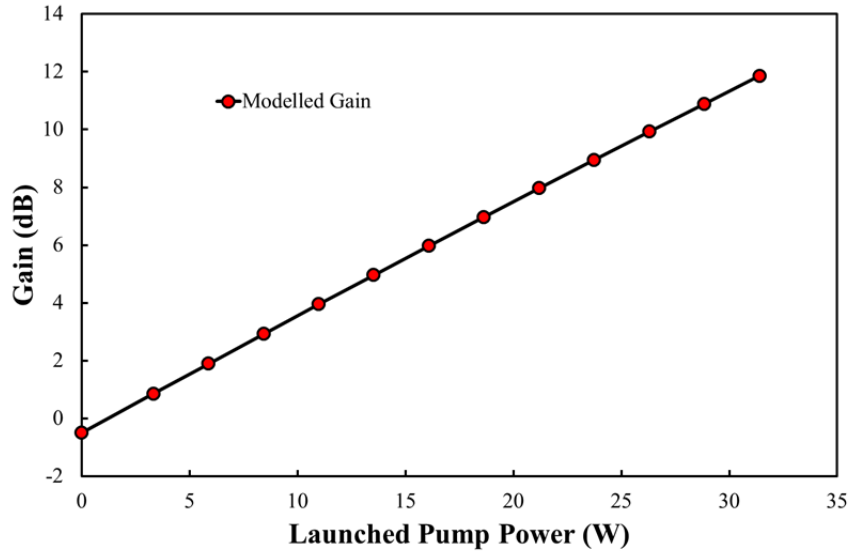
Figure 5.12: Modelled gain for hypothetical amplifier device based on NP35V(2).

5.3.5 Conclusion

The objective of this preliminary investigation was to ascertain the suitability of the fiber-rod device for power scaling applications. The glass performed well in terms of fabrication, with no sign of crystallisation in the two fiber-rod devices. Furthermore, whilst a rod-in-tube preform was not drawn, the compatibility between the doped and undoped glass was excellent, with less than 2% difference in T_g and the CTE. A beam transmission experiment revealed that the fiber-rod device fabricated from NP35V(1) was not suitable, since the beam was severely distorted, whilst the fiber-rod device fabricated from the homogenised NP35V(2) glass showed negligible distortion. However, very high transmission losses were measured for the signal and pump beam of 11dB/m and 12dB/m respectively, which are believed to be due to contaminants in the glass. This had a serious detrimental impact on performance, and prevented a net gain from being achieved. The device geometry was not optimised for performance and achieved a gain of -0.14dB, which was in good agreement with the model. It was concluded that significantly reduced core dimensions, whilst still operating in the fiber-rod regime, would be beneficial to performance.

Ideally, we would go round the loop again, and perform another manufacture run. Here we would pay particular attention to reducing contaminants in the glass, to minimise losses. We would then commission processing of the bulk glass to produce rod and tube structures suitable for rod-in-tube fiber-rod fabrication. The fiber-rod would be fabricated with smaller transverse dimensions, in order to realise an improved gain performance and pave the way for further amplifier and laser experiments.

However, experimental work on this project was unfortunately abandoned. The cost of obtaining further glass samples was significantly increased. Furthermore, since this would only be the third

glass manufacture run there is no guarantee of significantly reduced losses. Additionally, processing the glass into rod and tube structures is a very expensive process. Finally, the lead time for glass manufacture and preform processing was not in line with the timescale of this PhD project.

Nevertheless, this investigation has showed real promise for the soft glass fiber-rod concept. The glass was well suited to fabrication, the gain levels are in line with expected values and the fiber-rod withstood pumping up to the multi-10W level in a simple heat-sinking configuration. With a more accessible source of glass, this project could make progress.

5.4 Fiber-Rod Characterisation: Source II Glass

Despite the poor quality of the fiber-rod fabricated from Q246 and KF-2, a laser investigation was carried out. Initially an emission spectrum was recorded, to determine the wavelength of peak emission and hence the wavelength that will be targeted for laser operation. A simple laser was then constructed, with signal losses and output power performance characterised.

5.4.1 Emission Spectrum

The emission spectrum of the Q246 sample discussed in section 4.6 was taken to confirm the peak emission wavelength. The sample was irradiated at 808nm by a fiber-coupled diode laser, resulting in the excitation of neodymium ions, followed by radiative decay leading to a fluorescence spectrum. The fluorescence was captured by a multimode fiber, which was connected to an OSA. Fig. 5.13 shows the obtained power spectral density between 850nm and 1450nm. Three clear peaks can be identified, corresponding to a quasi-three-level transition at 895nm, and four-level transitions at 1059nm and 1332nm. The strongest transition, and the one targeted for laser experiments, is at 1059nm, with a FWHM of 27nm.
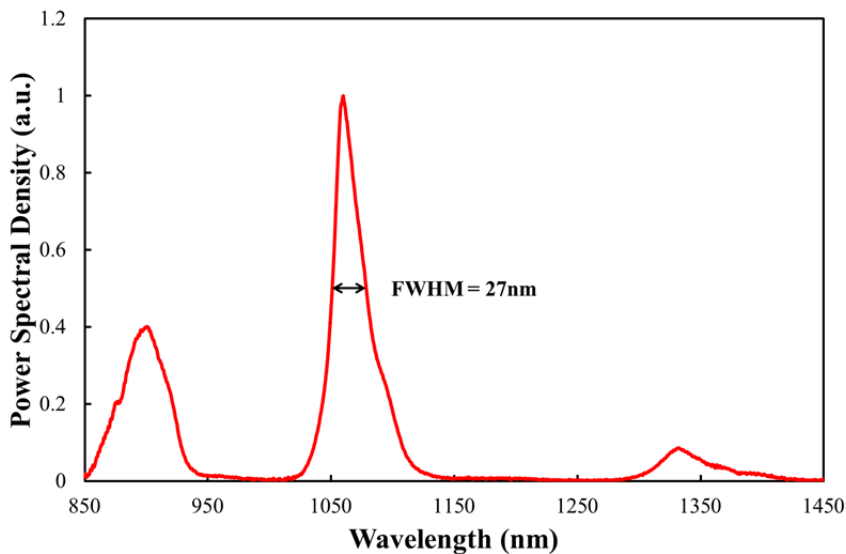
Figure 5.13: Emission spectrum as a function of wavelength.

5.4.2 Laser Configuration

The set-up shown in fig. 5.14 was used to investigate laser performance in a short length of fiber-rod. The fiber-rod was visually inspected and a section with the least amount of scattering centres was chosen for laser experiments. This corresponded to a 21mm length of fiber-rod, which was polished on the outer surface and end-faces with 1μm diamond grit paper. The core/cladding diameter was 75μm/500μm. The fiber-rod was housed in a water bath with the ends waxed into position, providing heat-sinking for the fiber-rod and creating a pump guide at the cladding/water interface. The device was pumped by an 808nm fiber-coupled diode, with a fiber diameter of 200μm and NA of 0.22. The pump beam was chopped with a 15% duty cycle to minimise thermal loading. The output of the pump delivery fiber was imaged into the fiber-rod, using a 65mm collimating lens and a 50mm focusing lens, to create an input spot diameter of approximately 154μm with an NA of 0.29. This small pump spot size in relation to the cladding diameter was chosen to increase the portion of pump light guided in the core, thus increasing pump absorption and offsetting the short device length. This configuration led to a single pass pump loss of approximately 72%. However, of this lost pump radiation it is unclear how much is absorbed and how much is lost through scattering at the core/cladding interface and the cladding/water interface.

A simple cavity was formed by carefully positioning dichroic mirrors very close to the end-faces of the fiber-rod. At the pump input end, a mirror with high transmission at 808nm and high reflection at 1059nm was positioned, whilst at the output face various mirrors were aligned ranging from 50% to 95% reflectivity at 1059nm. The output radiation was collimated by a lens and sent to a dichroic mirror angled at 45° with high transmission for the pump wavelength and high reflection for the signal wavelength. The pump radiation was sent to a beam dump, whilst the signal radiation was sent on to diagnostics.
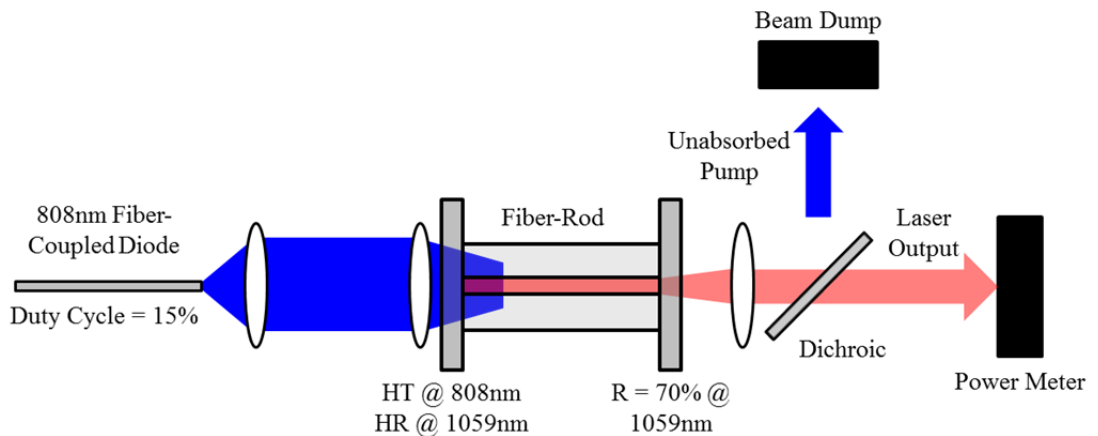
Figure 5.14: Laser configuration.

5.4.3   Signal Losses

Signal losses due to absorption or scattering within the laser cavity were estimated using the Findlay-Clay analysis [6]. This approach calculates the round-trip losses in the cavity by considering the threshold pump power for a range of output couplers with different reflectivities at the lasing wavelength. The laser threshold occurs when the gain experienced by the laser photons on a round-trip is equal to the loss. This requirement can be written as:

$$R_M G^2 (1 - L) = 1 \tag{5.6}$$

where R_M is the reflectivity of the output coupler, $G = \exp(gl_{fr})$ represents the single-pass gain where g is the gain coefficient and l_{fr} is the length of the TGFR, and L represents the round-trip loss. Rearranging equation 5.6, and assuming $L \ll 1$, leads to:

$$2gl_{fr} = L - \ln R_M \tag{5.7}$$

Furthermore, $g = n_2\sigma_{se}$, and n_2 at threshold can be calculated using equation 2.19 with $\phi = 0$, leading to an expression for the gain coefficient at threshold, g_{th}:

$$g_{th} = r_p \tau_f \sigma_{se} \tag{5.8}$$

One can then utilise equation 2.25 and equation 2.34 to rewrite equation 5.7 as:

$$-\ln R_M = mP_P - L \tag{5.9}$$

where $m = \frac{2r_0 \eta_{QE} \eta_{abs} \sigma_{se} \tau_f l}{h\nu_p}$. Equation 5.9 is instantly recognisable as the equation for a straight line, commonly written as: $y = mx + c$. Furthermore, plotting $-\ln R_M$ against P_P should yield a straight line, which intercepts the y-axis at -L, allowing the total loss of the resonator to be inferred.

The threshold pump power was measured for several output couplers ranging from 50-95% reflectivity at 1059nm. A photodiode was used to determine the lasing threshold, identified by relaxation oscillations. The data is plotted in fig. 5.15, with a reasonable straight line fit through the data, indicating $L = 0.1258$, which corresponds to a very high loss of 13dB/m. It was assumed that Fresnel losses from the fiber-rod end faces could be neglected due to the laser configuration, hence this loss corresponds solely to propagation losses along the device.
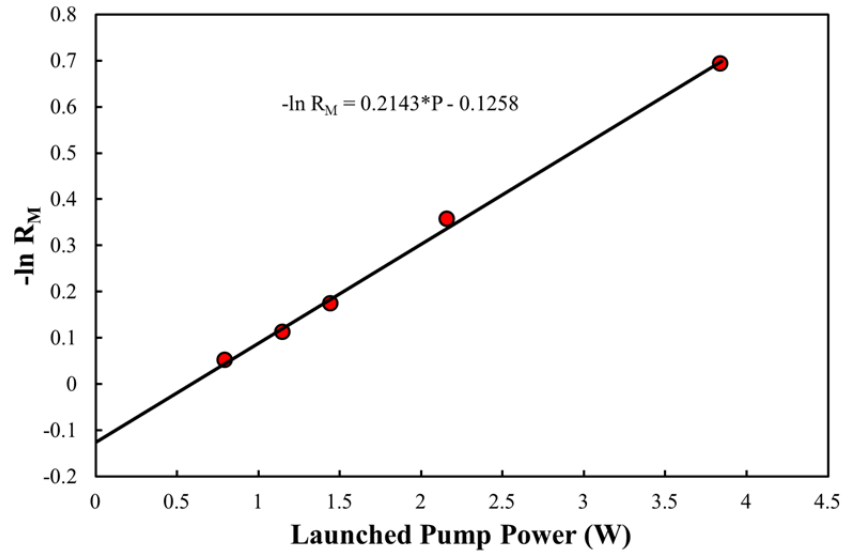
Figure 5.15: Resonator losses estimated from threshold power.

5.4.4 Laser Performance

Fig. 5.16 shows the output power as a function of launched pump power for a 95% and 70% reflectivity output coupler. The presented data has been corrected for the 15% pump duty cycle. For the 95% reflectivity output coupler, threshold was reached for a launched power of approximately 800mW and a slope efficiency of 1.5% was achieved with respect to launched power, whilst for the 70% reflectivity output coupler, threshold was at 2.16W with a slope efficiency of 3.9%.

The laser operated at 1059nm as expected, with a FWHM measured as just below 0.1nm, limited by the resolution of the OSA (fig 5.17). A highly multimode output beam was obtained (fig. 5.17 (inset)).
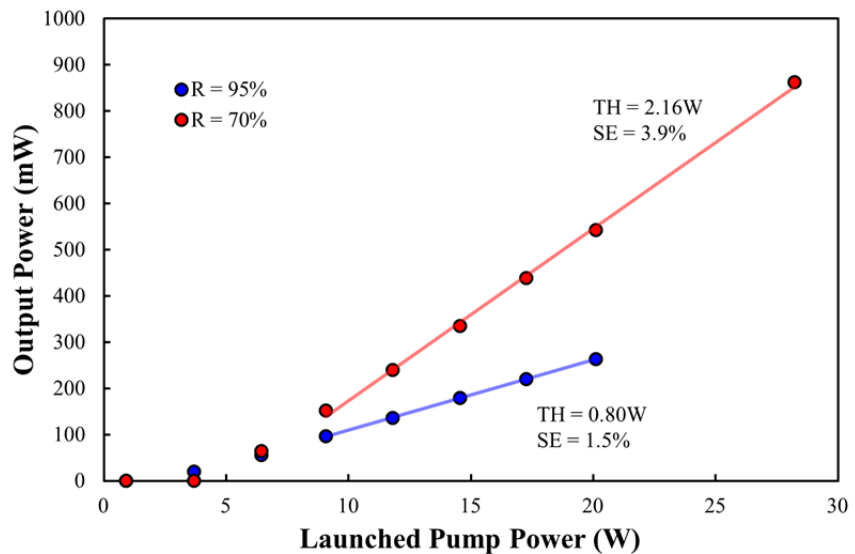
Figure 5.16: Output power for 95% and 70% reflectivity output coupler.
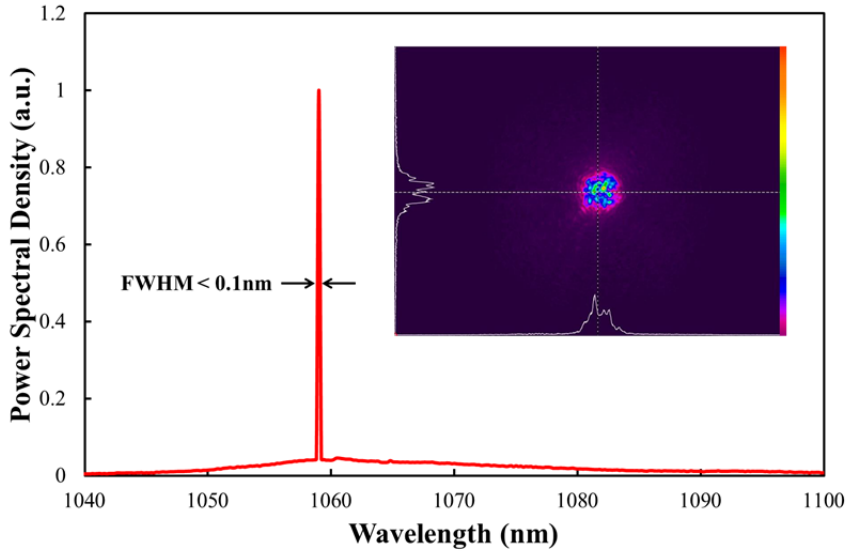
Figure 5.17: Operation wavelength and output beam profile.

5.4.5   Analysis

The laser performed poorly in terms of power scaling, with a high threshold and very low slope efficiency. It is interesting to determine the underlying mechanisms that may be responsible for this performance. The threshold power and slope efficiency for a four-level laser with a top hat pump and signal intensity distribution is quantified by equation 2.39 and equation 2.40 respectively. Table 5.1 displays the relevant values these calculations. Here we have assumed that the inversion region, defined in this case by w_P, and the signal mode are the same size and completely fill the core. Note that T is replaced by $-\ln R$ for values of R which are not close to one. We can only define an upper limit of 0.72 for the fraction of absorbed power, since we cannot confirm the pump power that is lost through scattering and unwanted absorption within the fiber-rod device.

Table 5.2 displays the measured threshold power, TH_M, for five output couplers as displayed in fig. 5.15. Also displayed is the threshold calculated from equation 2.39 assuming that no pump power is lost through scattering or unwanted absorption, i.e. $\eta_{abs} = 0.72$. This is the best case scenario for achieving a low threshold and is labelled TH_{MIN}. Interestingly, the ratio of the measured and best case threshold values is relatively constant, given by $TH_M/TH_{MIN} \approx 5$. Thus whilst the absolute values of the predicted threshold are significantly higher than the measured values, the trends are well-matched. Furthermore, since we do know all the terms in equation 2.39 to a high level of accuracy, a discrepancy in absolute values is not surprising. For example, the crystallisation at the core/cladding interface and at the cladding/water interface will certainly incur significant pump losses, thus reducing our value of η_{abs}.

Parameter	Value
L	0.1258
ν_P	3.71×10^{14} s^{-1}
ν_L	2.83×10^{14} s^{-1}
w_P	3.75×10^{-5} m
w_L	3.75×10^{-5} m
σ_{se}	2.9×10^{-24} m^{-2} [7]
τ_f	3.3×10^{-4} s [7]
η_{QE}	0.85 [3]
η_{abs}	Unknown < 0.72

Table 5.1: Parameters for calculating threshold and slope efficiency.

R_M (%)	TH_M (mW)	TH_{MIN} (mW)	TH_M / TH_{MIN}
95	799	164	4.87
89.4	1153	221	5.22
84	1448	279	5.19
70	2163	448	4.83
50	3845	760	5.06

Table 5.2: Measured and predicted threshold values.

Table 5.3 presents the measured slope efficiency, SE_M, for two output couplers, as displayed in fig. 5.16. Again we consider the best case scenario, with no unwanted pump power, resulting in slope efficiencies, SE_{MAX}, approximately an order of magnitude greater than SE_M, as shown in the final column of table 5.3. Again, we see that whilst the absolute values for the slope efficiency are considerably higher than the measured values, the trend is well matched. As for the thresholds, this can be explained by a lack of accurate knowledge of all the factors in equation 2.40. Again, reduced pump absorption will act to decrease the slope efficiency. Furthermore, the overlap factor between the pump and laser mode could be less than unity, since the gain will be higher in the centre of the device, and larger modes may experience a higher loss due to crystallisation at the core/cladding interface. Thus, even though the predicted performance was considerably better than the measured performance, the trends agree well, therefore allowing the performance of other lasers based on this device to be predicted.

R_M (%)	SE_M (%)	SE_{MAX} (%)	SE_{MAX} / SE_M
95	1.5	13.5	9.0
70	3.9	34.5	8.8

Table 5.3: Measured and predicted slope efficiencies.

5.4.6   Conclusion

The fiber-rod laser fabricated from a rod-in-tube preform consisting of Q246 and KF-2 glass performed poorly. A simple laser was constructed consisting of a butt-coupled mirror configuration. Very high propagation losses of 13dB/m were estimated using the Findlay-Clay analysis, which is over an order of magnitude larger than values reported in the literature [8]. This in itself does not explain the low slope efficiencies, with a maximum slope efficiency of 3.9% achieved for a 70% reflectivity output coupler. To explain the poor performance, it was postulated that the absorbed pump power may be lower than the maximum possible value of $\eta_{abs} = 0.72$, due to losses resulting from crystallisation and damage at the core/cladding and cladding/water interface. Furthermore, the overlap factor could be less than unity as a consequence of a tightly confined beam. Importantly, predicted trends were in good agreement with the measured performance, allowing one to predict the performance in other devices based on this configuration.

The source of the poor laser performance is clearly related to the low quality of the fabricated fiber-rod device. This in turn can be attributed to the lack of compatibility between the glasses with regards to drawing temperature and CTE mismatch. Furthermore, both Q246 and KF-2 have been described as having a strong tendency to crystallise. This is unfortunate, since these glasses have excellent optical properties, with Q246 displaying a loss of just 0.009dB/m in bulk form [7]. Ideally, the excellent optical properties of Q246 and KF2 could be combined with the excellent drawing properties of NP35V and NP35, to create a device with significantly lower losses at the pump and signal wavelength.

5.5   Fiber-Rod Characterisation: Source III Glass

The fiber-rod device fabricated from CL1:Nd and CL1 was investigated in a laser configuration. Initially, the homogeneity of the device was investigated, followed by a measurement of the emission spectrum. The laser configuration will then be described, with signal losses and laser performance presented and analysed.

5.5.1   Homogeneity Investigation

A HeNe beam was passed through the core of a section of fiber-rod to qualitatively determine the effect of inhomogeneities in the glass, in the same manner as section 5.3.1. A 20mm long section of

fiber-rod, with a core/cladding diameter of 300μm/900μm was used for this investigation. Care was taken to ensure the HeNe beam did not interact with the core/cladding interface, and thus only passed through core glass material, with an average beam size 75μm through the fiber-rod. Fig. 5.18 shows the beam before (left) and after (right) transmission. Clearly extreme beam degradation has occurred, which is attributed to an inhomogeneous glass structure. This could potentially be due to poor glass homogenisation during manufacture. Furthermore, the glass is produced in very small volumes, on the order of 100g, and it is difficult to achieve good homogenisation across the majority of such a small sample.
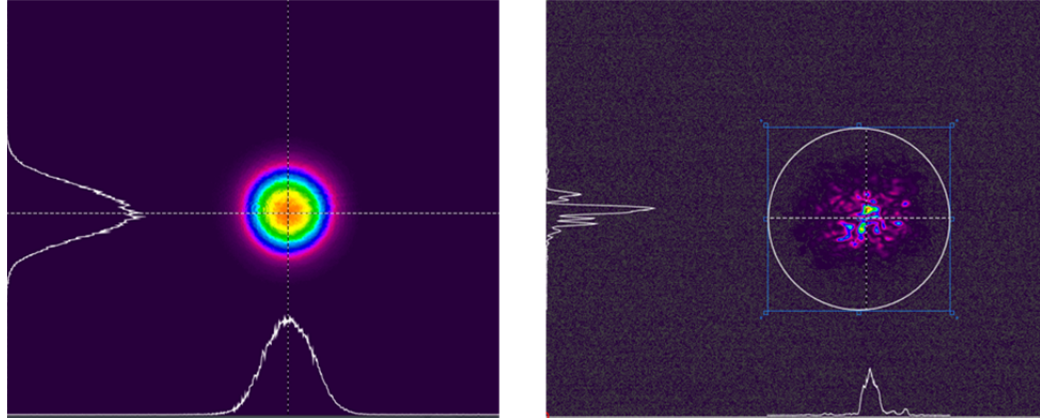
Figure 5.18: Beam profile before (left) and after (right) transmission through the fiber-rod.

5.5.2   Emission Spectrum

The emission spectrum of the CL1:Nd sample was taken under irradiation at 795nm to confirm the peak emission wavelength, as in section 5.4.1. Fig. 5.19 shows the obtained power spectral density between 1010nm and 1150nm. The peak emission wavelength occurs at 1054nm, with a FWHM of 29.5nm. Therefore 1054nm will be targeted for laser operation.
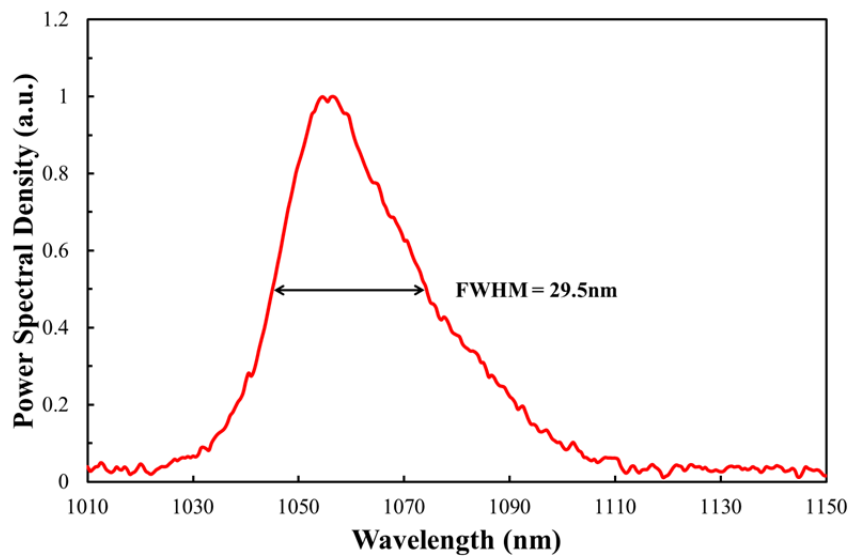
Figure 5.19: Emission spectrum as a function of wavelength.

5.5.3   Laser Configuration

A 60mm length of fiber-rod with a core/cladding diameter of 270μm/800μm was used in laser experiments. The laser was incorporated in the same configuration as shown in fig. 5.14, but with a different pumping arrangement. The fiber-rod device was cw pumped with a fiber-coupled diode laser operating at 795nm with a core diameter of 200μm and an NA of 0.22. The output of the pump delivery fiber was imaged into the fiber using two lenses acting as a 1:2 imaging system, thus creating a 400 mm diameter pump spot with an NA of 0.11 at the front face of the fiber-rod, which satisfies the conditions for guiding in the cladding. A laser cavity was implemented by aligning appropriate mirrors close to the polished faces of the fiber-rod. At the pump input face a mirror with high transmission at 795 nm and high reflection at 1054 nm was positioned, whilst at the other end an output coupler mirror was placed with a reflectivity at 1054nm between 50-95%. The output radiation was collected by a lens and sent to a dichroic mirror angled at 45° with high reflection at 1054 nm and high transmission at 795 nm. Therefore, residual pump radiation can be split from the laser signal. The remaining pump power was sent to a beam dump, whilst the laser signal power was sent on to diagnostics. A pump propagation loss of 111dB/m was measured at 795nm, leading to an upper value for the fraction of absorbed pump power of $\eta_{abs} = 0.78$, however it is expected that due to pump losses the actual fraction of absorbed pump power will be less.

5.5.4   Signal Losses

Following the approach described in section 5.4.3, signal losses within the laser cavity were estimated. Fig. 5.20 displays the relationship between output coupler reflectivity and the launched pump power required to reach threshold. A straight line can be fit to the data, giving a value of $L = 0.1569$, which corresponds to a loss of 5.7dB/m, considerably less than that measured for the Source II glass fiber-rod device and more in line with values from the literature [9].
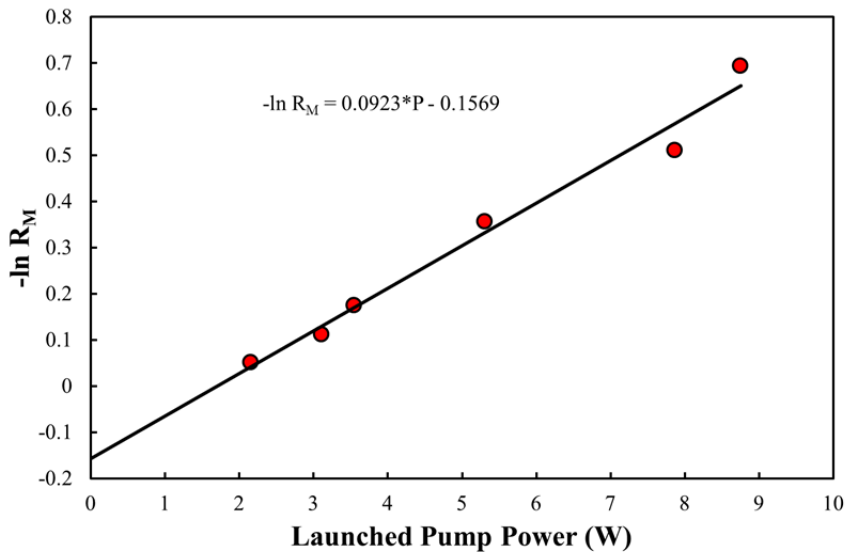
Figure 5.20: Resonator losses estimated from threshold power.

5.5.5 Laser Performance

Fig. 5.21 shows the output power as a function of launched pump power for a 95% and 70% reflectivity output coupler. For the 95% reflectivity output coupler, threshold was reached for a launched power of approximately 2.16W and a slope efficiency of 13.5% was achieved with respect to launched power. For the 70% reflectivity output coupler, threshold was at approximately 5.3W with a slope efficiency of 28.5% and a maximum achieved output power of 2.5W.

The laser operated on numerous longitudinal modes around 1054nm with a FWHM = 1.3nm, as shown at maximum output power in fig 5.22. A highly multimode output beam was obtained as shown in fig. 5.22 (inset), with a measured beam propagation factor of $M^2 \approx 60$.
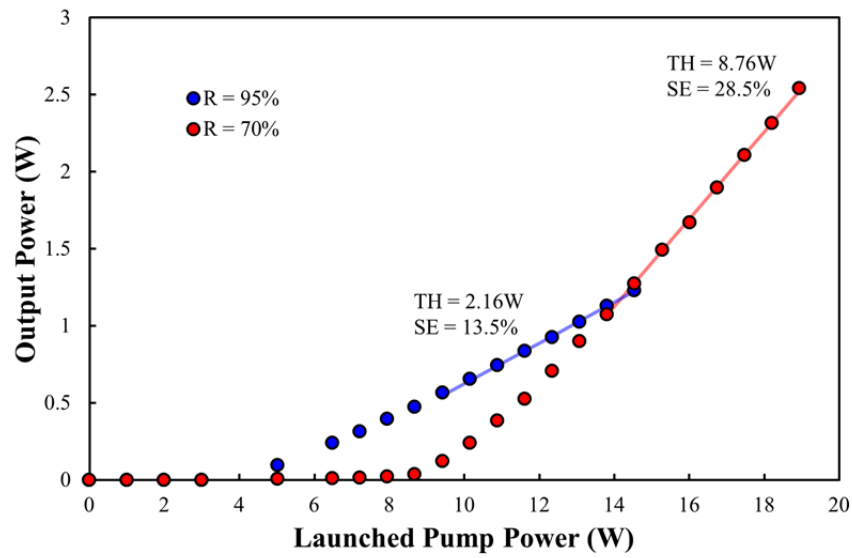
Figure 5.21: Output power for 95% and 70% reflectivity output coupler.
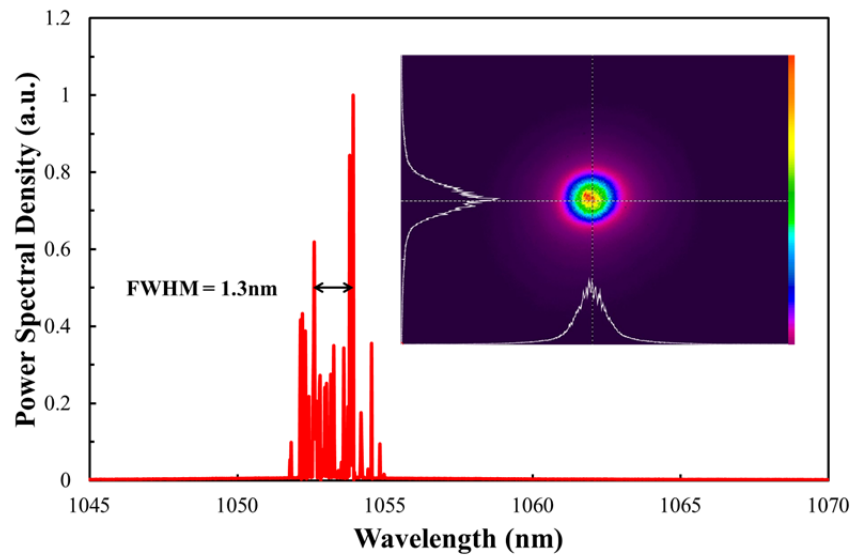
Figure 5.22: Operation wavelength and output beam profile.

5.5.6   Analysis

As in section 5.4.5 the measured threshold and slope efficiency of the laser can be compared to the values predicted by equation 2.39 and equation 2.40 respectively. Table 5.4 displays the relevant values required for these calculations. Once again the fraction of absorbed pump power is defined with an upper-limit.

Parameter	Value
L	0.1569
ν_P	3.77×10^{14} s^{-1}
ν_L	2.85×10^{14} s^{-1}
w_P	1.35×10^{-4} m
w_L	1.35×10^{-4} m
σ_{se}	3.5×10^{-24} m^{-2} [5]
τ_f	3.26×10^{-4} s [4]
η_{QE}	0.85 [3]
η_{abs}	Unknown < 0.78

Table 5.4: Parameters of interest for threshold and slope efficiency.

Table 5.5 displays the measured threshold power, TH$_M$, for six output couplers as displayed in fig. 5.20. Also displayed is the minimum possible threshold assuming the maximum pump absorption factor and the relevant values presented in table 5.4, labelled TH$_{MIN}$. Here we note good agreement, with an average discrepancy between measured and predicted values of approximately 12.5%. In the final column, we present the predicted threshold if we assume the idealised case where losses for the signal radiation are just 1dB/m, leading to $L = 0.0276$, and assume an improved pump absorption of $\eta_{abs} = 0.9$. This threshold is labelled TH$_I$. The percentage difference between this idealised scenario and the measured threshold is shown in brackets. As one would expect, the benefit of this regime is most apparent for low output coupling, since the internal losses represent a much larger fraction of the total loss of the laser. As the output coupling increases, the predicted threshold values of the idealised case tend towards the measured values.

Table 5.6 presents the measured slope efficiency, SE$_M$, for three output couplers. Also displayed is SE$_{MAX}$, where we have assumed $\eta_{abs} = 0.78$. Again we note good agreement, with an average discrepancy between the measured and predicted slope efficiencies of approximately 10.5%. The final column presents the predicted slope efficiencies for the idealised scenario, SE$_I$, as described above. Here we see a very significant difference in performance, with considerably higher slope efficiencies achieved for this scenario. The difference between measured and modelled slope

efficiency decreases as output coupling increases, as the predicted slope efficiency tends towards the maximum value and is limited by the other efficiency factors. Consequently, for power scaling applications, minimising the losses and maximising the pump absorption is critical to achieving efficient operation.

R_M (%)	TH_M (W)	TH_{MIN} (W)	TH_I (W)
95	2.16	1.97	0.83 (61.6%)
89.4	3.11	2.55	1.46 (53.1%)
84	3.55	3.14	2.11 (40.6%)
70	5.31	4.86	4.02 (24.3%)
60	7.88	6.32	5.63 (28.6%)
50	8.76	8.05	7.54 (13.9%)

Table 5.5: Measured and predicted threshold values.

R_M (%)	SE_M (%)	SE_{MAX} (%)	SE_I (%)
95	13.5	12.3 (%)	37.3 (176.3%)
89.4	21.0	20.9 (%)	46.0 (119.0%)
70	28.5	34.8 (%)	53.3 (87.0%)

Table 5.6: Measured and predicted slope efficiencies.

5.5.7   Conclusion

The fiber-rod device consisting of a CL1:Nd core and a CL1 cladding was characterised in terms of laser performance. Homogeneity was poor, resulting in extreme beam break-up. A simple laser was constructed consisting of a butt-coupled mirror configuration. Propagation losses of 5.7dB/m were estimated using the Findlay-Clay analysis, which is significantly less than the 13dB/m measured from the Q246/KF-2 device, but still high compared to other reported phosphate devices i.e. 3dB/m [9]. It is expected that the poor glass homogeneity stems from the manufacture process, which produces small quantities of glass thereby making it challenging to achieve good homogeneity across the entire sample.

A maximum output power of 2.5W was achieved in a highly multimode beam, with a slope efficiency with respect to launched power of 28.5% for an output coupler with 70% reflectivity at 1054nm. The measured and predicted threshold and slope efficiency values agree well. It is clear that further improvements, particularly in the slope efficiency and thus the maximum achievable

output power, will be achieved for lower propagation losses and a higher pump absorption factor. This will be essential for power scaling and can be achieved through improved glass manufacturing.

5.6 Conclusion

The aim of this chapter was to assess the suitability of the fabricated fiber-rod devices for power scaling applications in a TGFR configuration. Initially, we introduced a tunable fiber seed laser, capable of producing 10W-class single-mode output from 1024-1090nm, with a FWHM of 0.2nm. This seed laser was utilised as a useful tool for gain and loss measurements, and provided a probe beam for the thermal-guiding investigation covered in section 6.3.

The bulk of the chapter investigated the laser performance of fiber-rod devices fabricated from three different glass sources as presented in section 4.7. The overall performance of these devices was limited by the relatively high propagation losses. The Source I glass had an inherently high bulk transmission loss of 11dB/m, believed to be due to contaminants in the glass network. It should be pointed out that the site whereby this glass was manufactured (GTS) does not specialise in laser glass. In the limited number of glass manufacture attempts it is not surprising that losses may be considerably higher than commercial standards. The origin of the loss in the device based on the Source II glass provided by the commercial laser glass company Kigre Inc., stems from the poor compatibility between the core and cladding material. These glasses are unrelated to each other and are not intended for fiber drawing. Furthermore, damage and crystallisation along the device resulted in very high propagation losses of 13dB/m. The Source III glass provided by the Politecnico di Torino performed best, giving an estimated loss of 5.7dB/m. However the beam transmission experiment revealed poor glass homogeneity, potentially resulting from the very small production quantities. The thermally-induced mode control technique was not investigated with the soft glass fiber-rod devices, owing to the poor laser performance.

The gain model gave a reasonably good agreement with the measured gain values for the Source I glass operating in an amplifier configuration. The fit between measured and modelled data was optimised by varying unknown parameters such as the emission cross section and upper-state lifetime, which were kept within reasonable limits as defined by the literature. The model was then utilised to predict the performance of the Source I glass in a more suitable geometry with a smaller transverse cross-section, resulting in a significantly improved performance. The deleterious impact of the high propagation losses were apparent from the laser characterisation experiments performed on the Source II and Source III glasses. It was apparent that lower losses would drastically improve the slope efficiency of the laser devices. This can be illustrated by considering the Source III fiber-rod with a 70% reflectivity output coupler, which was the best performing laser in terms of output power achieving 2.5W. If these losses were reduced to 1dB/m, and the absorbed pump slightly increased to $\eta_{abs} = 0.9$, the efficiency of this device would almost double. Improvements in

performance are even more significant when considering laser configurations with lower output coupling.

In order to realise the potential of this concept, the issue of glass sourcing must be resolved. Ideally, the glass would have the excellent optical qualities of a commercial laser glass, with the closely matched thermal properties of the glasses intended for fiber-rod manufacture. To achieve this, I believe the best approach would be a dedicated self-manufacture project. Clearly to achieve the desired parameters in the glass, particularly the optical quality, many manufacturing attempts will be necessary. Through an iterative process one would be able to zero in on the best composition. The two manufactured attempts of the Source I glass highlight this fact, with NP35V(1) exhibiting extreme beam degradation, whilst NP35V(2) allowed good beam transmission. Further iterations to improve the losses within this glass could have proved promising. Unfortunately, such a source of dedicated glass manufacture was not available within the budget or timeline of this project.

In order to fully test the intended concept, including the vital thermally-guided mode control technique, a commercial very large core silica fiber was procured as will be described in Chapter 6. This fiber was chosen since it matched the intended operating regime in terms of geometry and was known to have excellent optical quality optimised with over a thousand manufacturing runs. Whilst this fiber is not manufactured from the intended soft glass network, the results obtained in the investigation will still be valid for potential future soft glass fiber-rod devices, when soft glass of sufficient quality can be obtained.

References

1. D. Marcuse, "Loss analysis of single-mode fiber splices," Bell System Technical Journal **56**, 703 (1977).

2. W. W. Rigrod, "Saturation effects in high-gain lasers," J. Appl. Phys. **36**, 2487 (1965).

3. W. Koechner, Solid-State Laser Engineering, 6 ed., Sixth Revised and Updated Edition (Springer, 2005).

4. E. Ceci-Ginistrelli, C. Smith, D. Pugliese, J. Lousteau, N. G. Boetti, W. A. Clarkson, F. Poletti, D. Milanese, "Nd-doped phosphate glass cane laser: from materials fabrication to power scaling tests," J. Alloys Compd. **722**, 599 (2017).

5. J. H. Campbell, J. S. Hayden, A. Marker, "High-Power Solid-State Lasers: a Laser Glass Perspective," J. Appl. Glass Sci. **2**, 3 (2011).

6. D. Findlay, R. A. Clay, "The measurement of internal losses in 4-level lasers," Phys. Lett. **20**, 277 (1966).

7. Kigre Inc., "Q246" (2017), retrieved http://www.kigre.com/products/laser_glass.pdf

8. Y.W. Lee, H.Y. Ling, Y.H. Lin, S. Jiang, "Heavily Tm3+-doped silicate fiber with high gain per unit length," Opt. Mat. Ex. **5**, 549 (2015).

9. Y. W. Lee, M. J. F. Digonnet, S. Sinha, K. E. Urbanek, R. L. Byer, S. Jiang, "High-Power Yb3+-Doped Phosphate Fiber Amplifier," IEEE J. Quantum Electron. **15**, 93 (2009).

Chapter 6   Silica Thermally-Guided Fiber-Rod Device Testing

6.1   Chapter Overview

This chapter explores the TGFR concept in a silica glass host. Section 6.2 will introduce the TGFR device and present important device considerations. The thermally-induced guiding concept will be experimentally investigated in section 6.3. Section 6.4 will compare measured gain levels in the device with the predicted performance based on the model introduced in section 3.4. In section 6.5, we will use the results obtained in the previous sections to design and construct TGFR laser devices. Finally, section 6.6 will conclude the chapter.

6.2   Demonstration Considerations

6.2.1   Demonstration Material

Initially the TGFR concept was planned for soft glasses, but in light of the developments of Chapter 5 it was not considered worthwhile with the current materials available. Therefore, rare-earth ion-doped silica was deemed an excellent candidate for demonstrating the TGFR laser concept, owing to its high fracture limit, positive thermo-optic coefficient and because there are well-established fabrication techniques for producing high purity material with exceptionally low background loss. Fortunately, an extra-large mode area silica fiber supplied by Nufern became available towards the end of the PhD project, and was thus selected for the demonstration. The all-glass fiber (cross-section shown in fig. 6.1) consisted of a 300μm diameter core with an NA of 0.11 doped with Yb_2O_3, a 400μm octagonal inner-cladding with an NA of 0.22 and a 480μm outer-cladding. Sophisticated fabrication techniques ensure that this fiber has impressive doping uniformity. The core material can act as a thermally-induced guiding structure such that the signal does not interact with the core/cladding interface. Additionally, the core provides guidance for the pump radiation, ensuring a good pump/signal overlap efficiency and short pump absorption length, benefitting quasi-three-level operation and the mitigation of nonlinear effects.

6.2.2   End-Capping System

In a high gain system, such as a traditional fiber laser, a resonator can tolerate fairly substantial intracavity losses without seriously decreasing the laser efficiency. Should these same losses be present in a low gain system the efficiency would be significantly reduced and the laser may not

operate at all. Gain modelling (presented in section 6.4) for some typical TGFR device lengths under the available pump power suggest fairly modest small-signal single-pass gain levels, in the region of 5dB. Thus for optimal laser performance it will be imperative to keep intracavity losses to an absolute minimum. Consequently, it was deemed a necessity to negate the loss associated with Fresnel reflections from the cleaved fiber end-faces, with each face accounting for approximately 3.4% loss, resulting in a significant potential round-trip loss of 13.6% from the fiber end-faces alone i.e. 2 end-faces with a round-trip corresponding to a double-pass of the device.
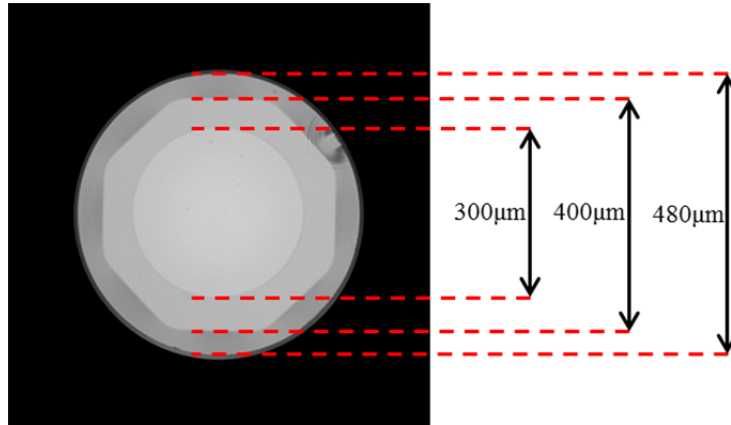

Figure 6.1: Cleaved cross-section of extra-large mode area fiber used for TGFR demonstration.

Taking this information into consideration, two clear solutions were available. An appropriate antireflection (AR) coating could be applied to the fiber end-face, or AR-coated end-caps could be spliced on to the fiber end-faces. The former solution was disregarded in this instance owing to the fact that substantial heat will be generated in the fiber core, particularly at the input face, which could damage any applied coatings. Furthermore, excessive cost and lead times made this option impractical. Therefore, splicing AR end-caps directly on to the fiber end-faces was pursued, resulting in a physical separation between the generated heat and the AR coating.

To achieve this requirement, a simple but effective end-capping system was developed. The end-caps were obtained from a standard Thorlabs B-coated silica window, providing < 0.5% loss at 915nm (the intended pump wavelength), and at 976-980nm and 1030-1040nm (the intended signal wavelengths). The window, measuring 4mm thick with a 38.1mm diameter, had the AR coating removed on one side by polishing, before being diced into approximately 7mm x 7mm x 4mm cubes, by a glass processing company (Crystran Ltd).

In order to fuse the silica fiber to the silica end-caps, the end-cap and fiber must be heated to an appropriate temperature, which is in the region of 2000°C [1]. This was achieved by using a CO_2 laser, which produces an output at 10.6μm and heats the silica by absorption of radiation. The laser was directed onto the uncoated face of the end-cap, which strongly absorbs 10.6μm radiation with an absorption depth on the order of microns at the splicing temperatures [2].

As one would expect, the fiber end-face and uncoated end-cap surface must be well aligned before splicing, that is, the faces should be flat and parallel to each other. This alignment was achieved by

viewing the fiber/end-cap interface with a microscope through the end-cap (fig. 6.2). The fiber, which has 3-dimensional control, is brought very close to the intended splice point of the end-cap (i.e. the centre). When illuminated through the end-cap with light from the microscope, a fraction of the light is reflected from the uncoated end-cap face, and a fraction is reflected from the cleaved fiber end-face. These two reflected portions can then interfere, creating a phase difference determined by the physical separation of the two faces. If the wavelength of the illuminating microscope is λ_m, then a separation of $\lambda_m/4$ between the two faces means that the portion of light reflected from the fiber face has travelled a total distance of $\lambda_m/2$ (there and back) further than the light reflected from the end-cap face, which in terms of phase, equates to a phase difference of π. On reflection from the fiber face the light is reflected at an interface between a lower refractive medium (air), and a higher refractive medium (silica), and therefore incurs an extra π phase shift. Therefore a total phase shift of 2π occurs, thus the interfering light portions constructively interfere and we would observe a bright fringe on the fiber end-face. In fact a bright fringe would occur for any separation which is equal to an odd-number multiple of $\lambda_m/4$, i.e. $\lambda_m/4$, $3\lambda_m/4$, $5\lambda_m/4$, and so on. Similar logic can be used to prove that any even-number multiple of $\lambda_m/4$, i.e. $2\lambda_m/4$, $4\lambda_m/4$, $6\lambda_m/4$, etc. would give a dark fringe. Thus, the separation difference between consecutive dark fringes is $\lambda_m/2$. A poorly aligned example of a 400μm coreless silica fiber is shown in fig. 6.2 (top), where multiple fringes can be observed. The end-cap is attached to a mirror-mount with pitch and yaw control, therefore the parallelism can be actively improved as shown in fig. 6.2 (bottom). In this case the alignment is improved, and only a few, wide fringes can be observed, indicating good parallelism between the splicing surfaces.
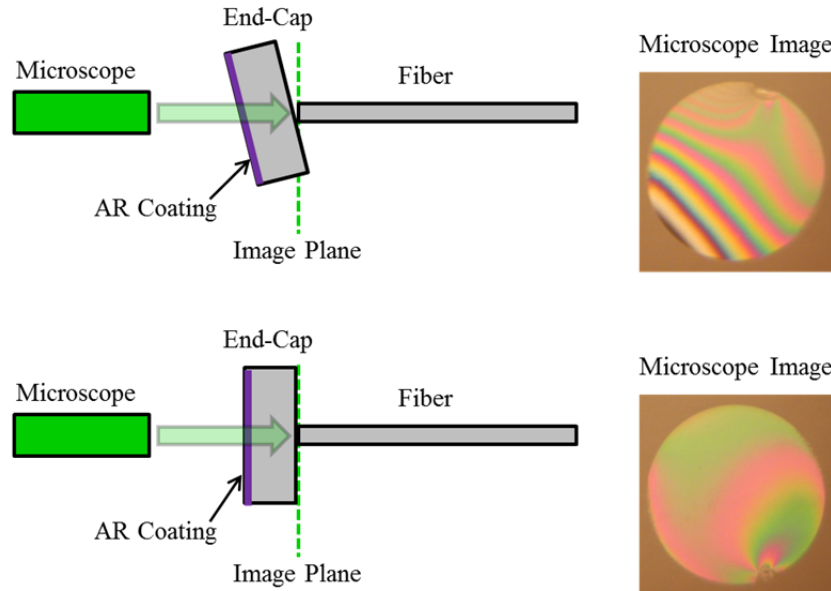

Figure 6.2: Fiber and end-cap with poor (top) and good (bottom) alignment.

Fig. 6.3 shows the arrangement for splicing after the necessary alignment has been optimised. The fiber is backed away from the end-cap by approximately 4mm using a motorised stage. The CO_2

laser is then directed on to the end-cap, with a beam diameter of a few mm at approximately 30W to give a golden glowing region in the centre. After 10 seconds of heating the fiber is then moved forward 4.1mm, with the 0.1mm overshoot allowing the two surfaces to push against each other and create a strong bond. After 5 seconds the laser power is turned off and a strong bond is formed (fig. 6.3). Note that it was necessary to directly contact a polished metal block on to the AR coated surface of the end-cap, in order to improve heat extraction and thus prevent the AR coating from being destroyed.
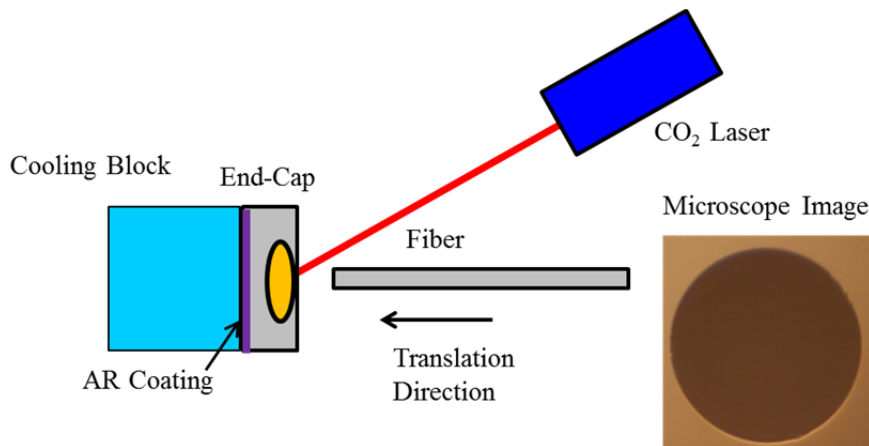
Figure 6.3: Splicing configuration with good bond formed.

Once this process was optimised for the 400μm coreless fiber, it was transferred to the extra-large mode area fiber used for the TGFR laser demonstration with no modifications. Fig. 6.4 shows an example of a section of this fiber with end-caps spliced on both ends, and the microscope image after a successful splice.
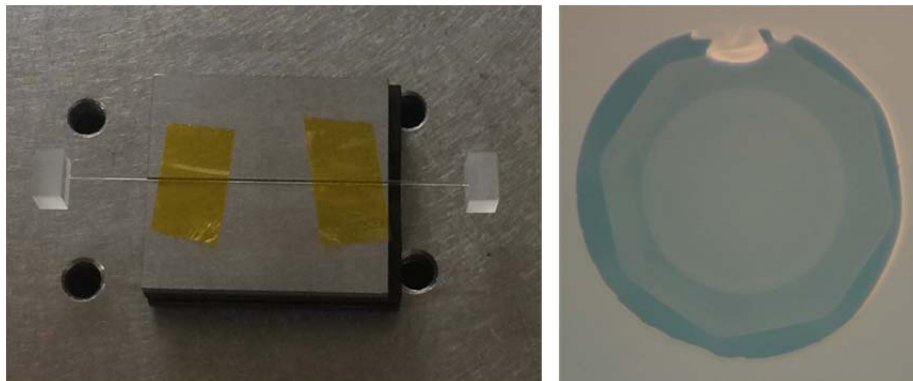
Figure 6.4: Example of end-capped TGFR (left) and splice image (right).

6.2.3   Straightness Considerations

An important assumption in the mode control modelling presented in section 3.3 is that the TGFR is kept perfectly straight throughout operation. Furthermore, preliminary experiments investigating beam transmission through the TGFR indicated that straightness of the device was crucial. A diffraction-limited beam at 1080nm was focused through a 59mm length of the TGFR without interacting with the core (see section 6.3 for details). The TGFR was taped down in a v-groove. The output face of the TGFR was imaged revealing a good quality beam profile for this scenario

(fig. 6.5, left). This qualitative study was repeated, with the TGFR mounted in exactly the same way but with a 50μm thick strip of copper foil positioned under the centre of the fiber, causing a slight bend. After re-optimising the alignment of the input beam it was deemed no longer possible to pass a high quality beam through the TGFR. Instead, interference fringes appeared in the direction of the bend (i.e. vertical), indicating that this 50μm bend was more than sufficient to completely destroy beam transmission (fig 6.5, right). Whilst this very simple and crude experiment does not provide quantitative tolerances on the acceptable bend of the device before transmission is degraded, it does highlight the fact that bends on the order of tens of microns are more than sufficient to prevent the desired outcome. A quantitative study would be extremely interesting for future experiments.

As a consequence of this realisation, it was important to design a mounting system to hold the TGFR straight. This design must allow for the thermal expansion of the TGFR which occurs as a result of pumping, whilst simultaneously providing effective cooling. A jig (fig. 6.6) was designed and manufactured in-house to meet these requirements. It consisted of two hollow aluminium halves, with a 10mm square cut-out in the bottom half. The end-capped fiber was lowered into the square cut and the top half of the mount was bolted down. The end-caps were then greased into place with very close fittings frames, which were in turn sealed onto the mount with silicone sealant. Water was gently flowed from a flow-restricted water tower into the lower half and out the upper half of the mount, resulting in a steady stream of water passing directly over the TGFR, thus providing surface cooling. When the TGFR is pumped, it will heat up and expand due to thermal expansion. The grease within the close fitting frames allows the end-caps to move freely as the fiber thermally expands and contracts. Should the end-caps be fixed in place i.e. with the silicone sealant, then this expansion would have to be taken up by a bend in the TGFR, which would be detrimental to device performance.
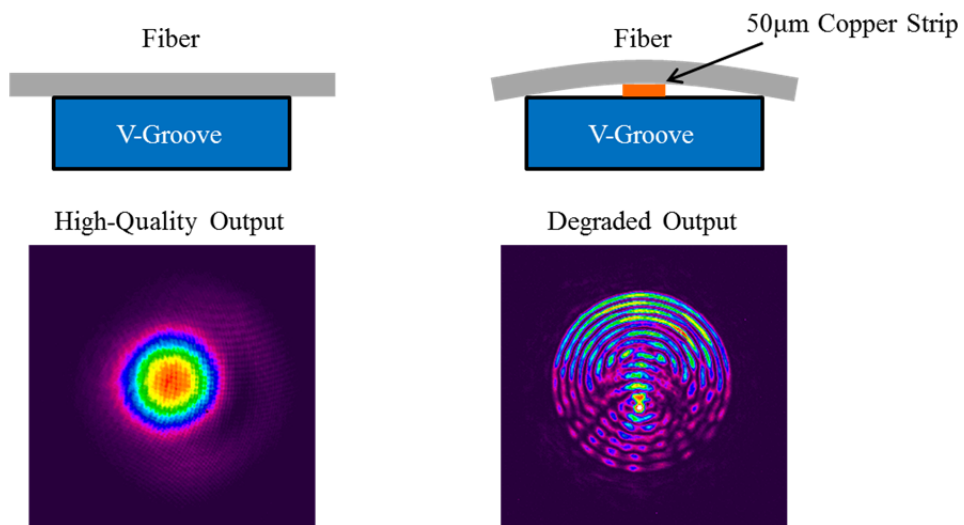

Figure 6.5: Imaged beam transmission through a straight (left) and slightly bent (right) TGFR.
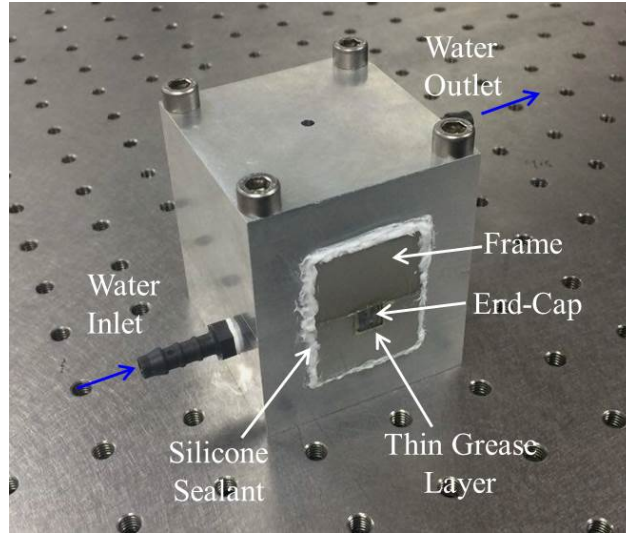
Figure 6.6: Jig to hold end-capped TGFR.

6.3 Mode Control

6.3.1 Experimental Configuration

In order to experimentally validate the thermal-guiding model, the experimental set-up shown in fig. 6.7 was employed. In this arrangement a diffraction-limited seed beam at 1080nm provided by the tunable fiber laser (section 5.2) was launched into one end of the TGFR, with known beam parameters at the input face. A fiber-coupled diode laser operating at 915nm was launched into the signal output end of the device in a counter-pumping configuration. This wavelength was chosen for thermal guiding, amplifier and laser experiments, since it corresponds to a broad absorption peak for Yb-doped silica (fig. 6.15). Pumping at the higher absorption peak at 975nm was not an option since this wavelength will be targeted for amplifier and laser experiments. The pump fiber had a core diameter of 105μm and a core NA of 0.22, and was imaged into the device using an imaging system consisting of collimating lens with a 25mm focal length and a focusing lens with a 50mm focal length. This pump configuration creates a beam waist of 105μm, with an NA of 0.11, at the TGFR end-face, satisfying the condition for core guidance. The signal is imaged from the output face of the TGFR using a 1:1 imaging system, consisting of two identical lenses of 50mm focal length separated by 100mm. Therefore, the beam evolution from the output plane of this imaging system can be considered identical to the beam evolution from the output of the TGFR. Furthermore, one can measure the evolution of the beam radius from the output plane as a function of pump power. This evolution can be used to verify the thermal-guiding principle, since we know the input beam parameters, q_{in}, the ABCD matrix, and the output beam parameters, q_{out}. By varying the pump power, we can vary the thermal lens strength in a controllable way. This will change the parameters of each ABCD matrix that makes up the TGFR. Therefore, the accuracy of the model can be determined by comparing the modelled and measured output beam evolution across a range of pump powers.
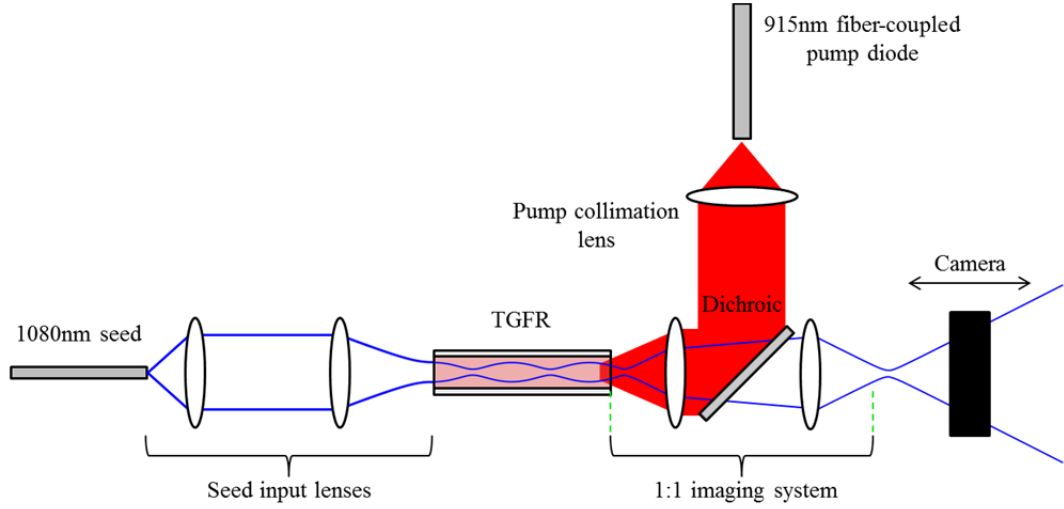
Figure 6.7: Experimental set-up used to investigate thermal-guiding within the TGFR device.

6.3.2   Non-Pumped Investigation

Before investigating the effectiveness of the model in predicting thermal-guiding, we first explored the simplified case where no pump power is launched. Here we assume the refractive index maintains a uniform profile radially and longitudinally, since no heating process occurs to generate a parabolic profile. Considering equation 2.46, we see that the Rayleigh range increases in proportion to the refractive index, therefore a Gaussian beam diffracts slower through a material with a higher refractive index. A beam that propagates through a medium of length l_Ω and refractive index n_Ω, will lag a beam that propagates a length l_Ω solely though air by a distance $d_{lag} = l_\Omega - l_\Omega/n_\Omega$ (assuming $n_{air} = 1$).

Before testing the TGFR device, a 3mm diameter, 60mm long Yb:YAG rod was investigated. This material is known to have a good optical quality and a uniform refractive index profile, and can therefore be used to confirm the experimental configuration is performing as expected. Assuming a refractive index of $n_{YAG} = 1.8$, we expect $d_{lag} = 26.7$mm. To test this empirically, a beam at 1030nm was focused to a waist of approximately 90μm, before being 1:1 imaged as discussed in section 6.3.1, with the image plane at 60mm. Fig. 6.8 (left) displays the input beam data overlaid with the imaged beam data, which has been shifted by the length of the imaging system (200mm). We observe good agreement between the data sets, confirming the imaging system is performing appropriately. The experiment is repeated with the Yb:YAG rod inserted in the input beam, with the imaged data also shown in fig. 6.8 (left). By shifting this data by d_{lag} we observe a good overlap between the input data and the imaged data after propagation through the Yb:YAG rod, as shown in fig. 6.8 (right). This confirms the set-up is working sufficiently to conduct the investigation on the TGFR.
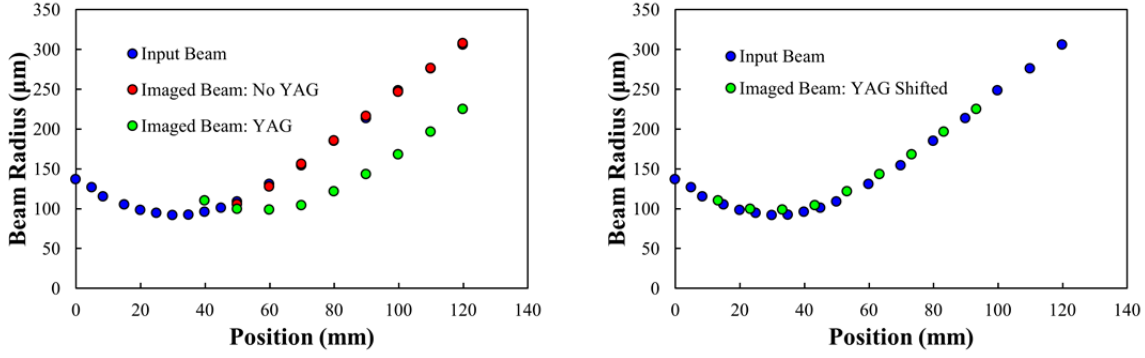
Figure 6.8: Input and imaged beam with no shift (left), and with d_{lag} shift (right) for Yb:YAG rod.

The beam evolution investigation was conducted on a 59mm long section of the TGFR. An input beam, at 1080nm, was focused to a waist of approximately 78μm, at a longitudinal position of $z = $ 0mm. The longitudinal position of the input face of the TGFR, z_{TGFR}, was shifted relative to the waist position. Fig. 6.9 displays the input beam evolution and the predicted beam evolution assuming a radially homogeneous refractive index profile for a single position: $z_{TGFR} = 13$mm, although a similar situation was observed for seven positions ranging from $z_{TGFR} = -8$mm to $z_{TGFR} = $ 13mm. Here, we would predict the beam to interact with the core/cladding interface, leading to guiding within the highly multimode core and a corresponding reduction in beam quality. However, the figure also displays the actual measured beam evolution and output beam profile, which does not correspond to the predicted evolution and displays good beam quality. This implies that the model does not correctly predict beam evolution through the TGFR with the current assumptions.
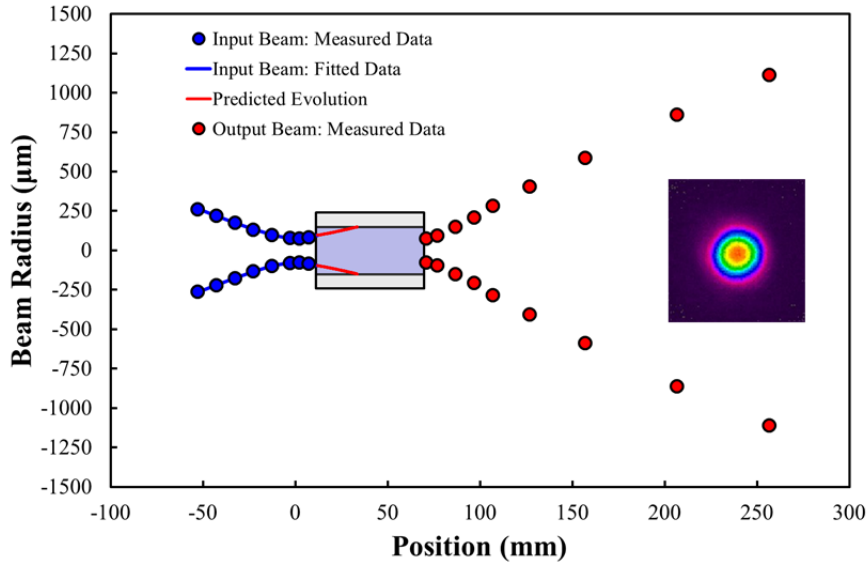
Figure 6.9: Measured and predicted beam evolution through the TGFR for $z_{TGFR} = 13$mm.

It was postulated that the origin of this discrepancy may be the modelling of the refractive index profile (RIP), which was assumed to be radially homogeneous. Taking a closer look at the preform RIP (fig. 6.10), it is apparent that this assumption is incorrect as the refractive index clearly decreases radially, perhaps as a consequence of the fabrication process.
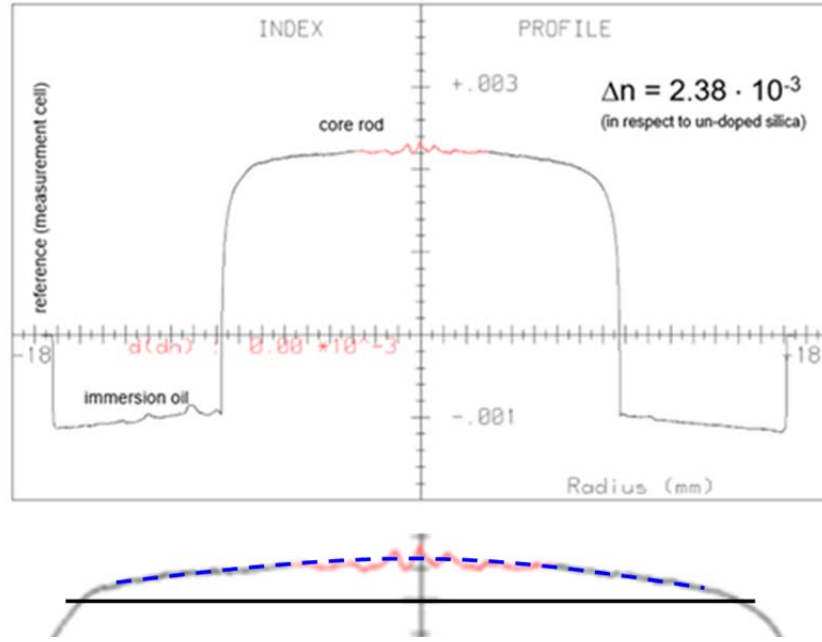
Figure 6.10: Preform RIP, with close-up view showing deviation (blue) from flat profile (black).

It was consequently assumed that the RIP displayed an approximately parabolic dependence in order to incorporate it into the model, allowing each slice of TGFR to be described by the matrix presented in scenario 3 from Table 3.1. In order to find an appropriate solution for n_{th}, which was assumed to be longitudinally constant, we considered the input and output beam parameters. Since both q_{in} and q_{out} are known, we can scan over a range of n_{th} to determine the predicted output, and therefore find the solutions which satisfy our requirements. Fig. 6.11 depicts this process, where we have plotted output beam size and wavefront radius of curvature for $z_{TGFR} = 13$mm.

We have scanned the output beam parameters for $n_{th} = 0 - 5,000\text{m}^{-2}$, in order to cover several oscillations of the beam along the length of the device. This can be seen from the oscillating beam size, as the output of the device periodically coincides with a crest or trough of the undulating beam, and also from periodic switching of the radius of curvature from positive (expanding beam) to negative (converging beam). The red lines shown in fig. 6.11 correspond to the measured output beam parameters; therefore the intersection points of the plots indicate values of n_{th} that will satisfy the output beam parameters. The green circles in the radius of curvature plot indicate the solutions which satisfy the measured values. The red circles in the beam radius plot indicate solutions whereby the beam radius satisfies the measured value, and has the beam has the correct sign for the radius of curvature, which for this example is positive as the beam is expanding at the output. Here we note three solutions for the beam size which satisfy these requirements. The purple regions indicate the discrepancy between each of the three solutions and the two nearest solutions for the radius of curvature, i.e. one solution either side. Here we note the discrepancy is smallest for the first solution.

This examination technique was applied across the range of z_{TGFR} positions, and it was observed that the solutions tended to centre on the same solutions shown in fig. 6.11. Taking an averaged solution for the region around the first red circle of $n_{th} = 3,600\text{m}^{-2}$, we observed excellent agreement with the measured data. Fig. 6.12 shows the predicted and measured beam evolution for $z_{TGFR} = 13\text{mm}$, whilst fig. 6.13 shows predicted and measured beam evolution from the output plane for four z_{TGFR} positions.

Due to a lack of a reliable RIP on the TGFR core itself, we are unable to confirm whether the solution from region 1 is in close agreement with the measured profile. However, this solution provides close agreement with the measured beam evolution, and therefore allows us to investigate the thermal-guiding model.
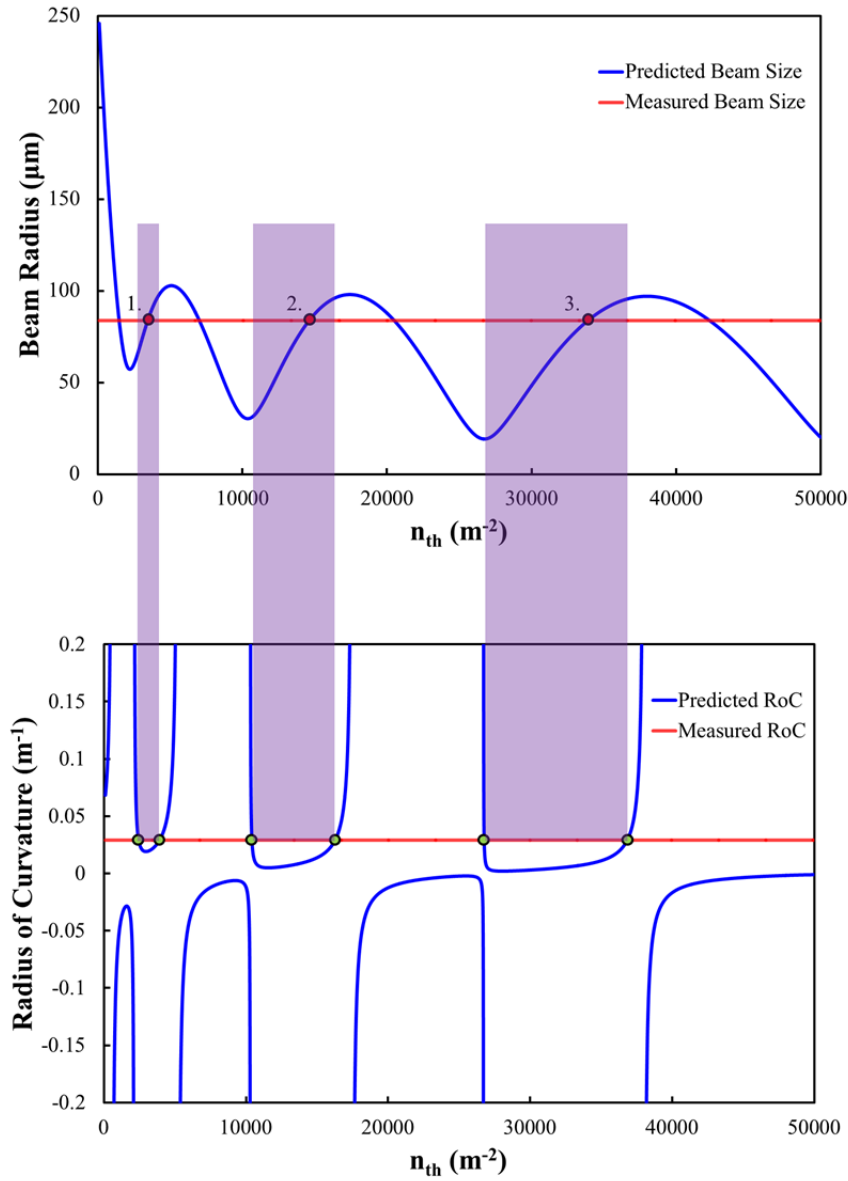
Figure 6.11: Output beam size (top) and radius of curvature (bottom) as a function of n_{th} for $z_{TGFR} = 13\text{mm}$.
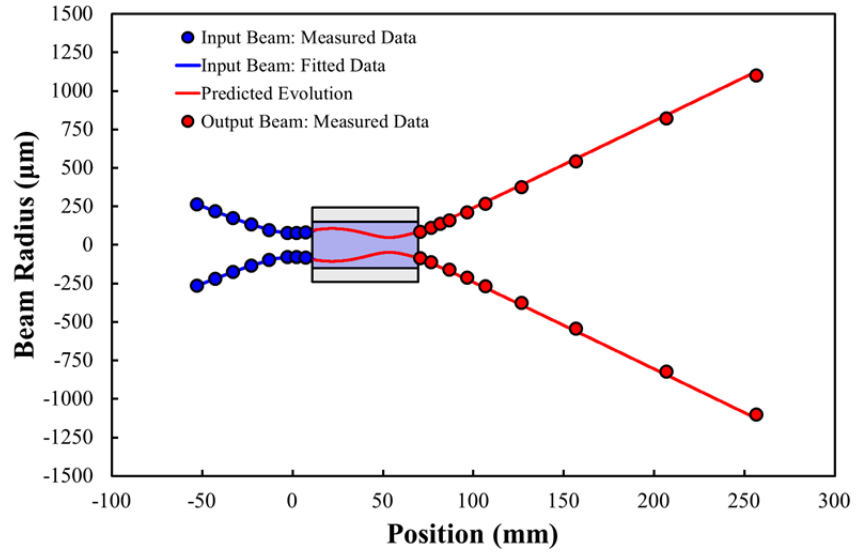
Figure 6.12: Measured and predicted beam evolution through the TGFR for z_{TGFR} = 13mm assuming a parabolic RIP with n_{th} = 3,600m^{-2}.
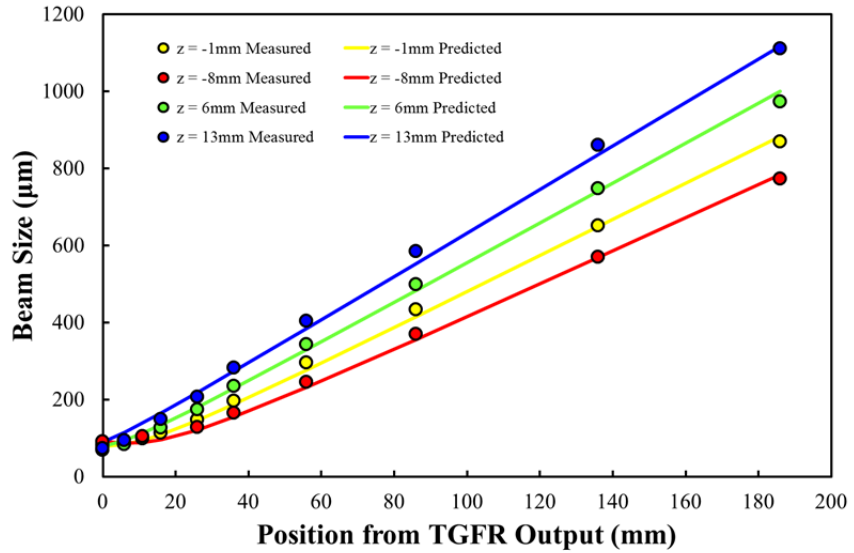
Figure 6.13: Measured and predicted beam evolution from TGFR output for z_{TGFR} = -8mm, -1mm, 6mm and 13mm, assuming a parabolic RIP with n_{th} = 3,600m^{-2}.

6.3.3   Pumped Investigation

The thermal-guiding aspect of the model was then explored on the same TGFR device. In this investigation a beam at 1030nm, was focused to a waist of approximately 69µm, with the TGFR positioned at z_{TGFR} = 5mm. These input conditions were kept constant, whilst the launched pump power was varied. Assuming the previously determined solution of n_2 = 3,600 m^{-2} and a value of dn/dT of 12.9K^{-1} [3], we observed excellent agreement with the measured data across the full range of launched pump power, up to a maximum of 30W. The predicted and measured beam evolution for the range of pump powers is shown in fig. 6.14. This excellent agreement proves the validity of

107

the thermal guiding model, confirming it as a powerful tool that can be utilised to optimise amplifier and laser performance.
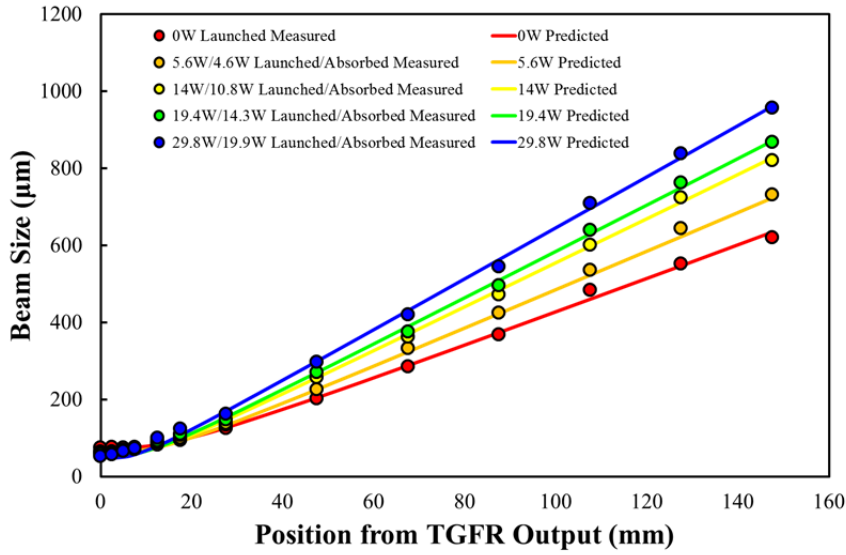
Figure 6.14: Measured and predicted beam evolution from the TGFR for various launched pump powers.

6.4 Amplifier Performance

Following the mode control investigation, the TGFR was characterised in terms of amplifier performance. In this section we will experimentally measure gain in the device at 976nm and 1030nm, and compare this to the predicted performance. To investigate the single-pass gain within the TGFR device, a similar set-up to that used for the mode control investigation was used, as shown in fig. 6.7. However, a power meter replaced the camera in order to determine the output power over a range of pump powers.

Spectroscopy

Fig. 6.15 shows the absorption and emission cross-section data [4] for ytterbium-doped aluminosilicate glass. Point A represents the broad absorption band around 915nm that was utilised to pump the TGFR. Point B indicates the peak in emission and absorption cross-section at 975nm. Since both emission and absorption cross-sections are equal at 975nm, this is a true three-level transition; hence transparency at this wavelength will occur when 50% of the ytterbium ions are excited. To investigate single-pass gain at point B, a single-mode, fiber-coupled diode laser operating at 976nm was used as a seed source. Point C indicates a broader emission peak occurring at 1030nm. At this wavelength the emission cross-section is approximately an order of magnitude greater than the absorption cross-section, and therefore this is a quasi-three-level transition, hence we would expect to reach transparency at a lower excitation density than for 975nm. According to equation 2.20, transparency would occur at 1030nm when approximately 8.5% of the ytterbium ions are excited. Furthermore, once above transparency, we would expect the gain at 975nm to

increase quicker, owing to the larger emission cross-section. The laser discussed in section 5.2 was tuned to 1030nm to investigate the single-pass gain at point C.
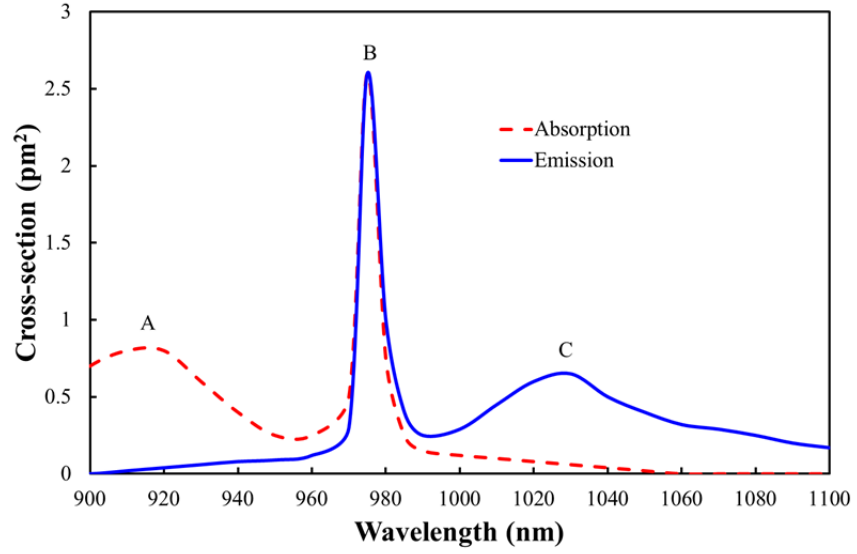
Figure 6.15: Absorption and emission cross-section for ytterbium-doped aluminosilicate glass.

Table 6.1 summarises important spectroscopic parameters used in the gain modelling of the TGFR device. The doping concentration, n_T, was estimated from the absorption, using the spectroscopic data. The cross-sections are depicted $\sigma_{A/B/C\_a}$ for absorption transitions, and $\sigma_{A/B/C\_e}$ for emission transitions on points A/B/C respectively. For the gain modelling, the cross-section values were considered to be accurate to within 15%.

Parameter	Value
n_T	4.2×10^{25} m^{-3}
τ_f	840µs [5]
σ_{A_a}	0.8×10^{-24} m^2
σ_{A_e}	0.03×10^{-24} m^2
σ_{B_a}	2.6×10^{-24} m^2
σ_{B_e}	2.6×10^{-24} m^2
σ_{C_a}	0.06×10^{-24} m^2
σ_{C_e}	0.65×10^{-24} m^2

Table 6.1: Spectroscopic parameters of the TGFR device.

Pump Absorption

Prior to the gain measurements, pump absorption at 915nm was measured. Pump radiation was launched into the TGFR as depicted in fig. 6.7, and transmitted power was recorded across the

entire pump power range. Note that a bandpass filter was used at the TGFR output which allowed high transmission from 900-950nm whilst blocking other wavelengths. This was essential to ensure that fluorescence from the 975nm and 1030nm peaks did not contribute to the measured power. The measured and modelled absorbed power is shown in fig. 6.16. Here we note good agreement, which provides confidence in the values for doping concentration, fluorescence lifetime and the relative transition cross-sections.

976nm Gain

Gain measurements were made at 976nm, following the set-up depicted in fig. 6.7, with an appropriate dichroic mirror to separate unabsorbed pump from the signal radiation. The input beam was focused to a waist of approximately 60μm at the input face, which led to an estimated average beam radius of 60μm throughout the TGFR, according to the thermal-guiding modelling presented in section 6.3. The measured and modelled gain values for an input seed power of 60mW and 450mW are shown in fig. 6.17, which shows a reasonable agreement over the range of pump powers. A maximum gain of 4.1dB was achieved for the 60mW seed resulting in an output power of 155mW, and 2.2dB for the 450mW seed resulting in an output power of 750mW.
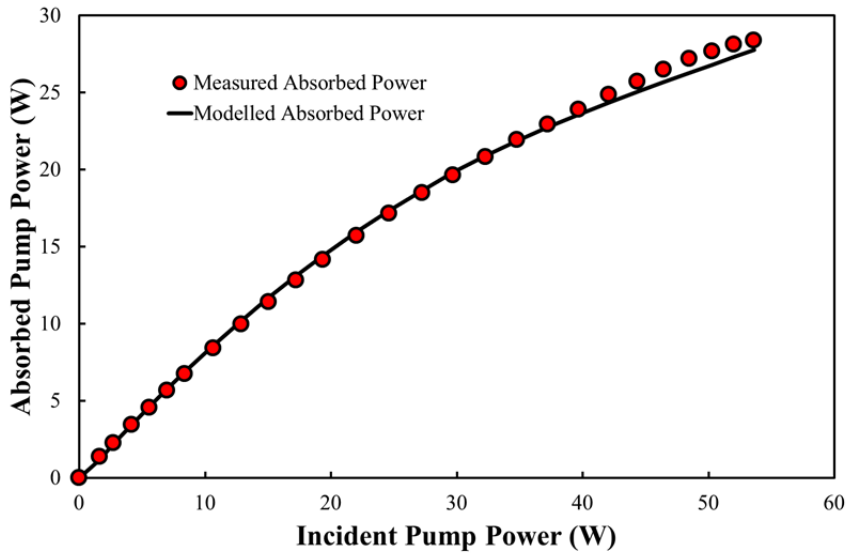
Figure 6.16: Measured and modelled pump absorption.

1030nm Gain

The experiment was repeated at 1030nm, again utilising an appropriate dichroic for the device output. The input beam was focused to a waist of 70μm at the input face, which led to an estimated average beam radius of 60μm throughout the TGFR. The measured and modelled gain values for an input seed power of 50mW and 1.1W are shown in fig. 6.18, which again shows a reasonable agreement. A maximum gain of 5.0dB was achieved for the 50mW seed resulting in an output power of 160mW, and 3.9dB for the 1.1W seed resulting in an output power of 2.7W.
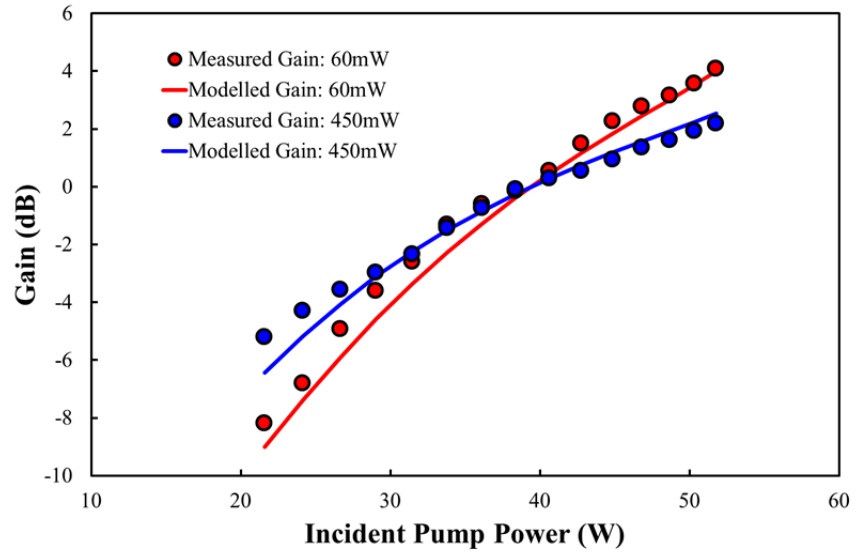
Figure 6.17: Measured and modelled gain at 976nm.
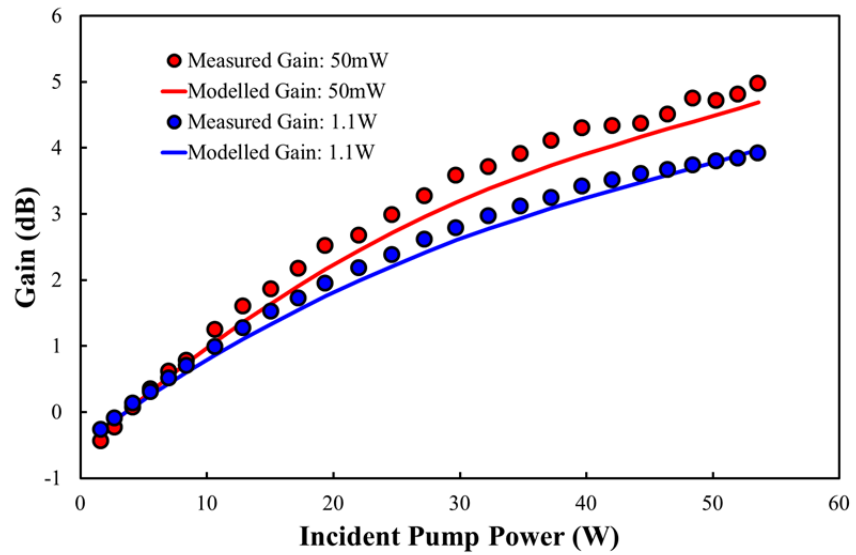
Figure 6.18: Measured and modelled gain at 1030nm.

Beam Quality

The beam quality in these gain experiments remained excellent, i.e. $M^2 < 1.1$, at both 976nm and 1030nm, over the full range of seed and pump powers. Fig. 6.19 shows the beam quality in the x-direction and beam profile at maximum pump power for the 50mW 1030nm beam amplified at the maximum pump power.

Conclusion

The results from the amplifier investigation are encouraging. The measured single-pass gain values are in reasonable agreement with the modelled values. As expected, the transparency for the 1030nm transition is significantly less than for the 975nm transition i.e. approximately 4W versus

111

40W respectively. Additionally, the gain increases faster above transparency for the 975nm transition. Furthermore, excellent beam quality is maintained throughout amplification. This promising performance, combined with the mode control results, paves the way for laser based experiments, where the modest gain levels are more than adequate for laser investigations.
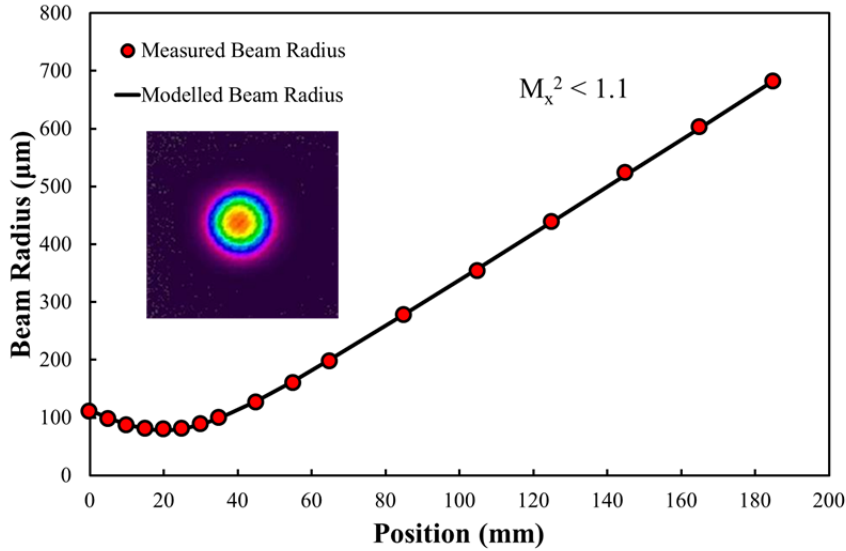
Figure 6.19: Beam quality and beam profile at 1030nm for 50mW at the maximum pump power.

6.5 Laser Performance

The final experimental section of this chapter utilises the results obtained thus far to explore the TGFR device in a laser configuration. The mode control investigation informs the design of a stable cavity (section 6.5.1), whilst the gain performance investigation allows an estimation of threshold powers (section 6.5.2), thus dictating appropriate intracavity optics. This investigation explores laser operation on the two emission peaks previously discussed, i.e. 975nm and 1030nm. Due to the quasi-three-level nature of the 1030nm transition, as compared with the true three-level character of the 975nm transition, we expect a lower threshold for 1030nm, and therefore would expect this transition to be dominant in a laser cavity with no wavelength-dependent losses. Owing to this simplicity, the 1030nm laser will be discussed first in section 6.5.3, before discussing the 975nm laser in section 6.5.4, which requires additional complexity.

6.5.1 Laser Cavity Design

For a stable resonator mode, we require that the beam profile is self-reproducing, i.e. the transverse profile remains constant over each round-trip, as discussed in section 2.3.3. It is useful to be able to predict which cavity configurations are stable, and what the resulting beam size will be throughout the cavity in that configuration. Consider a potential cavity design as shown in fig. 6.20. This cavity comprises of a plane mirror, M1, an intracavity lens, L1, the TGFR, a second intracavity lens, L2, and a second plane mirror, M2. The ABCD matrix for a round-trip through this cavity can

be constructed by multiplying the ABCD matrices for each component, in the correct order. For this example, starting at M1, the beam propagates through free-space over a distance d_1, followed by a lens, L1, followed by free-space propagation over a distance d_2, followed by the first slice of the TGFR which exhibits a parabolic refractive index profile, followed by the next slice, and so on until we reach M2 at which point we work our way back to M1 to complete a round-trip. The product of the matrices that describe each of these elements will produce an ABCD matrix which describes the entire laser cavity. It is important to consider that this ABCD matrix will clearly change as the pump power, and thus the thermally-induced lensing of the TGFR, is varied.
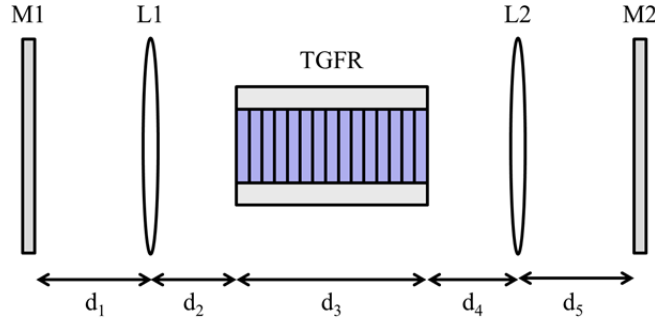
Figure 6.20: Potential cavity design.

Since we stipulate that the beam must be self-reproducing, we can rewrite equation 3.7 as:

$$q = \frac{Aq + B}{Cq + D} \tag{6.1}$$

where A, B, C and D represent the ABCD components of the laser cavity for a round-trip starting/finishing at M1. The beam will form a waist on the plane mirrors, therefore from equation 2.47 and equation 6.1, the beam size on M1, w_{M1}, can be given by [Appendix 6.1]:

$$w_{M1} = \left[\frac{\lambda^2}{\pi^2} \left(\frac{1 - D^2}{C^2} \right) \right]^{0.25} \tag{6.2}$$

The beam can then be propagated through each ABCD matrix to build up a picture of how the beam evolves through the cavity. Unstable cavity configurations will show up as imaginary values for w_{M1}.

6.5.2   Threshold Estimation

It is very useful to predict the threshold pump power for 975nm and 1030nm operation. Knowledge of this value allows appropriate intracavity optics to be selected. For example, an output coupler with a higher transmission will increase slope efficiency but also increase threshold (equation 2.39 and equation 2.40), therefore knowledge of the relationship between the output coupler and threshold can be used to make an informed choice. Additionally, threshold will be reached at a

lower pump power for 1030nm, and thus threshold information can dictate the required suppression at this wavelength to ensure 975nm reaches threshold first.

Both laser cavities were constructed with an input coupler that displayed high transmission at the pump wavelength, i.e. T > 95% at 915nm, with high reflectivity at the laser wavelengths, i.e. R > 99.9% at 975nm and 1030nm, and an output coupler that provided a reflectivity of R = 70% at 975nm and 1030nm. For this analysis, we will assume there are no wanted losses due to scattering, unwanted reflections, unwanted leakage through the high reflector and bulk absorption losses, i.e. $(1 - L) = 1$. Furthermore, equation 5.6 can thus be written as:

$$G = \sqrt{\frac{1}{R_M}} \tag{6.3}$$

Consequently, threshold will be reached at the particular wavelength the satisfies the condition of equation 6.3. In this scenario $R_M = 0.7$, therefore threshold will occur for a gain of $G = 1.2$, or 0.8dB. Utilising the gain model discussed in section 3.4, we can plot the small-signal gain at 975nm and 1030nm as a function of launched power, as shown in fig 6.21. Here we note that the required gain at 975nm is achieved at approximately 41W of launched pump power. Repeating this process at 1030nm we find that the required gain is reached at approximately 9W. Therefore, as expected, with no wavelength dependent losses, the laser will reach threshold at 1030nm at a significantly lower pump power. It is also interesting to note that wavelength-independent losses will impact the 1030nm transition threshold more significantly than the 975nm transition threshold, since the gain above transparency increases at a slower rate for the 1030nm transition.
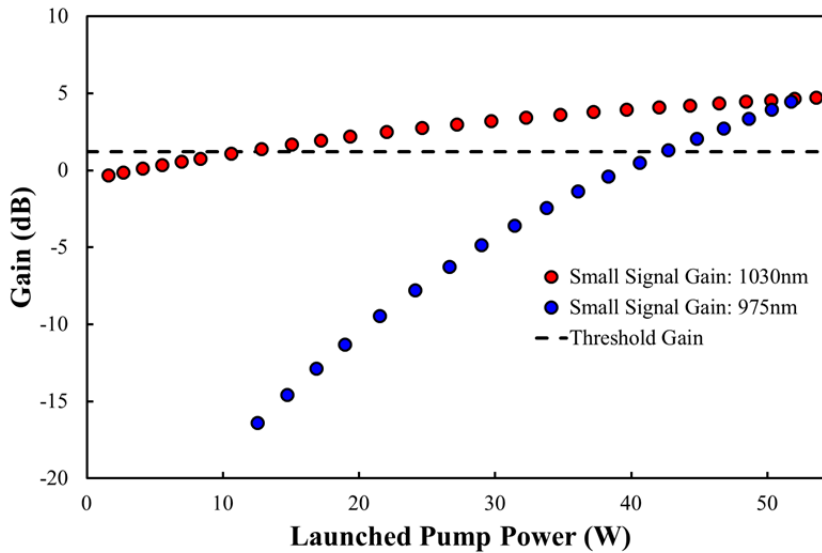

Figure 6.21: Small-signal single pass gain for 975nm and 1030nm as a function of pump power.

6.5.3   1030nm Laser

Laser Configuration

Various laser configurations were modelled and trialled, however, in order to minimise the degrees of freedom within the cavity and improve alignment stability, it was decided that the simplest configuration should be employed. This essentially consisted of the TGFR device and the two cavity mirrors, each positioned approximately 5mm from the end-face of the TGFR. This configuration is shown schematically in fig. 6.22, with the modelled signal beam profile shown in red at a launched pump power of 50W. This configuration gave an average beam size through the TGFR of approximately 75μm, with little deviation in beam size across the range of pump powers.

Figure 6.22: Laser configuration for 1030nm investigation.

Output Power

The cavity was optimised for maximum output power. Threshold was reached at approximately 14W. A maximum output power of 13.1W was achieved, with a corresponding maximum slope efficiency of 44% with respect to launched power and 53% with respect to absorbed power, as shown in fig. 6.23. Note that the slope efficiency increases as the laser is operated further above threshold, as is expected, owing to the signal radiation saturating gain in the beam wings.

The threshold value of 14W is in reasonable agreement with the value of 9W predicted in section 6.5.2; especially since this estimation assumes all other intracavity losses are zero. It is also worth noting that since the cavity was optimised for performance at maximum pump power, it was not necessarily optimised for the lowest threshold value. The slope efficiency with respect to absorbed power, 53%, is reasonable, with the theoretical limit for this transition approaching 89% according to the quantum defect. Minimising intracavity losses through improved AR coatings on the end-caps would improve the slope efficiency. Additionally, one would expect the slope efficiency to improve by operating the laser further above the threshold power.
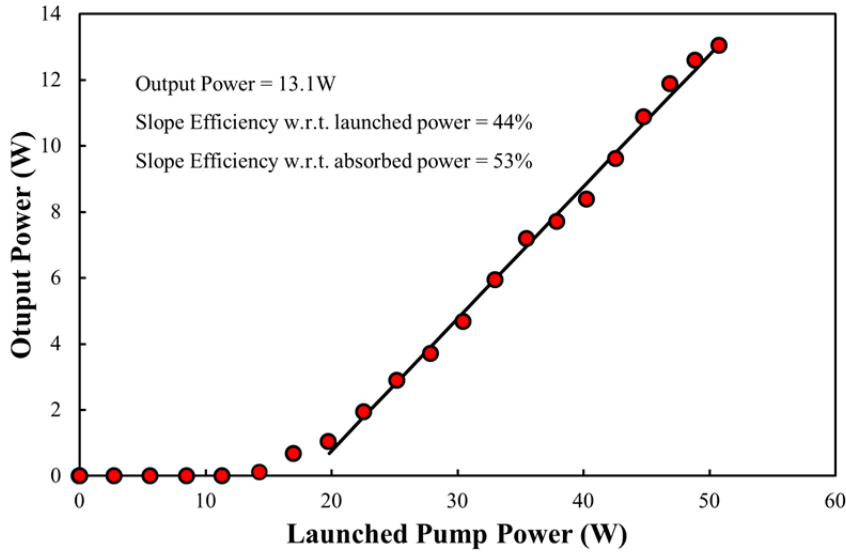
Figure 6.23: Output power as a function of launched power.

Wavelength

Fig. 6.24 shows the wavelength spectrum at maximum output power. The wavelength spectrum is fairly broad with several peaks, which is not surprising considering that no wavelength selection was employed in this configuration. The main peak is centred on 1032.5nm with a FWHM of 1.3nm.
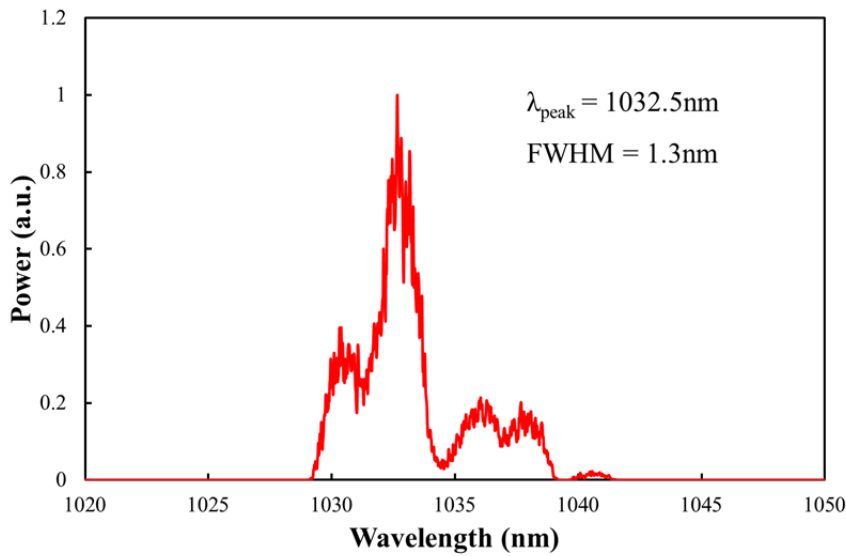
Figure 6.24: Output wavelength at maximum pump power.

Beam Quality

Excellent beam quality was achieved at maximum output power with $M^2 < 1.1$. Fig. 6.25 shows the beam quality in the x-direction and the beam profile at maximum pump power.
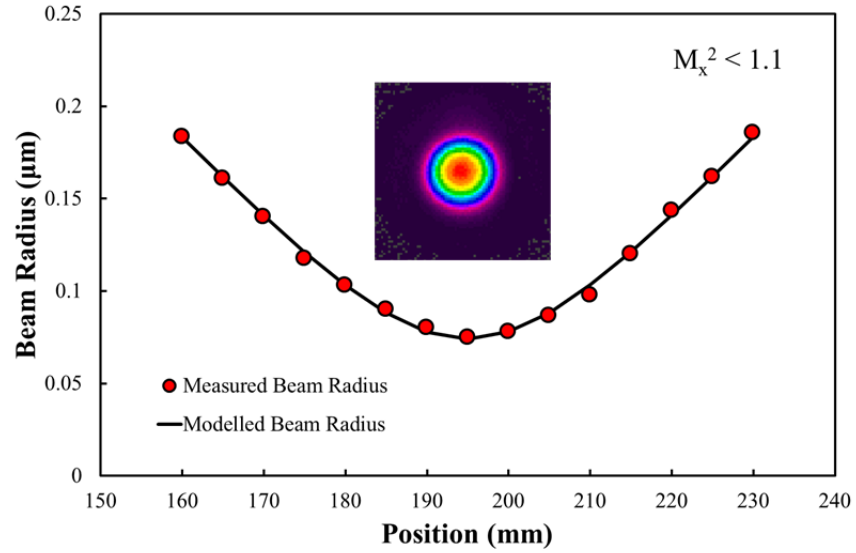
Figure 6.25: Beam quality and beam profile at maximum pump power.

6.5.4 975nm Laser

1030nm Suppression

The laser configuration employed for the 975nm laser was complicated by the fact that sufficient suppression must be provided at 1030nm. To calculate the suppression necessary, it is helpful to consider the gain experienced at 1030nm for 41W of launched pump power, i.e. the threshold power for the 975nm transition. In order to suppress the 1030nm oscillation, the losses at this wavelength must be sufficient so that the gain experienced at 41W is less than the threshold gain, i.e. 0.8dB. With no losses, the small-signal gain for 1030nm at 41W is approximately 4dB. Equation 5.6 can then be employed to calculate the total round-trip losses required at 1030nm, L_{1030}, to set 41W as the threshold pump power for 1030nm. This leads to a value of L_{1030} = 0.77, or ≈ -6.5dB. Therefore, inserting a device which incurs a round-trip loss greater than -6.5dB at 1030nm, and negligible loss at 975nm, and assuming all other losses are negligible, we would expect 975nm to reach threshold at 41W and saturate the gain, thus becoming the dominant output wavelength. A notch filter was used to achieve this suppression, achieving ≈98% single-pass transmission around 976-980nm and blocking wavelengths between 850-970nm and 990-1300nm, with a single-pass loss at 1030nm of greater than -40dB, which is more than sufficient from the desired suppression.

Laser Configuration

Simplicity of design was again considered important. The cavity consisted of an input mirror positioned approximately 5mm from one end-face of the TGFR, an intracavity lens of focal length 50mm, positioned approximately 60mm from the end face of the TGFR, and an output mirror, positioned approximately 55mm from the lens. The lens-mirror feedback arm was necessary to accommodate the notch filter, which was inserted at a slight angle (to prevent 1030nm feedback)

into the cavity, between the TGFR end-face and the lens. This configuration is shown schematically in fig. 6.26, with the modelled signal beam profile shown in red at a launched pump power of 50W. This configuration gave an average beam size through the TGFR of approximately 70μm, with little deviation in beam size across the range of pump powers.
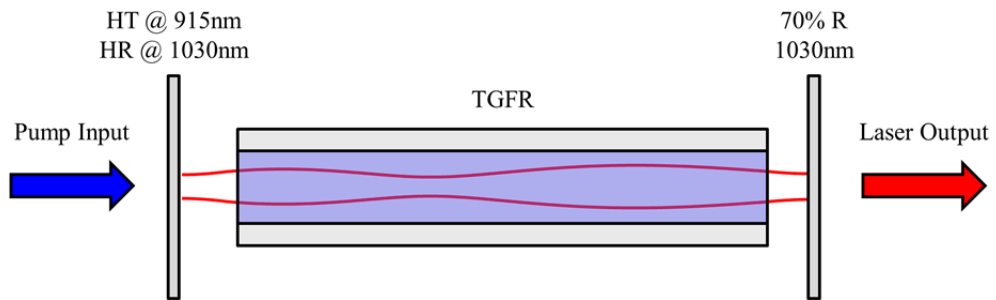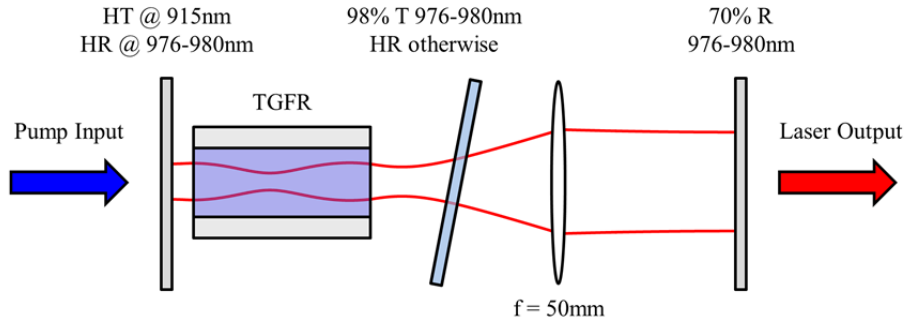

Figure 6.26: Laser configuration for 975nm investigation.

Output Power

As with the 1030nm laser, this cavity was optimised for maximum output power. Threshold was reached at approximately 42W, and a maximum output power of 1W was achieved, with a corresponding maximum slope efficiency of 8% with respect to launched power, as shown in fig. 6.27. Owing to the fact that the notch filter also blocked the pump wavelength, it was not possible to measure the unabsorbed pump power during lasing, thus a slope efficiency with respect to absorbed power is absent. However, the absorbed power at threshold was measured to be 25W.

If we account for the additional loss at 975nm due to the notch filter, we would expect threshold to be achieved at approximately 41.5W, which is in excellent agreement with our measured value. Note that the lasing threshold was only just achieved with the available pump power, and the slope efficiency is expected to increase at higher pump powers, once the system has been brought several times above threshold. Additionally, as before, minimising losses at 975nm would improve the slope efficiency and lower the threshold. Ideally, the 1030nm suppression would be achieved by cavity mirrors which are highly transmissive at 1030nm. Not only would this eliminate the need for an intracavity notch filter, it would also allow for the simpler design employed by the 1030nm laser. Unfortunately, mirrors with these specifications are difficult to manufacture due to the close proximity of the wavelengths of interest, and were therefore not available for this experiment.

Wavelength

Fig. 6.28 shows the wavelength spectrum at maximum output power, which is centred on 978.5nm with a FWHM of 2.8nm. Note that no wavelengths occur outside the bandwidth of the notch filter.

Beam Quality

As before, excellent beam quality was achieved at maximum output power with $M^2 < 1.1$. Fig. 6.29 shows the beam quality in the x-dimension and the beam profile at maximum pump power.

Figure 6.27: Output power as a function of launched power.

Figure 6.28: Output wavelength at maximum pump power.

Figure 6.29: Beam quality and beam profile at maximum pump power.

6.6   Conclusion

In this chapter we demonstrated the concept of the TGFR using an extra-large mode area ytterbium-doped silica fiber, which displayed numerous attractive properties including a crucially important positive thermo-optic coefficient. A technique developed in-house for splicing AR-coated end-caps onto the TGFR was presented.
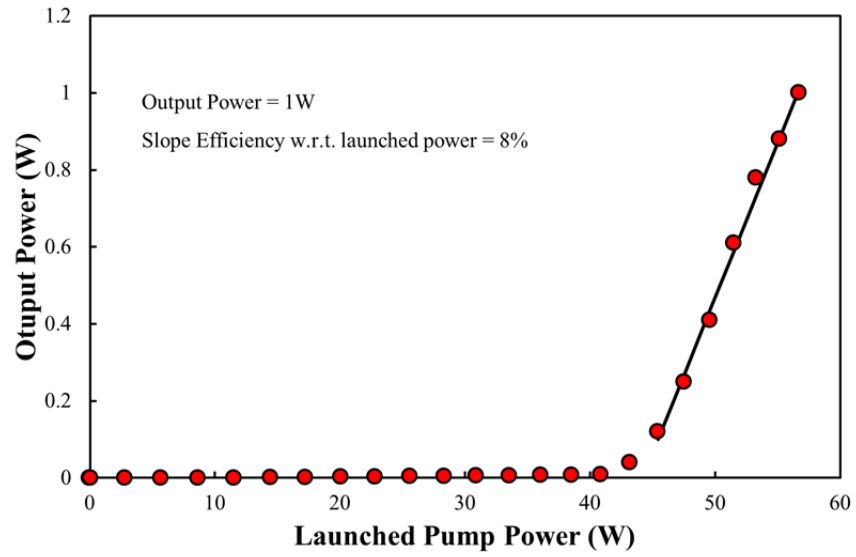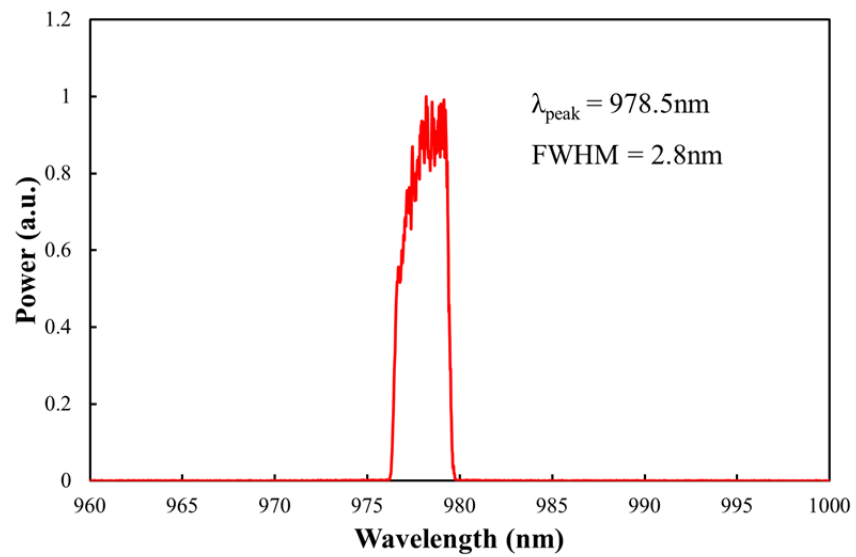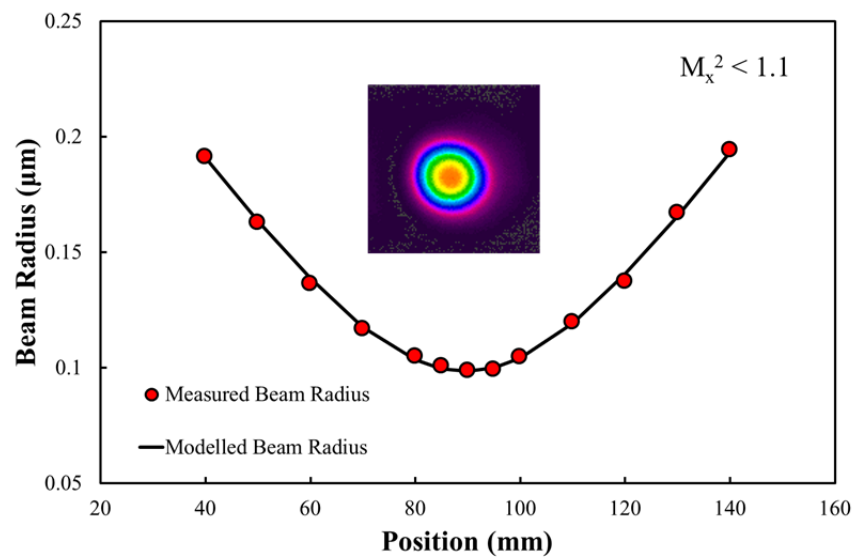
The thermally-induced mode control technique presented in section 3.3 was experimentally investigated. Beam evolution through the TGFR was investigated, and it was discovered that a degree of guiding was built into the device even in the absence of pumping. The effect of this guidance was estimated by considering the output beam evolution from the device for a range of input beam parameters, leading to good agreement between measured and modelled beam evolution. Thermally-induced guidance was then investigated by considering the in-built guidance alongside that expected from pumping the TGFR. Again, good agreement between measured and modelled beam evolution was achieved, confirming that the model is a valuable tool for predicting beam guidance through the TGFR.

The performance of the TGFR as an amplifier was investigated. The gain model presented in section 3.4 was used to predict the single-pass gain through the TGFR. Amplification data was recorded at 976nm and 1030nm, and was found to be in reasonable agreement with the modelled data. At 976nm a maximum gain of 4.1dB was achieved for a 60mW seed resulting in an output power of 155mW, and 2.2dB for a 450mW seed resulting in an output power of 750mW. For 1030nm a maximum gain of 5.0dB was achieved for a 50mW seed resulting in an output power of 160mW, and 3.9dB for a 1.1W seed resulting in an output power of 2.7W. Excellent beam quality was maintained throughout amplification with $M^2 < 1.1$ at the maximum gain levels for both 976nm and 1030nm.

The obtained results were then utilised to investigate the performance of the TGFR as a laser. The mode control investigation was used to construct a model for predicting laser resonator stability. The model can predict how the fundamental mode would propagate in the cavity. One might expect the cavity to operate as a highly multimode laser owing to the large V-number of the device. However, the diffraction losses for the guided, highly-multimode radiation are considerably higher than the thermally guided mode. The amplification model was employed to predict laser thresholds and the suppression required at the 1030nm transition to achieve lasing on the 975nm transition. Simple laser devices were constructed based on the 1030nm and 975nm transition. The first device, operating at 1032.5nm, reached threshold at 14W which agreed reasonably well with the predicted value, and achieved a maximum output power of 13.1W with a slope efficiency of 44% with respect to launched power and 53% with respect to absorbed power. Excellent beam quality was achieved at maximum output power with $M^2 < 1.1$. The second device, operating at 978.5nm, incorporated a notch filter in order to suppress 1030nm oscillation. Threshold was achieved at 42W,

which was in excellent agreement with the predicted value, and a maximum output power of 1W was achieved with a slope efficiency of 8% with respect to launched power. Again, excellent beam quality was achieved at maximum output power with $M^2 < 1.1$. The slope efficiencies of both of these devices, particularly the latter, are expected to increase with higher pump powers which would bring the system further above threshold, allowing the laser mode to saturate gain in the beam wings. Ideally the losses of both systems would be minimised by improving the AR-coatings of the end-caps. Furthermore, achieving 1030nm suppression in the 975nm laser through the use of cavity mirrors would improve cavity design and lower intracavity losses.

The TGFR concept has displayed encouraging performance, with good agreement between the modelled and experimental data. This introduction is really only the beginning for these devices, and it confirms that this device generally operates as expected. More powerful pump sources can potentially improve the output power and efficiency. Q-switching experiments would be very interesting, as these devices have good energy storage potential owing to the large mode area. Furthermore, experiments exploring radially-polarised operation, combined with Q-switched operation, could have significant implications for materials processing.

References

1. S. Boehme, E. Beckert, R. Eberhardt, A. Tuennermann, "Laser splicing of end caps - process requirements in high power laser applications," Proc. SPIE **7202**, 720205 (2009).

2. A. D. McLachlan, F. P. Meyer, "Temperature dependence of the extinction coefficient of fused silica for CO_2 laser wavelengths," Appl. Opt. **26**, 1728 (1987).

3. T. Toyoda, M. Yabe, "The temperature dependence of the refractive indices of fused silica and crystal quartz," J. Phys. D: Appl. Phys. **16**, L97 (1983).

4. Private communication.

5. H. M. Pask, R. J. Carman, D. C. Hanna, A. C. Tropper, C. J. Mackechnie, P. R. Barber, J. M. Dawes, "Ytterbium-Doped Silica Fiber Lasers: Versatile Sources for the 1-1.2 µm Region," IEEE J. Sel. Topics Quantum Electron. **1**, 2 (1995).

Chapter 7 Radially Polarised Beam Amplification in a Thin-Slab

7.1   Chapter Overview

Thus far, we have been concerned with power scaling the fundamental Gaussian beam, owing to its desirable attributes. However, higher-order modes also offer some interesting benefits. In this chapter we explore a novel power scaling geometry for cylindrical vector (CV) beams. These unique beams have numerous applications, with high power operation being particularly relevant for materials processing. In this chapter we demonstrate that the polarisation purity of cylindrical CV beams can be maintained after amplification in a thin-slab, opening up a new route for power scaling these beams. We begin in section 7.2 by outlining our motivation to scale the output power of CV beams. Here, we highlight the numerous applications of CV beams, with particular attention paid to the benefits these beams offer for materials processing. We then describe various CV beam amplification techniques, and suggest the advantages of utilising the slab architecture. In section 7.3 we describe the operating principles of the radially polarised seed source constructed for the amplification experiments. This source consists of an Yb:YAG rod which exploits thermally-induced bi-focussing for direct generation of a radially polarised beam. Characterisation of the source will cover beam quality, polarisation purity and output power. Section 7.4 describes the Yb:YAG thin-slab amplifier used to amplify the seed beam, taking into account the important consequences of the Gouy phase shift, and how this must be managed to retain excellent radial polarisation purity. In section 7.5 amplification results will be presented, confirming the validity of this approach. Considerations for power scaling this configuration will be discussed in section 7.6, covering pump/signal overlap and a mitigation strategy for birefringence effects. Finally, section 7.7 will conclude the chapter.

7.2   Motivation

7.2.1   CV Beam Applications

CV beams have unique characteristics whereby the polarisation state across the beam cross-section is not uniform, as with linear or circularly polarised light, but in fact forms an axially symmetric distribution. Consequently, this leads to an intensity null at the beam centre owing to the polarisation discontinuity. Radially and azimuthally polarised beams form an interesting subset of CV beams, where the polarisation direction is orientated in the radial and tangential directions

respectively. Fig. 7.1 indicates several common polarisation states, where the white arrows indicate the direction of electric field oscillation.

Numerous applications for these exotic beams have been identified including particle acceleration [1] and particle trapping [2], which utilise the intense longitudinal electric field produced by a strongly focused radially polarised beam. A remarkable feature of radially polarised beams is their ability to be focused to smaller beam sizes than linearly polarised beams, leading to applications in high-resolution imaging [3]. Material processing, including cutting and drilling metal, is another area where these beams have attracted great interest. It has been shown that cutting efficiency can be 1.5-2 times higher using radial polarisation rather than circular polarisation [4], and drilling can be 1.5-4 times more efficient with azimuthal polarisation compared to linear and circular polarisation [5].
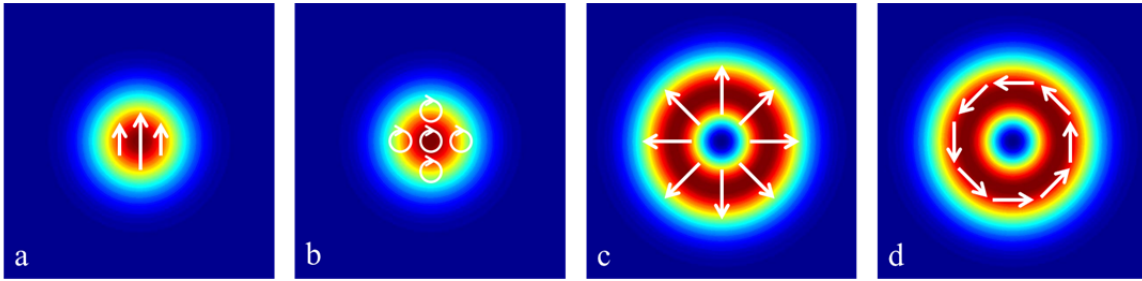
Figure 7.1: Vertically polarised Gaussian mode (a), circularly polarised Gaussian mode (b), radially polarised LG_{01} mode (c), and azimuthally polarised LG_{01} mode (d).

To understand the superior efficiency of CV beams within materials processing, it is helpful to consider an example. Here, we will explain the advantages of using a radially polarised beam for metal cutting. Fig. 7.2 shows a schematic of laser metal sheet cutting.
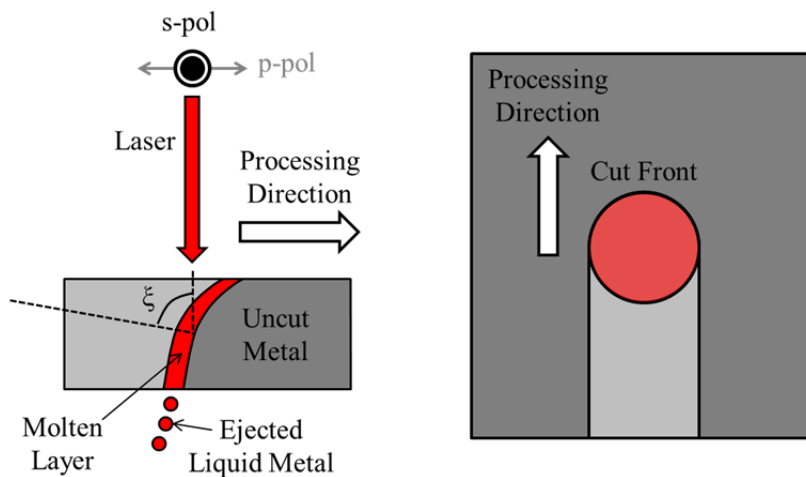
Figure 7.2: Schematic of laser cutting for side-view (left) and top-view (right).

The angle of incidence, ξ, which defines the angle between the incident beam and the surface normal, can approach 90° for this configuration [6]. The power of the incident laser beam is decomposed into a reflected and an absorbed component. The fraction of reflected power is a function of incident angle and polarisation state, and can be quantified by the Fresnel equations [6]:

$$R_S(\xi) \;=\; \left\| \frac{\cos \xi - \sqrt{n_m^2 - \sin^2 \xi}}{\cos \xi + \sqrt{n_m^2 - \sin^2 \xi}} \right\|^2$$

$$\text{(7.1)}$$

$$R_P(\xi) \;=\; \left\| \frac{n_m^2 \cos \xi - \sqrt{n_m^2 - \sin^2 \xi}}{n_m^2 \cos \xi + \sqrt{n_m^2 - \sin^2 \xi}} \right\|^2$$

where R_s and R_p represent that fraction of power reflected for s and p-polarisation states respectively, n_m is the refractive index of the material, and it has been assumed that the laser beam travels to the material in a medium with a refractive index of unity i.e. a vacuum. The refractive index of a metal consists of a real and an imaginary component, i.e. $n_m = n + i\chi$. The familiar real component, n, describes the phase velocity, v_p, of light within the material via $v_p = c/n$. The imaginary component, χ, known as the extinction coefficient, accounts for attenuation in the material, and defines an absorption depth, d_{abs}, at a wavelength λ of $d_{abs} = \lambda/4\pi\chi$. For metals, $\chi > 1$ for typical incident wavelengths, and therefore the absorption depth is on the sub-wavelength scale. Fig. 7.3 (left) displays the fraction of absorbed power for both polarisation states as a function of incident angle for aluminium at a wavelength of $1\mu m$, with $n_m = 1.5192 + 9.2643i$ [7]. Also shown in fig 7.3 (right) is the ratio of the absorbed powers, which clearly depicts the much stronger absorption of p-polarised radiation, especially at large angles such as those present in the metal cutting process.
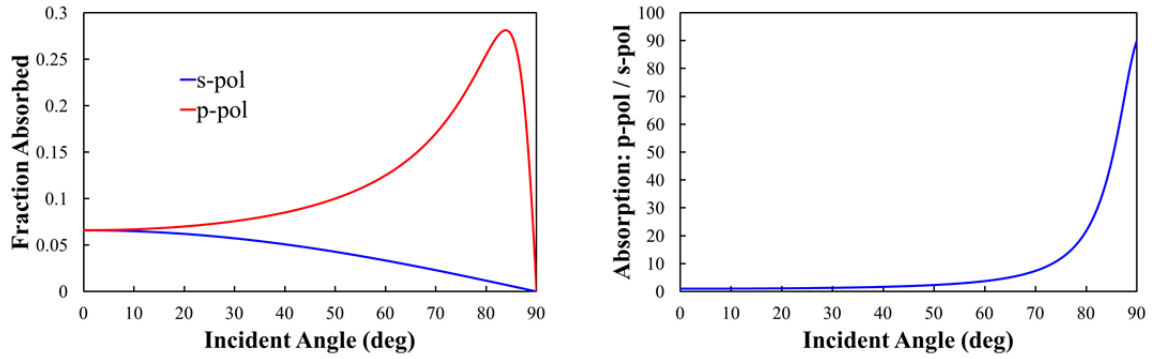
Figure 7.3: Absorption of s and p-polarisations in aluminium as a function of angle (left), and ratio of absorbed power i.e. p-polarisation/s-polarisation.

Figure 7.3 highlights a major limitation of using linearly polarised radiation for metal cutting, namely that the absorption efficiency within the metal will vary over the circumference of the laser beam. As shown in fig 7.4 (left), a linear polarised beam can achieve maximal absorption at a single point on the circumference of the cut i.e. the cut front, but experiences a decreasing absorption away from this point. Circularly polarised radiation bypasses this issue, and presents a time-average of the s and p-polarisation states, achieving equal absorption at each point on the cut circumference. However the fraction of absorbed power is between the maximum for p-polarisation and the minimum for s-polarisation. Radial polarisation not only achieves equal absorption at each

point on the cut circumference, it also achieves maximum absorption at each point, since it always presents a *p*-polarisation state with respect to the metal, as shown in fig. 7.4 (right). Furthermore, this excellent property is maintained regardless of processing direction. An additional advantage of processing materials with CV beam arises from the doughnut-shaped intensity profile of the radially and azimuthally polarised LG_{01} modes. This results in a steeper intensity gradient compared to the fundamental Gaussian beam, leading to a profile which is closer to the desired flattop distribution.
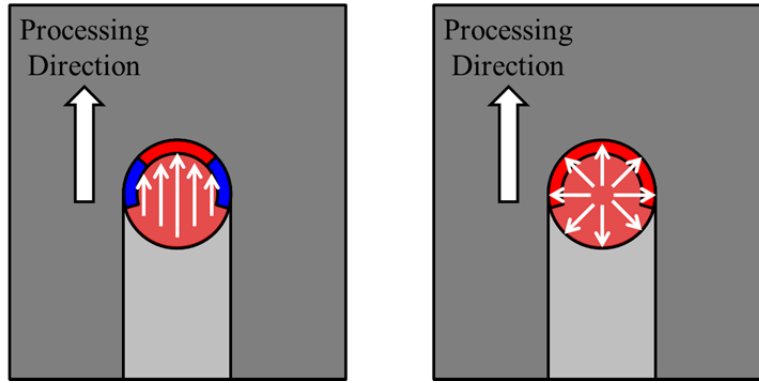
Figure 7.4: Metal cutting with a linearly polarised beam (left) and a radially polarised beam (right). The red/blue regions indicate high/low power absorption.

7.2.2   CV Beam Amplification

To realise their potential within material processing and other applications, CV beams must be produced with sufficient power. Therefore a system that produces CV beams amplified to a high power level is desirable. Various architectures have been employed for CV beam amplification, including thin-disc [8], fiber [9, 10], single crystal fiber [11] and rod [12]. It is critically important to avoid depolarisation effects during amplification. This is achieved in the thin-disc configuration by geometry, which minimises thermally-induced bifocusing with a predominantly one-dimensional longitudinal heat-flow. The axial symmetry of the other architectures ensures the birefringence axes are orientated in the radial and tangential direction, resulting in different focal lengths for radial and azimuthal polarised beams when thermally-stressed. Furthermore, a pure radial/azimuthal polarisation state will not experience depolarisation loss.

However, CV beam amplification in a slab architecture, which lacks axial symmetry, has not been investigated. The slab design, as shown in fig. 7.5, is utilised in high power systems and provides cooling across the large surfaces, which are in close proximity to the pumped region. Thus under pumping, an essentially one-dimensional heat gradient is established in the direction of heat extraction, leading to a cylindrical thermal lens and perpendicular birefringence axes in the *x* and *y* direction. Therefore, one can avoid depolarisation loss for a linearly polarised beam by ensuring the polarisation state is parallel to the one of the birefringence axes, i.e. polarised along the *x* or *y* axis. Furthermore, the high aspect ratio of the slab results in a superior thermally-induced stress fracture

limit when compared to the rod design. Temperature gradients generated in the laser material result in stresses which can lead to material fracture. Equation 7.2 compares the maximum permissible heat power per unit length, $P_{H/L}$, for the slab and the rod architecture [13]:

$$\frac{(P_{H/L})_{rod}}{(P_{H/L})_{slab}} = \frac{2\pi}{3}\left(\frac{t_s}{\omega_s}\right) \tag{7.2}$$

where t_s is the slab thickness and ω_s is the slab width. Thus for an aspect ratio of $\omega_s/t_s > 2.1$ the slab will withstand a higher pump power per unit length than the rod architecture. These benefits have allowed slab amplifiers to produce 400W of nearly diffraction limited output power [14], and 1.1kW of multimode output power [15].
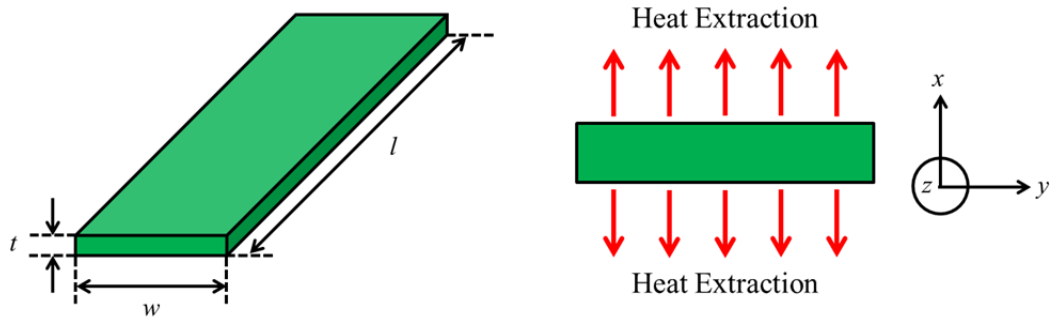
Figure 7.5: Slab concept.

The slab concept offers an interesting route for power scaling CV beams to high average powers. Firstly, the superior power handling ability as displayed in equation 7.2 will allow higher pump powers, and ultimately a higher output power, compared to the rod design. As a bulk architecture, the beam will propagate as a free-space mode, and therefore deleterious mode-coupling issues associated with CV beams in fiber architectures can be negated. Additionally, amplification in a slab is simpler than in a thin-disc, which due to the very short interaction length requires a complex multi-pass arrangement to achieve an appreciable gain. Birefringence may cause concern at high power levels, and act to reduce the purity of a radially or azimuthally polarised beam. However, with effective heat-sinking this effect can be minimised. Furthermore, a technique to compensate for potential depolarisation at high pump powers will be discussed in section 7.6.2.

7.3   Radially Polarised Seed Source

In order to conduct this investigation, we require a radially polarised seed source. This section briefly highlights several common techniques for producing a radially polarised output. It then discusses how the desired LG_{01} mode is targeted and explains the thermally-induced bifocusing technique employed to achieve radial polarisation. Finally, the performance of the laser is characterised, particularly in terms of radial polarisation purity.

7.3.1   Generating Radial Polarisation

Various methods of producing CV beams have been implemented over the decades. CV beam generation can be broadly divided into two distinct categories; intracavity and extracavity techniques. Intracavity techniques rely on a cavity design that ensures one polarisation, i.e. radial or azimuthal, is dominant over the other and is therefore emitted from the laser directly. One popular approach is to exploit thermally-induced bi-focusing in host materials such as YAG to render the resonator unstable for one polarisation, or yield a lower threshold for one polarisation by virtue of having a more favourable spatial overlap with the inversion distribution [16]. Alternatively, intracavity elements to provide polarisation discrimination, such as calcite crystals [17], Brewster-angled axicons [18], conical Brewster prisms [19], grating mirrors [20], or nanograting waveplates [21] can be employed. Extracavity techniques typically convert more traditional polarisation states, such as linear or circular polarisation, into radial or azimuthal polarisation. This can be achieved interferometrically, through the combination of orthogonal linearly-polarised HG_{10} and HG_{01} beams [22]. Alternatively, a spatially-variable retardation plate can be used to convert linear polarisation to radial or azimuthal polarisation [23].

7.3.2 LG_{01} Mode Operation

We desire a radially polarised seed source operating on the LG_{01} mode. These are two separate requirements, since a beam may operate on the LG_{01} mode and not be radially polarised, whilst a beam may be radially polarised and operate on some higher-order mode. This section will briefly explain the principle behind LG_{01} mode selection, whilst the next section will describe how we can achieve a radial polarisation state for this mode.

The normalised intensity profile as a function of radial distance from the beam centre, r, of an LG_{0n} mode can be described by [24]:

$$I(r) \; = \; \frac{1}{n!}\left(\frac{2r^2}{w^2}\right)^n \exp\left(\frac{2r^2}{w^2}\right) \qquad\qquad (7.3)$$

where w is the beam radius for the lowest-order Gaussian mode. The intensity profiles of the first three LG_{0n} modes are shown in fig. 7.6. The LG_{00} mode corresponds to the familiar fundamental Gaussian mode, whilst the higher-order LG_{0n} modes exhibit a doughnut-shaped intensity distribution.

In order to obtain operation on a particular LG_{0n} mode, the threshold for this mode must be lower than the threshold for all other modes. To achieve this, the inversion profile within the laser gain medium can be shaped in order to achieve the best spatial overlap with the desired mode. The obvious choice for all modes with $n \neq 0$ is to use a ring-shaped pumped beam. All else being equal, the mode with the best spatial overlap with the pump beam will reach threshold first and become

the dominant mode in the cavity. One can thus tailor the pump beam to achieve a preferential overlap with the desired mode.

Furthermore, we can consider the impact of the pump beam parameters for mode excitation. We will denote the inner pump beam radius as r_i and the outer radius as r_o, and can assume these values and w remain constant over the length of the laser gain medium. Clearly, as the ratio r_i/r_o tends to zero, the pump beam profile tends to a top-hat, which is undesirable when exciting a doughnut-shaped beam. Additionally, the ratio r_o/w is important, with a smaller ratio favouring lower-order modes. This concept is shown schematically in fig. 7.6 for a ratio $r_i/r_o = 0.5$, where it can be seen that the larger ratio of r_o/w favours the LG_{01} mode, whilst the smaller ratio of r_o/w favours LG_{00} mode.
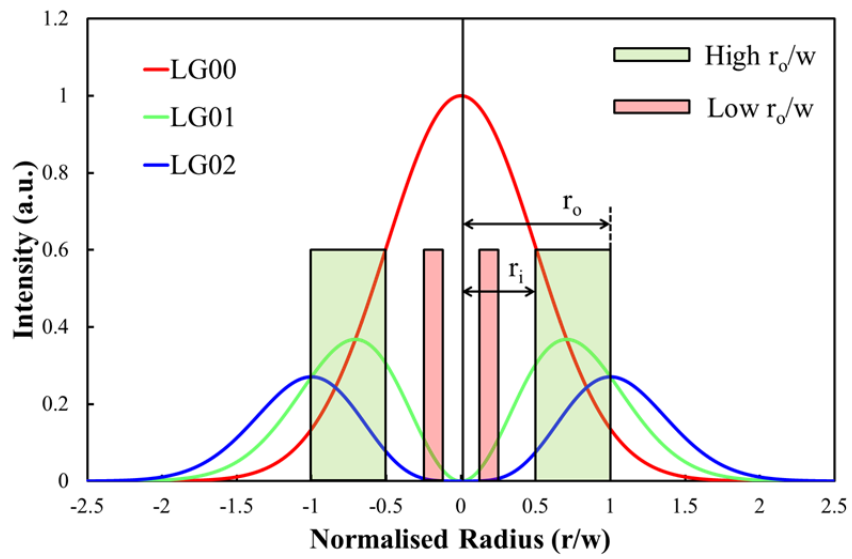
Figure 7.6: Intensity distribution of LG_{00}, LG_{01} and LG_{02} modes and ring-shaped pump beams.

An experiment was designed to investigate the concept of preferential excitation of LG_{0n} modes, as shown in fig. 7.7. The laser gain medium used was an Yb:YAG rod, measuring 2mm in diameter and 3mm in length, which was mounted in a water-cooled copper heat-sink. The end-faces of the rod were AR-coated at the pump and intended signal wavelength, i.e. 969nm and 1030nm respectively. Pump radiation was provided by a fiber-coupled diode, with a core and cladding diameter of 105μm and 125μm respectively. The output from this fiber was re-shaped to yield an annular near-field beam profile with the aid of a capillary fibre with an inner-hole diameter of 100μm and an outer pump guide diameter of 200μm. The end section of this fibre was tapered to a solid-glass structure of 125μm diameter to allow splicing to the pump delivery fibre with < 1% transmission loss. The output beam from the capillary fibre was relay-imaged using a simple telescope with a magnification factor of ~1.88 to yield a near-field annular pump intensity profile and hence inversion profile in the Yb:YAG rod with $r_o \approx 188$μm and $r_i \approx 94$μm. The pump intensity profile and computed LG_{01} intensity profile are shown in fig. 7.8.
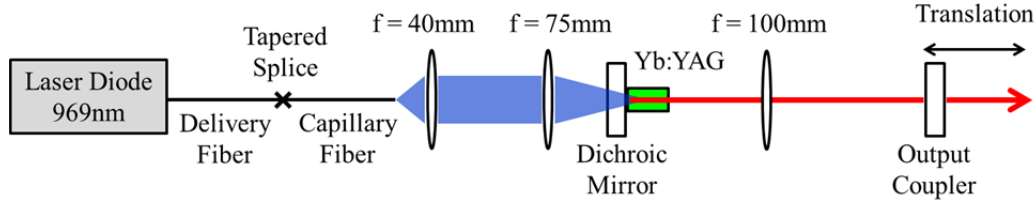
Figure 7.7: Investigation of LG0n mode selection.
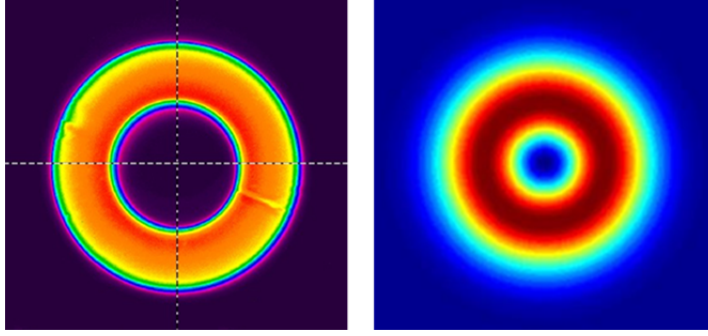
Figure 7.8: Measured pump intensity profile (left) and computed LG_{01} mode intensity profile (right).

A laser cavity was formed comprising of a plane pump input mirror with high reflectivity (R > 99.8%) at 1030nm and high transmission (T > 95%) at 969nm, an intracavity lens with a focal length of 100mm AR-coated at 1030nm, and a plane output coupler with 5% transmission at 1030nm. Hence the stability of the resonator was defined by the intracavity lens. The Yb:YAG rod was positioned in close proximity to the pump input mirror (approximately 2mm away), and the lens was positioned 110mm from the pump input mirror. The output coupler position was varied from 110mm – 170mm away from the intracavity lens. As the output coupler transitioned away from the lens, the calculated beam size for the fundamental mode in the Yb:YAG rod systematically decreased, which is equivalent to increasing the ratio of r_o/w. Therefore we would expect that as the output coupler transitioned away from the intracavity lens, we would excite higher-order modes. Fig. 7.9 shows the mode profile excited across a range of output coupler positions, and shows a clear increase in mode order as the estimated beam size of the fundamental mode in the crystal decreases, confirming our hypothesis. Note that this experiment was performed close to lasing threshold at approximately 10W/2W of launched/absorbed pump power. The generated beams were unpolarised, since the bifocusing effect, as explained in the next section, was not strong enough to allow discrimination between the radial and azimuthal polarisation states.

| LG_{00} | LG_{01} | LG_{02} | LG_{03} | LG_{04} |
| $r_o/w = 0.99$ | $r_o/w = 1.07$ | $r_o/w = 1.12$ | $r_o/w = 1.18$ | $r_o/w = 1.31$ |
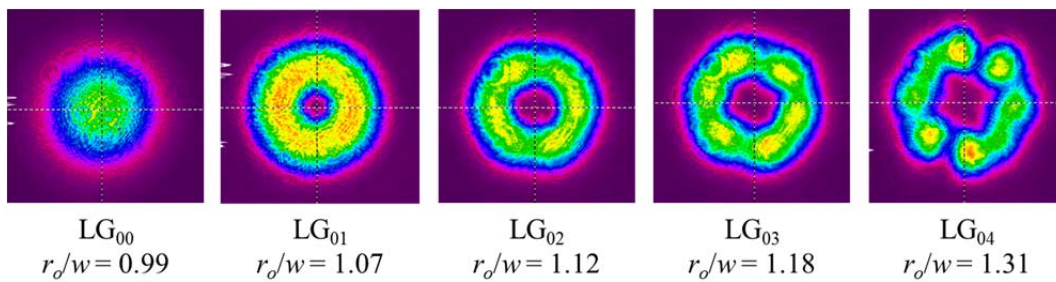
Figure 7.9: Generated LG_{0n} modes with estimated r_o/w ratio.

7.3.3 Thermally-Induced Bifocusing

A radially polarised output was obtained using thermally-induced bifocusing, which provides discrimination via different thermal lens focal lengths for the radially and azimuthally polarised beams. This simple approach does not require bespoke intracavity elements, and does not suffer from complicated extracavity conversion techniques which can result in significant power loss.

Thermally-induced birefringence was employed to achieve the bi-focusing effect. Yb:YAG is a cubic crystal and is not naturally birefringent, and thus possesses a spherical indicatrix, indicating that the refractive index is invariant to polarisation direction. When the crystal is pumped it heats up, predominantly due to quantum defect heating, resulting in a temperature gradient across the rod cross-section which can be approximated as entirely radial. This gradient establishes mechanical stresses in the radial and tangential directions (fig 7.10 (left)), due to cooler outer regions of the rod preventing the thermal expansion of hotter central regions. Since Yb:YAG has three independent elasto-optic coefficients, the indicatrix transforms into an ellipsoid due to the thermally-induced stresses [13]. Furthermore, the refractive index for light polarised in the radial direction, n_{rad}, is no longer equal to the refractive index for light polarised in the tangential direction, n_{az}.

Consider a beam polarised in the x-direction, given by $\underline{E}$, incident on the laser rod. At each point over the cross-section $\underline{E}$ can be decomposed into a radial and tangential component, as shown in fig 7.10 (right) for a point P which makes an angle ϑ with the x-axis. Since $n_{rad} \neq n_{az}$, a phase delay is established between the two components, resulting in a rotation of the polarisation state. This polarisation rotation will occur for all points over the beam cross-section, with the exception of points situated on the x and y-axis of the rod, which will solely experience n_{rad} and n_{az} respectively.

A simple experiment based on this principle was conducted to determine if the birefringence axes in the Yb:YAG rod would align with the radial and tangential directions when pumped with an annular intensity distribution. The set-up for this experiment (fig 7.11) consisted of the Yb:YAG rod positioned between a pair of crossed polarisers. A collimated HeNe beam, with a beam radius of 500μm, was directed through the polariser-Yb:YAG arrangement, and imaged onto a camera. The first polariser is orientated to allow transmission of light polarised in the y-direction, whilst the second is orientated in the x-direction. In the absence of pumping, the HeNe beam was completely extinguished by the second polariser, since no polarisation rotation occurred. Pump radiation was focused through the Yb:YAG rod in a counter-propagating configuration, forming an annular beam waist in the crystal with $r_o = 250$μm and $r_i = 125$μm. As predicted, polarisation rotation occurred under pumping, leading to the intensity profile shown in fig. 7.11 at a launched/absorbed pump power of 10W/2W. The intensity profile confirms the birefringence axes form in the radial and tangential directions, owing to the clear Maltese cross structure. The dark cross is aligned with the x and y axis indicating no rotation at these points, whilst intensity maxima occur in each quadrant at

45° to the axes, i.e. when the polarisation is decomposed equally between the radial and tangential direction. A slight distortion is observed on the lower two quadrants of the intensity profile, which is believed to be due to damage spots on the AR coating on the Yb:YAG rod. Owing to the difference in elasto-optic coefficient between the radial and tangential direction, it can be concluded that the refractive index profile will vary differently as a function of temperature in these directions, resulting in bi-focusing, i.e. a different thermal lens focal length for a radially and azimuthally polarised beam.
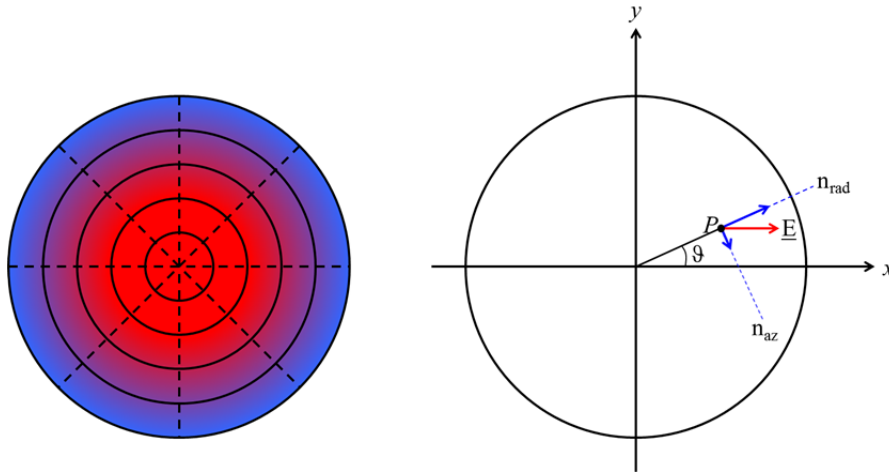
Figure 7.10: Radial (dashed) and tangential (solid) stress distribution across rod cross-section (left), radial and tangential components of an *x*-polarised beam at point P on the rod cross-section (right).
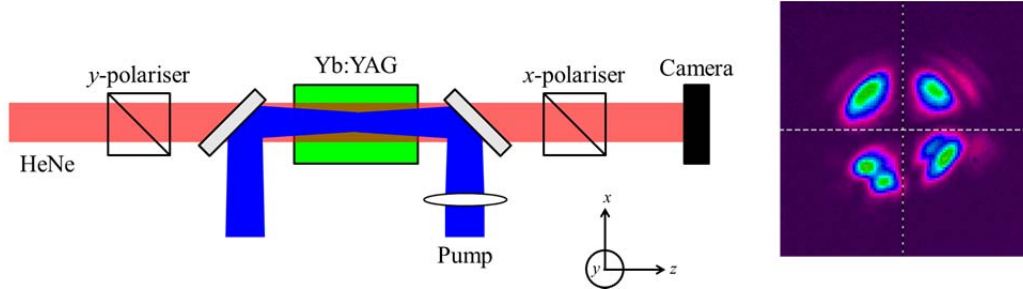
Figure 7.11: Experimental configuration used to investigate thermally-induced birefringence (left) and output intensity profile at 10W/2W of launched/absorbed pump power (right).

7.3.4   Seed Laser Configuration

The bi-focusing effect can be combined with the targeted LG_{0n} operation (section 7.3.2) to obtain a radially polarised LG_{01} beam. Appropriate cavity design can create a situation where the beam sizes of the radially and azimuthally polarised mode within the Yb:YAG rod are different. By matching the pump mode to one of these laser modes the polarisation with the best spatial overlap will reach threshold first and dominate over the other polarisation through gain saturation. A plane-plane cavity was chosen, since stability is provided by the induced thermal lens, rather than an intracavity lens or curved mirror, and thus a stronger discrimination between the radial and azimuthal polarisation states should ensue. Careful tailoring of the cavity length can create a situation where

there is sufficient difference in cavity mode size to produce an LG_{01} mode with a high degree of polarisation purity for either the radial or azimuthal polarisation state.

The cavity configuration for the seed laser is shown in fig 7.12. As in section 7.3.2 the resonator comprised of a plane pump input mirror with high reflectivity (R > 99.8%) at 1030nm and high transmission (T > 95%) at 969nm, and a plane output coupler with 5% transmission at 1030nm. To achieve radial polarised operation, the pump diode was operated near maximum power to allow a strong bifocusing effect and achieve a high output power. The laser was initially aligned with the mirrors as close as possible, resulting in a small beam size for the fundamental mode in the Yb:YAG rod and thus a high r_o/w ratio, leading to high-order LG_{0n} operation. The output coupler was then translated away from the Yb:YAG rod, resulting in an increase in of the fundamental mode size in the Yb:YAG crystal. The output coupler was away until moved until LG_{01} operation was achieved, after which very careful length adjustments and mirror alignments allowed the bi-focusing effect to result in preferential lasing on the radially polarised LG_{01} mode due to a more favourable spatial overlap with the inversion distribution compared to the azimuthally polarised mode.
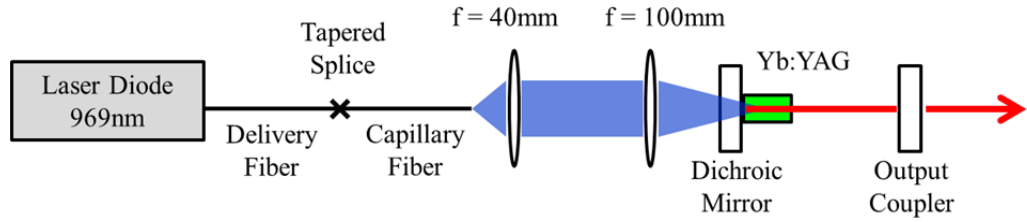
Figure 7.12: Schematic of the radially polarised seed source.

7.3.5   Seed Laser Characterisation

A radially polarised LG_{01} mode was achieved for a cavity length of 57 mm, with the Yb:YAG rod pump input face positioned approximately 2mm from the pump input mirror. A maximum power of 6.9W was obtained for 17W of absorbed power, corresponding to a conversion efficiency of 41%. Radial polarisation was maintained from 6W → 6.9W of output power, and for a change in cavity length of approximately ±2.5mm around 57mm. The intensity profile at maximum power, shown in fig. 7.13, confirms that a high quality doughnut beam was produced. Also shown in fig. 7.13 are the intensity profiles of the beam after passing through a linear polariser orientated at the angles depicted by the arrows. The clean two-lobed structure indicates excellent radial polarisation purity. The beam propagation factor was measured, giving a value of $M^2 = 2.3$ in both the x and the y-direction, which is in close agreement with the theoretical value of 2. Fig 7.14 shows the measured beam quality in the x-direction.

The intensity of the two-lobed profiles after transmission through a linear polariser was measured along a circular path of radius r from the beam centre, where r is selected to maximise the intensity. A given point on the circle can be described by an azimuthal angle, θ, ranging from $0°-360°$, as shown in fig. 7.13. The angle of the polariser is defined by θ_p. For a perfect radially polarised beam one would expect the intensity at each radial and azimuthal position, $I(r, \theta)$, to adhere to the following relation:

$$I(r,\theta) \;=\; I(r)\cos^2(\theta - \theta_p)$$

(7.4)

The measured data for a single polariser orientation, $\theta_p = 90°$, is shown in fig. 7.15, alongside the modelled intensity from equation 7.4 which describes a beam with perfect polarisation purity. To determine the radial polarisation extinction ratio (RPER) the intensity at the predicted maxima i.e. $\theta = 90°$ and $\theta = 270°$, is averaged and divided by the averaged intensity at the predicted minima i.e. $\theta = 0°$ and $\theta = 180°$, to yield an extinction ratio. The final RPER is the average of this extinction ratio over four arbitrarily chosen polariser orientations: $\theta_p = 0°$, $45°$, $90°$ and $135°$. The RPER of the source was > 15dB, confirming a high degree of radial polarisation purity.
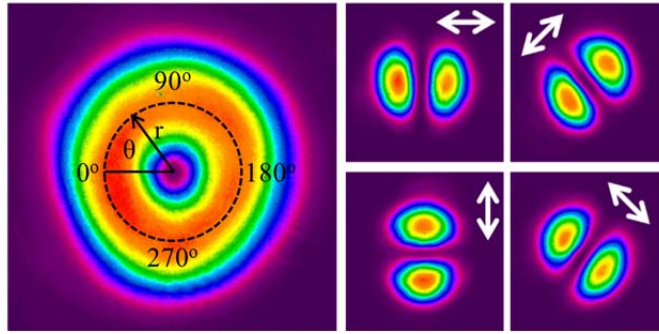

Figure 7.13: Intensity profile of generated radially polarised LG_{01} mode (left) and intensity profiles after the beam has passed through a polariser orientated at the angles indicated by the arrows (right).
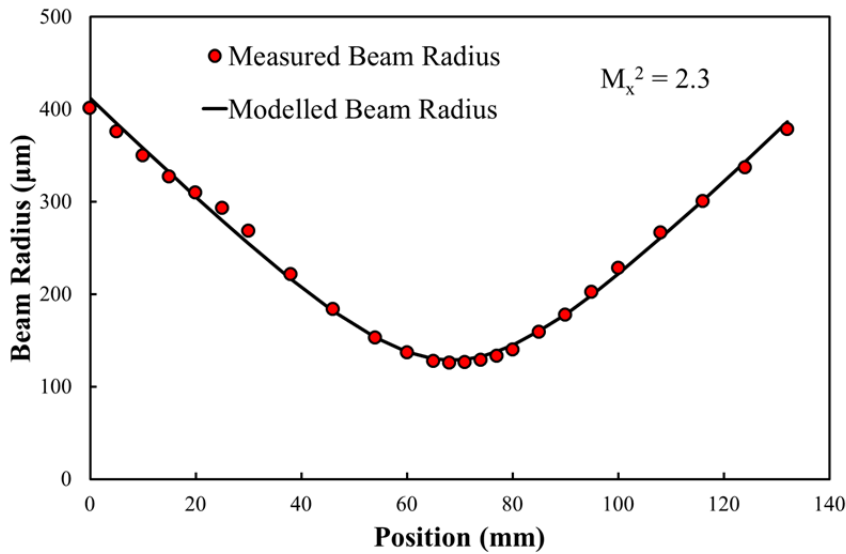

Figure 7.14: Beam quality of the radially polarised beam.
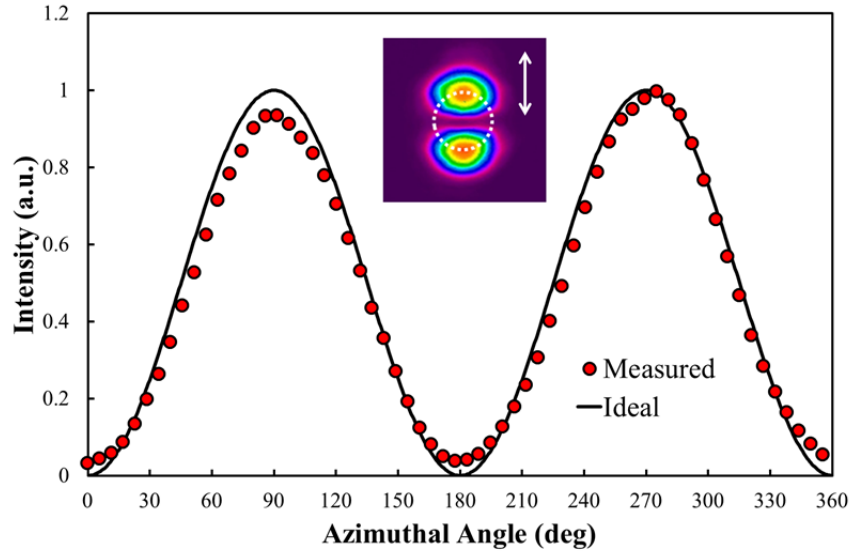
Figure 7.15: Measured and ideal intensity profile as a function of azimuthal angle for the radially polarised beam after it has passed through a linear polariser orientated in the direction of the arrow.

7.4   Amplifier Configuration

7.4.1   Slab Amplifier Configuration

The set-up used for amplification of the radially polarised seed beam is shown in fig. 7.16. The gain medium was an Yb:YAG slab with transverse dimensions 1mm × 5mm by 5mm long and 5 at. % Yb^{3+} doping concentration. The slab was mounted in a copper heat-sink arranged to provide conduction cooling of the 5mm × 5mm faces, and hence heat flows predominantly in the x-direction. The end faces were AR-coated at the pump and seed wavelengths. Pump light at 940nm was provided by a 50W diode-bar collimated in the fast direction (x) by a cylindrical microlens and in the slow direction (y) by a cylindrical microlens array. The resulting beam was focussed into the slab with the aid of an AR coated spherical lens of focal length 50mm to yield a rectangular inversion region with approximate waist transverse dimensions of 1mm (y direction) × 85μm (x direction), and hence an aspect ratio of ~12:1. Over 90% of the pump radiation was absorbed in a single-pass. The radially polarised seed source was directed into the Yb:YAG at a small angle of incidence (~3°) whilst being focused in the x direction with an AR coated cylindrical lens of focal length 50mm. This arrangement yielded a seed beam profile that was approximately spatially matched to the inversion distribution, with beam dimensions of ~55μm (x-direction) and ~700μm (y-direction) in the slab. After a first pass through the slab the seed beam was reflected by a plane dichroic mirror with high reflectivity (>99.8%) at 1030nm and high transmission at 940nm. Thus the beam made a second pass through the slab, with the exiting beam re-collimated in the x-direction by the cylindrical lens before being re-directed to the beam diagnostics.

135

Figure 7.16: Yb:YAG slab amplifier arrangement.

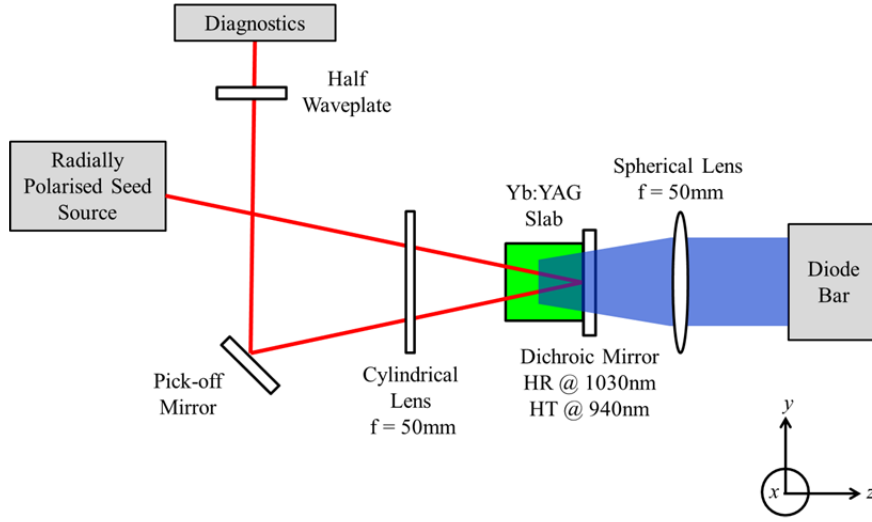## 7.4.2 Gouy Phase Shift

The amplification set-up involves astigmatic focusing and subsequent re-collimation of the amplified beam with the cylindrical lens. This has a very detrimental impact on the polarisation purity due to the different Gouy phase shifts of the constituent HG modes. The radially polarised LG_{01} seed beam can be considered as a coherent superposition of an x-polarised HG_{10} mode and a y-polarised HG_{01} mode, as shown in the theoretical computation in fig. 7.17 (left). In general, the Gouy phase, Ψ_G, for each HG_{nm} component in the astigmatic region evolves according to [25]:

$$\Psi_G = 2\left[\left(n + \frac{1}{2}\right)\arctan\left(\frac{l_{eff}}{z_{Rx}}\right) + \left(m + \frac{1}{2}\right)\arctan\left(\frac{l_{eff}}{z_{Ry}}\right)\right] \tag{7.5}$$

where l_{eff} is the effective path length between the focusing and re-collimating cylindrical lens. In this scenario $l_{eff} = 2f$, where f is the focal length of the cylindrical lens, and z_{Rx} and z_{Ry} are the corresponding Rayleigh ranges in the x and y-directions respectively. This assumes that the beam is non-astigmatic in the regions before focusing and after re-collimation. Therefore, through the astigmatic region the phase of each HG_{nm} mode evolves differently. Once the beam has been re-collimated and enters the non-astigmatic region, the Gouy phase of each HG_{nm} mode will evolve identically, thus any phase difference that occurred during passage through the astigmatic region will be maintained. As the beam is focused in the x-direction, z_{Rx} is significantly smaller than z_{Ry} in the astigmatic region. Consequently, in this set-up, it can be assumed that $2f \gg z_{Rx}$ and $2f \ll z_{Ry}$ ($2f = 100$mm, $z_{Rx} \approx 4$mm, $z_{Ry} \approx 650$mm). Hence, in equation 7.5, the inverse tangent of the first term tends to $\pi/2$ whilst the inverse tangent of the second term tends to 0. One can subsequently deduce that the Gouy phase of the HG_{10} mode will evolve by $3\pi/2$, whilst the Gouy phase of the HG_{01} mode will evolve by $\pi/2$ in the astigmatic region. Consequently, a net π phase shift is established between the orthogonally-polarised HG_{10} and HG_{01} modes. The amplified output beam (i.e. after re-collimation) is the superposition of these modes and the resultant polarisation is a hybrid radial-azimuthal polarisation distribution (fig. 7.17 (right)). To recover a pure radially polarised beam a

half-waveplate with its fast axis orientated in the *x* or *y*-direction is incorporated into the output arm of the amplifier configuration after re-collimation. This creates a further π phase shift between the HG_{10} and HG_{01} modes, hence compensating for the Gouy phase shift introduced during passage through the astigmatic region, yielding a radially polarised output beam.
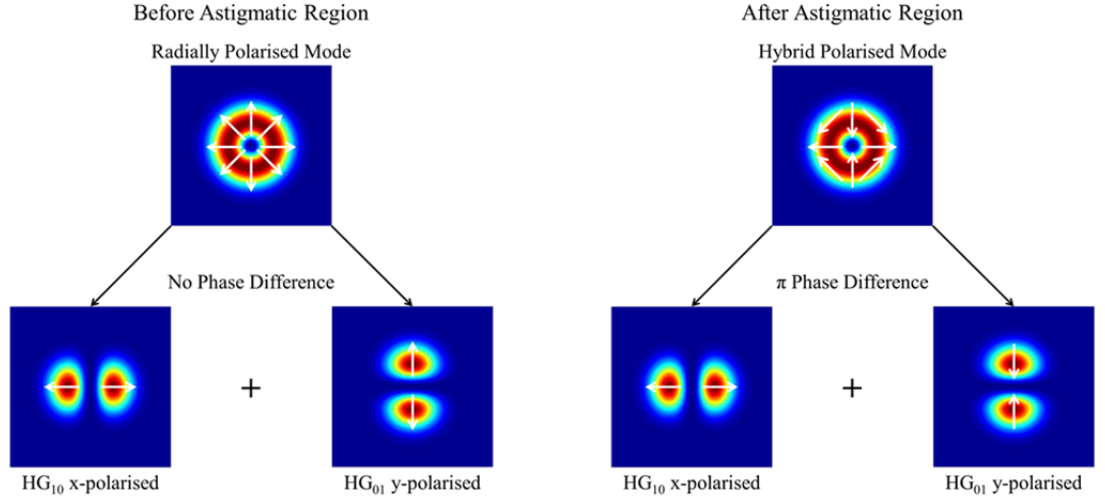
Figure 7.17: Computation of radially polarised input (left) and hybrid output mode (right).

7.5 Amplifier Characterisation

7.5.1 Gain

Fig. 7.18 shows the measured gain as a function of pump power for the arrangement shown in fig. 7.16. Amplifier gain was measured for a range of input seed powers which were varied external to the Yb:YAG seed laser with the aid of appropriate partially reflective dielectric mirrors in order to preserve the seed beam characteristics. As the seed power launched into the amplifier increases the gain decreases, as expected due to gain saturation.
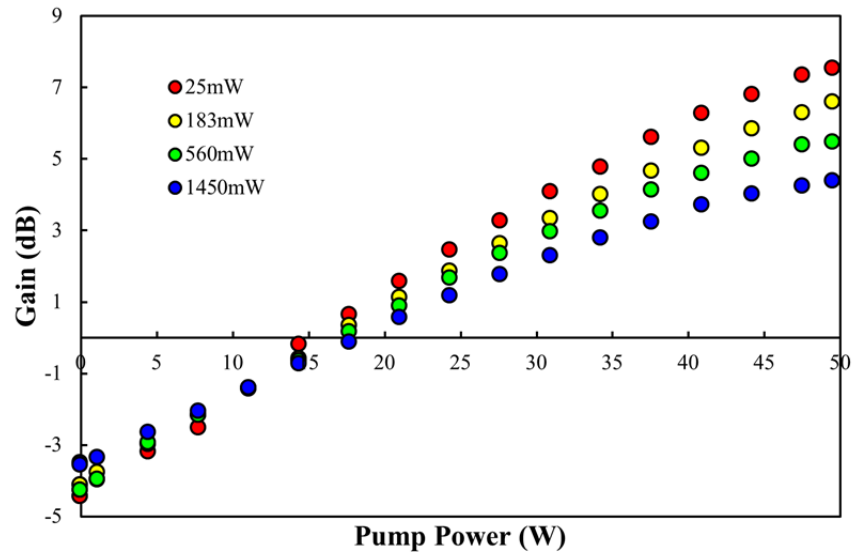
Figure 7.18: Measured amplifier gain for various seed powers as a function of pump power.

The launched pump power required to reach transparency, P_T, for each seed power was interpreted from the data presented in fig. 7.18 and is shown in table 7.1. One can predict the power necessary to reach transparency for a top-hat pump beam, by initially considering equation 2.20, which states the inversion density required to achieve transparency, n_{2_Tr}. Furthermore, the number of absorbed pump photons per unit volume necessary to achieve this inversion at a given point in time, ϕ_{Tr}, is simply:

$$\phi_{Tr} = \frac{n_{2T}}{\eta_{QE}} \qquad (7.6)$$

The population of n_2 decays exponentially, on a timescale dictated by the upper-state lifetime, as described by:

$$n_2(t) = n_2(t = 0) \exp\left(-\frac{t}{\tau_f}\right) \qquad (7.7)$$

Differentiating equation 7.7 with respect to time, and evaluating the solution in the limit of $t \to 0$, results in:

$$\frac{dn_2}{dt} = -\frac{n_2(t = 0)}{\tau_f} \qquad (7.8)$$

Utilising equation 7.8, one can derive the total number of photons required per unit time to maintain transparency, Ω, given by:

$$\Omega = \frac{\phi_{Tr}}{\tau} V \qquad (7.9)$$

where V is the volume of the pumped region given by the pump beam area A_P multiplied by the length of the gain medium, l. Since power is simply energy per unit time, we can write the required launched pump power to reach transparency, P_T, as:

$$P_T = \frac{\Omega h \nu_p}{\eta_{abs}} \qquad (7.10)$$

where $\eta_{abs} = 1 - \exp(-\sigma_{pa}(\nu_p)n_T l)$ in the regime where the pump power is well below the saturation pump power, which is applicable to this scenario. We can evaluate equation 7.10 for the slab amplifier, with the Yb:YAG parameters given by $n_T = 6.9 \times 10^{26} \text{m}^{-3}$, $\sigma_{sa} = 0.12 \times 10^{-24} \text{m}^2$ at 1030nm, $\sigma_{se} = 2.2 \times 10^{-24} \text{m}^2$ at 1030nm, $\sigma_{pa} = 0.75 \times 10^{-24} \text{m}^2$ at 940nm, $\tau_f = 950 \mu s$ [26], QE ≈ 0.9 [27], and the configuration parameters given by $A_P = 3.4 \times 10^{-7} \text{m}^2$ and $l = 5 \times 10^{-3} \text{m}$. This results in a value of $P_T = 16.2$W, which is excellent agreement with the measured transparency values presented in table 7.1.

One would expect the transparency power to be independent of seed input power, and therefore the gain of each seed should cross through the same point. However, in table 7.1 we notice a slight discrepancy between the transparency pump powers, with a range of 2.5W. However, in the region between 11W $\to$ 14.5W of launched pump power we observe very close agreement between the

gain values of each seed beam, spanning a range from -1.4dB → -0.5dB. This observation can be explained by considering that the internal losses due to imperfect AR/HR coatings on the lenses and mirrors respectively, and scattering within the bulk material of the system are not accounted for in the gain values. Furthermore, this range from -1.4dB → -0.5dB can be considered as representing the internal losses of the system.

Also shown in table 7.1 is the maximum gain value, g_{MAX}, and output power, P_{MAX}, achieved at the maximum diode pump power of 50W for each input seed. For a 25mW input seed power a maximum gain of 7.5dB was achieved, resulting in an output power of 140mW. The gain decreased to 4.4dB for a maximum input seed power of 1.45W, corresponding to a maximum amplified output power of approximately 4W, with an extraction efficiency of 5.7%. The limited extraction efficiency will be addressed in section 7.6.1.

Input Power (W)	P_T (W)	g_{MAX} (dB)	P_{MAX} (W)
0.025	15.2	7.5	0.14
0.18	16.2	6.6	0.84
0.56	16.2	5.8	2.11
1.45	17.7	4.4	3.99

Table 7.1: Amplification results.

7.5.2 Radial Polarisation Purity

Crucially, the beam quality and polarisation purity were maintained for the amplified output beam over the full range of pump and seed powers available, despite the highly asymmetric nature of the gain region and associated thermal effects. Fig. 7.19 shows the intensity profile of the amplified beam at the maximum gain level for the lowest (top) and highest (bottom) seed power, along with the corresponding intensity profiles after the beam had passed through a linear polariser orientated at the angles depicted by the white arrows. One can clearly see that the beam intensity profile is preserved along with the high degree of radial polarisation purity. It is worth noting that without the half-waveplate providing the necessary compensation, the computed hybrid mode in fig. 7.17 was produced. In terms of the beam intensity profile of this hybrid mode, the horizontal and vertical lobes (i.e. a. and c. in fig. 7.19) remained unchanged, whilst the diagonal profiles (i.e. b. and d.) were exchanged. Beam quality measurements show that the beam propagation factor was $M^2 = 2.3$ for the lowest seed input power, i.e. no degradation, and $M^2 = 2.4$ for the highest seed input power, i.e. a very slight degradation. Fig. 7.20 shows the measured beam quality in the x-direction for the lowest seed input power at the maximum gain level. An example of a RPER plot is

shown in fig. 7.21 for a single polariser orientation, $\theta_p = 0^o$, at the maximum gain level for the lowest seed input power. The measured intensity agrees well with the ideal scenario, and the RPER was maintained at > 15dB for the lowest and the highest seed input powers.
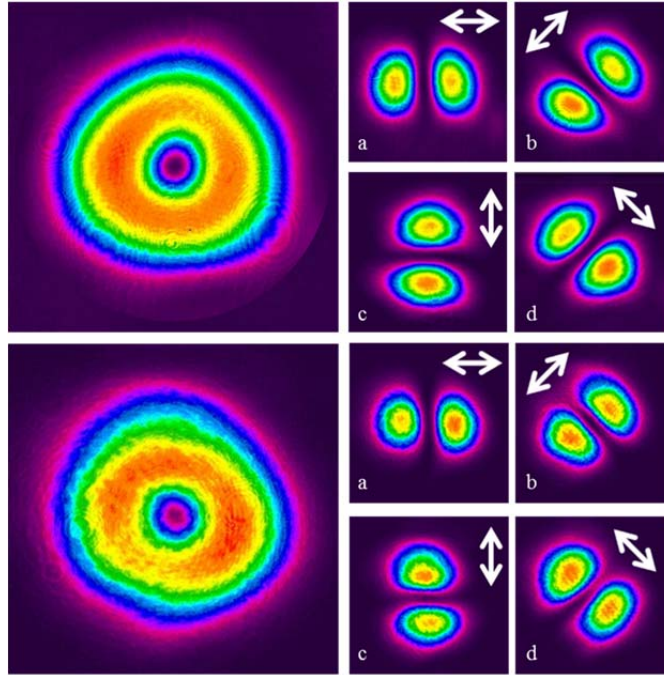

Figure 7.19: Intensity profile of the output beam at maximum gain level and intensity profiles after the beam has passed through a polariser orientated at the angles indicated by the arrows for the 25mW input beam (top) and 1.45W input beam (bottom).
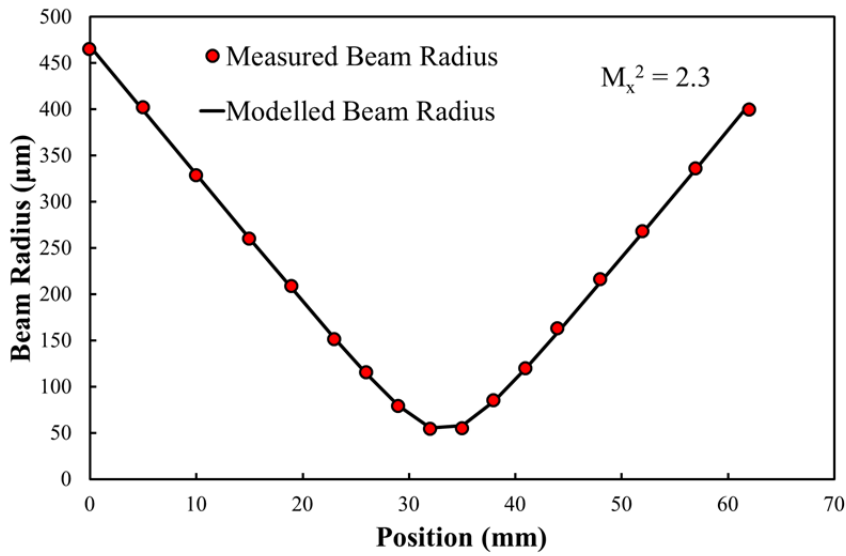
Figure 7.20: Beam quality of lowest seed input power at the maximum gain level.
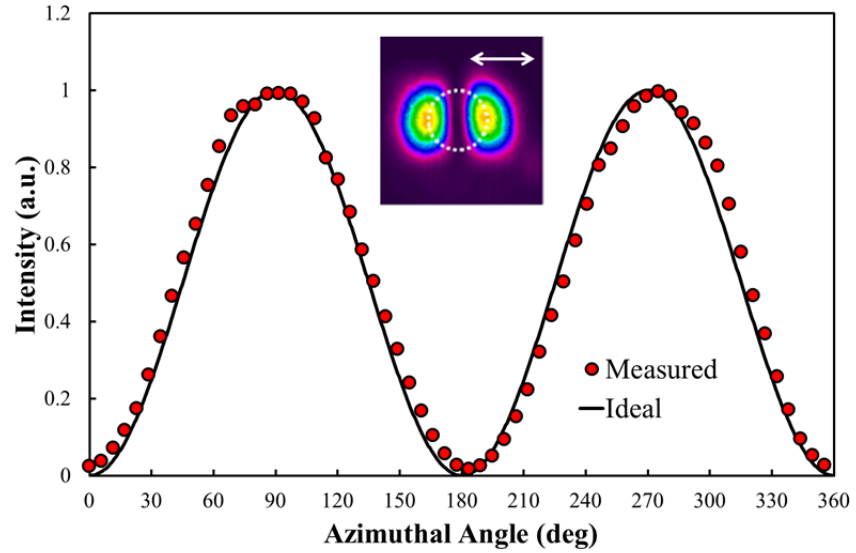
Figure 7.21: Measured and ideal intensity profile as a function of azimuthal angle for the amplified beam after it has passed through a linear polariser orientated in the direction of the arrow.

7.6   Power Scaling Considerations

7.6.1   Pump Overlap

The results from the previous section suggest that amplification of radially polarised beams in a thin-slab architecture is a potential route for power scaling. Transparency within the amplifier was reached at the expected value, and high quality beams were obtained with excellent radial polarisation purity at the maximum pump power. However, the amplifier extraction efficiency was low, and was limited by the available pump power and by non-optimum spatial overlap of the inversion region with the seed beam profile. The seed beam cannot extract inversion in the intensity null central region of the doughnut profile. This is shown schematically in fig. 7.22, where we depict the beam overlap in the slab for an LG_{01} mode with radius w_0 and a top-hat pump beam. Fig. 7.22 (left) shows a two-dimensional representation of the overlap, whilst fig. 7.22 (right) shows the beam intensity profiles through the centre of the beams (white dashed lines). The top-hat approximation is reasonable for the slow axis of the pump beam, however in the fast axis there will be significantly more power in the beam centre, overlapping the region of minimum seed beam power. Therefore, in order to improve the extraction efficiency, pump shaping techniques should be employed to minimise the pump intensity in the central region of the seed beam and maximise the overlap factor between the pump beam and signal mode.

Figure 7.22: Schematic showing the computed overlap of the LG_{01} mode and the approximated top-hat pump mode in the slab shown in two-dimensions (left) and through beam centre (right).

7.6.2 Birefringence Compensation

Excellent radial polarisation purity was maintained up to the maximum power level available for this experiment. However, it is anticipated that as this configur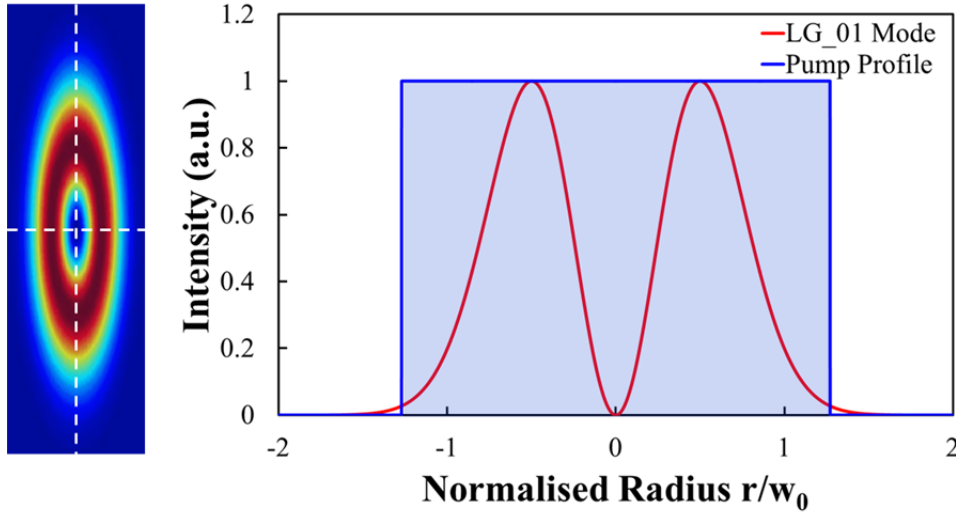ation is scaled to higher pump powers, birefringence will act to depolarise the beam, reducing the purity of the polarisation state. This is the result of thermally-induced stresses within the slab, which are different in the x and y directions, as depicted in fig. 7.23. These stresses produce strains which lead to a different refractive index for the x and y-polarisation state, as a consequence of the photoelastic effect. A beam polarised in the x/y-direction will experience a change in phase, $\Delta\varphi$, of:

$$\Delta\varphi = kn_{x/y}\Delta z \tag{7.11}$$

where k is the wavenumber, given by $k = 2\pi/\lambda$, $n_{x/y}$ is the refractive index in the x/y direction, and Δz is the distance travelled through the slab.

Furthermore, we can consider the impact of this effect on a radially polarised beam propagating through the slab. As in section 7.4.2., we can decompose the radially polarised beam into an in-phase superposition of a x-polarised HG_{10} mode and a y-polarised HG_{01} mode. Fig. 7.24 depicts the phase difference acquired by each HG_{nm} mode, $\Delta\varphi_{nm}$, on the first and second pass through the slab, where l is the length of the slab. In this scenario, after the double-pass, the HG_{10} mode acquires a total phase of $\Delta\varphi_{10} = 2kn_x l$, whilst the HG_{01} mode acquires a total phase of $\Delta\varphi_{01} = 2kn_y l$. Since $n_x \neq n_y$, the phase acquired by each HG_{nm} component is different, and thus the phase relationship between the components is lost, resulting in a depolarisation of the beam. This loss of radial polarisation purity will be exacerbated as the pump power, and thus the birefringence, increases. Note that for the time being, we have neglected the Gouy phase shift.

142
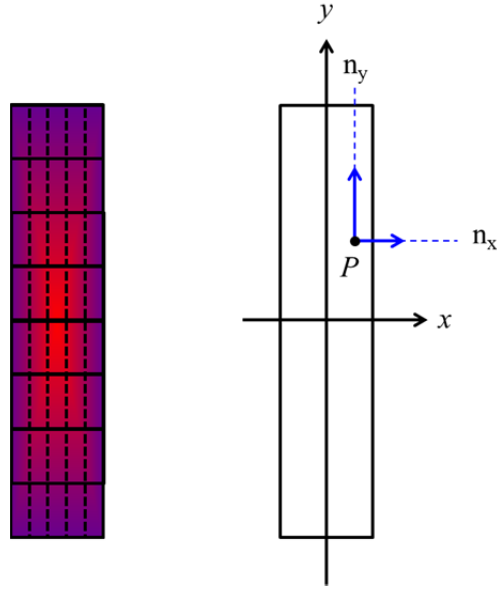
Figure 7.23: Stress distribution across the slab cross-section in the x (solid) and y (dashed) direction (left) and x and y components of the refractive index at point P on the cross-section (right).
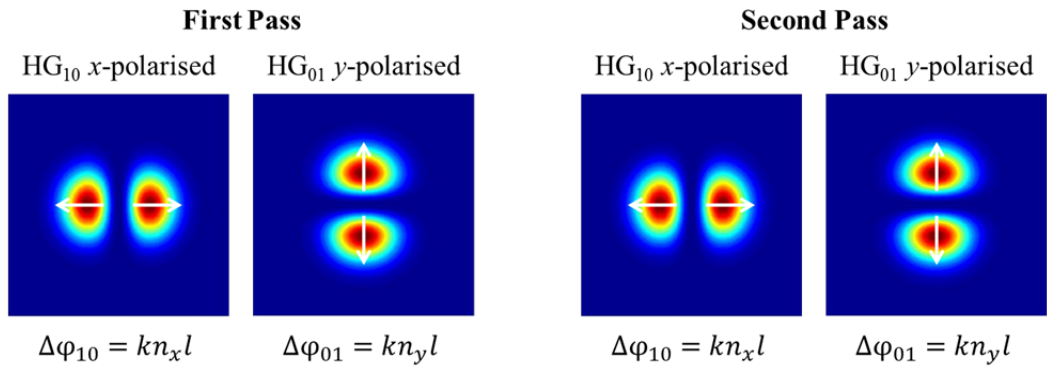
Figure 7.24: Phase acquired for each HG_{nm} component on the first (left) and second (right) pass through the slab.

In light of this reasoning, a conceptual birefringence compensation technique was developed. This technique suggests that the polarisation state of each HG_{nm} mode could be exchanged after the first pass but before the second pass through the slab, as shown in fig. 7.25. Therefore in this instance, the HG_{10} mode would experience a refractive index of n_x on the first pass and n_y on the second pass, whilst the HG_{01} mode would experience a refractive index of n_y on the first pass and n_x on the second pass. Crucially, the total phase seen by each HG_{nm} mode is equal over a double-pass, and is given by $\Delta\varphi_{nm} = k(n_x + n_y)l$. This ensures the phase relationship is maintained between the HG_{10} and HG_{01} mode.
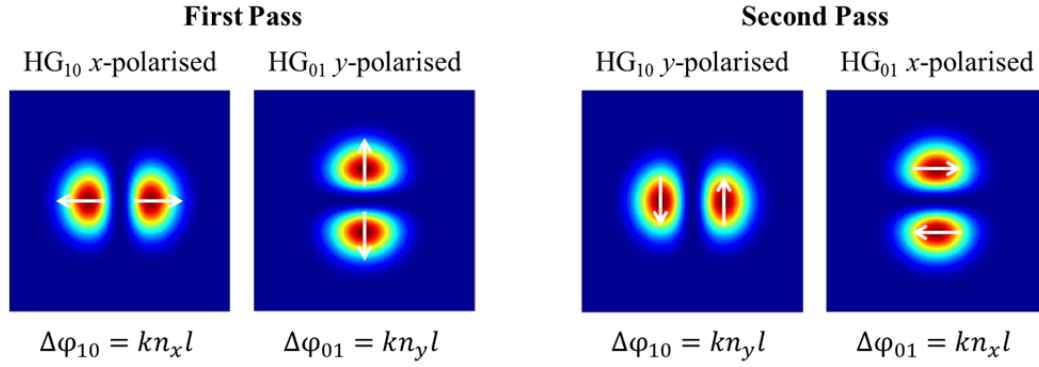
Figure 7.25: Phase acquired by radially polarised beam on the first (left) and second (right) pass through the slab with the polarisation states exchanged between passes.

The polarisation state of each HG_{nm} mode can be exchanged between passes through the slab by inserting a quarter-waveplate between the slab and dichroic mirror. Orientating the quarter-waveplate with its fast or slow axis at 45° to the x-axis will ensure that a double-pass through the waveplate will rotate the polarisation components of each HG_{nm} mode by 90°, achieving the desired effect. The output beam, given by the in-phase superposition of the HG_{nm} components shown in fig. 7.25 (right) has a hybrid polarisation state, similar to that displayed in fig. 7.17 (right) but rotated by 45°. However, the Gouy phase shift forces a further π phase shift between the HG_{nm} components. This is equivalent to reversing the direction of the arrows on one of the HG_{nm} components in fig. 7.25 (right), resulting in an output beam with an azimuthal polarisation state. This azimuthally polarised beam can be converted to a radially polarised beam simply by using a pair of half-waveplates with a 45° angle between the fast axis of each waveplate. This approach is equally valid for amplification of an azimuthally polarised beam.

7.7   Conclusion

In this chapter we have introduced the concept of CV beams, which have a cylindrically symmetric polarisation state across the beam cross-section. The benefits of utilising these beams in materials processing are highlighted, and an explanation of the advantages of cutting metal with radially polarised beams is presented. A seed source which adopts the technique of thermally-induced bi-focusing to allow the radially polarised mode to dominate over the azimuthally polarised mode is described, in addition to the mechanism by which this is possible. Characterisation of the seed source includes the description of a method for quantifying the radial polarisation purity of a beam. The seed source produced a maximum output power of 6.9W, with a conversion efficiency of 41% with respect to absorbed pump power. The beam quality was measured as $M^2 = 2.3$, whilst the RPER was > 15dB.

It was demonstrated that the seed source could be amplified in a highly asymmetric thin-slab gain medium whilst maintaining beam quality and, most importantly, radial polarisation purity. The requirement for astigmatic focusing of the seed laser beam to match the rectangular inversion

region leads to a change in the polarisation that results from different Gouy phase shifts of the constituent orthogonally-polarised HG_{10} and HG_{01} modes. We have shown that this can be compensated in a very simple, power-scalable manner by the inclusion of a half-waveplate in the output beam path. Amplifier experiments yielded a gain of 7.5dB for a 25mW seed input power, and 4.4dB for a 1.45W seed input power, resulting in a maximum output power of 4W. The beam propagation factor at the maximum gain level was maintained at the lowest seed input power at M^2 = 2.3, and was only slightly degraded to M^2 = 2.4 at the highest seed input powers. Crucially, the RPER was maintained at >15dB for both cases.

The overall performance of the amplifier was limited by non-optimum spatial overlap of the inversion profile with the seed beam profile and by available pump power. Noting the power scaling potential of slab gain media, we anticipate that the availability of higher pump power along with further optimisation of the pump beam profile to minimise inversion in the intensity null of the beam centre, should offer a pathway to considerably higher powers. Furthermore, as the concept is scaled to higher pump power, we anticipate birefringence will act to depolarise the beam. Therefore, we suggest a birefringence compensation technique whereby the polarisation state of each HG_{nm} component of the radially polarised beam is exchanged between passes through the slab, ensuring each component experiences the same phase evolution. It is worth pointing out that the techniques presented in this chapter are equally applicable to azimuthally-polarised beams and hence will be of interest for a range of applications, particularly laser processing of materials, where high power CV beams can yield significant benefits.

References

1. Y.I. Salamin, "Electron acceleration from rest in vacuum by an axicon Gaussian laser beam," Phys. Rev. A **73**, 043402 (2006).

2. Q. Zhan, "Trapping metallic Rayleigh particles with radial polarization," Opt. Expr. **12**, 3377 (2004).

3. Q. Zhan, "Cylindrical vector beams: from mathematical concepts to applications," Adv. Opt. Photon. **1**, 1 (2009).

4. V.G. Niziev, A.V. Nesterov, "Influence of beam polarization on laser cutting efficiency," J. Phys. D: Appl. Phys. **32**, 1455 (1999).

5. M. Meier, V. Romano, T. Feurer, "Material processing with pulsed radially and azimuthally polarized laser radiation," Appl. Phys. A **86**, 329 (2007).

6. R. Weber, A. Michalowski, M. Abdou-Ahmed, V. Onuseit, V. Rominger, M. Kraus, T. Graf, "Effects of Radial and Tangential Polarization in Laser Material Processing," Phys. Procedia **12**, 21 (2011).

7. Refractive index database, "Refractive index of aluminium" (2017), retrieved https://refractiveindex.info/?shelf=3d&book=metals&page=aluminium.

8. A. Loescher, J. P. Negel, T. Graf, M. A. Ahmed, "Radially polarized emission with 635W of average power and 2.1 mJ of pulse energy generated by an ultrafast thin-disk multipass amplifier," Opt. Lett. **40**, 5758 (2015).

9. M. Fridman, M. Nixon, M. Dubinskii, A. A. Friesem, N. Davidson, "Fiber amplification of radially and azimuthally polarized laser light," Opt. Lett. **35**, 1332 (2010).

10. S. Kanazawa, Y. Kozawa, S. Sato, "High-power and highly efficient amplification of a radially polarized beam using an Yb-doped double-clad fiber," Opt. Lett. **39**, 2857 (2014).

11. S. Piehler, X. Délen, M. Rumpel, J. Didierjean, N. Aubry, T. Graf, F. Balembois, P. Georges, M. A. Ahmed, "Amplification of cylindrically polarized laser beams in single crystal fiber amplifiers," Opt. Expr. **21**, 11376 (2013).

12. I. Moshe, S. Jackel, A. Meir, "Production of radially or azimuthally polarized beams in solid-state lasers and the elimination of thermally induced birefringence effects," Opt. Lett. **28**, 807 (2002).

13. W. Koechner, Solid-State Laser Engineering, 6 ed., Sixth Revised and Updated Edition (Springer, 2006).

14. P. Russbueldt, T. Mans, G. Rotarius, J. Weitenberg, H. D. Hoffmann, R. Poprawe, "400 W Yb:YAG Innoslab fs-amplifier," Opt. Expr. **17**, 12230 (2009).

15. P. Russbueldt, T. Mans, J. Weitenberg, H.D. Hoffmann, R. Poprawe, "Compact diode-pumped 1.1 kW Yb:YAG Innoslab femtosecond amplifier," Opt. Lett. **35**, 4169 (2010).

16. J. W. Kim, J. I. Mackenzie, J. R. Hayes, W. A. Clarkson, "High power Er:YAG laser with radially-polarized Laguerre-Gaussian (LG01) mode output," Opt. Expr. **19**, 14526 (2011).

17. D. Pohl, "Operation of a Ruby laser in the Purely Transverse Electric Mode TE01," Appl. Phys. Lett. **20**, 266 (1972).

18. J. F. Bisson, J. Li, K. Ueda, "Radially polarized ring and arc beams of a neodymium laser with an intra-cavity axicon," Opt. Expr. **14**, 3304 (2006).

19. Y. Kozawa, S. Sato, "Generation of a radially polarized laser beam by use of a conical Brewster prism," Opt. Lett. **30**, 3063 (2005).

20. M. A. Ahmed, A. Voss, M. Vogel, T. Graf, "Multilayer polarizing grating mirror used for the generation of radial polarization in Yb:YAG thin-disk lasers," Opt. Lett. **32**, 3272 (2007).

21. D. Lin, J. M. O. Daniel, M. Gecevičius, M. Beresna, P. G. Kazansky, W. A. Clarkson, "Cladding-pumped ytterbium-doped fiber laser with radially polarized output," Opt. Lett. **39**, 5359 (2014).

22. S. C. Tidwell, D. H. Ford, W. D. Kimura, "Generating radially polarized beams interferometrically," Appl. Opt. **29**, 2234 (1990).

23. G. Machavariani, Y. Lumer, I. Moshe, A. Meir, S. Jackel, "Spatially-variable retardation plate for efficient generation of radially- and azimuthally-polarized beams," Opt. Commun. **281**, 732 (2008).

24. D. Lin, "Doughnut-shaped beam generation in solid-state and fibre lasers," (PhD thesis, 2015).

25. M. W. Beijersbergen, L. Allen, H. E. L. O. van der Veen, J. P. Woerdman, "Astigmatic laser mode converters and transfer of orbital angular momentum," Opt. Commun. **96**, 123 (1993).

26. R. Paschotta, "YAG Lasers" (2017), retrieved https://www.rp-photonics.com/yag_lasers.html.

27. N. P. Barnes, B. M. Walsh, "Quantum efficiency measurements of Nd:YAG, Yb:YAG, and Tm:YAG," ASSL Quebec City, (2002).

Chapter 8   Conclusion

The ability to produce high power laser radiation is essential to numerous industries. Solid-state lasers are capable of producing multi-kW power levels with excellent beam quality. However, as the output power is scaled various deleterious effects stemming from thermal gradients or nonlinear processes can act to reduce performance. The aim of this thesis was to develop novel power scaling solid-state architectures within the bulk and fiber regime to achieve high power operation.

8.1   Conclusion

This thesis begins with a short introduction in Chapter 1, covering the relevant history in the story of the laser. Various applications for lasers are discussed, along with the unique and desirable properties of these fascinating devices. The requirement for high power operation is stressed, and several examples of high power solid-state designs are presented.

Chapter 2 introduces relevant background theory for high power laser operation. The interaction of light and matter is described on the atomic scale, covering the principle of gain and various energy level systems. An expression describing the performance of a laser in terms of output power is derived, followed by the introduction of the modes of a laser resonator. The chapter then discusses prevalent limitations for power scaling laser devices, covering thermal and nonlinear effects. This leads into a description and justification of bulk devices, including the rod, slab and thin-disc laser, and fiber devices. The relevant advantages and disadvantages of each architecture are presented. It is apparent that although both bulk and fiber lasers can achieve multi-kW power levels with excellent beam quality, neither is without limitation.

In light of the discussion in Chapter 2, Chapter 3 introduces the concept of the TGFR. This device occupies a domain between traditional fiber and bulk rod devices, with the intention of capitalising from the impressive thermal management properties of fiber lasers, whilst enjoying reduced nonlinearities due to a larger beam size and shorter device length. Thermally-induced guiding is suggested as a mechanism for mode control and therefore a model is presented which is capable of predicting the beam evolution through the TGFR device for various pumping arrangements. Additionally, a gain model is introduced, which allows the amplifier and laser performance of the TGFR to be predicted.

Chapter 4 suggests soft glass as the host material for the TGFR. The excellent solubility of rare-earth ions compared to silica can allow for short device lengths, therefore reducing nonlinearities. Furthermore, these glasses and ultimately the TGFR devices can be produced with very uniform compositions, presenting a second advantage over silica. The fabrication of soft glass was

described, with particular emphasis placed on the relevant thermal properties that should be optimised, namely the transition temperature, the crystallisation temperature and the coefficient of thermal expansion. Three glass sources are identified, with each one being drawn into appropriate dimensions for TGFR experiments. In this stage it was apparent that glass homogeneity and compatibility between the various glasses may present serious limitations.

In Chapter 5 the three TGFR devices are characterised in terms of power scaling potential. Initially, a tunable fiber laser is introduced, which acted as a seed source for gain and loss experiments, and also as a probe beam to investigate the thermally-induced guiding concept in Chapter 6. Overall, the devices performed poorly. The Source I device, which consisted of an amplifier constructed from in-house fabricated Nd:phosphate displayed considerably high propagation losses of 11dB/m. This high propagation loss is believed to be due to contaminants in the glass. Furthermore, the dimensions of the drawn glass were not optimised for performance, and thus small-signal gain measurements resulted in a small-signal gain of -0.14dB (i.e. a loss) for 31.5W of launched pump power. The gain model predicted a gain of 11.9dB would be possible in this device for the same heat loading per unit length and propagation losses, if the dimensions were to be reduced from a 700μm square cross-section to a 200μm diameter core, 400μm diameter cladding structure. The Source II device consisted of Nd:silicate core and an undoped silicate cladding. These glasses were not well-matched in terms of fabrication properties, and consequently crystallisation and damage occurred at the core/cladding and the cladding/water interface. A Findlay-Clay analysis revealed that propagation losses were extremely high at 13dB/m, leading to very poor laser performance with a maximum slope efficiencies just 3.9%. The Source III device was a Nd:phosphate provided by the Politecnico di Torino, and displayed the lowest losses of the three source, with the Findlay-Clay analysis revealing a 5.7dB/m loss. However, this glass displayed very poor homogeneity, and it was not possible to pass a beam through a 20mm long section of device with serious degradation. Operating as a laser, this device achieved a maximum power of 2.5W, with a corresponding slope efficiency of 28.5%. It was predicted that if the losses were reduced to 1dB/m the efficiency of the device would almost double. Due to the high losses and poor homogeneity of these devices, the thermal-guiding concept was not explored.

In order to fully test the TGFR concept, an extra-large mode area Yb:silica fiber was procured, as introduced in Chapter 6. A description of an end-capping set-up is presented, essential to reducing Fresnel losses from the end faces of the TGFR. Whilst investigating the thermal-guiding concept it became apparent that the refractive index profile across the core was slightly parabolic, leading to in-built guiding within the device. The thermally-induced guiding concept was then investigated, and good agreement was observed between the predicted and measured data. As an amplifier the device also displayed encouraging performance, agreeing well with predict gain values producing a small-signal gain of 4.1dB at 976nm and 5.0dB at 1030nm for a launched maximum pump power of approximately 50W. The guiding and gain data suggested these devices would perform well in a

laser configuration. Simple laser devices were constructed with 13.1W achieved at 1032.5nm with a slope efficiency with respect to launched power of 44%, and 1W at 978.5nm with a slope efficiency with respect to launched power of 8%. The threshold powers of these lasers agreed well with those predicted from the gain modelling. Excellent beam quality, $M^2 < 1.1$, was achieved at maximum power for both laser devices. The low slope efficiency of the 978.5nm device can at least partially be explained by the very close proximity to threshold.

Finally, Chapter 7 explores another power scaling concept. Here, we are concerned with generating high power CV beams which have promising applications in materials processing. Traditionally, CV beams have been amplified in devices with cylindrical symmetry in order to preserve the polarisation. However we propose amplification of these beams in an Yb:YAG thin-slab architecture, with the intention of utilising the slab geometry to obtain high output powers. A seed source was developed, which utilised thermally-induced bi-focusing to emit a radially polarised beam with a maximum power of 6.9W and a conversion efficiency of 41% with respect to absorbed pump power. This beam displayed a beam propagation factor of $M^2 = 2.3$ which is close to the theoretical value of 2, and displayed excellent radial polarisation purity with RPER > 15dB. The seed beam amplified in the thin-slab maintained beam quality and polarisation purity, thus demonstrating the validity of this concept. Astigmatic focusing of the seed beam resulted in a loss of polarisation owing to the Gouy phase shift, which was compensated for by the inclusion of a half-waveplate. A gain of 7.5dB was achieved for a 25mW seed input power, and 4.4dB for a 1.45W seed input power, resulting in a maximum output power of 4W. The beam propagation factor at the maximum gain level was maintained at the lowest seed input power at $M^2 = 2.3$, and was only slightly degraded to $M^2 = 2.4$ at the highest seed input powers. Crucially, the RPER was maintained at >15dB for both cases. The non-ideal overlap between the seed beam and pumped region was a limiting factor for power extraction.

8.2　　Future Work

The work presented in this thesis opens the door to many exciting future prospects. The concept of the TGFR performed well with the extra-large mode area silica fiber. To realise this concept in soft glass, a source of high quality glass should be identified which is appropriate for the intended fabrication. Ideally, this glass would be manufactured in-house, thus allowing an entirely holistic process whereby the glass is manufactured, devices are developed and laser experiments are conducted. This would provide strong control over the desired performance, and potential problems downstream could be traced to their source. Unfortunately there was only time to conduct very simple laser experiments with the silica based TGFR. However, future experiments could involve Q-switched operation, to capitalise on the large pulse energy potential of this device. Additionally,

amplification of radially polarised beams within the device could offer a promising route to high power operation.

The amplification of radially polarised beams in the slab amplifier was limited in terms of performance due to a non-ideal overlap. This could be improved through the use of pump-shaping techniques to reduce the power in the intensity null of the seed beam. Additionally, higher pump power would improve extraction. We anticipate that birefringence will eventually become an issue, and therefore suggest a birefringence compensation technique based on exchanging the polarisation state of the constituent HG_{nm} modes between the first and second pass through the slab.

Appendix

Appendix P

Journal Papers

1. <u>C. R. Smith</u>, S. J. Beecher, J. I. Mackenzie, W. A. Clarkson, "Amplification of a radially polarised beam in an Yb:YAG thin-slab," Appl. Phys. B. (2017).

2. E. Ceci-Ginistrelli, <u>C. Smith</u>, D. Pugliese, J. Lousteau, N.G. Boetti, W.A. Clarkson, F. Poletti, D. Milanese, "Nd-doped phosphate glass cane laser: from materials fabrication to power scaling tests," J. Alloys Compd. **722**, 599 (2017).

3. <u>C. R. Smith</u>, N. Simakov, A. Hemming, W. A. Clarkson, "Thermally-guided fiber-rod laser," (In progress).

Conference Papers

1. M.Eckold, <u>C.R.Smith</u>, J.I.Mackenzie, W.A.Clarkson, "Power scaling of solid-state lasers using a rotating cavity configuration," EuroPhoton, Neuchatel (2014).

2. <u>C. R. Smith</u>, S. J. Beecher, J. I. Mackenzie, W. A. Clarkson, "Amplification of a radially-polarised beam in an Yb:YAG thin-slab architecture," EuroPhoton, Vienna (2016).

3. <u>C. R. Smith</u>, S. J. Beecher, J. I. Mackenzie, W. A. Clarkson, "Radially-polarised beam amplification in an Yb:YAG thin-slab architecture," Photonics West, San Francisco (2017).

4. <u>C. R. Smith</u>, S. J. Beecher, J. I. Mackenzie, W. A. Clarkson, "Radially-polarised beam amplification in an Yb:YAG thin-slab architecture," ILAS, Grantham (2017).

5. <u>C. R. Smith</u>, N. Simakov, A. Hemming, W. A. Clarkson, "Thermally-guided fiber-rod laser," CLEO Europe (2017).

6. <u>C. R. Smith</u>, T. Jefferson-Brain, N. Simakov, A. Hemming, W. A. Clarkson, "Thermally-guided ytterbium-doped fiber-rod laser," Photonics West, San Francisco (2018) [Accepted].

Appendix

Appendix 3.1

Assuming that the coolant is water, which is housed in a concentric flowtube and creates a turbulent flow over the TGFR, then h_T can be approximated by [1]:

$$h_T = 10.47 \times 10^{-3} \frac{\left(\frac{D_{HS}}{D_L}\right)^{0.53}}{(D_{HS} - D_L)(D_{HS} + D_L)^{0.8}} F_R^{08} \qquad (3A.1)$$

where h_T is given in W/cm.K, D_{HS} is the inner diameter of the flowtube in cm, D_L is the diameter of the TGFR in cm, and F_R is the flowrate in cm^3/s. For the example given in figure 3.3, $D_{HS} = 4$cm, $D_L = 0.048$cm, $F_R = 10$cm^3/s, resulting in $h_T = 0.057$W/cm.K or 570W/m.K.

Appendix 3.2

Oscillation Period

The oscillation period, d_o, can be found simply by considering equation 3.7 and the relevant ABCD matrix. By considering only the sinusoidal components of the ABCD factors, it is apparent that factors A and D are out of phase with B and C by $\pi/2$. If we consider the beam at position 1, with complex q-parameter, q_1, and the beam at position 2 after exactly one oscillation, with complex q-parameter, q_2. The beam is identical after one oscillation therefore, $q_1 = q_2$. To balance equation 3.7, we can set A = 1, B = 0, C = 0 and D = 1, or A = -1, B = 0, C = 0 and D = -1. Since A and D repeat this cycle every π radians, it is clear that one oscillation is separated by:

$$d_o = \pi \sqrt{\frac{n_m}{n_{th}}} \qquad (3A.2)$$

and since n_{th} is proportional to P_H, we conclude that d_o is proportional to $1/\sqrt{P_H}$.

Beam Waist Product

Consider the minimum beam waist, w_{min}, at position $d_1 = 0$, and the maximum beam size, w_{max}, half an oscillation further on at $d_2 = d_o/2$. From equation 3.7 it follows that:

$$w_{min} w_{max} = \frac{\lambda}{\pi} \frac{1}{\sqrt{n_m n_{th}}} \qquad (3A.3)$$

thus it follows that $w_{min}.\ w_{max}$ is proportional to $1/\sqrt{P_H}$.

Perfect Guidance

If we specify that the input and output beams are equal waists, w_p, we can use equation 3.7 to write:

Appendix

$$q = \frac{Aq + B}{Cq + D}\frac{D - Cq}{D - Cq} \qquad (3A.4)$$

Considering that $q = i\pi w_p/\lambda$, and that AD – BC = 1, we can equate imaginary parts of 3A.4 to obtain equation 3.11.

Appendix 3.3

Differentiating equation 3.12 for with respect to z, and evaluating in the limit of $z \rightarrow 0$, we obtain the rate of change of pump power per unit distance, dPp/dz, given by:

$$\frac{dP_P}{dz} = -n_1\sigma_{pa}P_{P0} \qquad (3A.5)$$

Dividing equation 3A.5 by the area of the pump beam, we obtain the pump power absorbed per unit volume:

$$\frac{dP_P}{dV} = -n_1\sigma_{pa}I_{P0} \qquad (3A.5)$$

Since power is equal to the energy per unit time, per unit area, we can thus deduce that the pump rate density can be written as equation 3.18.

Appendix 3.4

Intensity is equal to energy per unit time per unit area. The total energy of the laser radiation, E_T, is given by:

$$E_T = \Phi h\nu \qquad (3A.6)$$

Thus dividing equation 3A.6 by area, A, and time, $t = z/c$, and using the fact that volume $V = Az$, we obtain the intensity given in equation 3.19.

Appendix 5.1

Fig. 5A.1 shows the laser cavity formed from an active fiber and two mirrors with reflectivity R_1 and R_2, with a power P_1 emitted from the mirror with R_1 and P_2 emitted from the mirror with R_2. We can simply follow the power evolution through the fiber, starting from R_1 and travelling to the right. At R_2 the power in the fiber has grown by an amount G accounting for the gain. A fraction (1 – R_2) is then coupled out at R_2 allowing equation 5A.1 to be written. The remaining power travels

left, again increasing in power by G when it reaches R_1, where a fraction $(1 - R_1)$ is coupled out, allowing equation 5A.2 to be written.
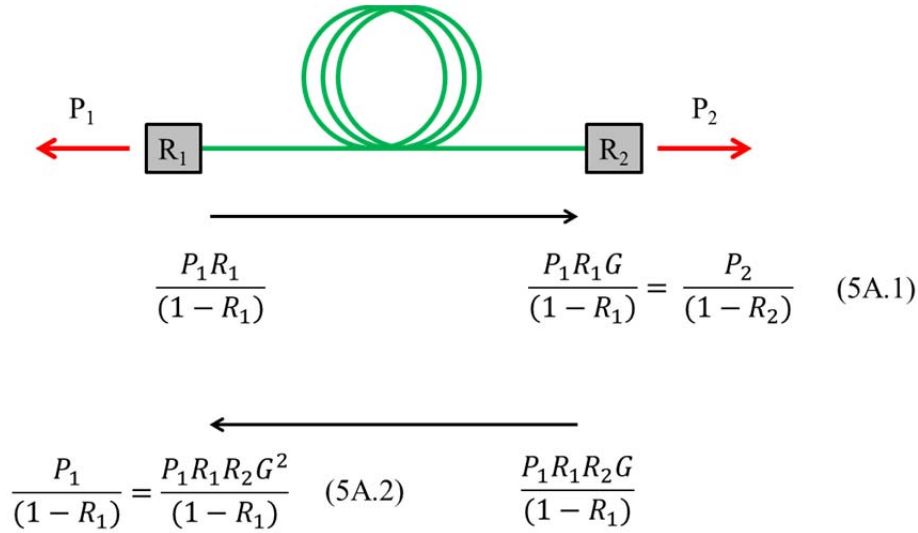

$$\frac{P_1 R_1}{(1 - R_1)} \qquad \frac{P_1 R_1 G}{(1 - R_1)} = \frac{P_2}{(1 - R_2)} \qquad \text{(5A.1)}$$

$$\frac{P_1}{(1 - R_1)} = \frac{P_1 R_1 R_2 G^2}{(1 - R_1)} \qquad \text{(5A.2)} \qquad \frac{P_1 R_1 R_2 G}{(1 - R_1)}$$

Figure 5A.1: Power evolution in fiber laser configuration.

From Equation 5A.2 we can conclude:

$$R_1 R_2 G^2 = 1 \qquad \qquad \text{(5A.3)}$$

which allows us to rewrite equation 5A.1 to give the desired relation:

$$\frac{P_1}{P_2} = \frac{1 - R_1}{1 - R_2} \sqrt{\frac{R_2}{R_1}} \qquad \qquad \text{(5A.4)}$$

Appendix 6.1

Since the beam is at a waist q is purely imaginary. In order to write equation 6.1 in terms of real and imaginary parts, one can multiply the numerator and denominator by $D - Cq$, to obtain:

$$q = \frac{q(AD - BC)}{D^2 - q^2 C^2} \qquad \qquad \text{(6A.1)}$$

Since the determinant is equal to unity, therefore equation 6A.1 can be rewritten as:

$$q^2 = \frac{D^2 - 1}{C^2} = -\frac{\pi^2 w_{M1}^4}{\lambda^2} \qquad \qquad \text{(6A.2)}$$

which can be rearranged in terms of w_{MI} as presented in equation 6.2.